

In-situ Environmental Transmission Electron
Microscopy Investigation of Perovskite Oxide
Thin Films During Electrochemical Oxygen
Evolution Reaction.

Dissertation
for the award of the degree
"Doctor rerum naturalium" (Dr.rer.nat.)
of the Georg-August-Universität Göttingen

within the doctoral program of physics
of the Georg-August University School of Science (GAUSS)

submitted by
Gaurav Lole
from Pune, India

Göttingen, 2022

Thesis Committee:

Prof. Dr. Christian Jooss
Institut für Materialphysik, Georg-August-Universität Göttingen

Prof. Dr. Michael Seibt
IV. Physikalisches Institut, Georg-August-Universität Göttingen

Prof. Dr. Simone Techert
Institut für Röntgenphysik, Georg-August-Universität Göttingen
Deutsches Elektronensynchrotron DESY, Hamburg

Members of the Examination Board:

Reviewer: Prof. Dr. Christian Jooss
Institut für Materialphysik, Georg-August-Universität Göttingen

Second Reviewer: Prof. Dr. Michael Seibt
IV. Physikalisches Institut, Georg-August-Universität Göttingen

Further members of the Examination Board:

Prof. Dr. Simone Techert
Institut für Röntgenphysik, Georg-August-Universität Göttingen
Deutsches Elektronensynchrotron DESY, Hamburg

Prof. Dr. Peter Blöchl
Institut für Theoretische Physik, TU Clausthal
Institut für Theoretische Physik, Georg-August-Universität Göttingen

Prof. Cynthia A. Volkert, PhD
Institut für Materialphysik, Georg-August-Universität Göttingen

Prof. Dr. Vasily Moshnyaga
I. Physikalisches Institut, Georg-August-Universität Göttingen

Date of the oral examination: 15.02.2022

Contents

1	Introduction	1
1.1	Hydrogen, a future energy source	1
1.2	Electrochemical Oxygen Evolution Reaction (OER)	3
1.3	Cost effective and low overpotential catalyst	5
1.4	Challenges for this thesis	6
1.4.1	Studying the real dynamical structure of the water - electrode interface	6
1.4.2	Active sites	7
1.4.3	Formation of the active sites on the surface	8
1.4.4	Defect reactions	9
1.4.5	Connection to stability and corrosion	10
2	Oxide catalyst for Oxygen Evolution Reaction	12
2.1	Binary oxides	12
2.2	Scaling relation	13
2.3	Perovskite oxides	14
2.4	OER mechanism in Perovskites	15
3	Transmission Electron microscopy	18
3.1	Contrast mechanism in HRTEM	18
3.1.1	Two beam condition	19
3.1.2	Kinematical and Dynamical diffraction conditions	20
3.1.3	Lens Aberrations and Phase contrast	22
3.1.4	Image (C_s) corrector and Image simulation	24
3.2	Electron Energy Loss Spectroscopy (EELS)	31
3.2.1	Elastic and inelastic scattering	32
3.2.2	EELS instrumentation	33
3.2.3	Zero loss peak (ZLP) and Thickness of the specimen	34
3.2.4	EELS spectrum	37
3.2.5	Dual-EELS mode	38
3.2.6	Core loss excitations	38

3.2.7	Electron Monochromator for EELS	40
3.3	Environmental Transmission Electron microscopy (ETEM)	41
3.4	Sample preparation for the ETEM	44
3.4.1	Focused Ion Beam (FIB)	44
3.4.1.1	Dual-Beam approach	45
3.4.1.2	Ga ion - material interaction	46
3.4.2	Precision Ion Polishing System (PIPS)	47
3.4.3	Plasma Cleaning	48
4	In Situ Preparation of $\text{Pr}_{1-x}\text{Ca}_x\text{MnO}_3$ and $\text{La}_{1-x}\text{Sr}_x\text{MnO}_3$ Cat- alysts Surface for High-Resolution Environmental Transmission Electron Microscopy	50
5	Dynamic observation of manganese adatom mobility at perovskite oxide catalyst interfaces with water	67
6	Contrasting $\text{Pr}_{1-x}\text{Ca}_x\text{MnO}_3$ OER catalyst with different valence and covalence: $x = 0.1$ and $x = 0.33$	78
7	Atomistic insights into activation and degradation of $\text{La}_{0.6}\text{Sr}_{0.4}\text{CoO}_{3-\sigma}$ electrocatalysts under oxygen evolution condi- tions	104
8	Discussion and Summary	122
	Appendix A Supplementary Information	125
A.1	In-situ surface preparation	125
A.1.1	Supporting Movies	137
A.2	Dynamic observation of manganese adatom mobility	138
A.2.1	Supporting Movies	160
A.3	Contrasting $\text{Pr}_{1-x}\text{Ca}_x\text{MnO}_3$ OER catalysis	161
A.3.1	Supporting Movies	172
A.4	$\text{La}_{0.6}\text{Sr}_{0.4}\text{CoO}_3$ surface dynamics	173
A.4.1	Supporting Movies	183
	References	184
	List of figures	204
	List of Tables	205

Author contributions and publications	208
List of Abbreviations	209
Acknowledgments	210

Chapter 1

Introduction

1.1 Hydrogen, a future energy source

An acceleration in global energy demand and extended dependence on fossil fuels for energy production and transportation, are responsible for a global energy crisis [1–3]. The immoderate burning of fossil fuels depletes natural resources, and it plays a significant role in carbon dioxide emissions [4]. Using natural gas to produce Hydrogen, consumes a large number of natural resources and contributes to increasing the greenhouse effect [5, 6]. Experts assume these processes are accountable for rising average global land-ocean temperatures [7–10] [Fig. 1.1]. Hydrogen is perceived in compounds and produced by decomposition or conversion of other molecules such as hydrocarbons or water splitting. Transforming hydrogen to electric energy using a fuel cell produces only water and heat as a byproduct [Fig. 1.2]. Therefore, hydrogen and fuel cells may play an essential role in the future energy strategy for various applications across all areas, e.g., transport, industry, and domestic field [5]. Possessing high efficiency and almost zero carbon emissions, hydrogen can reduce greenhouse gas emissions [4]. Despite being the most abundant element on the earth, elemental hydrogen is not available in significant quantities. However, several other fundamental difficulties must be overcome for hydrogen to be adopted widely in future green energy infrastructure [11].

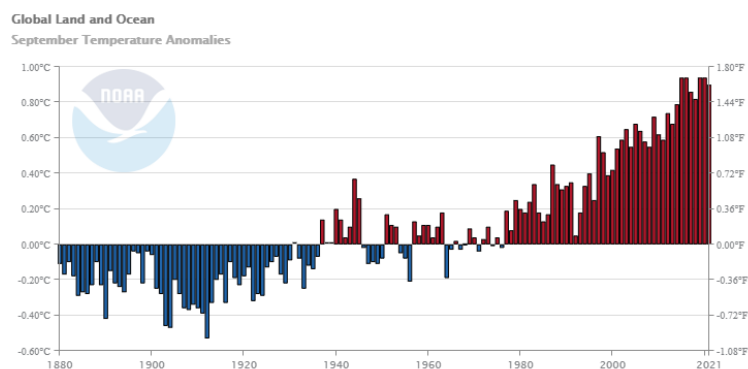


Figure 1.1: Annually global land and ocean temperature correlation to the 20th-century aggregate from 1880–2021. Cold years are indicated by blue bars ; red bars indicate hotter years. Reprinted with permission from [12].

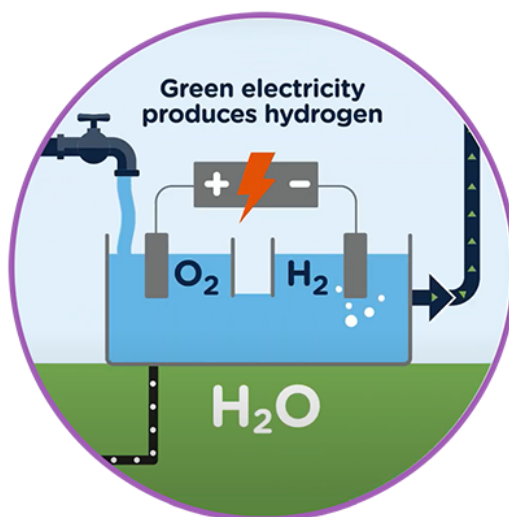


Figure 1.2: Electrocatalytic water splitting uses electricity to produce hydrogen, leaving out water as a byproduct. Reprinted with permission from [13].

To fulfill the increasing energy demand, we need to consider the future potential for a range of renewable methods such as environment friendly, onshore and off-shore wind, hydroelectric energy, wave and tidal energy, geothermal energy, solar and electrochemical energy [6] [Fig. 1.3]. Electrochemical water splitting (EWS) is a reliable technique to produce clean and sustainable hydrogen from water. Production of hydrogen relies on the low-cost catalyst, low overpotential, the highly active, and stable catalyst for oxygen evolution reaction (OER)/ hydrogen evolution reaction (HER).

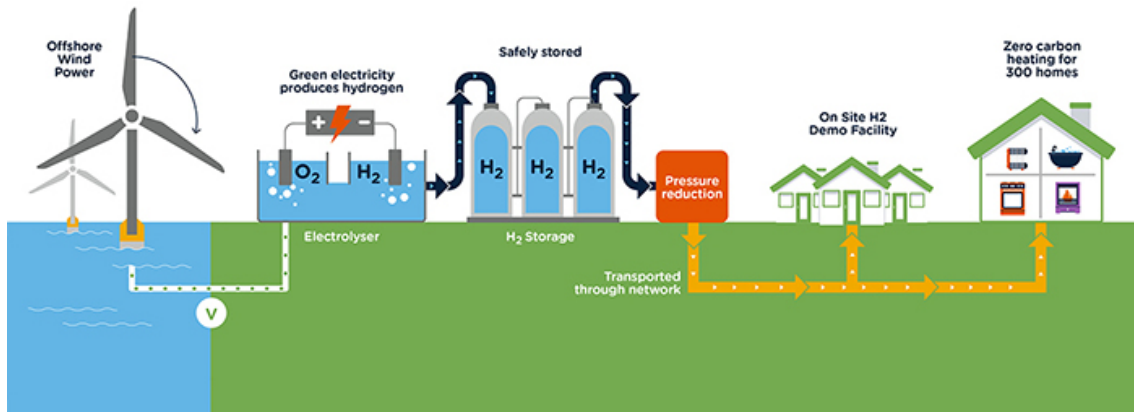


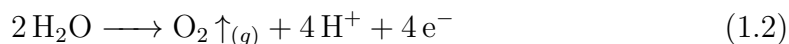
Figure 1.3: Green hydrogen production, storage, and transportation for the domestic use. Reprinted with permission from [13].

1.2 Electrochemical Oxygen Evolution Reaction (OER)

Electrochemical water splitting (EWS) is one of the promising techniques to produce hydrogen in a more convenient, affordable, and sustainable way. All other methods have drawbacks as they suffer from corrosion, sensitivity, and purity for hydrogen production. For example, steam reforming of hydrocarbon generates byproducts of CO₂, CO and sulfur oxides, along with hydrogen. Photochemical hydrogen production is the slowest technique amongst all. Precursors and reagents experience corrosion via metal hydride acid hydrolysis. Furthermore, these techniques also need high temperature and pressure [14]. Large-scale production of bulk hydrogen could be achieved through EWS [15]. Electrolysis is well-suited to pair with renewable energy sources such as wind and solar energy [3]. A typical EWS process includes two half cell reactions, the OER occurs at the anode, and HER at the cathode [Fig. 1.4]. The efficiency of both the OER and HER process depends on the electrolyte solutions (i.e., acidic or alkaline), and catalyst materials. The overall water-splitting reaction can be represented as shown below,



Equation 1.1 shows the overall reaction of electrochemical water splitting process, this reaction splits into two half cell reactions,





The equations 1.2 represents OER at the anode and equation 1.3 shows HER at the cathode. Among the two half-cell reactions of water splitting, the anodic OER typically requires a large overpotential [16]. The theory implies that the OER should happen at 1.23 V versus reversible hydrogen electrode (RHE), while the HER should operate at 0 V versus RHE [14, 17]. Despite this, due to the sluggish kinetics of OER in alkaline environments, the required potential of a OER is larger than 1.23 V, even with the highly active noble metal electrocatalysts [16, 18].

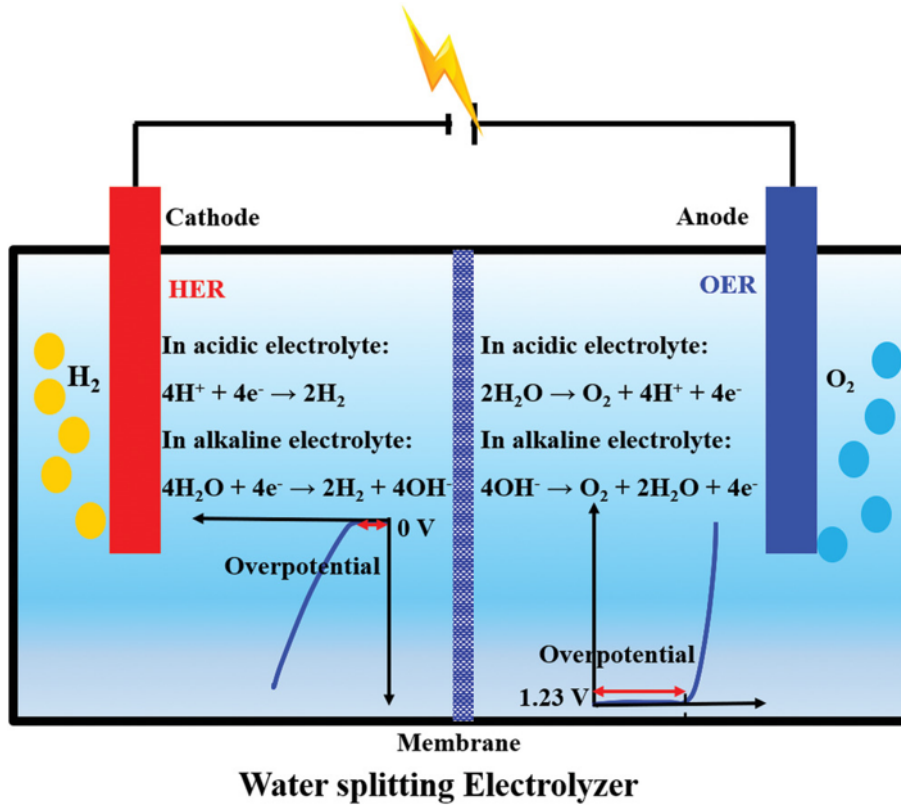
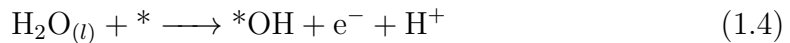
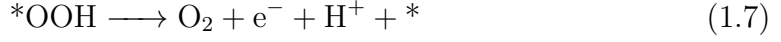
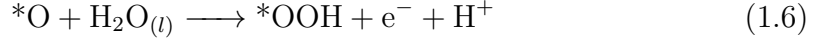


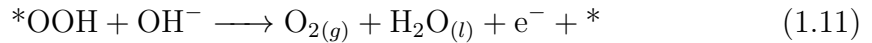
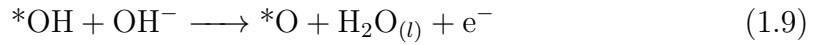
Figure 1.4: Schematic drawing of the electrocatalytic water splitting and reaction kinetics of HER and OER. Reprinted with permission from ref [19] Copyright © 2019 WILEY-VCH Verlag GmbH and Co. KGaA, Weinheim.

In OER, O₂ is generated via four electron coupled proton transfer processes (ECPT). The OER is highly pH-sensitive. The standard OER mechanism in the acidic condition is shown as follows [14, 20],





The mechanism in alkaline or neutral media shown is below [14, 20],



The * indicate the active site on the catalyst surface. Due to the high thermodynamic limitation, it is difficult for the newly formed intermediate *O, to produce a molecular oxygen immediately [18, 20]. In alkaline condition in OER, an active site on the electrocatalyst surface adsorbs hydroxyl radical to produce a *OH radical. An intermediate of *O is generated after eliminating coupled proton and electron from *OH. The nucleophilic attack of OH⁻ on *O yields another intermediate *OOH in the next step. Eventually, another ECPT procedure yields one oxygen molecule [21]. The OER process manifest a significantly faster reaction rate in alkaline condition than in acidic [17, 22]. Due to the complex nature of the four-electron transfer kinetics, the OER is considered a much more complicated process than HER. Thus, it is regarded as the bottleneck of the electrochemical water-electrolysis system.

1.3 Cost effective and low overpotential catalyst

Electrochemical water splitting (EWS) seems superior for hydrogen production until the cost-effectiveness come into focus. High OER efficiency is achieved by circumventing high energy due to the overpotential in water electrolysis. This can only be possible with discovering electrocatalytic materials for HER and OER by attuning and improving their electrocatalytic properties [14]. The cost-efficiency of large scale EWS depends on the electrode materials used to fabricate cathode and anode. In the early eighties and nineties, expensive nopal metals and metal

oxides such as Platinum (Pt), Iridium oxide (IrO_2), and Ruthenium oxide (RuO_2) were used [23, 24]. Since these electrode materials are expensive and rare, large-scale hydrogen production is practically not possible with these materials. Many researchers have made great efforts in developing non-noble but highly active electrocatalysts for both HER and OER electrocatalysis. Such electrocatalysts include transition metal (TM) (oxy)hydroxides [25–28], layered double hydroxides (LDHs) [14], chalcogenides [29], phosphides [30], nitrides [31, 32], borides [33], and carbides [34, 35]. Several crucial reaction intermediates like H^* , O^* , HO^* , and HOO^* are involved in an OER process and are hence essential for EWS. Electrode material properties administer this process. Therefore, electrocatalysts that can form these surface intermediate species with proper bonding energies are thus counted as a favorable electrocatalysts [36]. In this circumstance, noble metals (NM) (e.g., Ir, Ru, Pt, Palladium (Pd)) based electrocatalysts are the most desirable candidates for EWS. Despite this, the high cost and limited resources of NMs substantially restrict their large-scale applications [37]. Therefore, it is necessary to develop cost-effective, catalytic active, and robust electrocatalysts for EWS. Conveniently, several earth-abundant TM (e.g. Manganese (Mn), Iron (Fe), Nickel (Ni), Cobalt (Co)), based catalysts manifest superior electrocatalytic performance concerning HER or OER or for both. These low-cost materials have recently been particularly studied in the last few years. Some of them show remarkably high EWS activity that is equivalent to NM-based catalysts [3].

1.4 Challenges for this thesis

1.4.1 Studying the real dynamical structure of the water - electrode interface

Solid-liquid interfaces dominate most fundamental chemical processes in specific topics in materials science, electrochemistry, photochemical process, catalysis, corrosion science, mineral science, environmental science, lubrication, etc. [38, 39]. Interfacial reaction at the edge among the electrode materials and the electrolyte has an extensive impact on electrocatalysis. The H_2O / electrolyte - catalyst interface is critical to understand for the complex electrochemical process. A cation/anion from the catalyst surface and intermediate ions from the electrolyte can act as booster for specific reaction mechanism. The deliberate control of these interfacial reaction signifies a promising chemical approach for tuning the electrolyte-catalyst interface to procure excellent catalytic activity. The OER includes complicated interaction between electrolyte, crystalline/amorphous catalyst, gaseous phase, and liquid phase intermediates and reaction products [40, 41]. Many modern spectroscopic techniques used to analyze solid - liquid interfaces like Vibra-

tional, IR-absorption, and Raman scattering provide vibrational information of the adsorbates. UV-Visible and Fluorescence emission investigate information about electronic structure. Ellipsometry provide thickness information. X-ray absorption (XAS) reveal electronic and local structure. Neutron scattering characterizes vibrational properties. X-ray photoelectron spectroscopy (XPS) provide information of essential electronic and chemical properties [38, 42]. However, these techniques could not study solid-liquid interface properly due to the liquid’s high vapor pressure and the maintenance of an ultra-high vacuum in presence of a liquid. An additional challenge is to investigate proper signals from the atoms or molecules at the interface and avoid the contribution of the bulk signal [38]. Although significant improvement has been made over the last decades, interpreting these interfaces is still challenging. The fast diffusion of the liquid allows accumulation of the trace amount of bulk contamination at the interface; it complicates the preparation of pure, pristine liquid-solid interface under a controlled environment [39]. There are a couple of significant reasons for such experimental limitations: i) the catalyst surface is concealed under the solid or liquid electrolyte, and conventional spectroscopic techniques could not quickly reveal it [41], ii) catalytically active species are either bound to catalyst surface or mobile on the surface, which prevents a proper investigation of the electrochemical activities in conventional measurements [43]. Significant work reports on rate-determining steps and classifying descriptors for the OER activity by thermodynamic approach [16, 44]. There is substantial progress on connections between catalytic and electronic properties of catalyst materials, supported by employing spectroscopic techniques and first-principles computations [16, 18, 45]. However, fewer studies are reported on the actual observations of H₂O-catalyst surface dynamic interface, particularly in-depth knowledge about atomic-scale. There are still open questions for the H₂O-catalyst interface, which drags attention, for example, heat and electric charge transport at the solid-liquid interface [46], structural changes at the interfaces under highly reducing, oxidizing conditions, variable current densities in electrochemical reactions and electric double layer [47, 48], multielectron/-proton transfer processes [49], molecular-level understanding of water at interfaces [48], dissolution and leaching study of A and B site atoms in doped oxides at the interface [50]. To answer these questions, there is a need for atomic resolution in-situ/ operando studies, time-resolved surface-specific spectroscopy, and theoretical simulations [47, 48].

1.4.2 Active sites

In 1925 H.S.Taylor proposed that the concentration of the reactive sites where the actual rate-determining catalytic process emerges is much smaller than the concentration of the total existing surface sites [51]. The nature of the active sites depends on where the bond breaking occurs, and it differ from the different types

of chemical bonds. For example, dissociation of H_2 occurs at a single metal atom [52] or at the step edge and at the metal surface with kinks but not on the smooth crystalline facet of Pt (111) [53–55]. Although a lot of research is done towards an understanding of the O_2 dissociation but less is known about how many atoms participate in the dissociation process or how the lattice oxygen vacancy plays a role as an active site [56]. Few electrocatalytic OER studies report the formation of an amorphous phase that suggests active sites exert a different structure than the pristine catalyst material [57–59]. Recent operando spectroscopy studies report evidence of the activity of multiple active sites in Iron-Cobalt oxides in electrocatalytic OER [60] and formation of active oxyhydroxide phase of Nickel [61] in electrocatalytic OER process. A combination of the electrochemical and computation studies reveals the improvement of oxygen reduction reaction (ORR) activity due to favorable adsorption energies of oxygen intermediates on the single Cu atom active sites [62] and improved OER activity and charge transfer due to the formation of active sites in low crystalline Iron/Nickle bimetallic metal-organic framework [63]. As the electrocatalytic OER occurs at the catalyst surface, regardless of significant progress in the OER, understanding the intrinsic activity of active sites is still unknown [63]. This thesis will study perovskite oxide surface structure and termination in contact with H_2O .

1.4.3 Formation of the active sites on the surface

Most of the research reports improved OER activity by the formation of catalytic active sites due to surface transformation, drastic self surface-reconstruction, active oxyhydroxide type phase formation, and amorphization of the catalyst. Pristine catalyst surface undergo small or indeed overall structural transformation, instead of straight OER catalysis process on their surfaces. Such surface transformation signifies the physical modifications of electronic properties and atomic structure of the pristine surface. It balances the electrochemical environment and forms the electrochemically favorable active sites during OER electrocatalysis. The pristine surface does not show any changes in nonreactive conditions. The reconstructed or transformed surface acts as the actual electrocatalyst or an active site in the OER. The catalytic processes proceed at the interface, controlled by more highly active sites than bulk. Many defects and surface vacancies can exist on the amorphous or an active catalyst surface during OER [64–66]. In recent studies, the surface transformation of catalyst materials have been reported in HER and CO_2 reduction reaction (CRR) [67, 68]. Baumer et al. have demonstrated how the Ni- and La-termination governs the surface transformation of (001) $LaNiO_3$ epitaxial thin films, which regulate the electrocatalytic activity for the OER [69]. Surface transformation of Co_3O_4 to a $Co_3O_4-CoS_x$ by surface sulphurization process improved OER activity and enhanced overall catalytic performance due to the transforma-

tion of CoS_x into cobalt oxyhydroxide (CoOOH), which acts as the active site in the OER process [70]. Bo et al. also report improvement of OER activity in Nickel (oxy)hydroxide due to Iron (Fe) Chromium (Cr) doping which forms a defective complex of Cr, Fe-sub-b-NiOOH [71]. Lopes et al. report formation of a thin layer of Co hydr(oxy)oxide (CoOxHy) on a $\text{La}_{0.6}\text{Sr}_{0.4}\text{CoO}_3$ perovskite surface during the OER process due to the A-site dissolution into the electrolyte and surface oxygen vacancy formation [72]. Fabbri et al. reports dynamic self reconstruction of the surface is the primary component for the active perovskite catalyst for OER [73]. Furthermore, it is crucial to understand the nature of surface reconstruction, particularly identifying the actual active site at the surface [74]. Besides, a proper understanding of the correlation between active sites and their catalytic behavior depends on operando structural investigation at atomic resolution. Even the complex structure of the heterogeneous materials restricts the precise structural analysis, which makes OER mechanism understanding very challenging. [75]. Although transition metal (TM) acts as an active site due to flexible valence in many catalysts, it is still unclear why different TM-based catalysts show distinct OER activity [75]. A clear understanding of a surface transformation/reconstruction process will be very effective in designing excellent electrocatalysts for the OER. It is challenging to trace and control the surface reconstruction process carefully during the OER due to the limitations of ex-situ characterization techniques. An in-depth understanding of the origin of structural transformation that underlay the formation of the active state of a surface-interface to water and the corresponding influential factors is critical to evaluate the eventual state of materials under OER conditions. This thesis will attempt to comprehend the atomic dynamics at $\text{La}_{0.6}\text{Sr}_{0.4}\text{CoO}_3$ surface with- H_2O interface.

1.4.4 Defect reactions

Unlike perfect lattice, a defect site incorporates unique electronic properties that benefit electrocatalytic activity. Defect sites bind reaction intermediates which improve selectivity and activity. Significantly, defects alter the electronic structure in the vicinity and secure the active sites. It is worth investigating the role of defect sites in electrocatalytic OER, which will improve the fabrication of the ideal catalyst [76]. To fabricate a cost-effective and more active catalyst few questions are crucial to answer, i) does cation doping, cation vacancies, cation leaching, and oxygen vacancies tune the OER mechanism?, ii) if yes, then how? and iii) how defect engineering can be used to improve the OER activity of earth-abundant oxides materials to overcome activity of IrO_2 and RuO_2 ? [76, 77]. The OER favors the surface of catalyst where electrons, intermediate species, reactant, and product can be transferred [73, 78]. Introducing an oxygen deficiency at the surface can tune the electronic properties to improve the chemical species adsorption, generate more

active sites, and enhance the OER activity [78–81]. Although promising materials, perovskite oxides need additional improvement to exceed noble-metal-based OER catalysts [80]. In general, perovskite oxides have high crystallization temperature and low surface area; hence, they are in large bulk size and thus exhibit low catalytic activity, but oxygen vacancies at the surface control the electronic properties of the perovskite materials, which improves OH adsorption and enhances the OER activity [78]. A-site and B-site atom doping [82], and low-temperature hydrogen reduction of perovskites [81, 83] techniques used to generate oxygen-deficient sites to improve OER performance. In addition to oxygen vacancies, A and B sites metal cation vacancies impact OER activity [77] due to their orbital and electron distribution, which is also challenging to investigate [78]. Chen et al. report the formation of Tin (Sn) vacancies in $\text{SnCo}_{0.9}\text{Fe}_{0.1}(\text{OH})_6$ by Ar plasma etching, which generates abundant CoFe active sites results in improved OER activity [78]. Also A-site double cation defects improve the OER activity due to increase in oxygen content and higher oxidation states of Iron and Cobalt atoms in the $\text{La}_{0.6}\text{Sr}_{0.4}\text{Co}_{0.8}\text{Fe}_{0.2}\text{O}_{3-\delta}$ and $\text{Ba}_{0.5}\text{Sr}_{0.5}\text{Co}_{0.8}\text{Fe}_{0.2}\text{O}_{3-\delta}$ [84]. Xiao et al. reports an exciting approach to study pristine spinel Co_3O_4 and oxygen vacancy rich Co_3O_4 to investigate defect mechanism and dynamic activity of defect sites in electrocatalytic OER by using a combination of operando techniques. The oxygen vacancies play a crucial role in improving the catalytic activity of Co_3O_4 [85]. Along with dynamic behavior, it is worth studying the reversible and irreversible nature of the defect sites to study the stability behavior of the catalyst. Although some efforts are made to investigate defect mechanisms in OER catalysis, few open questions still exist and drag attention, e.g., i) how to control types of defect, i.e., single type defect as an active site without side effect, ii) stability of defect in harsh electrocatalytic conditions, iii) how to combine in-situ/ operando experimental investigations with theoretical understandings to answer defect dynamics in catalyst surface, and iv) how to scale up the energy conversion performance of defect sites to improve the engineering of an ideal catalyst and enhanced mass and charge transport at the electrolyte-catalyst interface [76]. This thesis studies on understanding the defect reactions on the catalyst surface in contact with H_2O .

1.4.5 Connection to stability and corrosion

Most of the catalysts developed in the past few years show OER activity (for small current density, e.g., 10 mA cm^{-2}) up to several tens of hours, and rarely some of them can last for a few hundreds of hours [86, 87]. The stability of OER catalyst decreases over large current densities (e.g., 1000 mA cm^{-2}) [88, 89]. The poor stability during OER can be induced by the formation of catalytical inactive phase e.g. surface reconstruction, oxidative decomposition, cation leaching, and irregular agglomeration [90]. Corrosion is a spontaneous process that dramatically damages

metal-based devices in industrial applications [91]. In typical corrosion mechanism, oxidation-reduction reactions occur spontaneously at different regions of the metal surface, which usually produces the corrosion layers of the metal rust [92]. This metal rust can be utilized as an active nanomaterial for electrochemical reactions. The pristine metal/catalyst surface exerts low catalytic activity for water oxidation. However, these pristine surfaces can corrode due to the dissolution of the electrode material to generate metals ions interacting with strong corrodents. These ions react with electronegative radicles or hydroxyl groups from corrosion layers in nanosheets that act as active materials for the OER and HER from corrosion [92]. Liu et al. report the improved OER activity of Iron-substrate-derived electrodes by corrosion engineering with stability for more than 6000 hours at large current densities [90]. Increasing OER activity by the formation of corrosion resistance $\text{Ni}_{0.67}$, $\text{Fe}_{0.33}$ oxide layer on stainless steel by dissolution-based mechanism provides the significance of corrosion engineering for the stability of OER catalysts [93]. Abbou et al. report enhanced long-term stability of the SnO_2 aerogel support due to the doping of the electronically similar lattice species like Sn^{4+} but with different valence electrons. Doped SnO_2 aerogel support acts as corrosion resistance material in the acidic medium and limits the detachment of the catalytically active Ir_x nanoparticles, which improves OER stability, and activity [94]. These valuable findings suggest that corrosion engineering can improve the stability and activity of the OER catalyst. However, there are still open questions [95], for, eg. i) how the catalyst corrodes during OER and how it impacts the stability and activity of the OER process, ii) how to avoid degradation of the catalyst, iii) distinguish irreversible processes involved in active layer formation from corrosive processes. This thesis will study the diverse behavior different perovskite oxide thin films in contact with H_2O .

Chapter 2

Oxide catalyst for Oxygen Evolution Reaction

2.1 Binary oxides

Non-nobal transition-metal (TM) cations, especially flexible valence metal cations in binary oxide materials, show high catalytic activity and are the main active sites in electrochemical reactions [17]. The eco-friendly binary metal oxides (mostly TMOs) have been found to manifest excellent catalytic activity along with adequate natural abundance. Thus, it is possible to use them for electrocatalysis at a comparatively low cost. Although they are beneficial in many applications, several TMO differs in their crystal structure and electrocatalytic activity [96]. Due to the superior electrochemical properties and long-term durability, binary metallic oxide, mainly (nobal metal oxides) RuO_2 and IrO_2 electrode materials are broadly utilized in numerous applications, specifically water splitting, chloralkali generation, wastewater management, metallic electro-deposition, etc [97, 98]. The electrocatalytic activity of such electrodes materials are assigned to the surface area and their natural catalytic properties [99–101]. By doping with non noble materials, the electrocatalytic properties of the binary oxides can be drastically improved [102]. A definite proportion of mixture of two noble metal binary oxides of $\text{IrO}_x:\text{RuO}_x$ improves OER performance with small crystal size [103]. Non-nobal transition metal binary oxides for example Nickel (Ni)-Cobalt (Co) [104], (Manganese -Chromium) $\text{Mn}_x\text{Cr}_{1-x}\text{O}_{1.5}$ [105], (Cobalt Ferrite Iron) CoFe_2O_4 [106], Ni-Co oxide, Mn-Fe oxide [107], (Cobalt-Cerium) $\text{Co}_{1-y}\text{Ce}_y\text{O}_x$ [108] show significance improvement in their OER activity due to flexible valence of transition metal and tunable structural and electronic properties.

2.2 Scaling relation

The scaling relation of adsorption energies of energy descriptor in a four concerted electron coupled proton transfer (ECPT) process such $\Delta G(^*O)-\Delta G(^*OH)$ is an essential benchmark for the screening of the thermodynamic overpotential and OER activity of the catalyst [16, 109]. A proton is introduced into the electrolyte at each step in a ECPT, ultimately linking with a transferred electron at the cathode. First OH^- adsorbs on the surface-active site (equation 1.8). The adsorbed OH^* intermediate species undergo consecutive deprotonation to form O^* intermediate (equation 1.9). In the O–O bond formation step enables O^* to interact with another OH^- and generate the HOO^* intermediate (equation 1.10). O_2 is evolved in the last step through the deprotonation of HOO^* intermediate with the reproducing of the active site (equation 1.11).

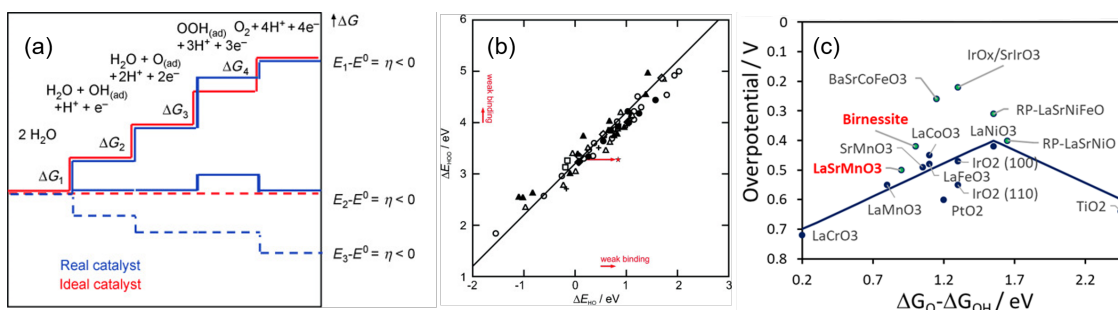


Figure 2.1: (a) Gibbs free energies of intermediates and reactive species at $U = 0$ for ideal and actual catalysts. Reprinted with permission from ref [44]. Copyright © 2010 WILEY-VCH Verlag GmbH and Co. KGaA, Weinheim. (b) Adsorption energy of HOO^* Vs. adsorption energy of HO^* on different catalyst surfaces such as perovskite, rutile, anatase, Mn_xO_y , Co_3O_4 , and NiO oxides. (c) Volcano shape plot for the Activities trends for OER for perovskites (compiled data from literature). (b and c) are reproduced from the ref [16], Copyright © 2011 WILEY-VCH Verlag GmbH and Co. KGaA, Weinheim

The overpotential of OER is determined by the positive values of the $\Delta G_1 - \Delta G_4$ steps [Fig. 2.1a]. The lowest overpotential of a catalyst can be used to describe a good electrocatalytic performance. Fig. 2.1a shows that an ideal OER electrocatalyst requires all four fundamental steps with reaction free energies of the same magnitude at $U = 0$ and OER equilibrium potential = 1.23 eV. This ideal situation is difficult to achieve in actual electrochemical experimental conditions [16, 44]. It is due to the linear correlation of adsorption energies of OER intermediate species HO^* , HOO^* , and O^* according to the Adsorbate Evolution Mechanism [16]. Usually, both HOO^* and HO^* binds by an oxygen atom with the catalyst surface via

a single bond, so the average binding energy of HO^* and HOO^* is with a constant difference of 3.2 ± 0.2 eV for catalyst (metals/oxide surfaces), despite the binding site. Therefore, the difference between ΔGO^* and ΔGHO^* can be utilized as a universal descriptor to anticipate their OER activity Fig. 2.1c [110, 111].

An ideal catalyst needs the adsorption strength of the critical intermediates to be not too strong or too weak. Man et al. report that the overpotentials depend on the binding strength of the intermediate species. That means if the reaction energy of one of the step from $\Delta\text{G1} - \Delta\text{G4}$ is changed, the other steps simultaneously changes too [16]. The standard scaling relationship between HO^* and HOO^* intermediates binding energies across many oxides catalysts. Fig. 2.1b shows that the binding energies of HOO^* and HO^* intermediates are linearly correlated, with a slope of about 1 and an intercept of 3.2 eV. The consistent variation between the HOO^* and HO^* intermediate species, the difference in the overpotential(η), η_{OER} from one oxide catalyst to the other are determined by the O^* adsorption energy. Hence, the plot of η_{OER} as a function of $\Delta\text{GO}^* - \Delta\text{GHO}^*$ directs to the universal volcano-shaped behavior autonomous of the catalytic materials. The calculated overpotentials differ from the experimentally observed potentials. The frozen surface approximation phenomenon is considered for the thermodynamic calculation of the overpotential. In this essential concept activation barriers, pH, current densities, and applied electric potentials are not considered. The effective surface area is unknown for such calculations. The plot of η_{OER} as a function of free energies $\Delta\text{GO}^* - \Delta\text{GHO}^*$ for the perovskite oxides shows volcano shape correlation Fig. 2.1c. The most active catalyst with low overpotentials does not follow this volcano shape trend. Recent experimental studies show dynamic TM adatoms on $\text{La}_{0.6}\text{Sr}_{0.4}\text{MnO}_3$ and $\text{La}_{0.6}\text{Sr}_{0.4}\text{CoO}_3$ surface (see chapter 5 and 7) and H_2O intercalation in Birnessite [112] under OER like conditions in ETEM which remain outside of this trend. It is interesting to investigate these materials as they do not follow the classical AEM approach.

2.3 Perovskite oxides

Perovskite oxides indicate a group of compounds with the general formula of ABO_3 , where A-sites are elements from the Lanthanide group or alkaline earth metal elements and B-sites are transition metals[113–119]. In this type of crystal structure, A-cation shares the closely-packed sites with three O^{2-} anions, and B-cation is involved completely in octahedral sites coordinated by oxygen Fig. 2.2 [120]. Tuning the A-site cations in the perovskite structure can affect the valence state of B-site cations or stimulate oxygen vacancy (V_{O}) formations. By different combinations of A and B sites, the electronic structure can be modified. This structural flexibility determines the electrocatalytic OER activities [113, 121]. A broad range

of perovskite oxide composites can be tuned by combinations of A-site and B-site cations, which modulate the electronic structure and OER activity [73, 122, 123].

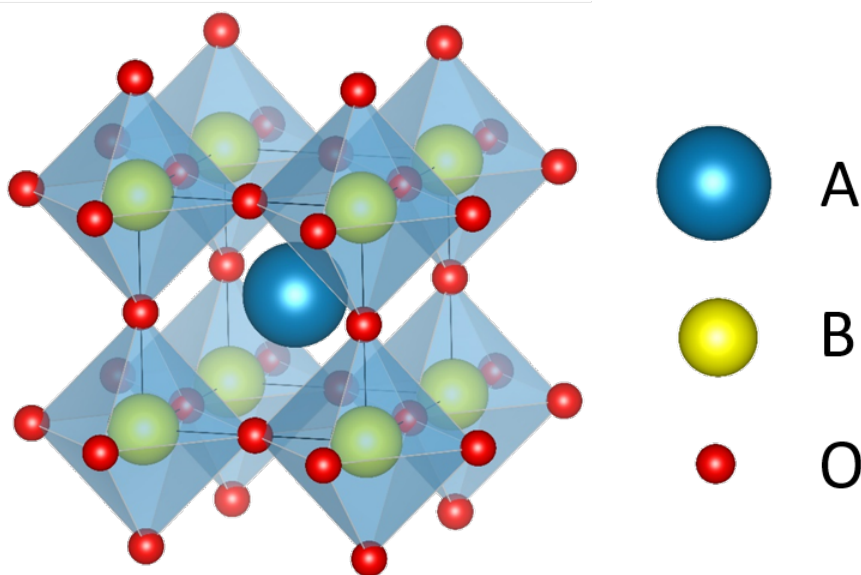


Figure 2.2: Schematic drawing of the simple cubic perovskite structure.

This flexibility can tune the electronic structure of perovskites and allow studying the correlation between structure and electrocatalytic activity. Consequently, numerous tactics can alter perovskite oxides' electronic and catalytic properties for enhanced electrocatalytic performance. Substantial attempts have been dedicated to develop perovskite electrocatalysts with leading OER performance [124].

2.4 OER mechanism in Perovskites

Nørskov and coworkers have theoretically proposed a primary oxygen evolution reaction mechanism by the Adsorbate Evolution Mechanism (AEM) [18]. The AEM is considered to incorporate four concerted electron coupled proton transfer (ECPT) reaction concentrated on the TM ion in alkaline condition, as illustrated in equation (1.8)–(1.11) [16, 18, 125] [Fig. 2.3(a)]. Though, several references recognize this mechanism [16, 126, 127], it is essential to understand that AEM is based on frozen surface approximation, i.e., the interaction of intermediate species with the H_2O at the interface is disregarded [16]. The crucial point of the AEM is that all the intermediate oxygen species react on the active sites on the metal without involving the oxygen in the lattice. This mechanism is employed to access scaling relation for the OER descriptor investigation [16]. Despite this, comprehensive efforts have shown an inconsistency between experimental electrocatalytic

activity and theoretical calculations based on the AEM. For example, perovskites systems such as $\text{La}_{0.5}\text{Ca}_{0.5}\text{CoO}_{3-d}$ and $\text{Ba}_{0.5}\text{Sr}_{0.5}\text{Co}_{0.8}\text{Fe}_{0.2}\text{O}_{3-d}$ with overpotentials of 0.28 V and 0.25 V, respectively. These values have lower thermodynamic barriers than pristine LaNiO_3 (0.33 V), which was supposed to be the optimum electrocatalyst [45, 122, 128]. Perovskite surfaces may hold multiple active lattice oxygen atoms to activate a different reaction mechanism than the conventional AEM approach. Liu et al report discrepancies in the experimentally observed oxygen reduction reaction (ORR) overpotential than the calculated overpotential based on the AEM [129]. These inconsistencies urge to seek new possible OER mechanisms on complex multi correlated systems.

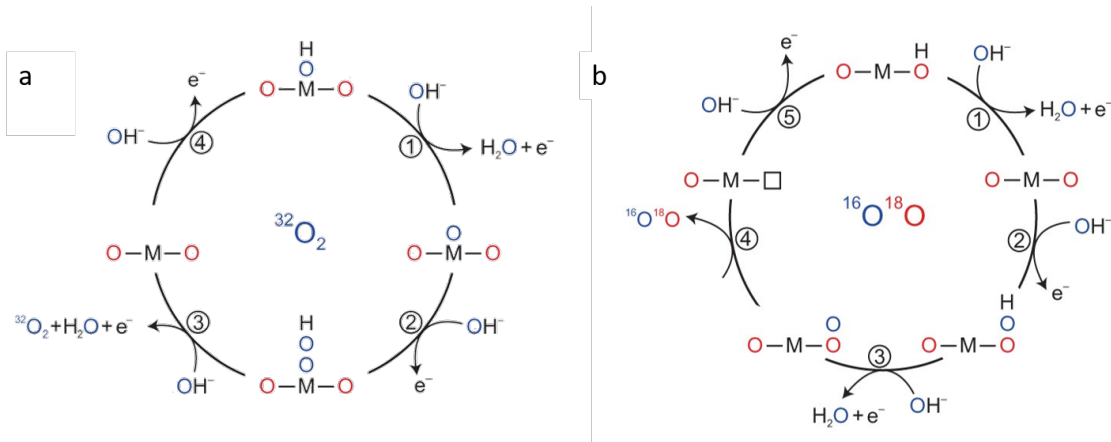


Figure 2.3: Schematic drawing of the OER mechanism. (a) Classical approach of AEM mechanism. (b) Possible OER mechanism involving lattice oxygen. Reprinted with permission from ref [45]. Copyright 2017 Springer Nature: Nature Chemistry

According to the AEM mechanism, this inconsistency may originate from excluding the lattice oxygen in the OER. The high activity in the $\text{La}_{1-x}\text{Sr}_x\text{CoO}_{3-d}$ system was derived from the participation of lattice oxygen, DFT calculations, and electrochemical characterization also supports this [126]. Shao-Horn et al. proposed the lattice oxygen-facilitated mechanism (LOM) in recent work Fig. 2.3 (b). It suggests LOM based on the reversible formation of oxygen vacancies [45], They have provided experimental proof to confirm that the oxygen generation in the OER process through from lattice oxygen via in situ ^{18}O -labeled mass spectrometry. Yoo et al. substantially confirmed the participation of lattice oxygen of the perovskite lattice through the electronic origin and kinetic feasibility by DFT calculations, suggesting that a perovskite's surface lattice oxygen can take part in OER via the nonelectrochemical route [130]. However, this mechanism is promising for the weakly binding perovskite oxide systems [130]. The adsorbed O^* diffuses from sur-

face TM to adjunct surface lattice oxygen and then surface lattice oxygen transfers out of the surface to form OO^* and oxygen vacancy. The origin of LOM can be understood as TM changing from the high oxidation state to the more stable lower oxidation state throughout the OER.

The experimental work carried out in this thesis also reports a drastic decrease in OER activity of $\text{Pr}_{0.67}\text{Ca}_{0.33}\text{MnO}_3$ due to irreversible formation and annihilation of oxygen vacancies on the surface during OER. However, in perovskite oxides, alkaline earth metals in the A-site can be leached out in an aqueous solution [121, 131]. Some perovskite oxides experience surface reconstruction or amorphization after OER in alkaline conditions [57, 69, 132]. Structural changes by cation leaching in electrolyte solutions are significant issues in perovskite oxide electrocatalysts for OER [133]. The experimental work presented in this thesis suggests consideration of the OER mechanism beyond AEM or LOM and frozen surface approximation. I discovered that the perovskite surface is dynamic under the OER conditions in in-situ environments. Importantly, I found surface transformation during in-situ observations in OER-like conditions. These findings provide insights into oxygen evolution catalysis's new possible reaction path, which is essential for developing electrochemical catalysts.

Chapter 3

Transmission Electron microscopy

In 1923 Louis de Broglie proposed that an electron is no longer regarded as a single particle but must also be related to the wave-like nature, its wavelength is possible to measure, and interference of these waves can be predicted [134]. Soon after, an idea of an electron microscope was proposed, and in 1932, M. Knoll and E. Ruska demonstrated the practical use of electrons to obtain optical images [135]. Louis de Broglie and E. Ruska received the Nobel prize for their outstanding contributions. This chapter aims to summarize the fundamentals of conventional transmission electron microscopy, contrast mechanism in high-resolution TEM (HRTEM), electron energy loss spectroscopy (EELS), and the environmental TEM (ETEM) approach. Further, I will elaborate on the main challenges in the TEM sample preparation and application of ETEM in the catalytic field that has led to the developments described in the following chapters 4, 5, 6 and 7.

3.1 Contrast mechanism in HRTEM

As the electron wave propagates through the specimen and interacts with the electrostatic potential, it changes its phase and amplitude. Both types of modifications contribute to the image forming contrast. In the transmission electron microscope (TEM), the image of the transmitted electron wave is the result of all scattering processes, elastic and inelastic as well as coherent and incoherent, undergone by the electron beam throughout its entire travel path and within the range of accepted scattering angles as determined by an aperture in the projection system. As it is useful to review the possible scattering contributions, the resulting image contrast, and the limitations that are thus imposed on the sample in order to achieve atomic resolution [136, 137]. In the following section 3.1.2, the concepts of image contrast formation within the kinematical and dynamical scattering theory are briefly introduced. Diffraction in the sample also contributes

to the amplitude contrast either using diffracted or un-diffracted beam due to the selection of specific aperture. On the other hand, image contrast can appear due to the alteration in the phase of the (direct and diffracted) electron waves leaving via a thin specimen. A TEM image could be constructed by recombination of direct, diffracted beam and the resulting interference pattern. However, the Interpretation of the phase contrast mechanism becomes complicated due to variations in the thickness and scattering potential of the different specimens and their orientations concerning the electron beam [136, 137]. As electron diffraction plays an essential role in the contrast mechanism, it is helpful to understand fundamental concepts of two beam condition, kinematic and dynamical electron scattering.

3.1.1 Two beam condition

In order to understand the contrast formation from a partially coherent incident electron wave interacting with a thin sample, it can be useful to first consider the simplified case of a coherent wave scattered once by a thin sample, which is oriented thus that only one strong interference direction is allowed within the imaging aperture. This case is colloquially referred to as the “two-beam condition for kinematical electron diffraction,” and the coherent elastic scattering direction from an ideal crystalline solid can be determined by Bragg’s law and the Ewald Sphere construction. This is achieved by using objective aperture [Fig. 3.1 (a) and (b)]. The specimen is tilted so that a single strong diffraction event occurs. So one can use dark field (DF) or Bright field (BF) mode alternatively to interpret the contrast, because in the perfect two-beam case, the BF contrast is simply the inverse of the DF. It is known as two beam condition [136, 138, 139]. The electron wave diffracted by the lattice planes in the crystal forms a beam propagating in different directions according to the Bragg diffractions conditions. The exiting electron wave from the specimen results in the change of the phase which is determined by the diffraction theory by quantum mechanics [140].

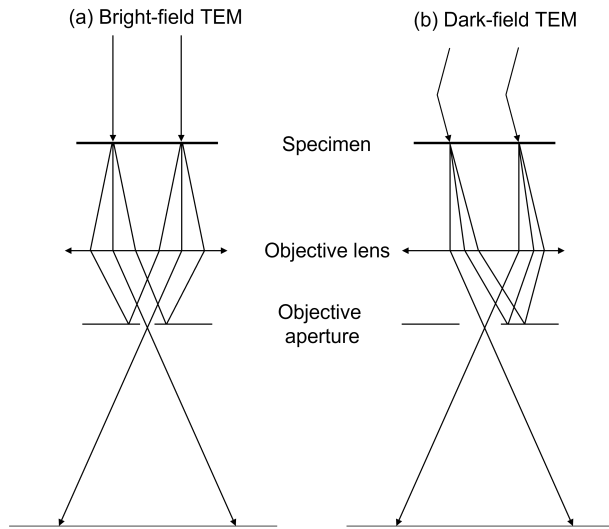


Figure 3.1: Schematics of Optic ray diagrams of (a) bright-field mode, and (b) dark-field mode.

3.1.2 Kinematical and Dynamical diffraction conditions

Two theories describe the diffraction contrast, kinematical and dynamical. In kinematical approximation, two beams are considered, direct and diffracted. The primary beam contains only the unscattered electrons. There is no absorption of electrons, so the intensity of the diffracted beam is smaller than the direct beam.

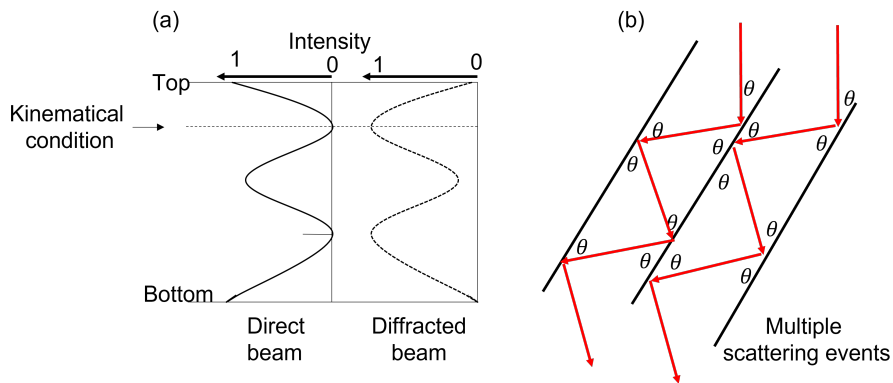


Figure 3.2: (a) Direct and diffracted beam. (b) Multiple scattering events.

Kinematical theory predicts the single scattering event (until the dotted horizontal line in Fig. 3.2 (a)) while the dynamic theory assumes coherent multiple scattering [Fig. 3.2 (b)]. That means the sample should be very thin to follow

the kinematic approach. It suggest, in the two-beam situation there will be one diffraction event for one traversing electron only, and the intensity that is lost in the direct beam is only transferred to the diffracted beam. In the kinematical limit, the scattering intensity is proportional to the square of the structure factor, which in turn is composed of the Fourier transform of the electrostatic potential, or atomic scattering power, of the unit cell. However, as the electron travels through a thin specimen, there will be oscillations between the relative intensities of the direct and diffracted beam, but diffracting back to the direct beam is also very likely as the Bragg condition is satisfied. This will provide the thickness variation contrast, for example, a very thin wedge shape sample prepared by ion milling. The thickness contrast of the wedge shape's sample is evaluated by the angle and the sample's extinction distance. Therefore, the image may show dark or bright contrast depending on the thickness of the specimen and the measurement area [137, 139].

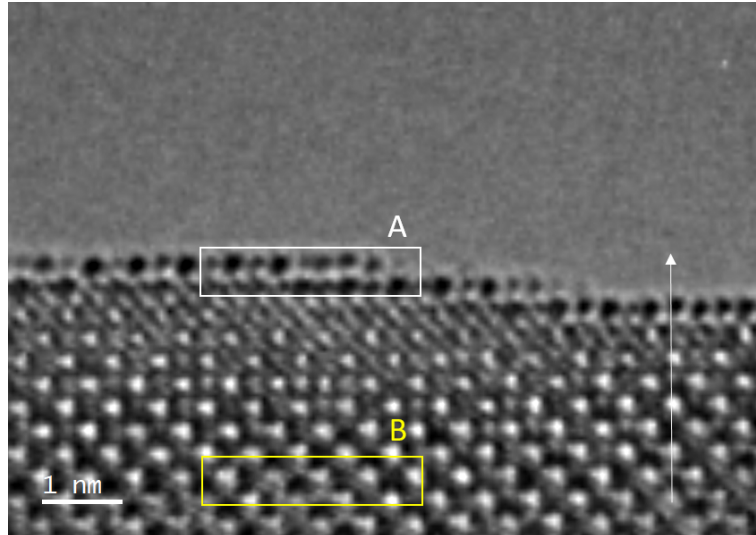


Figure 3.3: Change in the atomic contrast at two positions (white rectangle A and yellow rectangle B) due to thickness gradient at the $\text{Pr}_{0.9}\text{Ca}_{0.1}\text{MnO}_3$ surface. White arrow show direction of decrease in thickness.

Fig. 3.3 show difference in the atomic contrast of the position A and B of $\text{Pr}_{0.9}\text{Ca}_{0.1}\text{MnO}_3$ (112) surface. The white arrow shows a direction of decrease in thickness. The atomic contrast at the top edge (white rectangle A) show dark black spots while bright spots are in bulk due to a strong thickness gradient. In dynamical diffraction, incident beams scatter elastically from periodic alignment of parallel planes; if it is well aligned to the Bragg condition, then beam scatters to the next plane, and this process continues [Fig. 3.2 (b)]. As the sample gets

thicker, the electron continues to scatter elastically, and the kinematical diffraction condition is no longer valid in this situation [below the horizontal dotted line in Fig. 3.2 (a)] and the dynamical diffraction condition governs the process from that point. Typically, this is the practical situation in most crystalline samples [137, 141, 142].

3.1.3 Lens Aberrations and Phase contrast

The resolution of smallest feature on the specimen surface or focusing the smallest electron beam in the TEM is defined by the precise functioning of the objective lens. However, like other magnetic lenses, the objective lens suffers from aberration problems which results in degrading its performance [137]. The objective lens is affected by two principal aberrations, i) Spherical aberration and ii) Chromatic aberration. Chromatic aberrations dominates the phase-contrast imaging at lower acceleration voltages [143, 144]. Perovskite materials are studied at accelerating voltage of 300 kV in this thesis. Therefore this thesis focuses on spherical aberrations (C_s) and C_s correction.

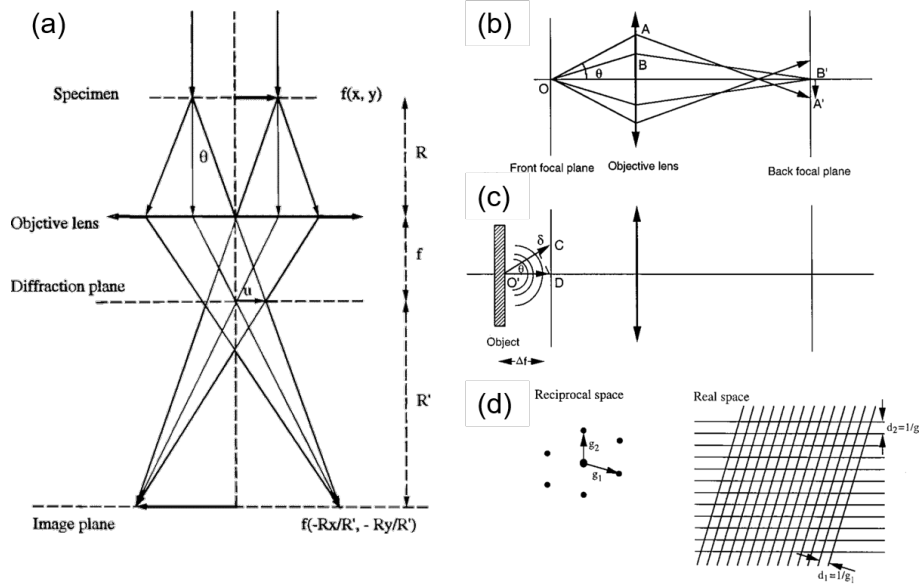


Figure 3.4: (a) Schematics of optic ray diagrams of general image formation mechanism in TEM based on the Abbe's theory. Schematic of the phase shift induced by (b) spherical aberration and (c) defocus of the objective lens due to the scattering of electrons off the optical axis. (d) The connection between the diffracted beam in reciprocal space and real space interference lattice fringes. Reprinted with permission from ref [140]. Copyright © 2000 American Chemical Society

Fig. 3.4 (a) shows the primary image formation mechanism in the TEM based on Abbe's theory [136, 140]. When an electron passes through the periphery of the objective lens, it gets refracted more than the electrons passing through the optical axis, therefore these peripheral refracted electrons will not reach the focal point and produce spherical aberration Fig. 3.4 (b). As the objective lens plays the most important role in an image formation, only an objective lens is considered in this mechanism. The exit wave $\psi(x,y)$ consists of structural information, but due to the aberrations produced in the objective lens, the transmitted wave will propagate non-linearly. The scattered electrons with an angle θ experience a phase shift due to the C_s and the defocus from the objective lens. A change in focal length due to spherical aberration acting on the off-axis portions of the electron wave corresponds to a phase shift in the image plane as a function of the scattering angle of electrons. The electron wave in real and reciprocal space is related by the Fourier transform (FT) for the Fraunhofer diffraction condition. Therefore if $\psi(\mathbf{u})$ is the FT of the exiting electron wave $\psi(\mathbf{r})$, then the amplitude of the diffraction is given by,

$$\psi'(\mathbf{u}) = \psi(\mathbf{u}) \exp [i\chi(\mathbf{u})] \quad (3.1)$$

where \mathbf{u} is the reciprocal space vector in the scattering angle $u = 2 \sin\theta/\lambda$, and $\chi(\mathbf{u})$ is a phase function-oriented by the objective lens, i.e. a complex phase factor describing the phase error induced by the aberrations of the objective lens which is determined by the (C_s) spherical aberration and the defocus Δf of the objective lens.

The phase function is given by,

$$\chi(\mathbf{u}) = \frac{\pi}{2}C_s\lambda^3u^4 - \pi\Delta f\lambda u^2 \quad (3.2)$$

where λ = wavelength of an electron. Fig. 3.4 (b) shows the resultant path difference due to the variation in the focal length of the ray OA and OB. The defocus represent relative phase shift of the scattered electron with an angle θ [Fig. 3.4 (c)]. According to the Huygens theorem, the spherical wave originated from the point O will have a path length difference, and the increasing scattering angle will increase the corresponding phase shift. The interference of the Bragg reflected beams forms a high-resolution TEM image of a crystalline specimen [Fig. 3.4 (d)]. As the phase of each Bragg beam is disturbed by the phase shift induced by the C_s and Δf perturbs the phase shift of each Bragg beam, and therefore the information is transformed non-linearly. A mathematical representation of the observed image intensity $I(x,y)$, i.e., inverse Fourier transform (FT^{-1}) of $\psi'(u)$ of the front focal plane, is:

$$I(x, y) = |\text{FT}^{-1}[\psi'(\mathbf{u})]|^2 = |\Psi(x, y) \otimes t_{\text{obj}}(x, y, \Delta f)|^2 \quad (3.3)$$

where \otimes is the convolution of the exit wave with the lens transmission function $t_{\text{obj}}(x, y, \Delta f)$, (x, y) which is then FT^{-1} of the phase factor $\exp[i\chi(\mathbf{u})]$. The convolution introduced in the phase contrast transfer function induces the transformation of nonlinear information of the objective lens which leads to the complex image interpretation. Equation 3.3 is found in Abbe's theory which relates the exit wave function $\psi(x, y)$ with the experimental image intensity $I(x, y)$. However, there are further functions that need to be multiplied into equation 3.2 to change the amplitude of the image wave; these are functions describing the aperture due to the largest scattering angle that can be collected in the TEM, as well as functions describing the effect of partial incoherence (for example - spatial and temporal) [140].

3.1.4 Image (C_s) corrector and Image simulation

The microscope's resolution can be improved by correcting the aberrations of the objective lens and thus reducing the phase error introduced above. In the current studies CETCOR - C_s corrector is used for FEI Titan ETEM G2 80–300 system. Using the C_s corrector, it is attempted to correct defocus ($C1$), 2 fold astigmatism ($A1$), second-order aberrations ($A2$ -3-fold astigmatism, $B2$ -axial coma) and third-order aberrations ($A3$ -4-fold astigmatism, $S3$ -star aberration, $C3$ -spherical aberration (C_s)).

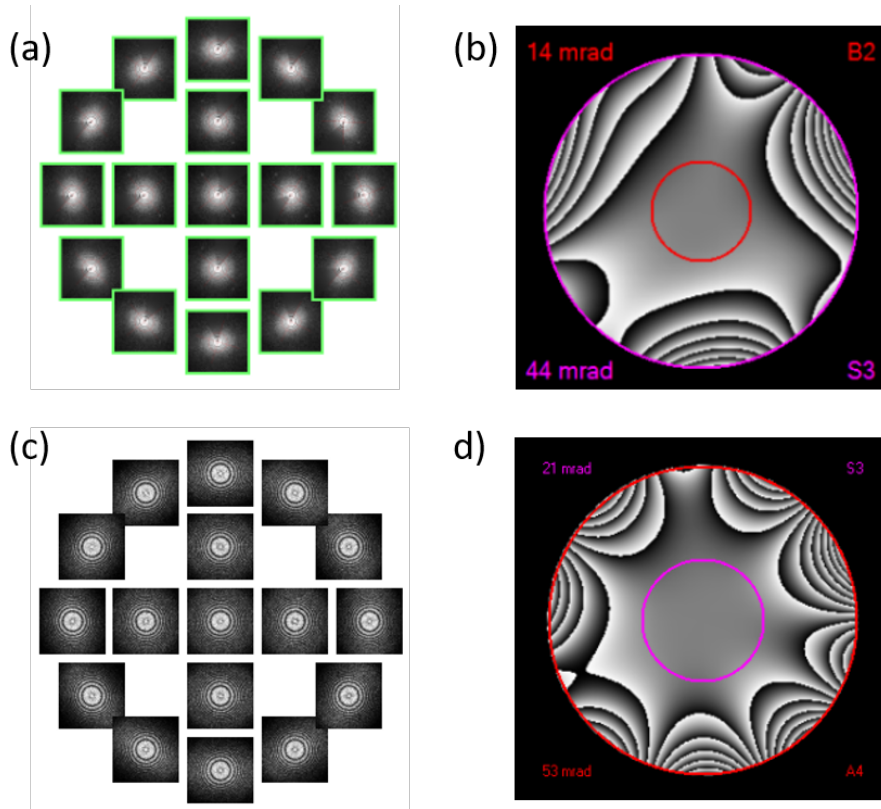


Figure 3.5: C_s corrector. Tableau (a) and phase plate (b) obtained for uncorrected and (c and d) for corrected state.

In order to determine the higher-order aberrations, a tableau of tilted diffractograms is recorded during the C_s correction. An amorphous material is selected for diffraction analysis (e.g., a thin carbon specimen) since crystalline materials can introduce a local ordering effect that influences the corrector algorithm. Revealing asymmetric aberrations suppressed in the on-axis imaging is done by tilting a series of diffractograms known as the Zemlin tableau technique [145, 146]. Fig. 3.5 shows (a) an uncorrected state of the C_s corrector. (c) shows corrected state with tableau series of diffractograms recorded by tilting in different angles around the optical axis. Fig. 3.5 (c) shows almost no two-fold (A_1) astigmatism or change in defocus for the tilted diffractograms. Fig. 3.5 (b) and (d) shows the phase plate, which is calculated by fitting the C1 and A2 values for different outer tilt angles of the optical axis and using these sampling points to calculate back a likely phase aberration function. The recording of tilt tableau series continues until the flat phase region (the range of scattering angles for which no or negligible phase errors are introduced) in the center extends up to a desired angle, which in turn determines the range of spatial frequencies that can be interpreted near-linearly, and

thus the ultimate resolution of the HRTEM image.

Aberrations	Values	Angle	Confidence
C1	-781 nm	-	3.53 nm
A1	13.2 nm	89.5°	3.92 nm
A2	88.6 nm	-131.3°	64.6 nm
B2	56.3 nm	91.9°	37.3 nm
C _s	-1.8 μm	-	3.06 μm
A3	1.23 μm	-31.8°	1.77 μm
S3	1.54 μm	-172.2°	1.04 μm

Table 3.1: Aberration values for uncorrected state

Aberrations	Values	Angle	Confidence
C1	-898 nm	-	3.16 nm
A1	5.2 nm	-156.3°	3.43 nm
A2	27.12 nm	-173.6°	58 nm
B2	8.67 nm	82.7°	33.64 nm
C _s	359.3 nm	-	2.83 μm
A3	1.34 μm	-125.3°	1.52 μm
S3	594.2 nm	-21.3°	932.7 nm

Table 3.2: Aberration values for corrected state

Table 3.1 and 3.2 shows the differences in aberration parameters for uncorrected state and after C_s correction. The confidence value gives a good estimation of the accuracy of the measurement. In order to achieve better results the confidence value should be greater than the obtained value of an aberration coefficient. Aberration values obtained from experimental aberration corrections are utilized for image simulation to gain better insights into the atomic contrast. The multislice image simulation is performed for the HRTEM images using QSTEM software [147].

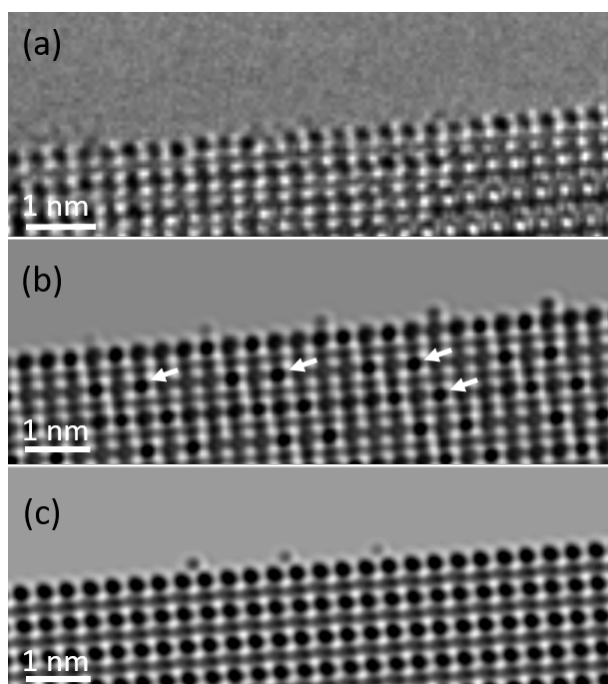


Figure 3.6: (a) The experimental image of an $\text{La}_{0.6}\text{Sr}_{0.4}\text{MnO}_3$ edge. (b) The simulated image shows A-site contrast fluctuations from randomization of the occupancy and (c) homogeneous A-site contrast.

Fluctuation of the A-site contrast is observed in the simulated image due to the random distribution of A-site atoms. Fig. 3.6 (b) shows a simulated image of $\text{La}_{0.6}\text{Sr}_{0.4}\text{MnO}_3$ (001) surface. The clustering of dark black contrast of A site (La/Sr) atomic columns due to random distribution of the La or Sr atoms (indicated by white arrows) is clearly visible in the Fig. 3.6 (b). However, this behavior is absent in the experimental image Fig. 3.6 (a). To avoid complete randomization of the doping concentration of A-site atoms, the atomic models of the perovskite unit cells are prepared using a python based script, which adjusts doping concentration after the initial model creation. It avoids the agglomeration of similar A-site (La or Sr) atoms to avoid the inhomogeneous A-site contrast effect, thus matching the experimental HRTEM contrast, as shown in the Fig. 3.6 (c).

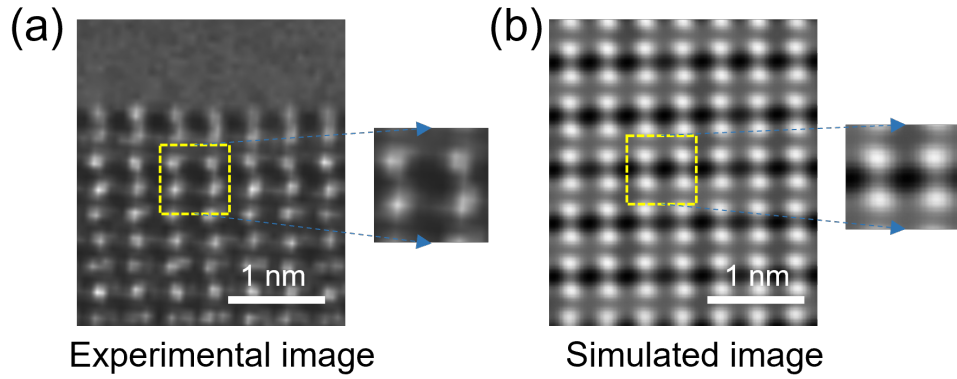


Figure 3.7: Selection of a single A-site unit cell for fitting of lens aberrations and thickness parameter from (a) the experimental, and (b) the simulated image of $\text{La}_{0.6}\text{Sr}_{0.4}\text{MnO}_3$ (001) surface.

To estimate the experimental conditions, a single unit cell is extracted from the sub-layer of the surface in the experimental image [Fig. 3.7 (a)] and the simulated image [Fig. 3.7 (b)]. The lens aberrations C_1 , A_1 , A_2 , B_2 , S_3 , C_s , and thickness parameters of the experimental and simulated images are fitted by minimizing the root mean square (RMS) difference after parameter adjustment of the simulation. The minimization algorithm makes use of the metropolis method and the decrease in virtual temperature as a function of the iteration step as reported in the ref [148].

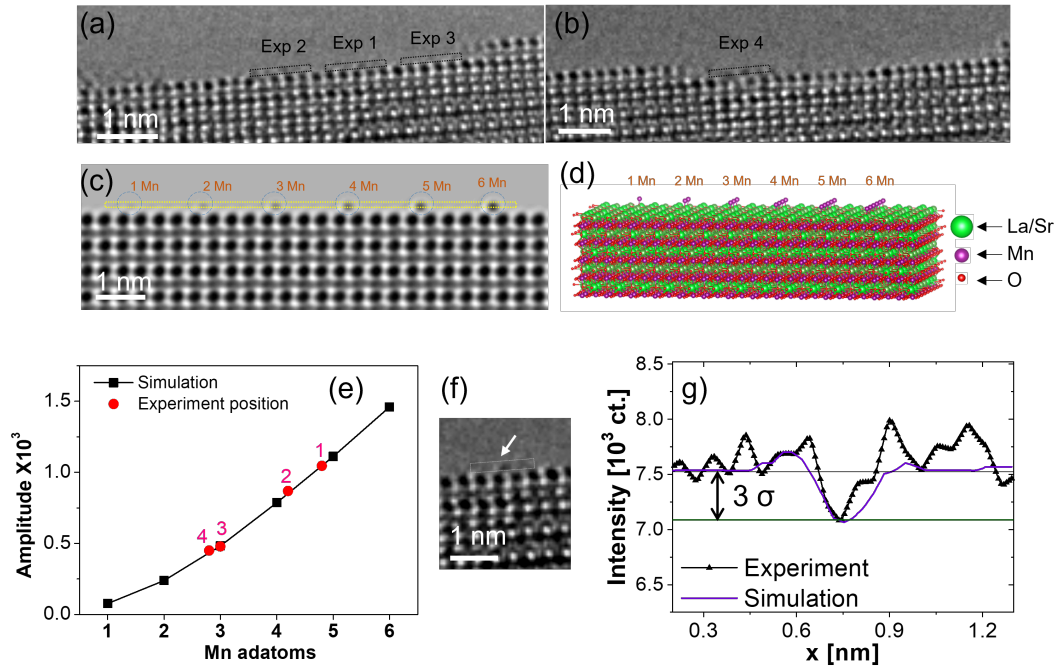


Figure 3.8: (a and b) The experimental images of $\text{La}_{0.6}\text{Sr}_{0.4}\text{MnO}_3$ (001) surface used for the selection of position of adatom contrast calibration. (c) A simulated image of $\text{La}_{0.6}\text{Sr}_{0.4}\text{MnO}_3$ (001) surface with 1-6 Mn adatoms on A-site terminated surface. (d) Show the atomic model of $\text{La}_{0.6}\text{Sr}_{0.4}\text{MnO}_3$ prepared using python based script for the image simulation. (e) Comparison of amplitude of simulated and experimental adatoms contrast. (f) Experimental adatom contrast marked by the white arrow show good agreement with the simulated 3 Mn adatom contrast. (g) Comparison of the line profile of intensities of the simulated (purple) and experimental (black line with triangle symbols) images of 3 Mn adatoms. The 3σ indicate the lower limit of Mn adatom column detectability above noise level of the CCD

Aberration Parameters	$\text{La}_{0.6}\text{Sr}_{0.4}\text{MnO}_3$	$\text{Pr}_{1-x}\text{Ca}_x\text{MnO}_3$
C1	-3 nm	-6.3 nm
A1	2.023 nm	6.809 nm
A1 angle	1.18 rad	2.41 rad
C_s	-10.643986 μm	- 1.581758 μm
B2	0 nm	863.9 nm
Thickness	4.2 nm	4.3 nm
Focal spread	10 nm	10 nm
Calibration factor	24	-

Table 3.3: Contrast fitting parameters

The $\text{La}_{0.6}\text{Sr}_{0.4}\text{MnO}_3$ (001) surface is simulated [Fig. 3.8 (c)] with pseudo-cubic (110) zone axis with $R\bar{3}C$ space group to understand the contrast of atomic dynamics at the catalyst surface- H_2O vapour interface. Fig. 3.8 (d) show the atomic model of $\text{La}_{0.6}\text{Sr}_{0.4}\text{MnO}_3$ (001) surface used for the simulation. Table 3.3 show the lens aberrations and thickness parameter obtained by the minimizing the RMS difference, as mentioned earlier. To calculate a scaling factor, we have used an intensity ratio of a single A-site unit cell column from the experiment to the simulated image in Fig. 3.7. This scaling factor is multiplied by the simulated 1-6 Mn adatom intensity. Then the amplitude of the simulated adatoms is extracted and plotted against different experimental adatom positions shown in the Fig. 3.8 (a) and (b). The amplitude comparison in the plot Fig. 3.8 (e) suggests the presence of 3, 4, and 5 Mn adatom occupancies on the $\text{La}_{0.6}\text{Sr}_{0.4}\text{MnO}_3$ (001) surface. To confirm this, the intensity of the adatom column in the experimental image shown in the Fig. 3.8 (f) is plotted against the simulated 3 Mn adatom column Fig. 3.8 (g). Intensity line profile Fig. 3.8 (g) of the experimental position fits perfectly to the 3 Mn simulation intensity, and is in good agreement with the amplitude analysis. The details of Mn adatom hopping are discussed in the Chapter 5 and single and multiple A/B-site adatom contrast, on A-site and B-site, and the terminated surface is discussed in the Appendix A.2.

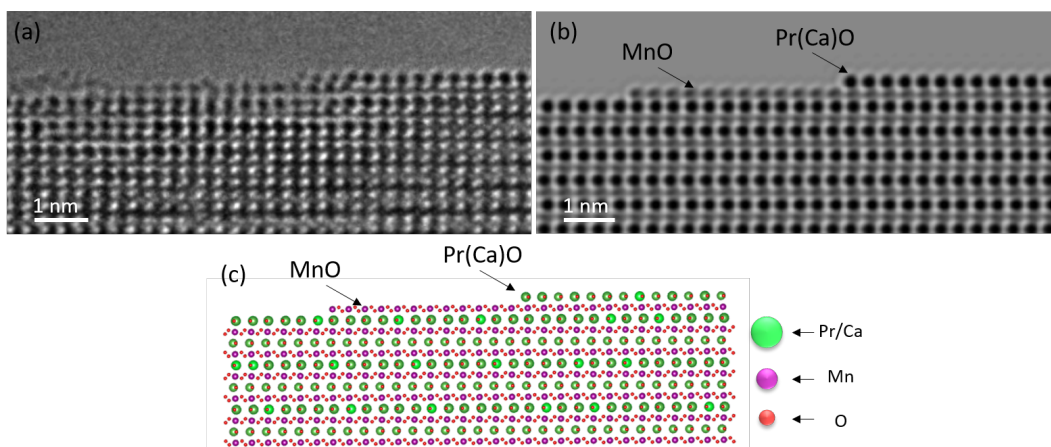


Figure 3.9: (a) The experimental image of the $\text{Pr}_{0.9}\text{Ca}_{0.1}\text{MnO}_3$ (001) surface recorded in HV. (b) A simulated image of $\text{Pr}_{0.9}\text{Ca}_{0.1}\text{MnO}_3$ (001) surface show the exact A-site and B-site mixed terminated surface. (c) Show the atomic model of $\text{Pr}_{0.9}\text{Ca}_{0.1}\text{MnO}_3$ prepared for the image simulation.

Fig. 3.9 (a) show an experimental image of the $\text{Pr}_{0.9}\text{Ca}_{0.1}\text{MnO}_3$ (001) surface with mixed termination. Fig. 3.9 (b) show a simulated image of $\text{Pr}_{0.9}\text{Ca}_{0.1}\text{MnO}_3$ (001) surface with mixed A-site and B-site termination like the experimental image. Similar to the previous process, a python-script-based atomic model is used for [Fig. 3.9 (c)] for the simulation. Simulated image enables to reveal the difference in A-site and B-site atomic contrast in the experimental image Fig. 3.9 (a). Information obtained from the image simulation of $\text{Pr}_{0.9}\text{Ca}_{0.1}\text{MnO}_3$ is used to understand the atomic dynamics in the Chapter 6.

3.2 Electron Energy Loss Spectroscopy (EELS)

Electron energy-loss spectroscopy (EELS) measures the energy dispersion of electrons after their elastic and inelastic interactions with the specimen. Utilizing the energy loss of the incident electron beam (in the range of 0-2000 eV), EELS can reveal information about the materials' valence electron excitation and vibrational modes (mostly at high energy resolution in the meV range close to ZLP). In high-resolution core loss EELS (HREELS), characteristic energy losses from the excitation of bound electrons lie in the range of a few hundred eV. HREELS allows the study of the chemical and physical properties of the adsorbed molecules or atoms [149–151].

3.2.1 Elastic and inelastic scattering

Elastic scattering of an electron signifies no exchange of energy. It is also referred to as the Coulomb interaction of the incident electron with an electrostatic potential of the specimen. When an incidence electron approaches an atomic nucleus, it gets deflected via a large angle by Coulomb interaction. Such long angle deflection agrees with Rutherford's calculation for the scattering of alpha particles. If such a deflection exceeds 90° , it is considered a backscattered electron. However, most of the incident electrons scatter through small angles in the range of 10-100 mrad for a 100 keV electron beam energy [Fig. 3.10 (a)] [149–151].

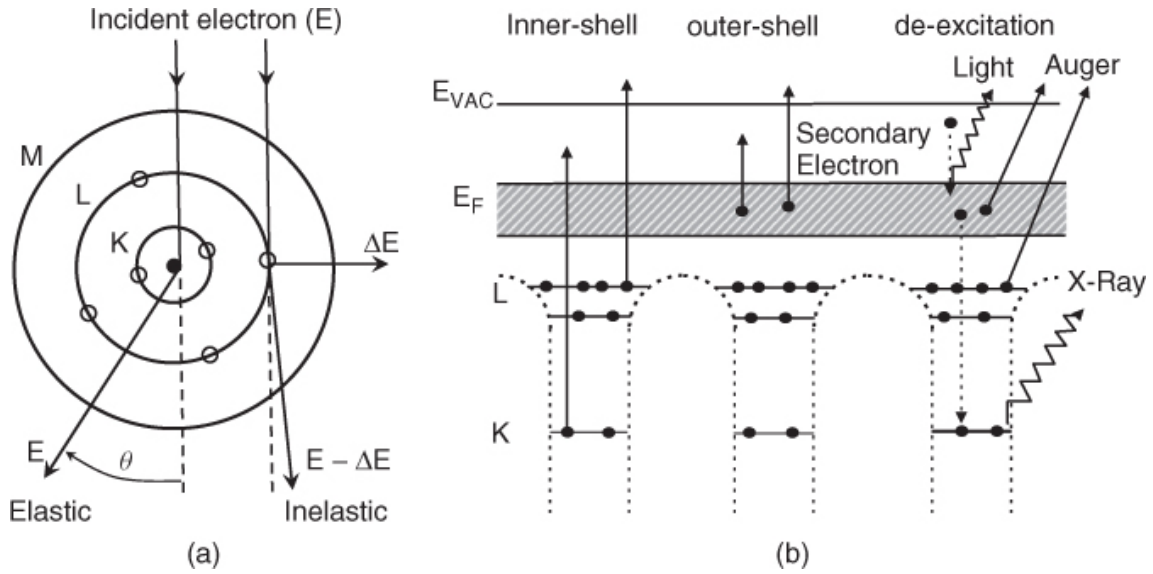


Figure 3.10: (a) Schematic drawing of elastic and inelastic scattering. (b) Schematic diagram of inelastic excitations. Reprinted with permission from ref [152]. Copyright © 2013, John Wiley and Sons.

The Coulomb interaction of an incident electron with the electron in the atomic shell is an inelastic scattering, that means as soon as the interaction process results in noticeable energy transfer, i.e. if the magnitude and not just the direction of the momentum vector changes, it is inelastic [Fig. 3.10 (a)]. If the incident electron provides sufficient energy to the inner shell electron greater than its binding energy, it can transit to the unoccupied states above the Fermi level. The incident electron loses this characteristic energy and scatters through a particular angle around 10 mrad for 100 keV electron beam energy, but it is important to mention that the inelastic scattering angle is material-dependent. An electron from the outer shell undergoes the recombination process and occupies this vacant core hole position by liberating excess energy in the form of the kinetic energy of atomic electron,

i.e. Auger electron or electromagnetic radiation (x-rays) [Fig. 3.10 (b)]. However, valence to conduction band excitations may occur due to inelastic scattering. The oscillations of the electron density in the conduction band, i.e., plasmons, are also visible in the EELS, since they are the primary inelastic interaction and predominantly determine the mean inelastic free path mentioned in the next section. [149–151].

3.2.2 EELS instrumentation

Fig. 3.11 shows a schematics of standard TEM-based post-column EELS system. The main component of the EELS setup is the high-resolution spectrometer. A single-channel electron detector was used for serial spectrum recordings in earlier times. However, position-sensitive detectors, for example, photodiode or charge-coupled diode (CCD), are developed for simultaneous spectrum recording [136, 150].

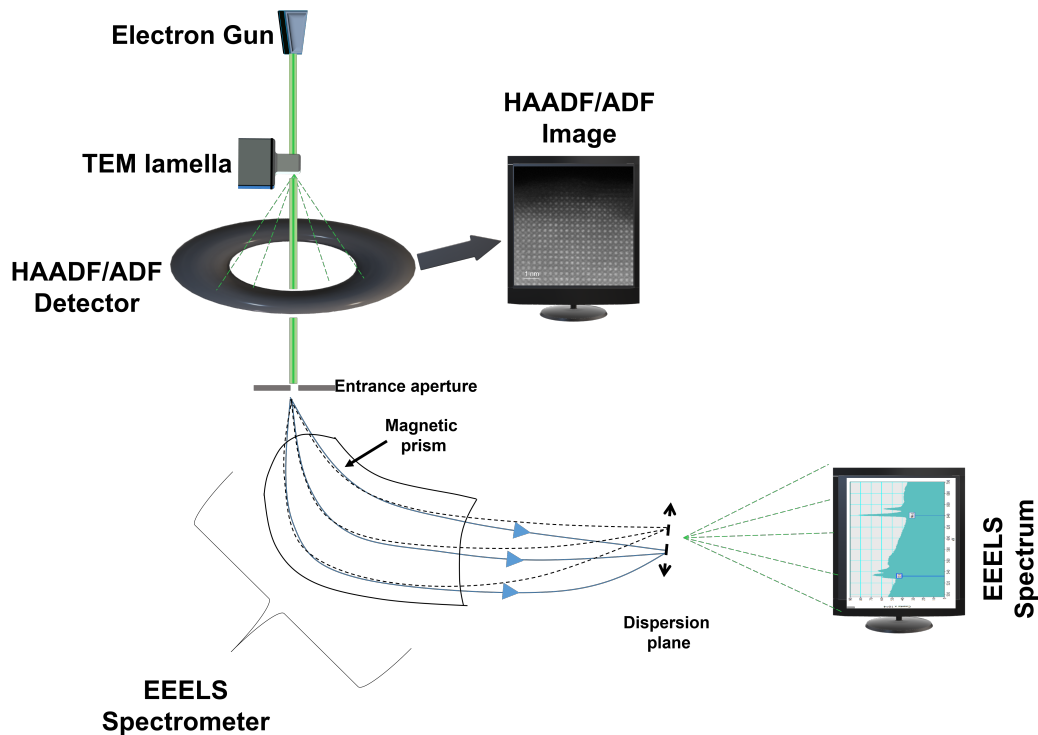


Figure 3.11: Schematic drawing of the postcolumn EELS setup

An advanced post-column Gatan imaging filter (GIF) introduces quadrupole and sextupole lenses to correct aberrations in the EELS spectrometer. This advanced GIF with a $2k \times 2k$ detector can perform correction of the pre-edge background

and elemental mapping for an appropriate core loss ionization [149–151]. The spectrum is recorded using a prism spectrometer. The scattered electrons enter the EELS spectrometer through an entrance aperture (variable in diameter, e.g., 1, 2, 3, and 5 mm). The electrons pass through a drift tube in the spectrometer and deflect by $\geq 90^\circ$ due to the magnetic field. A post-column filter can be operated in imaging (EFTEM) or spectrum (EELS) mode. Spectrum mode is functionally similar to placing the diffraction pattern on the entrance aperture, hence that is why the collection angle of the aperture is important for the quantification. Electrons that have lost more energy are deflected more than those suffering zero loss (the Lorentz force acting on a moving charge scaling with its velocity). A spectrum is then projected on the dispersion plane, recording the distribution of beam intensity versus loss of energy [136, 150]. Scanning transmission electron microscopy (STEM) mode focuses electron beam in a small probe, and then raster scans over the specimen surface to acquire a series of spectra for spatial information. In STEM mode, the spectrum imaging (SI) technique records a spectrum at each pixel to construct a SI on a spectrum-by-spectrum basis. Combination of spectroscopic and spatial information provides a broad range of data interpretation opportunities. Information of the single spectrum analysis technique can be transferred to the entire SI to perform spatially resolved analysis. This capability makes the STEM-EELS mode a powerful tool for material characterization and analysis [153].

3.2.3 Zero loss peak (ZLP) and Thickness of the specimen

Thickness is an essential parameter of the EELS analysis. It is helpful to know the local thickness of the specimen for the correct data interpretation of the elemental concentration, defect, or low and core loss EELS spectrum and also in the HRTEM image simulation. Log-ratio is the most commonly used procedure for thickness analysis. It calculates the ratio of the integrated intensity of the ZLP I_0 and integrated intensity of the entire spectrum I_t (contribution mostly from the plasmon peak ≈ 50 -100 eV). Therefore, according to the Poisson statistics of inelastic scattering gives the relative thickness,

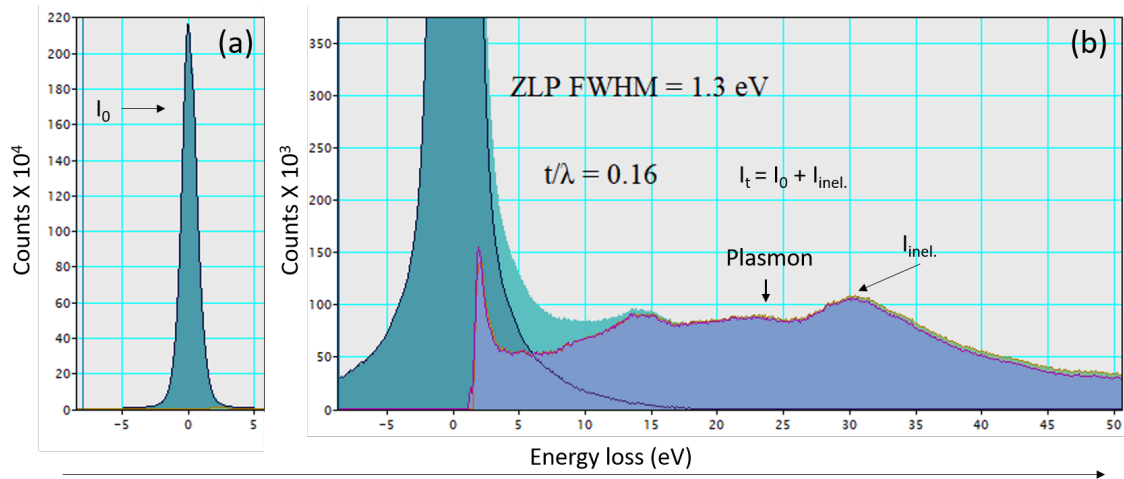


Figure 3.12: Calculation of relative thickness in Gatan digital micrograph. (a) Zero loss peak (I_0). (b) Deconvoluted plasmon region showing total transmitted intensity (I_t)

$$\frac{t}{\lambda} = -\ln\left(\frac{I_0}{I_t}\right) \quad (3.4)$$

where the λ is the inelastic mean free path (IMFP) of the electron. The ratio of the t/λ provides the relative thickness of the selected area of the specimen and it is useful for the EELS data interpretation [149–151].

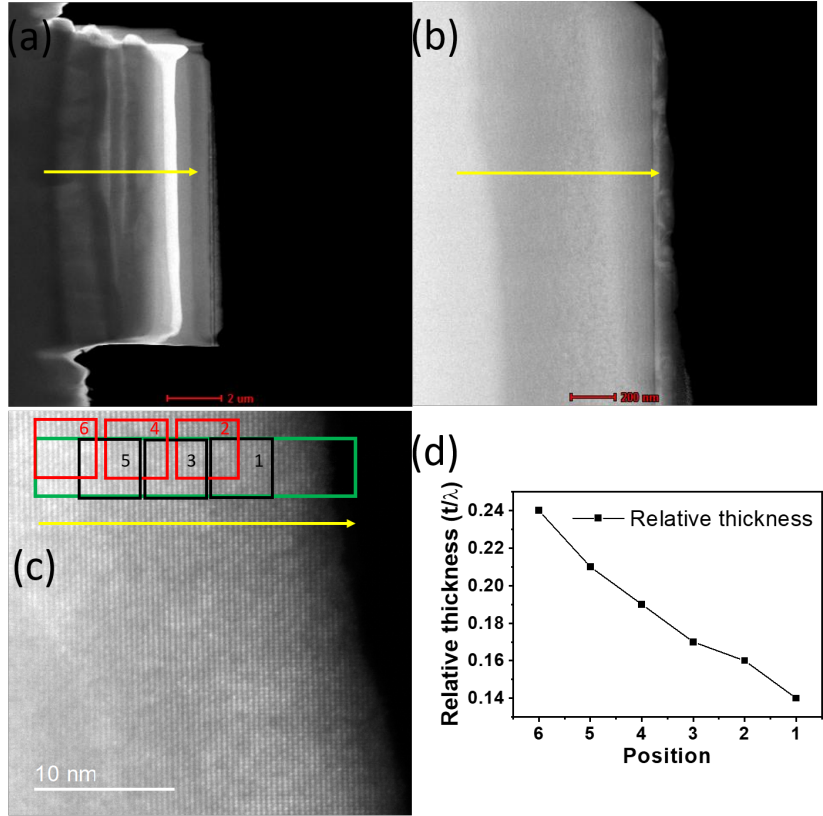


Figure 3.13: Calculation of relative thickness $\text{Pr}_{0.9}\text{Ca}_{0.1}\text{MnO}_3$ surface. (a and b) STEM image of $\text{Pr}_{0.9}\text{Ca}_{0.1}\text{MnO}_3$ lamella. (c) Annular dark field (ADF) image of surface. Green rectangle show a region of interest (ROI). Small numbered squares shows positions used for the calculation of t/λ . Yellow arrow in all images show direction of the decrease in thickness of the specimen. (d) t/λ calculated from the positions in the ROI shown in the (c).

Fig. 3.13 show a measurement of the relative thickness (t/λ) of the $\text{Pr}_{0.9}\text{Ca}_{0.1}\text{MnO}_3$ surface. Fig. 3.13 (a) and (b) shows the STEM images of the TEM lamella of $\text{Pr}_{0.9}\text{Ca}_{0.1}\text{MnO}_3$ specimen. The green rectangle show the region of interest for the t/λ measurement. The spectra is acquired in the STEM-EELS (dual) mode from the thick region to the thin region (position 6 - 1 in image c). Yellow arrows in all the images show the direction of the decrease in thickness. The thickness profile across the ROI is shown in image (d). A linear decrease in the t/λ indicates a thin region at the edge of the specimen. It also suggests the absence of plural scattering at the $\text{Pr}_{0.9}\text{Ca}_{0.1}\text{MnO}_3$ top surface (at the edge). The Malis method (included in Gatan digital micrograph) is the most common technique to calculate the IMFP. The λ depends on the electron energy, collection semiangle β and the material [154]. The current study uses 300 kV electron energy and

$\beta = 23$ mrad (with 2.5 mm entrance aperture) and 46 mrad (with 5 mm entrance aperture) for the EELS measurements. Therefore, using the Malis method, we get a rough estimation of $\lambda \approx 114$ nm (for $\beta = 23$ mrad) and ≈ 101 nm (for $\beta = 46$ mrad) for the perovskite oxides, respectively.

3.2.4 EELS spectrum

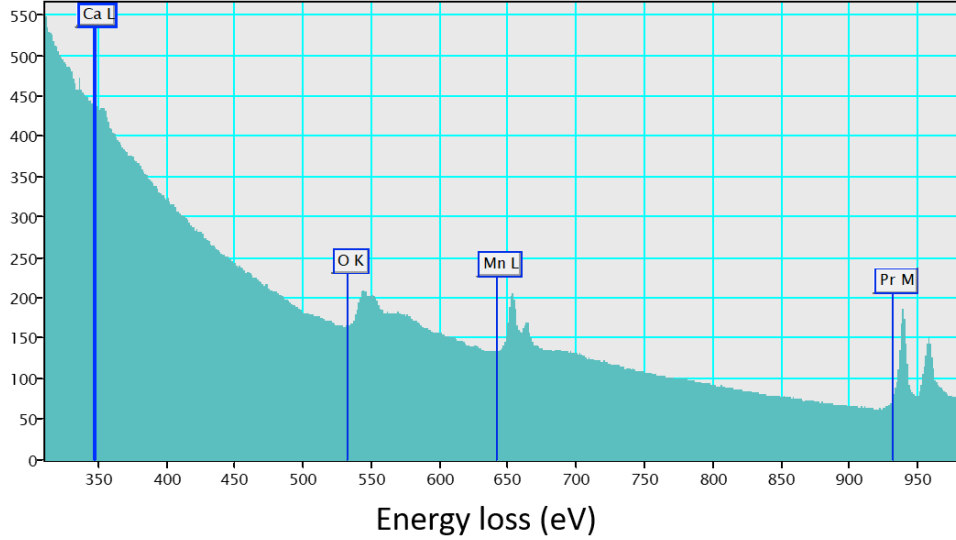


Figure 3.14: Core loss EELS spectrum of $\text{Pr}_{0.9}\text{Ca}_{0.1}\text{MnO}_3$ recorded at dispersion of 1 eV/Ch.

Fig. 3.12 (a) and (b) shows the low loss region, which includes information of the conduction and valence band electrons from the weakly bonded electrons [136]. The low loss region contains a ZLP at 0 eV and a peak from inelastically scattered electrons from the outer shell electron of the specimen. This peak is called a plasmon peak [150] is shown in the Fig. 3.12 (b) which is deconvoluted using the inbuilt function of Fourier log method in the Gatan DM. Though ZLP is a useful feature in the EELS data analysis, it may be problematic. It can damage the CCD detector or create a ghost peak if it is overdosed [136]. Fig. 3.14 show the overview of the EELS spectrum of the $\text{Pr}_{0.9}\text{Ca}_{0.1}\text{MnO}_3$. It contains information on the primary elements present in the specimen from tightly bound core-shell electrons [136]. The core loss edges show comparatively low intensity as compared to ZLP. The signal intensity decreases rapidly as the energy loss increases, and the signal is almost negligible above 2 keV [136]. Fig. 3.14 shows core loss of Calcium (Ca) L-edge, Oxygen (O) K-edge, Manganese (Mn) L-edge, and Praseodymium (Pr) M

edge. This thesis uses EELS analysis to understand Transition metal (TM)-oxygen (O) bonding and TM valence analysis. The detailed analysis of TM-O core loss edges is discussed in the section 3.2.6.

3.2.5 Dual-EELS mode

ZLP calibration while measuring core losses is typically not possible in single spectrum EELS mode. Dual-EELS mode allows measuring of core losses while monitoring the ZLP. It is possible to transfer the calibration from the zero-loss peak to the core loss spectra in the Gatan digital micrograph software.

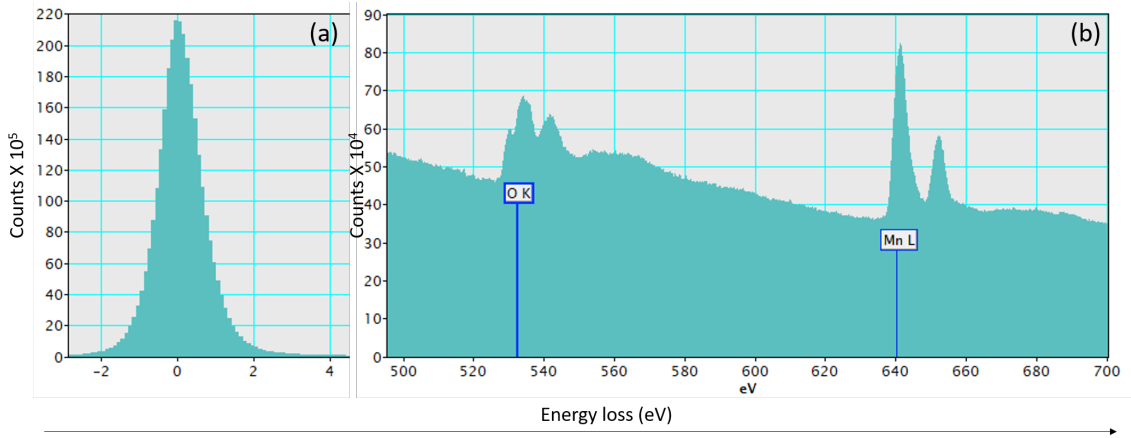


Figure 3.15: O K and Mn L edges recorded using Dual EELS technique in Titan ETEM operated at 300 kV. (a) Zero loss peak. (b) O k and Mn L edges in the core loss region.

Dual-EELS mode also improves the signal-to-noise ratio when measuring the strong elastically scattered zero-loss peak and weak core loss features simultaneously [155]. The Gatan spectrometer is enhanced with a fast electrostatic shutter that allows millisecond exposure times when recording an entire high loss spectrum and simultaneous capturing of the low-loss regions [150, 156]. O K and TM L edges are measured using Gatan Quantum 965ER post-column energy filter in the Dual-EELS mode. Fig. 3.15 Show (a) ZLP and (b) core loss of O-K and Mn-L edges recorded using 0.1 eV dispersion/Ch in the Dual-EELS mode.

3.2.6 Core loss excitations

Core loss is usually used to classify the elemental composition and its electronic states. Particularly for the transition of 3d states in the TM, perceived as “white line” (due to they emerged as white areas on a photographic negative when an x-ray

absorption spectrum was recorded) [150]. The inner-shell electrons located in the K and L shells of the atoms possess binding energies in the range of 400-2000 eV. Due to the characteristic energy loss of each element, these ionization edges provide characteristic chemical information. These ionization edges are superimposed on to the background [Fig. 3.14] caused by the plasmon loss, which can be extrapolated and extracted for structural or elemental analysis. Also, the background of the tails from the elements ionization edges coming before contributes to the next element [Fig. 3.16 b]. This background should be carefully removed [136].

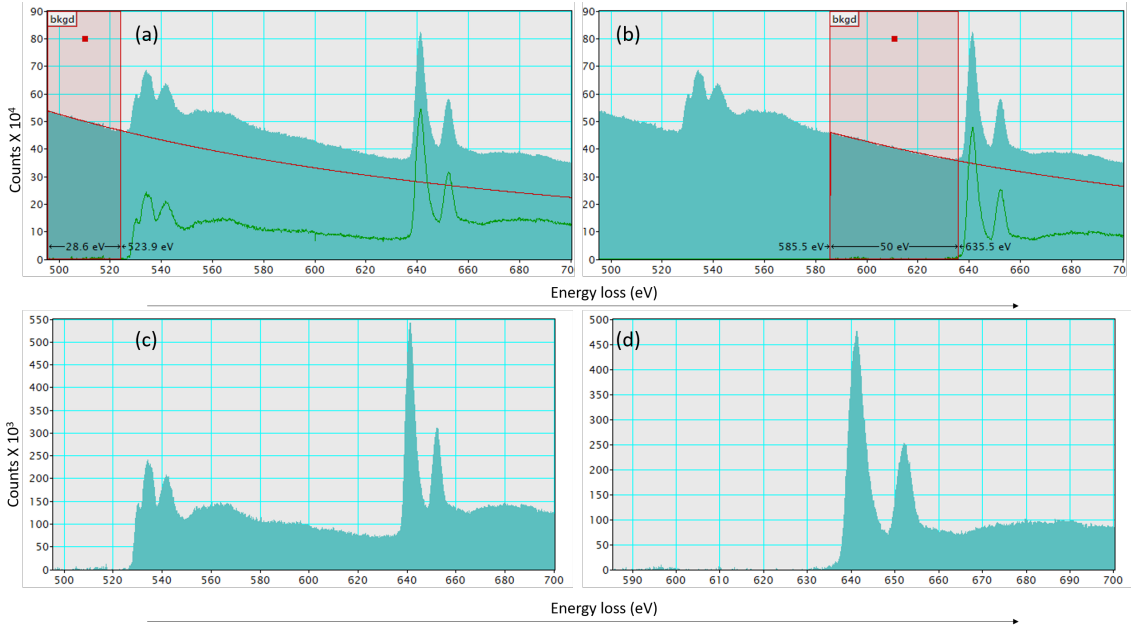


Figure 3.16: Background correction of O K and Mn L-edge of the $\text{Pr}_{0.9}\text{Ca}_{0.1}\text{MnO}_3$ surface. Background correction for the O K-edge (a) and Mn L-edge (b) using a power-law window of 29 eV and 50 eV, respectively. Background-corrected O K (c) and Mn L (d) edges.

The plasmon peak has the second-most intensity in the EELS spectrum after the ZLP. The background in the core loss edges arises from the decrease in the continuum after the maximum intensity of the plasmon loss (in the range of 15-25 eV). Fig. 3.16 (c) show that ionization of the O K-edge continuum contributes to the Mn L-edge background. This O K-edge contribution still interferes in the Mn-L edge intensity after background correction of the O K-edge. Therefore separate background correction should be done for the Mn L-edge as shown in the image Fig. 3.16 (b) and (d).

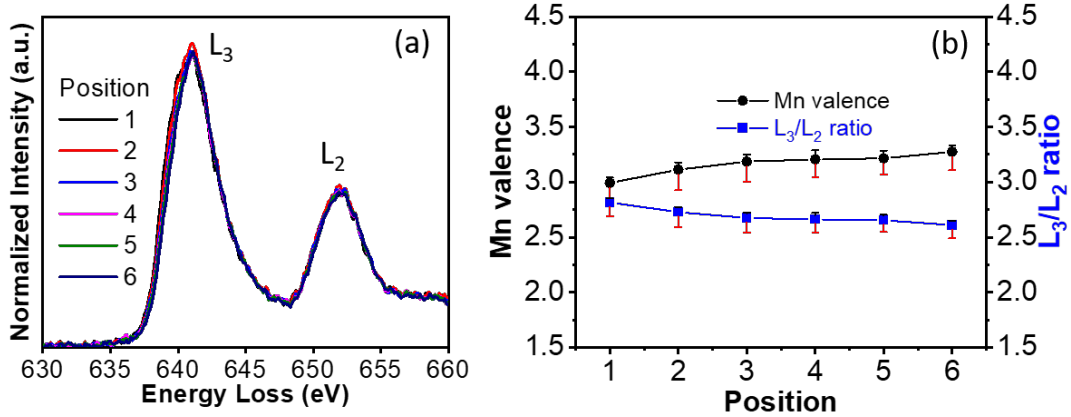


Figure 3.17: (a) Mn L edge recorded from positions in the ROI shown in the Fig. 3.13 (b) L_3/L_2 ratio and Mn valence calculated from Mn L edges in (a).

The sharp peaks shown in the Fig. 3.17 (a) arise due to the excitation of the core electron into the empty 3d states of TM. The L_3 and L_2 edges vary minor in energy and arise from the L shell's spin-orbit splitting. The spin-orbit coupling induces the 1/2 state (L_2) and has low energy than the (L_3) 3/2 state. The ratio and the chemical shift of the L_3/L_2 are useful to understand the change in the valence state of the TM [136, 137, 150]. The empty/half-occupied 3d orbitals are quite sensitive to the valence states of the TM, which can be efficiently investigated by analyzing the L_3/L_2 peak ratio and peak positions [149–151]. Fig. 3.17 (a) shows the Mn L_3 and L_2 edge, and (b) Mn valence as well as L_3/L_2 ratio extracted from the ROI shown in Fig. 3.13 (c). Further details of the EELS data interpretation and TM valence analysis can be found in chapters 5, 6, 7.

3.2.7 Electron Monochromator for EELS

The energy resolution is a crucial element in EELS analysis. A few meV energy resolution is desired to study fundamental aspects of vibrational mode excitations of atoms, fine structure, valence analysis, and electronic structural analysis. EELS resolution strongly depends on electron source; thermionic emission sources provide, Tungsten (W) 3 eV and Lanthanum hexaboride (LaB6) 1.5 eV, respectively. However, combining a field emission gun or a Schottky gun with a monochromator provides sub (0.1) eV EELS resolution. Commonly, Wien filters are used as monochromators with perpendicular magnetic and electrostatic fields allowing electron of particular energy distribution to pass through the TEM column [136, 150].

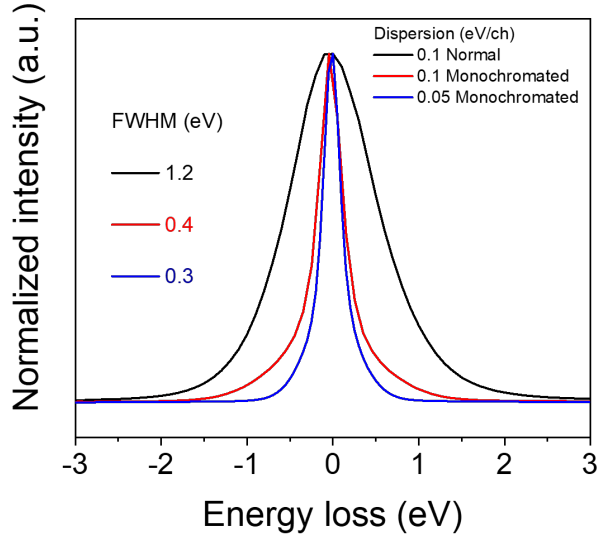


Figure 3.18: Zero loss peaks recorded from using normal and with the monochromated source in Titan ETEM operated at 300 kV. The full widths at half-maximum (FWHM) are 1.2 eV for normal, 0.4 and 0.3 monochromated setup, respectively.

Fig. 3.18 shows the zero peak acquired with and without a monochromator showing the decrease in full width at half maximum (FWHM). For the in-situ ETEM experiments, specific alignments are required for the gas regulations, EELS spectrometer alignments, and spherical aberrations. All these processes are time-consuming, and in-situ ETEM experiments may take 2-3 days. Therefore all these processes make it difficult to work with monochromated EELS [136, 150]. In this thesis conventional STEM-EELS measurements show sufficient information with 1.2 eV FWHM of the ZLP.

3.3 Environmental Transmission Electron microscopy (ETEM)

Nanomaterials and nanostructures play a critical role in the progress of some crucial technologies. Due to the high demand for nanomaterials in various energy fields, their characterization techniques are also concurrently developed. Due to the capability of studying nanomaterials at atomic resolution, high-resolution transmission electron microscopy (HRTEM) is one of the essential techniques used now [157, 158]. The Aberration-corrected Microscope could achieve spatial resolution up to 50 pm [159–162]. Generally, HRTEM studies of nanomaterials are

carried out under ultrahigh vacuum conditions ($\approx 10^{-7}$ mbar). However, such circumstances may be insufficient when studying the active state in heterogeneous catalysis. The reaction mechanisms, structural properties, and surface dynamics firmly depend on the surrounding reactive or inert environment [158] (see chapter 4, 5, 6 and 7). Under such circumstances, the HRTEM observations instead are carried out in in-situ/operando conditions under the controlled exposure of a reactive gas. However, due to a small mean free path of the electron beam in a gaseous environment, the use of TEM for in situ observations of complex reactions is problematic [158]. Accordingly, a constrain of the gas environment to the proximity of the solid nanomaterial is required to restrict the number of gas molecules along the electron beam path. Therefore a differentially pumped microscope vacuum column or a tight sealed environmental cell provided with an electron-transparent membrane have been developed [158, 163]. The lamella is directly exposed to the gas environment in an isolated pumped volume on the microscope column, or in the environmental cell in a differentially pumped microscope Fig. 3.19. Differential pumping apertures isolate the TEM sample and gas molecules from the microscope vacuum in the environmental cell. The coherence of the electron beam is reduced due to the scattering of electrons by the gas molecules and the electron-transparent membrane. Another way of decreasing the number of gas molecules in the microscope includes nozzles for localized gas injection [158, 164, 165].

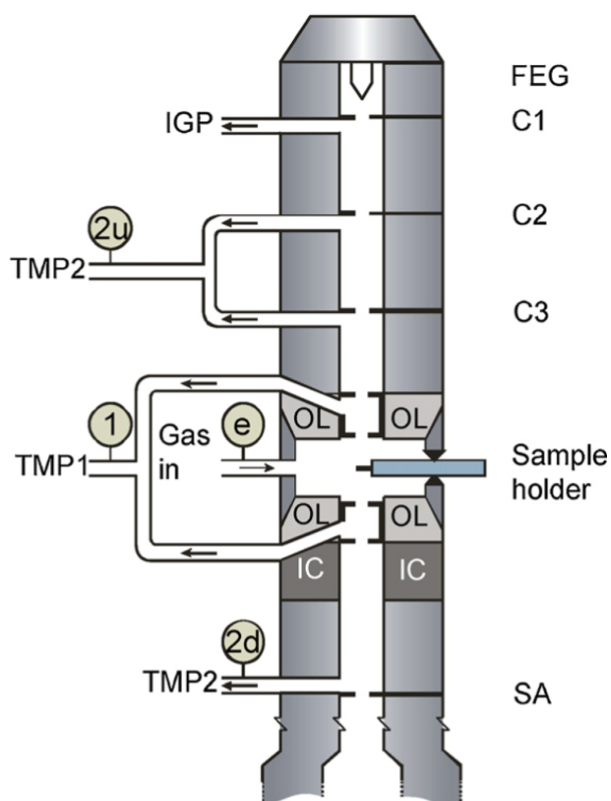


Figure 3.19: Schematic drawing of the differential aperture pumping system in ETEM. Reprinted with permission from ref [158] . Copyright 2012 Elsevier: Micron.

Pressure limiting apertures included keep the high-pressure area as small as possible. Pumping from turbomolecular and ion getter pumps maintain the pressure in Field emission gun (FEG) chamber $\approx 1e-9$ mbar, column $\approx 1e-7$ mbar and octagon $\approx 1e-7$ mbar in HV mode. In the ETEM mode using the differential pumping system octagon pressure ranges between $\approx 1e-5$ to 20 mbar depending on the gas type [166] [Fig. 3.19]. The great strength of in-situ TEM/ ETEM is to characterize local chemical and structural changes at the catalyst surface at atomic resolution. In-situ TEM/ETEM analysis allowed it to understand complex heterogeneous catalysis mechanisms [167]. The in-situ TEM/ETEM technique is used in critical reactions, such as improving the catalytic performance of exhaust gas catalysts [168], ammonia synthesis [169], nanocarbon growth [170, 171], carbon monoxide (CO) oxidation [172–174], water splitting [175], and oxidation and reduction reactions [176]. The combination of electron energy loss spectroscopy (EELS) and high-spatial-resolution in ETEM offers insights into the oxygen vacancy formation on catalyst surface [177]. Aberration corrected optics system in

ETEM observations allows real space atomic resolution of dynamic catalysts surface in few millibars of gaseous environment [178]. The capability to regulate the gas concentration through ETEM observations is a beneficial way of exploring the changes in the structure and electronic properties. Recent ETEM observations correlate surface atomic dynamics to real electrochemical studies in OER-like conditions (see chapter 5, 6, 7). Advancements towards monitoring the electron beam-induced and applied electric potentials in ETEM allow in-situ studies of dynamic catalyst-electrolyte/H₂O interface under OER like conditions [133]. These findings suggest that ETEM has excellent potential and a promising future in the field of heterogeneous catalysis development. In this thesis, in-situ TEM investigations are carried out with a FEI Titan ETEM G2 80–300 operated at 300 kV in the Collaborative Laboratory and User Facility for Electron Microscopy at Georg-August-Universität Göttingen [179].

3.4 Sample preparation for the ETEM

This section presents the instruments and a technique used to prepare thin lamellas for the in-situ ETEM observations.

3.4.1 Focused Ion Beam (FIB)

The FIB instrument consists of a liquid ion metal source, an ion source and column, a chamber with a vacuum system ($\approx 1 \times 10^{-10}$ mbar for field emission gun), a sample stage (vacuum range $\approx 1 \times 10^{-6}$ to -8 mbar, depending on the ion-gas molecule interaction), detectors, and a supporting gas delivery and computer system. For very small sample areas, sputtering is done with a liquid metal ion source (LMIS) in FIB. Gallium (Ga) is the most commonly used LIMS in FIB due to its i) low melting point (29.8° C) - which minimizes interdiffusion of liquid into the Tungsten (W) crucible chamber and possible reactions, ii) low volatility - which preserves the metal supply and results in longer life times, iii) low vapor pressure - due to this Ga can be used in pure liquid form since it does not evaporate, iv) low surface free energy - it stimulates viscous behavior on the W substrate, v) emission characteristic - it promotes high angular intensity at minimal energy spread, vi) excellent vacuum, mechanical and electrical properties. When Ga LMIS is heated, molten Ga flows and wets W metal needle. An electric field (10^8 V/cm) is applied to the W tip, which induces this molten Ga to form a 2-5 nm diameter point source in the shape of "Taylor cone" as a result of the balance of electrostatic and surface tension force due to the applied electric field. To ionize Ga an extraction voltage is applied by field evaporation of the metal at the end of the cone. A steady flow of Ga ions replaces the evaporated Ga ions. The emission current

of the Ga ions varies with the applied voltage in the range of 5 - 30 kV. The lifetime of the Ga LIMS depends on the amount of liquid material in the reservoir and the material properties. The lifetime is measured as μA - hours/available source material in milligrams. Usually, Ga has a lifetime of approximately 400 μA -hours/mg. Ga ions are more massive and travel at very low velocities; hence their Lorentz force is lower and magnetic lenses could not focus them effectively compared to the electrons [180]. Therefore, the Ga ion beam is focused using two electrostatic lenses [181]. Using a spot size of $\approx 5 - 10$ nm, it is possible to deposit material up to 30 nm and to mill the smallest feature (line pattern) down to 10 nm [182]. Helios G4 dual beam system is used for the ultra-thin TEM lamella preparation for in-situ studies in this thesis. This system has accelerating voltage from 200 eV - 30 keV, current range 01.pA-70 nA, and offers a range of in-line and retractable detectors for imaging with backscattered, secondary or forward-scattered electrons. This system is equipped with the easy lift technique for the fine controlled movement, and a Pt or carbon deposition gas injection systems [183].

3.4.1.1 Dual-Beam approach

The FIB system may be used only with an ion column, but in recently developed FIB system, it is combined with a scanning electron microscope (SEM) column, the FIB/SEM Dual beam system for advanced TEM lamella preparation.

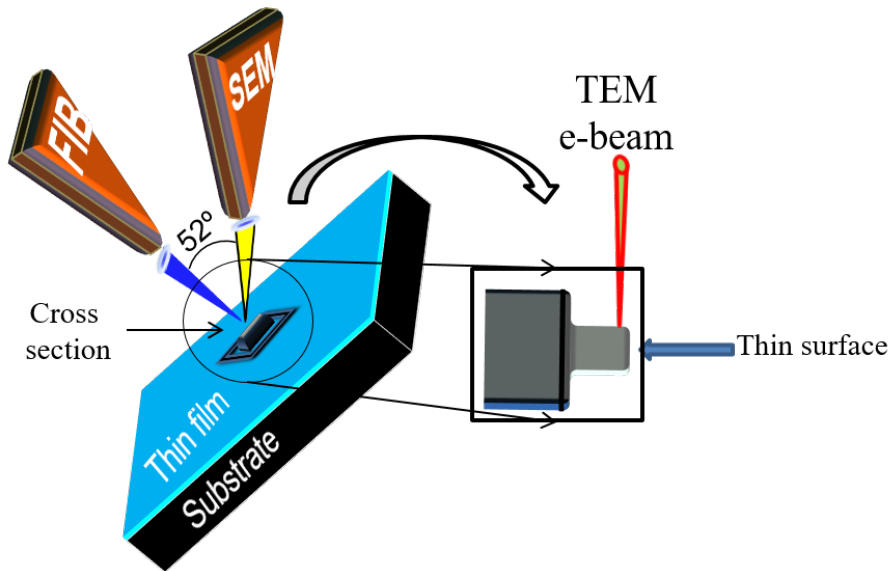


Figure 3.20: Schematics of FIB system.

This combination is particularly beneficial for cross-section TEM lamella prepara-

ration. SEM can monitor cross-section preparation, polishing, and thinning during the FIB works flows. Dual beam is configured so that the sample will be tilted to 52° for the milling process [Fig. 3.20], which is beneficial for the careful observation through SEM during complex thinning/polishing processes the TEM lamella [183].

3.4.1.2 Ga ion - material interaction

Ion milling is a process of physical sputtering. During sputtering, an ion that is incident to the material surface undergoes a series of collisions before coming to rest within the material, or being reflected. The displacement of sample atoms similarly proceeds in a cascade-like fashion, until one or multiple atoms are ejected from the surface or the energy dissipates to secondary effects (amorphization, electronic and vibrational excitations). A collision cascade is a group of neighboring energetic collisions of atoms caused by an energetic particle in a liquid or solids. If a surface atom receives enough kinetic energy to overcome the surface binding energy, it ejects as a sputtered particle. Phonons, plasmons, and secondary electrons are also generated due to inelastic scattering resulting from ion bombardment. Secondary electrons are used for image formation in the SEM, although in principle secondary ions can also be used [183].

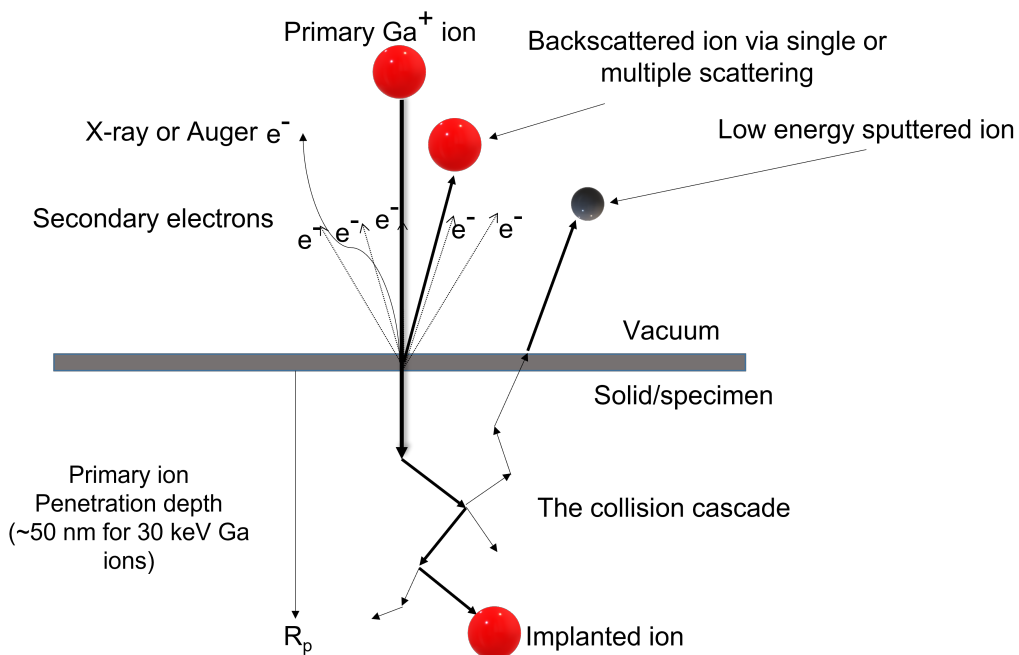


Figure 3.21: Schematics of Ga Ion-Solid interaction.

The kinetic energy of the incident Ga ion induces interaction between the ion and the solid surface. If Ga ion does not backscatter, it eventually comes to rest and is implanted within the solid at some depth R_p [Fig. 3.21]. Redeposition is also an important phenomenon that occurs due to the deposition of sputtered and backscattered ions in the proximity of the milling area. Surface degradation could result from the redeposition; therefore, special care must be taken while preparing cross-section TEM lamellas. Surface amorphization is the biggest drawback of the TEM lamella preparation in the FIB. The ion implantation is one of the cause of the formation of the amorphous phase in the material, while knock on damage is the other [183]. It is impossible to avoid amorphization completely, even with a careful low kV milling process. Argon (Ar) ion milling in the precision ion polishing system could more easily minimize this amorphous region due to the lower mass of Ar and lower accessible beam energy. However, due to the redeposition and lower controllability, the risk of surface damage and contamination is high during Ar ion milling. The solution of choice to this problem in the work presented here is the use of lower Ga ion beam acceleration voltage, but more critically the in-situ recrystallization of the damaged (amorphous surface) in ETEM under high partial pressure of oxygen. During the Ga ion milling step, the surface protection layer is an important aspect that needs to be considered here. Pt is the most common protection layer used in most cases. However, for ETEM observations under OER-like conditions this will not be helpful as it shows OER and ORR activity. A novel approach is developed using spin-coated Alkali Resistant Positive Photoresist X-AR-P5900/4 (Photoresist) as a protection layer [184]. [Appendix A.2]

3.4.2 Precision Ion Polishing System (PIPS)

In the present study, the Argon ion milling process is used to partially remove the residual surface protection layer as well as the amorphous layer formed during FIB thinning. For this, we used precise Ar ion milling of cross-sectional TEM lamellas using a Gatan precision ion polishing (PIPS) 691 and II systems. Generally, the Ar ion milling technique uses 0.5 - 6 keV accelerating potential. The ion beam penetration in the specimen is tuned by controlling the incident angle of the Ar ion beam. Low angle $\leq 5^\circ$ provides selective thinning and reduces ion implantation. However, incidence angle $< 5^\circ$ deposits the ion beam energy at the top layer of the specimen, which results in amorphization. Lower Ar ion beam energy will reduce the beam damage, but it consumes more time. Therefore, a proper combination of correct beam energy, incidence angle, and time makes Ar ion milling a valuable technique in sample preparation [136].

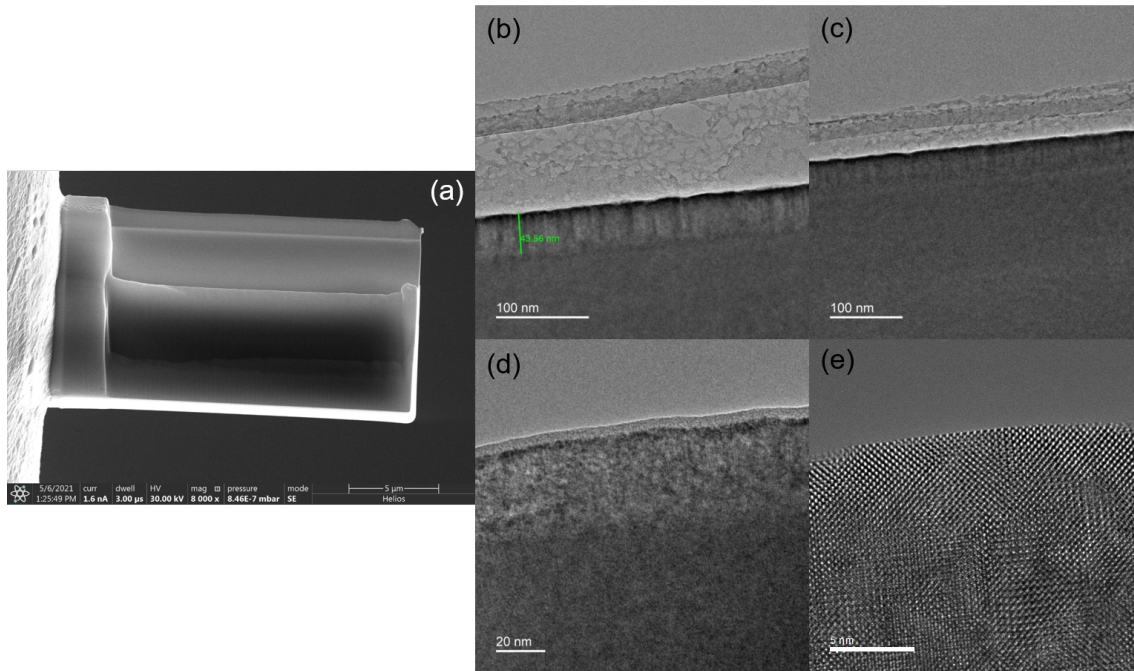


Figure 3.22: Procedure of surface cleaning and recrystallization. (a) As prepared TEM lamella with photoresist (top) layer. (b) Surface after 10 min plasma cleaning. (c) Surface after additional 10 min plasma cleaning. (d) Surface after 1 min of Ar ion polishing. (e) Recrystallized surface in 1 mbar of O₂ in ETEM

Fig. 3.22 shows the series of images of the single crystalline surface preparation for the ETEM observations. The as-prepared TEM lamella Fig. 3.22 (a) is cleaned using plasma (70% Ar and 30% O₂) cleaner for 10 minutes, Fig. 3.22 (b) and (c) respectively. However, the photoresist protection layer could not be removed by just using plasma cleaning, and a few tens of nanometer of photoresist were still on the surface. An Ar ion beam is used with 0.2 keV accelerating voltage with 25 μ A beam current with tilting offset of $\pm 5^\circ$ for 1 minute. Fig. 3.22 (d) show surface after Ar ion milling. Almost all the photoresist was removed from surface, and some of the crystalline surface was amorphized by the Ar ion beam. This amorphous surface was recrystallized in ETEM under the influence of electron beam in the presence of 1 mbar of O₂ [Fig. 3.22 (e)].

3.4.3 Plasma Cleaning

Carbon contamination on TEM lamella prepared in FIB systems influences the HRTEM imaging quality [185]. Contamination due to hydrocarbon growth is also regularly observed on samples during TEM observations [186]. Plasma cleaning expeditiously removes hydrocarbon from the TEM lamella surface. One could use


FIB milling for such cleaning, but it is time-consuming, and it may damage the specimen surface [187]. In this work, we used The Evactron® De-Contaminator System to clean the residual hydrocarbon and carbon from the TEM lamella. A low radio frequency (RF) plasma ionizes the gas mixture (used mixture in current work is 70% Ar and 30% O₂). The oxygen molecules are scattered by interacting with electrons and forms oxygen radicals. These oxygen radicals interact chemically with hydrocarbons and carbon atoms, producing carbon monoxide (CO), carbon dioxide (CO₂), and H₂O, which are easily removed by the system vacuum. This process is also referred to as “ashing”. At the same time, the Ar ions clean the surface since it does not react chemically with the specimen. The plasma is generated in the hollow cathode and flows relatively slowly to the sample. That in turn means that the kinetic energy of Ar ions is low (below 100eV on average at higher pressures), which results in better surface cleaning instead of damaging events. [188]. Fig. 3.22 (b) and (c) show surface after plasma cleaning for 10 minutes each, respectively. These two images show that the top layer of the photoresist is removed, but 100% removal of photoresist by plasma cleaning is not possible. Therefore, using PIPS and recrystallization in ETEM is reasonable way to achieve the desired crystalline sample surface for in-situ ETEM observations.

Chapter 4

In Situ Preparation of $\text{Pr}_{1-x}\text{Ca}_x\text{MnO}_3$ and $\text{La}_{1-x}\text{Sr}_x\text{MnO}_3$ Catalysts Surface for High-Resolution Environmental Transmission Electron Microscopy

Article

In Situ Preparation of $\text{Pr}_{1-x}\text{Ca}_x\text{MnO}_3$ and $\text{La}_{1-x}\text{Sr}_x\text{MnO}_3$ Catalysts Surface for High-Resolution Environmental Transmission Electron Microscopy

Vladimir Roddatis , Gaurav Lole and Christian Jooss *

Institute of Materials Physics, University of Goettingen, D-37077 Goettingen, Germany

* Correspondence: vroddatis@ump.gwdg.de (V.R.); cjooss@gwdg.de (C.J.);

Tel.: +49-551-39-25026 (V.R.); Tel.: +49-551-39-25303 (C.J.)

Received: 19 July 2019; Accepted: 29 August 2019; Published: 6 September 2019



Abstract: The study of changes in the atomic structure of a catalyst under chemical reaction conditions is extremely important for understanding the mechanism of their operation. For in situ environmental transmission electron microscopy (ETEM) studies, this requires preparation of electron transparent ultrathin TEM lamella without surface damage. Here, thin films of $\text{Pr}_{1-x}\text{Ca}_x\text{MnO}_3$ (PCMO, $x = 0.1, 0.33$) and $\text{La}_{1-x}\text{Sr}_x\text{MnO}_3$ (LSMO, $x = 0.4$) perovskites are used to demonstrate a cross-section specimen preparation method, comprised of two steps. The first step is based on optimized focused ion beam cutting procedures using a photoresist protection layer, finally being removed by plasma-etching. The second step is applicable for materials susceptible to surface amorphization, where in situ recrystallization back to perovskite structure is achieved by using electron beam driven chemistry in gases. This requires reduction of residual water vapor in a TEM column. Depending on the gas environment, long crystalline facets having different atomic terminations and Mn-valence state, can be prepared.

Keywords: perovskites; environmental transmission electron microscopy; surface chemistry

1. Introduction

Rational design of heterogeneous catalysts for high selectivity and turnover of chemical reactions requires detailed knowledge about the activity- and selectivity-determining structural properties, including catalytically active sites. Analysis of atomic and electronic structure of catalyst surfaces and subsurfaces under chemical reaction conditions thus is essential, since catalysts often undergo significant changes in surface and defect structure in their active state [1–3]. In situ atomic scale studies of electrocatalysts under working conditions can contribute substantially providing insights into the underlying reaction mechanism [4,5]. Environmental transmission electron microscopy (ETEM) offers unique opportunities in gaining atomic resolution images of surfaces and subsurfaces, formation of surface disorder, as well as spatially resolved spectroscopic information about the electronic structure and oxidation states of catalyst surfaces. In a dedicated ETEM instrument, a standard specimen chamber is replaced with a differently pumped environmental cell (E-cell) equipped with inlet and outlet lines [6]. The E-cell allows performing tomography [7], collecting high resolution images [8] and provides an easy access to use analytical techniques such as energy dispersive X-ray spectroscopy (EDX) and electron energy loss spectroscopy (EELS) [9,10], although the maximal pressure is limited to 20 mbar [11], or 100 mbar [12]. In its turn, dedicated gaseous holders [13] allow performing studies at pressures up to 4–5 bars [14], but field of view, spatial resolution, quality of images and use of analytical tools are limited because of silicon nitride membranes especially at low accelerating voltages [8]. Due to these recent technical improvements, ETEM has become a valuable instrument to reveal structural transformations of nanoparticles and catalyst surfaces in reactive environments [15–18].

At the same time, atomic resolution studies of catalysts require electron-transparent specimens with a thickness of only a few nanometers. Ideally, for reliable in situ experiments with cross-section specimens one needs to have an original surface of a catalyst showing no traces of preparation process in order to relate the obtained results with ex situ experiments. Conventional preparation methods include mechanical polishing and ion beam milling, where protection against surface damage is achieved by deposition of metal films [19]. In order to avoid sample thinning, Jacobs and Verhoeven [20] developed a method where a catalyst film is deposited onto a very thin Si_3N_4 membrane. Since the catalyst properties strongly depend on preparation methods and morphology, this method does not allow comparison with the properties of the system used in operando. Nowadays, focused ion beam (FIB) cutting combined with a lift-out technique is often applied for the preparation of ultrathin lamellas of almost any kind of material [21]. This also allows integration of lamella onto micro-electro-mechanical systems (MEMS) used in dedicated in situ holders. In order to minimize ion beam damages, the presence of protection layers such as Pt/C or W/C films is required [22]. However, both metals form clusters and can be very active as catalysts, thus masking the activity of studied material. Moreover, the presence of heavy atoms can change the contrast of high-resolution images collected to observe dynamical changes of catalysts surface. Alternative protection layers containing mainly carbon have been also reported [23].

Recently, it was demonstrated that electron beam driven epitaxial recrystallization of an amorphous surface layer developed during FIB cutting on the preexisting crystalline SrTiO_3 is possible with high beam currents in scanning TEM (STEM) mode [24]. However, in high vacuum the resulting oxygen stoichiometry cannot be controlled. In a gaseous environment, the effects caused by the interaction of electron beam with the sample can be combined with a control of chemical changes. For example, STEM EELS imaging of a manganite in 3 mbar of O_2 can give rise to sample oxidation by oxygen uptake [25]. This is in contrast to reduction of the same material in high vacuum at the same used electron fluxes due to oxygen knock out.

In this study, we demonstrate a FIB based two-step preparation method of cross-section TEM perovskite oxide specimens, resulting to well-ordered crystalline surface edges with controlled oxygen stoichiometry and avoiding any contamination by metallic impurities. We have selected (001) oriented epitaxial $\text{La}_{1-x}\text{Sr}_x\text{MnO}_3$ (LSMO) with $x = 0.4$ and $\text{Pr}_{1-x}\text{Ca}_x\text{MnO}_3$ (PCMO) with $x = 0.1$ and 0.33 thin films showing quite high activity as catalyst materials for the oxygen evolution reaction [17,26–28]. The first essential step for the lamella preparation is the FIB cutting using a protection layer of alkali resistant positive photoresist. After ion milling and removal of the photoresist by plasma etching thin amorphous layers still can present on materials. The second step is the in situ recrystallization of remaining amorphous surface layers. Epitaxial recrystallization can be achieved in O_2 as well as in He and N_2 with residual O_2 , leading to different surface terminations. The partial pressure of residual water in the column of electron microscope is found to be an essential parameter determining whether the epitaxial recrystallization of the perovskite or phase decomposition into a binary oxide evolves. Since the selected materials have significantly different electrical properties we think that observed effects are valid for many other complex oxides as well.

2. Results

The low magnification cross-section image of LSMO ($x = 0.4$) specimen prepared using photoresist protection layer is shown in Figure 1a. Two windows of different thickness are used to demonstrate the opportunity to control the thickness of lamella. The HRTEM image in Figure 1b and HRSTEM image in Figure 1c show that plasma cleaning during 5 min removes the rest of the photoresist completely.

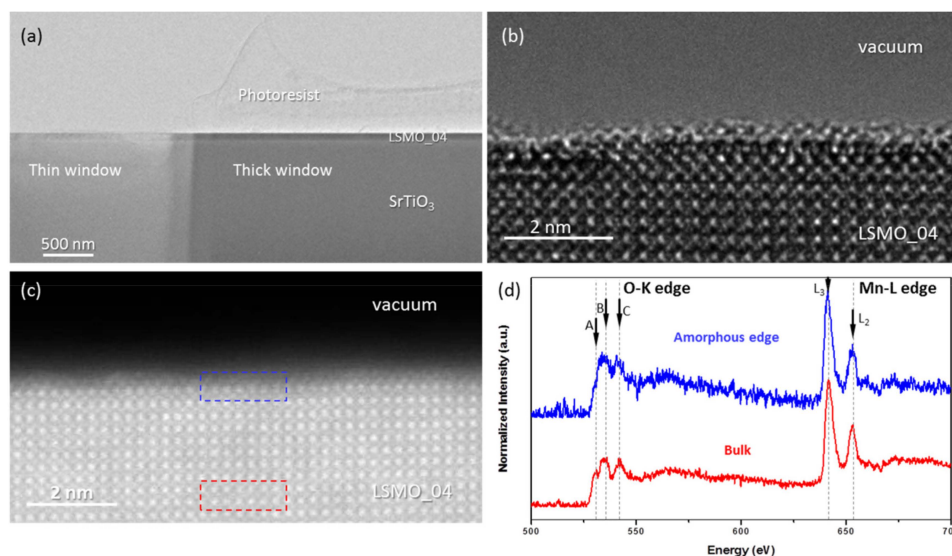


Figure 1. (a) Low magnification image of $\text{La}_{0.6}\text{Sr}_{0.4}\text{MnO}_3$ (LSMO) ($x = 0.4$) lamella prepared with the use of photoresist protection layer; (b) High-resolution transmission electron microscope (HRTEM) image of an edge collected from the thin window area; (c) high-resolution scanning TEM (HRSTEM) image, the areas marked with red and blue are used to collect electron energy loss spectroscopy (EELS) data (0.1 eV/channel) presented in (d). Spectral features marked with A, B, C, L_2 and L_3 are discussed in text.

Both the HRTEM and HRSTEM images show that the ~40–50 nm thin lamella has a crystalline structure, despite a thin subunit-cell thick disordered surface layer. EELS spectra presented in Figure 1d show that this disordered surface of LSMO film has lower oxidation state of Mn than the bulk. Three characteristic peaks of O K-edge are visible at 529 eV (A), 534 eV (B) and 543 eV (C). The prepeak (A) due to O 1s transitions to O 2p states hybridized with Mn 3d. It reflects the presence of O 2p holes. The other two peaks are due to transition from O 1s into O states which are hybridized with Ca d / Pr d states (B) and free electron like features (C) [29]. Since oxygen vacancies are electron donors, a decrease in the intensity of the prepeak A indicates an increasing amount of oxygen vacancies. Its lack in the spectrum from the surface points to a reduced state of Mn. This is also confirmed by the analysis of the Mn L-edge. The Mn L edge is due to transition of the spin-orbit split 2p into Mn 3d states and thus shows L_3 and L_2 subfeatures. The L_3/L_2 intensity ratio is a measure of the Mn oxidation state [30]. Our analysis yields an oxidation state between +2.6 and +2.8 for the amorphous material. Atomic force microscopy images of the same LSMO 0.4 films show crystalline surface which consist of atomically flat terraces and unit cell height steps [28] as a result of step flow growth mode on vicinal SrTiO_3 (STO) (001). There is some evidence that crystalline LSMO films on SrTiO_3 can have reduced surfaces after vacuum annealing [31]. Since the LSMO films studied here are annealed in oxygen after growth, complete oxidation of the surface as seen in [31] is expected. We thus attribute surface disorder and Mn reduction of the TEM lamella shown in Figure 1 to preparation-induced damage. Indeed, scattering of Ga ions during FIB thinning can give rise to preferential knock out of oxygen at the LSMO-photoresist interface.

The possibility of a beam stimulated transformation of preparation induced surface disorder to the perovskite crystal structure is demonstrated for a 2–3 nm thick amorphous PCMO layer on top of crystalline PCMO $x = 0.33$ in different gases, i.e. He, N_2 , and O_2 in Figure 2. The cross-section lamellas have been cut from the PCMO/LSMO/Nb-STO stack; 300 kV electron beam stimulation is performed in TEM mode with a beam of about 100 nm in diameter and ~4 nA current. Such illumination conditions result in a $14,000\text{--}20,000 \text{ e}^- \cdot \text{s}^{-1} \cdot \text{\AA}^{-2}$ dose rate. The process takes about 20–25 min in order to complete

the transformation of the amorphous layers in He (Figure 2a) or in N₂ (Figure 2c) to a surface facets having of a length of about a few dozen nanometers, Figure 2b,d, respectively. It is noteworthy that the first facets of several nanometers in length were formed already after the first three minutes. The corresponding movies S1, S2 and S3 show the real time changes of structure in N₂ gas ($p_{N_2} = 5$ ubar) at the beginning, after about 20 min and at the end of process, respectively. During all stages of process a pronounced atomic dynamics at the surface is observed similar to Epicier et al. [32]. Also, Figure 2b,d demonstrate that electron beam irradiation can result in different surface terminations. This will be discussed in detail further down. Thus, the process resembles the so-called solid phase epitaxial (SPE) growth, where an initially amorphous Si [33] or complex oxide [34] thin film is epitaxially recrystallized on a crystalline template at elevated temperatures. Remarkably, the electron-beam-induced SPE process in our environmental TEM study is observed at room temperature and depends on a reactive gas environment. The required electron flux is orders of magnitude lower than that reported for the transformation of amorphous STO into perovskite structure during operation the microscope in STEM mode (electron dose rate $\approx 1 \times 10^8 \text{ e}^- \cdot \text{s}^{-1} \cdot \text{\AA}^{-2}$, high vacuum conditions $p = 10^{-7}$ mbar) [24].

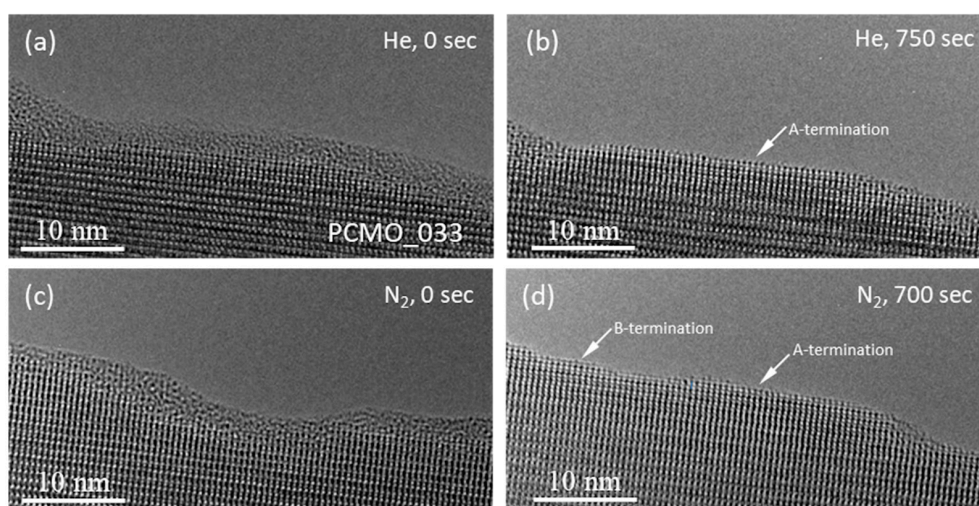


Figure 2. HRTEM images of an edge of Pr_{1-x}Ca_xMnO₃ (PCMO) ($x = 0.33$) material in He ($p_{He} = 50$ ubar) at the beginning (a), after 750 s (b), and in N₂ at the beginning (c) and after 700 s (d), respectively.

The crystallization in O₂ gas proceeds similarly as in He or N₂, however, it takes only about 5–6 min at the same illumination conditions. Snapshots of crystallization in O₂ are presented in Figure 3. At the beginning, during several minutes, only mobility of atoms in amorphous layer is visible, similar to observations in He or N₂ (Figure 3a–d). Then, the growth of small pyramidal islands is observed (one island is marked with the yellow arrow). These islands grow slowly and over time reach the surface of amorphous layer (Figure 3e). At the same time the thickness of amorphous layer is decreasing. Finally, the amorphous material between crystalline islands also becomes crystalline, and flat facets up to 10 nm in length are formed (Figure 3f–h). It is important to note that in all gases (He, N₂ and O₂), the final phase of crystallization, i.e. when crystalline islands have sprouted through the amorphous layer, proceeds faster.

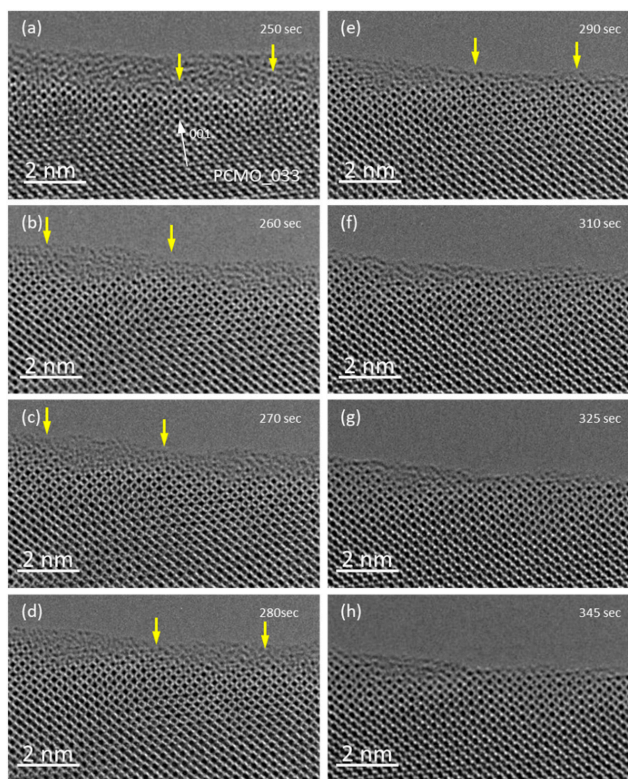


Figure 3. A series of images showing transformation of amorphous edge of PCMO ($x = 0.33$) into crystalline structure. The images were collected in O_2 , $p_{O_2} = 50$ ubar. (a) During several minutes only mobility of atoms in amorphous layer is visible. (b–d) The growth of small island of pyramidal shape is observed (the place is marked with the yellow arrow). (e) These pyramids grow slowly and reach the surface of amorphous layer. Its thickness becomes smaller at the same time. Finally, amorphous areas between pyramids also transform in crystalline perovskite oxide phase, and flat facets up to 10 nm in length are formed (f–h).

In order to verify the chemical composition of original, amorphous and recrystallized PCMO, the EELS spectra were collected at the beginning of experiment and after the recrystallization was completed. In addition, K- edges of oxygen and L-edges of Mn were collected with the better energy resolution to examine the oxidation state of Mn.

The HRSTEM images shown in Figure 4a,b demonstrate an edge of PCMO ($x = 0.33$) film before and after recrystallization in oxygen at $p_{O_2} = 50$ ubar, respectively. Clean and atomically sharp steps having a height of few unit cells are commonly observed. The corresponding EELS spectra are shown in Figure 4c. All spectra were aligned using a zero-loss peak (ZLP) as a reference, and then normalized. Note, that the spectrum collected from the amorphous edge looks noisier than other spectra because of smaller thickness of the edge. Based on the reduced intensity of the O K prepeak (A), the crystallization in He results in a reduced state of Mn at the surface. The analysis of L_3/L_2 ratio of Mn L-edge yields an average value of 3.30 ± 0.06 and a value of 3.24 ± 0.02 close to the surface (see Figure S1). In contrast, when the crystallization was performed in O_2 the average value of the Mn oxidation state is 3.36 ± 0.06 and 3.35 ± 0.06 at the surface (see Figure S2). All values are close to the value for the nominal composition as in bulk (+3.33). Thus, the use of oxygen leads to the epitaxial recrystallization of a stoichiometric PCMO, whereas in He, a crystalline edge with increased lattice disorder is developed. The average Mn valence state is the same in He as in O_2 within error based on the analysis of the

L_3/L_2 intensity ratio. However, there is a strong reduction of the O K prepeak at the surface, pointing towards a more reduced state in He. The effect of disorder on electronic properties is quite complex. For example, in addition to oxygen vacancies, charge neutral pair defects can contribute to the lattice disorder in He which can maintain the Mn valence while changing the O K edge. Nevertheless, for all three gases used, the lattice spacing up to most top unit cell corresponds to the bulk PCMO material within error.

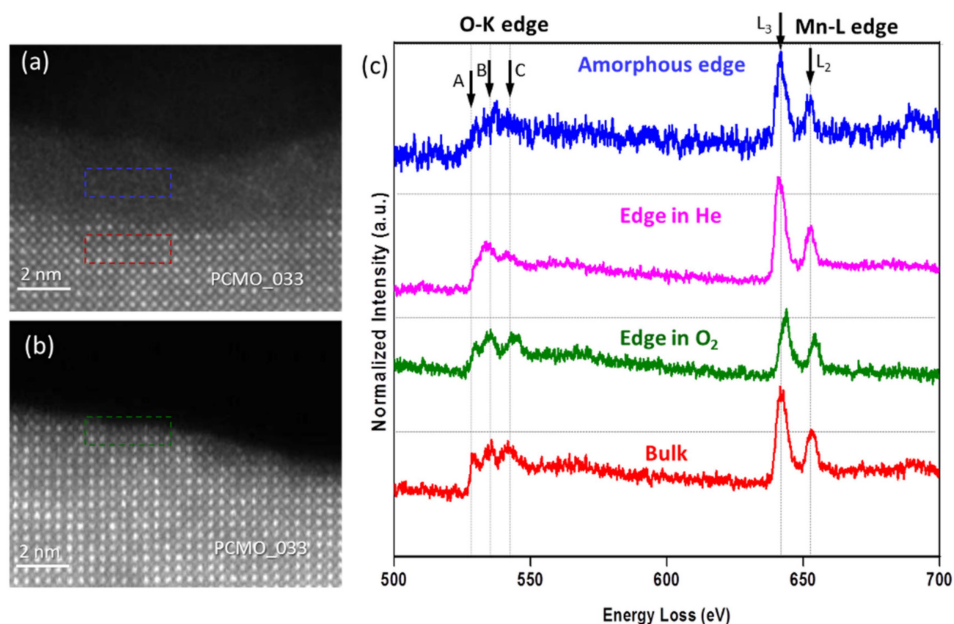


Figure 4. HRSTEM images of PCMO ($x = 0.33$) before (a) and after (b) crystallization under electron beam in oxygen, respectively. (c) EELS spectra (0.1 eV/channel) collected from the areas marked with different colors in (a) and (b). Spectral features marked with A, B, C, L_2 and L_3 are discussed in the text.

The chemical composition of the amorphous layer as well as recrystallized material was also verified using EELS, and only Pr, Ca, Mn, and O edges were detected; Figure 5 shows the results for the PCMO, $x = 0.33$. A HRSTEM image of the recrystallized area is shown in Figure 5a. The EELS spectra reveal a decrease of Ca content in the surface unit cells (Figure 5b). Since the properties of perovskite materials strongly depend on the amount of doping, a careful choice of the illumination conditions and the environment is very essential for control of the chemical composition of the recrystallized perovskite. A long lasting electron beam illumination to fully recrystallize the amorphous layer obviously results in element-specific knock out damage of light elements which is evidenced by chemical analysis (Figure 5). In addition, the lattice disorder of the recrystallized perovskite due to off-stoichiometry is visible by broadening of spots and changing of their intensities in corresponding FFT images calculated from the HRTEM images collected in all the gases used. The effect is notably less pronounced in series of HRTEM images collected from the same TEM lamella in O_2 (see Figures S3 and S4), supporting our statement of a less vacancy disordered structure because Mn acquires its nominal valence state.

As it was already described above, that flat facets were formed from the amorphous material at the surface of PCMO in all He, N_2 and O_2 gases used. Moreover, a careful inspection of the top atomic layer revealed that the termination of the recrystallized edge depends on the gas used. This effect is shown in Figure 6. Both A- and B-cation stable terminations were observed after recrystallization in N_2 (Figure 6a), while only the A-cation termination of facets was found after recrystallization in He (Figure 6d). The observation is verified by HRTEM image simulations presented in Figure 6b,c,e,f, respectively. The HRTEM images of PCMO along $[100]$ and $[010]$ look differently because of the

symmetry inherent in the Pbnm space group. The Mn-O (B-termination along [010]) is obviously recognized in Figure 6a,b because of a characteristic zigzag motif of Mn-O atomic columns (see Figure S6 for details). In the case of A-termination the difference in HRTEM images along [100] and [010] is almost invisible.

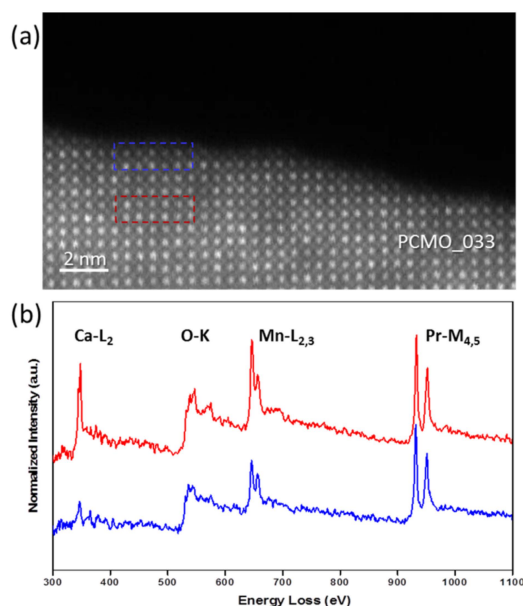


Figure 5. (a) HRSTEM image of PCMO ($x = 0.33$) with two selected area used to verify the chemical composition of original PCMO material and recrystallized amorphous layer. The corresponding normalized spectra (1 eV/channel) are shown in (b), and the signal from Ca is remarkably weaker at the last unit cell.

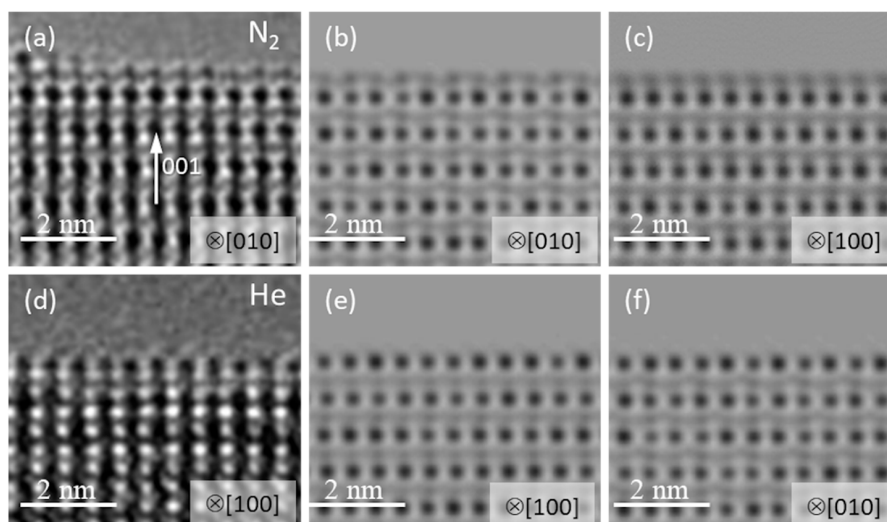


Figure 6. Experimental HRTEM images of PCMO ($x = 0.33$) collected in N_2 (a) and in He (d) at $p = 50$ ubar; (b,c,e,f) corresponding calculated images along [100] and [010] directions. Both A- and B-cation stable terminations are visible in N_2 , whereas only the A-cation termination of facets is visible in He.

As an example for the recrystallization of PCMO ($x = 0.1$), Figure 7a–c shows the evolution in He. The first crystalline facets showed up only after 28 min, compared with about 11 min for PCMO ($x = 0.33$). After such a long irradiation time, one can expect a high density of defects in the material. Indeed, the spots in the FFT image became more smeared after 28 min, which is evidence of the increased structural disorder (see Figure S5). The weak signal of Ca is still visible in the EELS spectra taken from the edge (Figure 7d,e) taking into account that the concentration of Ca is already very low in the original material. In general, the EELS data from PCMO ($x = 0.1$) sample are very scattered. In some areas the analysis of O-K and Mn-L edges shows that the oxidation state of Mn is in the +3.0–+3.3 range (Figure 7f) pointing against a large concentration of single oxygen vacancies as origin of the lattice disorder. However, very low values of the oxidation state of Mn were also observed (Figure S7).

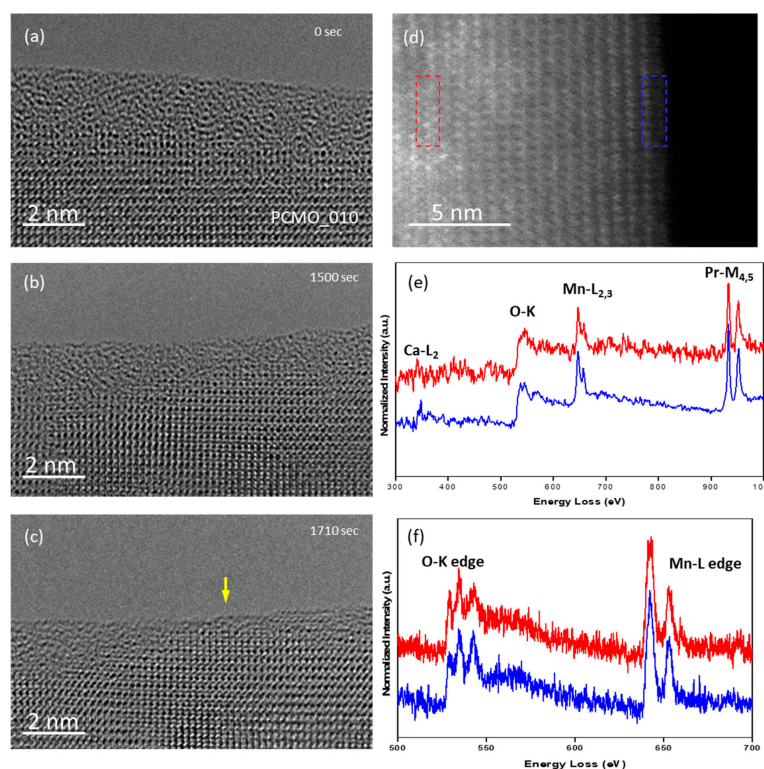


Figure 7. (a)–(c) HRTEM images showing transformation of amorphous edge into crystalline for the PCMO ($x = 0.1$) in He gas at pressure of 50 ubar. The first crystalline facets (marked with the yellow arrow in b) start to appear after ~28 min (1710 s). (d) High-angle annular dark field (HAADF) image of the recrystallized area. (e) EELS spectra (1 eV/channel) demonstrate the presence of Pr, Ca, Mn and O. (f) EELS spectra (0.1 eV/channel) reveal a slightly reduced Mn oxidation state.

Usually, the recrystallization of the edge in PCMO ($x = 0.1$) took much longer for all gases used. This is however consistent with cyclic voltammetry studies, showing a pronounced surface $\text{Mn}^{2+}/\frac{1}{2}\text{V}_\text{O} \leftrightarrow \text{Mn}^{3+}/\text{O}_\text{O}$ redox couple for PCMO (0.33) which is absent in $x = 0.1$. As an example, Figure 8 shows cyclic voltammograms of two epitaxial (001) oriented PCMO ($x = 0.1$ and $x = 0.33$) films on LSMO/Nb:STO at pH = 13 measured at a sweep rate of 10 mV/s. The electrochemical measurements were performed in 0.1 M potassium hydroxide (KOH) electrolyte prepared by diluting KOH stock solution with deionized water (for neutral pH see [17]). Both films show an exponential increase of currents at positive potential due to oxygen evolution reaction (OER), as verified by measuring the formed O_2 by a ring electrode. The pronounced redox peak for $x = 0.33$ indicates an easier oxygen vacancy formation and healing

process compared to $x = 0.1$ which explains the observation of faster epitaxial recrystallization for $x = 0.33$ compared to $x = 0.1$ in the ETEM experiments.

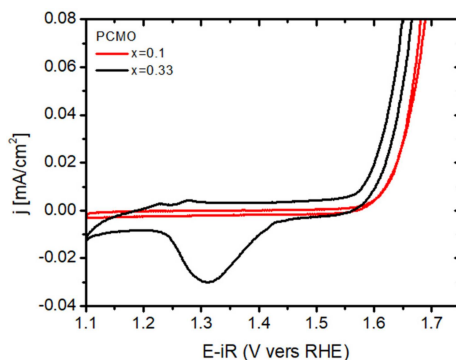


Figure 8. Cyclic voltammograms of (001) oriented PCMO ($x = 0.1$) and ($x = 0.33$) films in 0.1 M KOH. The $x = 0.33$ film shows a redox couple which is overlapping to the onset of OER at the anodic branch and well separated from OER at the cathodic branch. This redox couple is absent for PCMO ($x = 0.1$).

Finally, we note that the epitaxial crystallization only happens at the preexisting crystalline interface, when the partial water pressure is $p_{\text{H}_2\text{O}} < 5 \cdot 10^{-8}$ bar (Figure 9). In other words, the residual pressure of water vapor in the column should be below 0.1% of the working gas. Exemplary snap shot from the Quadera™ software (Figure 9a) shows two periods during the experiment in He when the cold trap was not used (Cold trap OFF) and after it was activated (Cold trap ON). At the higher pressure of water vapor ($p_{\text{H}_2\text{O}} = 25 \cdot 10^{-8}$ bar, Cold Trap OFF) the amorphous layer was transformed into randomly oriented PrO_2 particles as shown in Figure 9b (see also Figure S8). Similar structural transformations of initially amorphous areas were reported earlier for the ETEM experiments performed in water vapor at higher pressures of $5 \cdot 10^{-6}$ and $5 \cdot 10^{-5}$ bar [18], and this is consistent with the drop of OER activity in electrochemical experiments over time due to Mn leaching into the electrolyte [28]. After the cold trap was filled with liquid nitrogen and as soon as the partial pressure of water vapor dropped about an order of magnitude ($p_{\text{H}_2\text{O}} = 25 \cdot 10^{-9}$ bar), the epitaxial recrystallization was observed (Figure 9c) similar to results presented in Figures 2–4.

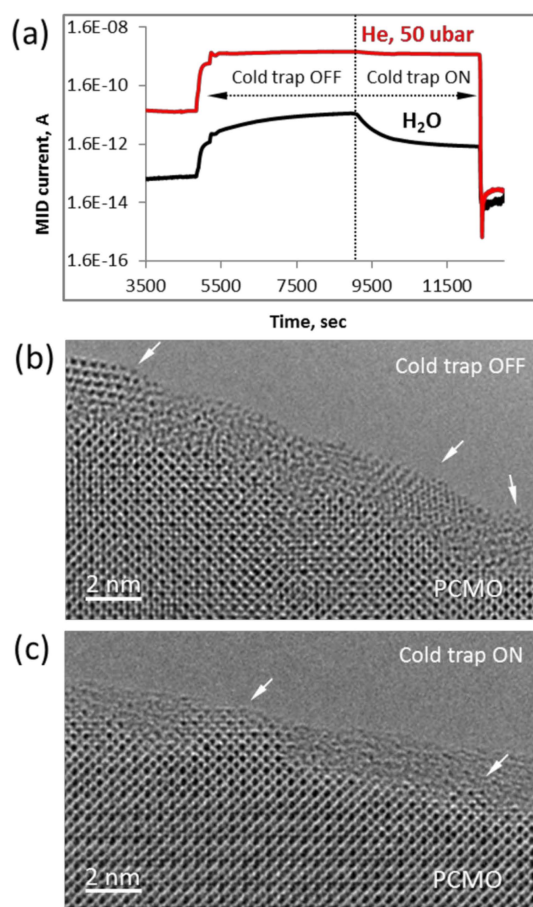


Figure 9. (a) A snapshot of Quadera™ software during environmental transmission electron microscopy (ETEM) experiment at 50 ubars of He with and without activated cold trap. Experimental HRTEM images in He when the cold trap was OFF and ON are shown in (b) and (c), respectively. The white arrows point out on randomly oriented PrO₂ particles, growing in amorphous layer (b), and epitaxially growing pyramids of PCMO ($x = 0.33$) (c).

3. Discussion

As already mentioned, the observed recrystallization of amorphous PCMO resembles SPE of an amorphous Si which happens via a moving amorphous/crystalline interface, where velocities of a few nm per min requires elevated temperatures above 500 °C [33]. The recrystallization temperature can be significantly reduced to around 200–300 °C, if the recrystallization is assisted by ion irradiation [34]. Although the electron-beam induced recrystallization reported here also happens via the movement of the crystalline/amorphous interface, it however strongly differs from the SPE. First of all, the beam induced temperature increase ΔT in the TEM lamella is irrelevant, excluding a thermally activated growth mechanisms. The upper limit of temperature increase for the used beam parameters is $\Delta T = 0.015$ K (see Appendix A). Furthermore, the epitaxial recrystallization in our experiments strongly depends on the gas environment. In high vacuum conditions, no epitaxial growth is observed. Here, the amorphous layer partially disappears on timescales of tens of minutes due to electron beam-induced sputtering of atoms from damaged areas.

In oxygen both amorphous PCMO $x = 0.1$ and $x = 0.33$ layers transform into a crystalline perovskite layer under oxygen uptake during the recrystallization process. This is confirmed by a change of

the Mn valence state from about +2.9 in the amorphous to close to the nominal value. There are three possible candidates for beam induced electronic excitations driven the observed solid state chemistry: (i) a photo-chemical process driven by beam induced generation of hole carriers. Since the lifetime of photo-holes (1 ns) is orders of magnitudes below the recrystallization rate (1 s per atom), a photo-chemical process is highly improbable. (ii) An electrochemical process driven by beam induced positive electric potentials due to secondary electron emission. Such an electrochemical mechanism is feasible: The relevant redox potential for oxygen in manganites is of the order of 1 V (see Figure 8), a potential which can be easily generated in semiconductors at dose rates above $10.000 \text{ e}/\text{\AA}^2\text{s}$ [35]. (iii) Radiolysis, the dissociation of molecules or covalently bound solids by inelastic scattering of primary electrons with bond forming valence electrons. Whereas radiolysis may be relevant for the dissociation of molecular oxygen and activation of O_2 for the solid state reaction, it is irrelevant in ionic or metallic solids. Here, this is confirmed by the formation of rather perfect crystalline perovskite structure in O_2 .

Beam-induced displacements of atoms by nuclear collisions is probable process for activating the growth of crystalline PCMO by a moving amorphous/crystalline interface as observed in O_2 as well as in the inert gases N_2 and He. However, it cannot explain the oxygen uptake in O_2 . Maximum energy transfer takes place by backscattering of electron which could displace surface adsorbed oxygen into the amorphous material on the top side of the lamella, but would lead to sputtering on the bottom side and at the edge. This would represent an “inverse sputtering process”, where in contrast to HV, oxygen vacancies are filled by activated surface oxygen. Conversely, in N_2 , one should then form oxynitrates, in contrast to observation.

The observation that the amorphous phase transforms into crystalline PrO_x nanoparticles in the presence of sufficient partial pressure of H_2O by preferential leaching of Mn and also Ca give strong hints about the beam induced chemistry involved. Based on the equation provided by Egerton et al. [36], for the energy transfer between a high energy electron and an atom due to elastic scattering, we calculate the upper limit for the different atomic species: E_{max} is 53.1 eV (O_2), 42.5 eV (Ca), 34.0 eV (Mn) and 14.4 eV (Pr). This must be compared to binding energies of $E_b = 50 \text{ eV}$ (O), 70 eV (A site) [14] and between 50–170 eV (Ti as an exemplary B-site in BaTiO_3) [37], depending on the crystal orientation of a perfect perovskite single crystal. This is consistent to the statement that $E_{max} < E_b$. However, E_b should be generally reduced in the amorphous phase of the same chemical elements, because of the lower density of packing, open voids and change of bond coordination. Remarkably, our experiments show that the preferential sputtering of atomic species strongly depends on the gas environment. In HV, the amorphous surface layer is partially removed with preferential sputtering of O, Ca and Mn without formation of PrO_x . In contrast, in O_2 or inert gases, the presence/absence of preferential leaching of Mn and Ca strongly depends on the $p_{\text{H}_2\text{O}}$. This reflects that the vacancy formation energy close to surfaces depends on the surface chemistry. The presence of adsorbed surface H_2O , where Mn^{2+} and Ca^{2+} is soluble, clearly facilitates the leaching of displaced Mn and Ca species, giving rise to the formation of PrO_x . In contrast, in O_2 this process is suppressed and the uptake of oxygen for example by occupation of V_O vacancy sites is the dominating process.

Clearly, the crystallization rate and thus the velocity of the amorphous/crystalline interface is slowed down in inert gases He and N_2 , compared to experiments in O_2 . This indicates, that beam induced atomic displacements cannot be the only driving force for the movement of the interface. Figure S9 shows that residual molecular and atomic oxygen is also present in an inert gas experiment, e.g., in He. Its relative concentration is only slightly reduced after switching on the cold trap. The epitaxial recrystallization in inert gases may thus be influenced by the presence of oxygen. The analysis of the Mn valence state after He in comparison with the amorphous material at the pristine lamellas does not provide evidence for a large amount of oxygen uptake, since the Mn valence state is the same within error. However, sputtering of oxygen may be still compensated by the electrochemical oxidation, which is slowed down at lower p_{O_2} . This could indicate that beam induced epitaxial recrystallization in inert gases is also accompanied by a solid state chemical reaction with oxygen.

Consequently, even without net uptake of oxygen, the presence of surface adsorbed oxygen species can alter the beam induced effects from absent in high vacuum, over leaching in H₂O to perovskite epitaxy in inert gases.

4. Materials and Methods

Thin films of Pr_{1-x}Ca_xMnO₃ (PCMO) with different Pr/Ca ratio ($x = 0.1$ and $x = 0.33$) were grown on Nb-doped SrTiO₃ (001) with a 20 nm thick epitaxial La_{0.6}Sr_{0.4}MnO₃ (LSMO) (001) interlayer by reactive Xe-ion beam sputtering in an oxygen atmosphere with a partial pressure of $1.4 \cdot 10^{-4}$ mbar at the deposition temperature of $T_{\text{dep}} = 1020$ K. The PCMO film of thickness of $d \approx 100$ nm reveals epitaxial growth with [001]/[110] growth domains, inevitably present due to twinning. The LSMO interlayer was grown in order to adjust the lattice misfit between STO and PCMO. The growth parameters and detailed structural characterization of studied films is published elsewhere [17,18,28].

Specimens for in situ TEM studies were prepared by lift-out technique using a NanoLab 600 (Thermo Scientific™, former FEI, Hillsboro, Oregon, USA) dual beam instrument operated at 30 and 5 kV. Conventional method with FIB lift-out technique usually starts from the deposition of platinum/carbon (Pt/C) protection layers by electron or ion beam [38]. Since Pt is highly active catalyst, its presence at the surface of perovskites should be excluded. All lamellas in this study were prepared using a protection layer of Alkali Resistant Positive Photoresist X AR-P 5900/4 (ALLRESIST GmbH, Strausberg, Germany) which was deposited onto the surface of LSMO and PCMO thin films before FIB cutting procedure. Electron transparent lamella was finally cleaned with Ar⁺ ions with energies from 500 eV to 100 eV using a Gatan PIPS 691 ion polishing system. The rest of protection layer was removed with a plasma cleaner prior TEM studies. High-resolution TEM (HRTEM), electron diffraction (ED) and STEM studies were performed using an aberration corrected Titan 80-300 environmental microscope (Thermo Scientific™, former FEI, Hillsboro, Oregon, USA) operated at 300 kV. The specimens were imaged along [010] and [110] crystallographic directions in the Pbnm space group. ETEM experiments are performed with N₂, He, O₂ gases. The chemical composition of gas environment was controlled by the Residual Gas Analyzer (RGA) QMG220 (Pfeiffer Vacuum GmbH, Germany) controlled by Quadera™ software (version 4.3, INFICON Aktiengesellschaft, Liechtenstein, 2010). During the experiments the deviations of pressure from desired values of 5 and 50 microbars did not exceed 5%. Other residual gases are always present in the inlet tubes and electron microscope column. In order to minimize their influence the inlet tubes were purged firstly with the working gas. Then, the specimen chamber was also purged with the working gas during at least half an hour, and the electron beam was blanked. These procedures allowed reducing the presence of other gases to be less than 1%. For example, during the used experimental setting, typical values are H₂O: 1% (cold trap off) and 0.05% (cold trap on); O₂: 0.2%; N₂: 0.04%; hydrocarbons (unspecified) and very low amounts of atomic nitrogen and oxygen. Switching on the cold trap thus changes the main residual gas impurity from H₂O to O₂ (see SI1). EELS data were collected with a Gatan Imaging Filter (GIF) Quantum 965ER (Gatan, Pleasanton, CA, USA). Atomic models were built using the Vesta software package (version 3.4.7, 2019) [39]. High-angle annular dark field (HAADF) contrast and spectrum imaging was used in order to visualize change in chemical composition. HRTEM images were simulated using QSTEM software (version 2.51, 2019) [40].

5. Conclusions

We successfully demonstrated high-quality preparation of cross-section TEM lamella of complex oxide thin films by FIB, using metal free protection layer, i.e. photoresist. Although beam damage is small, subunit cell disordered layers remain on the surface after plasma etching of photoresist which can be treated in situ by beam driven recrystallization in suitable gas environments. It allows the formation of well-ordered crystalline facets with different surface termination, dependent on the gas. This is an important prerequisite for the in situ atomic scale observation of active states of catalysts. The work also demonstrates the feasibility of direct imaging of solid state chemical and structural

transformations from amorphous to crystalline structures on atomic scale. The length of modified edge at TEM lamella varies in a range from several nanometers to several tens or even hundred nanometers. The chemical composition of the modified area depends on the gases used, as well as on the presence of residual water molecules in the column of electron microscope. The presence of water can cause selective leaching of atomic species (Mn and Ca) and thus irreversible chemical changes of surface of PCMO perovskites. By contrast, the reduction of water partial pressure below $5 \cdot 10^{-8}$ bar forms conditions, where crystalline perovskite oxide structure can be grown from a damaged amorphous material by electron-beam-induced solid phase epitaxy controlled by gas regulated solid state chemistry. The observation that the nominal Mn oxidation state can be reached from the reduced amorphous state in $p_{O_2} = 50 \cdot 10^{-6}$ bar points to the key role of residual oxygen in N_2 and He environments for the healing of preparation induced damage. At this point of our studies, we suggest that beam-induced atomic displacements drive the crystallization front between the amorphous and crystalline phase. However, this process is most probably accompanied by beam-induced electrochemical oxidation which compensates the sputtering of oxygen or can even drive oxygen uptake to the stoichiometric level. This statement is strongly supported by the observed higher speed of epitaxial recrystallization for the material with a pronounced electrochemical redox couple $Mn^{2+}/\frac{1}{2}V_O \leftrightarrow Mn^{3+}/O_O$.

The reported results are important both for the design of in situ experiments related to the study of heterogeneous catalysis and battery technology in oxide-based materials. The well controlled design of perovskite oxide surface edges in O_2 and inert gases at low p_{H_2O} is a vital requirement for the realization of a well-defined starting state of the surface in situ reactions. In order to have better control over size and chemical composition of the modified area, significant improvements of specimen stage stability, inlet and outlet systems of ETEM as well as chemical analysis of gaseous environment is highly desirable.

Supplementary Materials: The following are available online at <http://www.mdpi.com/2073-4344/9/9/751/s1>: Figure S1: The PCMO ($x = 0.33$) after electron beam treatment in He at 50 μ bars, Figure S2: The PCMO ($x = 0.33$) after electron beam treatment in O_2 at 50 μ bars, Figure S3: HRTEM image and rotationally averaged profiles of PCMO in O_2 and in He ($x = 0.33$), Figure S4: HRTEM image and rotationally averaged profiles of PCMO in He ($x = 0.1$), Figure S5: Analysis of broadening of spots in FFTs, lattice disorder in PCMO ($x = 0.1$), Figure S6: (1) Through focus series of HRTEM images of PCMO ($x = 0.33$) for the thickness of 10 nm, (2) Experimental and calculated HRTEM images of PCMO ($x = 0.33$) for the thickness of 3 nm, Figure S7: The PCMO ($x = 0.1$) after electron beam treatment in He at 50 μ bars, Figure S8: HRSTEM image and EELS spectrum of PrOx particle at the surface of PCMO ($x = 0.33$), Figure S9: An example of multiple ion detection scan in Quadera™ software, Table S1: Summary of the Mn valence PCMO ($x = 0.33$) after electron beam treatment in He at 50 μ bars, Table S2: Summary of the Mn valence of PCMO ($x = 0.33$) after electron beam treatment in O_2 at 50 μ bars. Table S3 (1): Simulation parameters for the through focus series, (2) Simulation parameters for individual experimental images, Table S4: Summary of the Mn valence of PCMO ($x = 0.1$) after electron beam treatment in He at 50 μ bars.

Author Contributions: Conceptualization: C.J. and V.R.; Formal analysis: G.L. and V.R.; Investigation: G.L. and V.R.; Resources: C.J.; Writing—original draft preparation: V.R.; Writing—review and editing: V.R., G.L. and C.J.; Visualization: V.R. and G.L.; Supervision: C.J. and V.R.; Project administration: C.J. and V.R.; Funding acquisition: C.J. and V.R.

Funding: The authors are grateful for financial support by the Deutsche Forschungsgemeinschaft, grant number CRC 1073 (Projects C02 and Z02).

Acknowledgments: The authors wish to thank V. Radisch, V. Moshnyaga and V. Bruchmann-Bamberg for excellent support in TEM specimen preparation.

Conflicts of Interest: The authors declare no conflict of interest.

Appendix A

We calculate the upper limit of TEM lamella heating in the irradiated area under the assumption that all excitations due to inelastic scattering of primary electrons are converted into heat. The energy uptake per unit volume and second (= adsorbed power P per unit volume V) is thus:

$$\frac{P}{V} = \frac{\Delta E W \dot{N}_e}{63 V}$$

where the rate of incident electrons is given by:

$$\dot{N}_e = \frac{jA}{e}$$

Here, A denotes the illuminated area of the lamella and j the electron current density of primary electrons. In order to estimate the temperature increase due to the absorbed power, we use the Fourier law in 1D:

$$J_q = -\kappa \frac{dT}{dx} = \frac{P}{A}$$

where κ is the thermal conductivity of the manganite, J_q is the heat flux density, which is equal to the absorbed power per unit area. From these equations it follows:

$$\Delta T = \frac{L}{\kappa} \frac{P}{A}$$

where L is the length where the heat must be transported before it hits the interface to the substrate with a much higher thermal conductivity. Heat transfer due to gas convection is negligible at the used pressure range of our experiments.

For the calculation, we use a current of $I = 4$ nA on a circle of 100 nm diameter. This corresponds to an average dose rate (flux) of $r = 3.18 \times 10^4$ e/Å²s. In semiconductors, the average energy transfer per inelastic excitation $\Delta E \sim 3 E_g$, where E_g is the bandgap of the material [41]. Since the low loss excitations are the dominating feature in EELS, we use this estimate. It gives $\Delta E = 3$ eV per inelastic scattering event in PCMO.

With a measured inelastic mean free path of $\lambda = 70$ nm, the scattering probability of an electron in the thin surface regions of $t = 10$ nm is $W = t/\lambda = 0.14$. Thermal conductivity of PCMO at $T = 300$ K is $k = 1.5$ W/mK [42]. The distance of the electron irradiated surface area to the substrate is around $L = 100$ nm. This yields an upper limit of beam-induced lamella heating of $\Delta T = 15$ mK.

References

1. Kanan, M.W.; Nocera, D.G. In situ formation of an oxygen evolving catalyst in neutral water containing phosphate and Co²⁺. *Science* **2008**, *321*, 1072–1075. [CrossRef]
2. Vendelbo, S.B.; Elkjær, C.F.; Puspitasari, I.; Creemer, J.F.; Dona, P.; Mele, L.; Morana, B.; Nelissen, B.J.; van Rijn, R.; Kooyman, P.J.; et al. Visualization of oscillatory behaviour of Pt nanoparticles catalysing CO oxidation. *Nat. Mater.* **2014**, *13*, 884–890. [CrossRef]
3. Bergmann, A.; Martinez-Moreno, E.; Teschner, D.; Chervov, P.; Glied, M.; Ferreira de Araújo, J.; Reier, T.; Dau, H.; Strasser, P. Reversible amorphization and the catalytically active state of crystalline Co₃O₄ during oxygen evolution. *Nat. Commun.* **2015**, *6*, 8625. [CrossRef]
4. Arrigo, R.; Hävecker, M.; Schuster, M.E.; Ranjan, C.; Stotz, E.; Knop-Gericke, A.; Schlögl, R. In situ study of the gas-phase electrolysis of water on platinum by NAP-XPS. *Angew. Chem. Int. Ed.* **2013**, *52*, 11660–11664. [CrossRef]
5. Zheng, F.; Alayoglu, S.; Guo, J.; Pushkarev, V.; Li, Y.; Glans, P.A.; Chen, J.L.; Somorjai, G. In-situ X-ray absorption study of evolution of oxidation states and structure of cobalt in Co and CoPt bimetallic nanoparticles (4 nm) under reducing (H₂) and oxidizing (O₂) environments. *Nano Lett.* **2011**, *11*, 847–853. [CrossRef]
6. Boyes, E.D.; Gai, P.L. Environmental high resolution electron microscopy and applications to chemical science. *Ultramicroscopy* **1997**, *67*, 219–232. [CrossRef]
7. Roiban, L.; Koneti, S.; Morfin, F.; Nguyen, T.S.; Mascunan, P.; Aouine, M.; Epicier, T.; Piccolo, L. Uncovering the 3D structure of combustion-synthesized noble metal-ceria nanocatalysts. *ChemCatChem* **2017**, *9*, 4607–4613. [CrossRef]
8. Hansen, T.W.; Wagner, J.B. Environmental transmission electron microscopy in an aberration-corrected environment. *Microsc. Microanal.* **2012**, *18*, 684–690. [CrossRef]

9. Hansen, T.W.; Wagner, J.B.; Dunin-Borkowski, R.E. Aberration corrected and monochromated environmental transmission electron microscopy—Challenges and prospects. *Mater. Sci. Technol.* **2010**, *26*, 1338–1344. [[CrossRef](#)]
10. Hansen, T.W.; Wagner, J.B.; Jinschek, J.R.; Dunin-Borkowski, R.E. The titan environmental transmission electron microscope: Specifications, considerations and first results. *Microsc. Microanal.* **2009**, *15*, 714–715. [[CrossRef](#)]
11. Thermo Fisher Scientific. Available online: <https://www.fei.com/products/tem/themis-etem-for-materials-science/> (accessed on 30 August 2019).
12. Tanaka, N.; Usukura, J.; Kusunoki, M.; Saito, Y.; Sasaki, K.; Tanji, T.; Muto, S.; Arai, S. Development of an environmental high voltage electron microscope and its application to nano and bio-materials. *J. Phys. Conf. Ser.* **2014**, *522*, 012008. [[CrossRef](#)]
13. FanWu, F.; Yao, N. Advances in windowed gas cells for in-situ TEM studies. *Nano Energy* **2015**, *13*, 735–756.
14. Yokosawa, T.; Alan, T.; Pandraud, G.; Damc, B.; Zandbergen, H. In-situ TEM on (de)hydrogenation of Pd at 0.5–4.5 bar hydrogen pressure and 20–400 °C. *Ultramicroscopy* **2012**, *112*, 47–52. [[CrossRef](#)]
15. Zhang, S.; Nguyen, L.; Zhu, Y.; Zhan, S.; Tsung, C.K.; Tao, F. In-situ studies of nanocatalysis. *Acc. Chem. Res.* **2013**, *46*, 1731–1739. [[CrossRef](#)]
16. Han, B.; Stoerzinger, K.A.; Tileli, V.; Gamalski, A.D.; Stach, E.A.; Shao-Horn, Y. Nanoscale structural oscillations in perovskite oxides induced by oxygen evolution. *Nat. Mater.* **2017**, *16*, 121–126. [[CrossRef](#)]
17. Raabe, S.; Mierwaldt, D.; Ciston, J.; Uijtewaal, M.; Stein, H.; Hoffmann, J.; Zhu, Y.M.; Blochl, P.; Jooss, C. In situ electrochemical electron microscopy study of oxygen evolution activity of doped manganite perovskites. *Adv. Funct. Mater.* **2012**, *12*, 3378–3388. [[CrossRef](#)]
18. Mierwaldt, D.; Roddatis, V.; Risch, M.; Scholz, J.; Geppert, J.; Abrishami, M.E.; Jooss, C. Environmental TEM investigation of electrochemical stability of perovskite and ruddlesden-popper type manganite oxygen evolution catalysts. *Adv. Sustain. Syst.* **2017**, *1*, 1700109. [[CrossRef](#)]
19. Newcomb, S.B.; Boothroyd, C.B.; Stobbs, W.M. Specimen preparation methods for the examination of surfaces and interfaces in the transmission electron microscope. *J. Microsc.* **1985**, *140*, 195–207. [[CrossRef](#)]
20. Jacobs, J.W.M.; Verhoeven, J.F.C.M. Specimen preparation technique for high resolution transmission electron microscopy studies on model supported metal catalysts. *J. Microsc.* **1986**, *143*, 103–116. [[CrossRef](#)]
21. Giannuzzi, L.A.; Geurts, R.; Ringnalda, J. 2 keV Ga⁺ FIB milling for reducing amorphous damage in silicon. *Microsc. Microanal.* **2005**, *11*, 828–829. [[CrossRef](#)]
22. Schaffer, M.; Schaffer, B.; Ramasse, Q. Sample preparation for atomic-resolution STEM at low voltages by FIB. *Ultramicroscopy* **2012**, *114*, 62–71. [[CrossRef](#)]
23. Park, Y.C.; Park, B.C.; Romankov, S.; Park, K.J.; Yoo, J.H.; Lee, Y.B.; Yang, J.M. Use of permanent marker to deposit a protection layer against FIB damage in TEM specimen preparation. *J. Microsc.* **2014**, *255*, 180–187. [[CrossRef](#)]
24. Jesse, S.; He, Q.; Lupini, A.R.; Leonard, D.N.; Oxley, M.P.; Ovchinnikov, O.; Unocic, R.R.; Tselev, A.; Fuentes-Cabrera, M.; Sumpter, B.G.; et al. Atomic-level sculpting of crystalline oxides: Toward bulk nanofabrication with single atomic plane precision. *Small* **2015**, *11*, 5895–5900. [[CrossRef](#)]
25. Kramer, T.; Mierwaldt, D.; Scherff, M.; Kanbach, M.; Jooss, C. Developing an in situ environmental TEM set up for investigations of resistive switching mechanisms in Pt-Pr_{1-x}Ca_xMnO_{3-δ}-Pt sandwich structures. *Ultramicroscopy* **2018**, *184*, 61–70. [[CrossRef](#)]
26. Matsumoto, Y.; Sato, E. Oxygen evolution on La_{1-x}Sr_xMnO₃ electrodes in alkaline solutions. *Electrochim. Acta* **1979**, *24*, 421–423. [[CrossRef](#)]
27. Bockris, J.O.; Otagawa, T. The electrocatalysis of oxygen evolution on perovskites. *J. Electrochem. Soc.* **1984**, *131*, 290–302. [[CrossRef](#)]
28. Scholz, J.; Risch, M.; Stoerzinger, K.A.; Wartner, G.; Shao-Horn, Y.; Jooss, C. Rotating ring-disk electrode study of oxygen evolution at a perovskite surface: Correlating activity to manganese concentration. *J. Phys. Chem.* **2016**, *120*, 27746–27756. [[CrossRef](#)]
29. Sotoudeh, M.; Rajpurohit, S.; Blöchl, P.E.; Mierwaldt, D.; Norpoth, J.; Roddatis, V.; Mildner, S.; Ifland, B.; Jooss, C. Electronic structure of Pr_{1-x}Ca_xMnO₃. *Phys. Rev. B* **2017**, *95*, 235150. [[CrossRef](#)]
30. Varela, M.; Oxley, M.P.; Luo, W.; Tao, J.; Watanabe, M.; Lupini, A.R.; Pantelides, S.T.; Pennycook, S.J. Atomic-resolution imaging of oxidation states in manganites. *Phys. Rev. B* **2009**, *79*, 085117. [[CrossRef](#)]

31. De Jong, M.P.; Bergenti, I.; Dediú, V.A.; Fahlman, M.; Marsi, M.; Taliani, C. Evidence for Mn²⁺ ions at surfaces of La_{0.7}Sr_{0.3}MnO₃ thin films. *Phys. Rev. B* **2005**, *71*, 014434. [[CrossRef](#)]
32. Bugnet, M.; Overbury, S.H.; Wu, Z.L.; Epicier, T. Direct visualization and control of atomic mobility at {100} surfaces of ceria in the environmental transmission electron microscope. *Nano Lett.* **2017**, *17*, 7652–7658. [[CrossRef](#)]
33. Rudawski, N.G.; Jones, K.S.; Morarka, S.; Law, M.E.; Elliman, R.G. Stressed multidirectional solid-phase epitaxial growth of Si. *J. Appl. Phys.* **2009**, *105*, 081101. [[CrossRef](#)]
34. Evans, P.G.; Chen, Y.; Tilka, J.A.; Babcock, S.E.; Kuech, T.F. Crystallization of amorphous complex oxides: New geometries and new compositions via solid phase epitaxy. *Curr. Opin. Solid State Mater. Sci.* **2018**, *22*, 229–242. [[CrossRef](#)]
35. Mildner, S.; Beleggia, M.; Mierwaldt, D.; Hansen, T.W.; Wagner, J.B.; Yazdi, S.; Kasama, T.; Ciston, J.; Zhu, Y.; Jooss, C. Environmental TEM study of electron beam induced electrochemistry of Pr_{0.64}Ca_{0.36}MnO₃ catalysts for oxygen evolution. *J. Phys. Chem. C* **2015**, *119*, 5301–5310. [[CrossRef](#)]
36. Egerton, R.F.; Li, P.; Malac, M. Radiation damage in the TEM and SEM. *Micron* **2004**, *35*, 399–409. [[CrossRef](#)]
37. Gonzalez, E.; Abreu, Y.; Cruz, C.M.; Piñera, I.; Leyva, A. Molecular-dynamics simulation of threshold displacement energies in BaTiO₃. *Nucl. Instrum. Methods Phys. Res. B* **2015**, *358*, 142–145. [[CrossRef](#)]
38. Giannuzzi, L.A.; Stevie, F.A. A review of focused ion beam milling techniques for TEM specimen preparation. *Micron* **1999**, *30*, 197–204. [[CrossRef](#)]
39. Momma, K.; Izumi, F. VESTA 3 for three-dimensional visualization of crystal, volumetric and morphology data. *J. Appl. Crystallogr.* **2011**, *44*, 1272–1276. [[CrossRef](#)]
40. Koch, C.T. Determination of Core Structure Periodicity and Point Defect Along Dislocations. Ph.D. Thesis, Arizona State University, Tempe, AZ, USA, May 2002.
41. Klein, C.A. Bandgap dependence and related features of radiation ionization energies in semiconductors. *J. Appl. Phys.* **1968**, *39*, 2029–2038. [[CrossRef](#)]
42. Thiessen, P.; Roddatis, V.; Rieger, F.; Belenchuk, A.; Keunecke, M.; Moshnyaga, V.; Jooss, C. Effect of charge ordering on cross-plane thermal conductivity in correlated perovskite oxide superlattices. *Phys. Rev. B.* **2018**, *98*, 195114. [[CrossRef](#)]



© 2019 by the authors. Licensee MDPI, Basel, Switzerland. This article is an open access article distributed under the terms and conditions of the Creative Commons Attribution (CC BY) license (<http://creativecommons.org/licenses/by/4.0/>).

Chapter 5

Dynamic observation of
manganese adatom mobility at
perovskite oxide catalyst
interfaces with water

Dynamic observation of manganese adatom mobility at perovskite oxide catalyst interfaces with water

Gaurav Lole^{1,2}, Vladimir Roddatis^{1,7}, Ulrich Ross ¹, Marcel Risch ^{1,3}, Tobias Meyer ⁴, Lukas Rump ^{4,5}, Janis Geppert ¹, Garlef Wartner ^{1,8}, Peter Blöchl ^{5,6} & Christian Jooss ^{1,2}✉

Real time in-situ microscopy imaging of surface structure and atom dynamics of heterogeneous catalysts is an important step for understanding reaction mechanisms. Here, using in-situ environmental transmission electron microscopy (ETEM), we directly visualize surface atom dynamics at manganite perovskite catalyst surfaces for oxygen evolution reaction (OER), which are ≥ 20 times faster in water than in other ambients. Comparing (001) surfaces of $\text{La}_{0.6}\text{Sr}_{0.4}\text{MnO}_3$ and $\text{Pr}_{0.67}\text{Ca}_{0.33}\text{MnO}_3$ with similar initial manganese valence state and OER activity, but very different OER stability, allows us to distinguish between reversible surface adatom dynamics and irreversible surface defect chemical reactions. We observe enhanced reversible manganese adatom dynamics due to partial solvation in adsorbed water for the highly active and stable $\text{La}_{0.6}\text{Sr}_{0.4}\text{MnO}_3$ system, suggesting that aspects of homogeneous catalysis must be included for understanding the OER mechanism in heterogeneous catalysis.

¹Institute of Materials Physics, University of Goettingen, Friedrich-Hund-Platz 1, 37077 Goettingen, Germany. ²International Center for Advanced Studies of Energy Conversion (ICASEC), University of Goettingen, D-37077 Goettingen, Germany. ³Helmholtz-Zentrum Berlin für Materialien und Energie GmbH, Young Investigator Group Oxygen Evolution Mechanism Engineering, 14109 Berlin, Germany. ⁴4th Physical Institute, Solids and Nanostructures, University of Goettingen, Friedrich-Hund-Platz 1, 37077 Goettingen, Germany. ⁵Institute for Theoretical Physics, University of Goettingen, Friedrich-Hund-Platz 1, 37077 Goettingen, Germany. ⁶Institute for Theoretical Physics, Clausthal University of Technology, Leibnizstr. 10., D-38678 Clausthal-Zellerfeld, Germany. ⁷Present address: Helmholtz-Zentrum Potsdam Deutsches GeoForschungsZentrum GFZ, Telegrafenberg 14473, Potsdam, Germany. ⁸Present address: Helmholtz-Zentrum Berlin für Materialien und Energie GmbH, Young Investigator Group Operando Interface-Photochemistry, 12489 Berlin, Germany. ✉email: cjooss@gwdg.de

The efficiency of electrochemical water splitting for the sustainable production of clean fuels from renewable energy sources is limited by a large overpotential of the anodic oxygen evolution reaction (OER)^{1–3}. Understanding of its origin requires knowledge about the pathway of the formation of di-oxygen O₂ out of 2 H₂O molecules by a proton-coupled electron transfer. Even for the best electrocatalysts, i.e., transition metal (M) oxides (O), the reaction path for O–O formation is not well understood. For heterogeneous systems, the reaction is catalyzed at active surface sites, where different sites and mechanisms are suggested. This includes single⁴ or dual^{5–7} transition metal (M) sites with flexible valence states, concerted proton–electron transfer^{8,9} as well as redox active lattice O^{10–12}, including oxygen vacancy formation and annihilation¹³. Despite remarkable progress in application of density functional theory (DFT) to the oxide–water interface, the theoretical understanding of the dynamic interface structure during OER is still limited since it requires serious approximations¹⁴. Among of the far-reaching are the frozen surface approximation and that solvation effects are, if at all, only considered as a static average. This underestimates the flexibility of M surface coordination due to interface solvent effects that is on the other hand known to be crucial in homogeneous catalysis for the formation of high- or hetero-valent M–O moieties that precede O–O bond formation¹⁵. There are controversial conclusions whether the predicted unsuitable scaling relation between metal M–OH and M–O adsorption energies^{9,16,17} as the origin of large overpotentials for single surface sites can be broken by bifunctional mechanism at two distinct M and M' sites¹⁸ or is restored by surface solvation¹⁹. Recent experiments show that ternary alloying of two different transition metals with a highly flexible coordination metals indeed lead to a remarkable reduction of OER overpotential in gelled oxyhydroxides²⁰. An improved theoretical understanding thus requires a comprehensive atomic scale understanding of the dynamic electrolyte–catalyst interface structure under OER conditions as an essential ingredient for the knowledge driven further improvement of electrocatalysts by material design.

In addition to OER activity, the stability is strongly affected by the interfacial electrolyte interactions. A distinction between reversible dynamics that emerges in a stationary state and irreversible processes that change the activity is essential. Such insights are promoted by the progress of operando studies that can address different types of dynamical changes. A first type of rather slow dynamics is the change of electrode surface during potential cycling. The important role of solvate interactions has been e.g., established for the noble metal Pt, where Pt surface oxide that is formed under anodic polarization adsorbs water that dissociates and forms hydrated Pt²¹. Metal oxides such as CoO_x can form a disordered surface during OER^{22,23}. A second type of rather fast dynamics is due to thermally activated mobility of surface atoms²⁴ or adatoms²⁵ that is hardly accessible in operando experiments. Clearly, surface adatom dynamics depends on temperature and surface barriers that can be modified due to H₂O solvation or dissociation²⁶ and is always present, even in thermal equilibrium. Driving the OER, the emerging non-equilibrium surface should show a reversible dynamics in a stationary state that depends on the formed atomic and chemical surface structure. Non-equilibrium dynamics of catalyst atoms may be even involved in OER mechanism²⁷. A third type of surface dynamics is irreversible defect reactions, typically the formation of oxygen vacancies^{13,28} or the dissolution of metallic species²⁹. Such processes are even gradually present at the highest performance system RuO₂³⁰. Metal dissolution can depend on overpotential^{31,32} surface symmetry³³, pH value and particle size³⁴. In order to avoid such corrosive processes, approaches for self-repair have been pursued³⁵. Despite a huge progress in

application of different operando techniques³⁶, comprehensive atomic scale understanding of all three classes of surface dynamics are far of reach at present, but are urgently required to establish the intimate connections between surface stability, the nature of the active sites and reaction pathways³⁷.

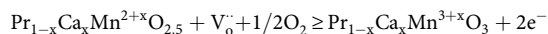
In situ environmental transmission electron microscopy (ETEM) in combination with aberration correction and image simulation has developed to a level where it can provide atomic resolution real space information about the equilibrium surface reconstruction in various ambient conditions^{38–40} including strategies for controlling the impact of electron beam^{41,42}. The recent development of atomic scale dynamic studies show surface mobility of Ce atoms on CeO₂ facets in high vacuum⁴³ and a transition of a TiO₂ surface reconstruction in H₂O from static to dynamic after adding CO⁴⁴. Steps towards the control of electron beam-induced and applied electric potentials at TEM samples enable in situ studies of electrode surfaces in ETEM under anodic polarization, approaching OER relevant potentials^{28,45}.

In this study, two perovskite manganites AMnO₃ were selected, where the Mn valence state can be controlled by A-site doping without changing the crystal symmetry. Specifically, La_{1–x}Sr_xMnO₃ at x = 0.4 (LSMO) is a metal-like electrode with high and stable oxygen evolution activity that is close to IrO₂²⁹. Moreover, Pr_{1–x}Ca_xMnO₃ at x = 0.33 (PCMO) is a semi-conducting small polaron material with high initial OER activity, yet less stability, due to oxygen vacancy formation and fast leaching of the resulting reduced Mn species. Thus LSMO is suitable for the study of reversible surface dynamics, whereas PCMO shows a pronounced irreversible defect reaction. Both systems have almost the same initial Mn valence but differ in Mn–O covalency and charge localization. This differences allows us to correlate in situ ETEM studies of surface structure and dynamics with ex situ analysis of electrochemical OER. We find that the (001) surfaces of both manganites show an at least 20 times higher Mn-adatom mobility in an adsorbed water layer compared to other ambients.

Results and discussion

Structure, activity, and stability of LSMO and PCMO (001).

Rotating ring disk electrode (RRDE) cyclovoltammetry (CV) was carried out at epitaxial (001) oriented thin film electrodes in 0.1 M aqueous KOH solution (Fig. 1). Both materials initially show good electrocatalytic oxygen evolution performance (for oxygen detection and Tafel analysis see Supplementary Figs. 1–3). Most striking is the different behavior just below the onset of the OER, where a redox wave is visible in PCMO as a negative current peak at $E = 1.3$ V vers reversible hydrogen electrode (RHE), complemented by a positive shoulder at the onset of OER. This feature is absent in LSMO. The redox couple is related to reversible formation and annihilation of oxygen vacancies, which are electron donors and thus induce a surface reduction of the transition metal¹³. The defect reaction is given by



For neutral pH values in an unbuffered solution, which is more relevant for the comparison to in situ XANES and ETEM studies, a similar behavior of the CV is observed¹³. The easy formation of V_o in PCMO indicates that lattice oxygen is redox active, such that transfer of holes between Mn3d and O2p states can oxidize O^{2–} to form O[–] and O₂(g); see e.g., refs. 46,47. For LSMO such a surface redox process is only observed when the cycling is extended to more negative potentials below $E = 0.6$ V vers RHE⁴⁸.

Comparing the cycle dependence of the OER activity for LSMO and PCMO in Fig. 1b, there is a strong difference in

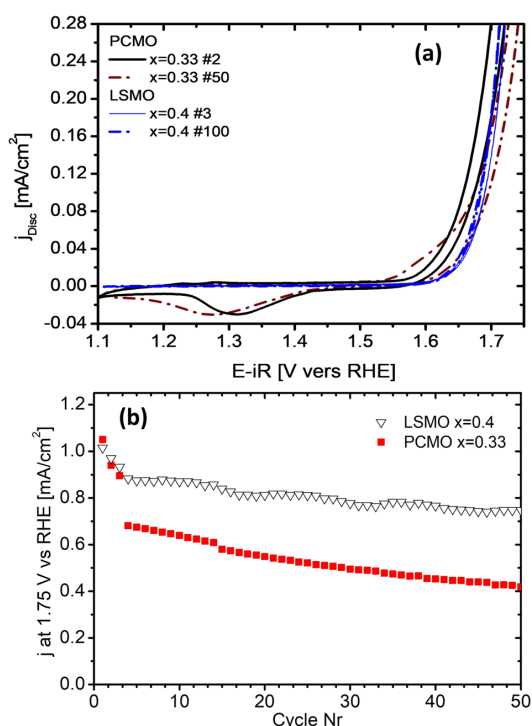


Fig. 1 Electrochemical characterization. **a** Cyclic voltammograms of (001) oriented epitaxial thin film manganite electrodes in 0.1 M aqueous KOH solution at 10 mV/s and rotated at 1600 rpm for cycles #2/#50 (PCMO) and #3/#100 (LSMO), respectively. In addition to the OER, PCMO shows a pronounced surface redox couple. **b** Temporal stability of the electrode current density at $E = 1.75$ V versus RHE for cycling from $E = 1.1$ – 1.75 V versus RHE and 7 min chronoamperometric OER between cycle 3 and 4 (see method section).

stability between both electrodes. Initially, the current density j of both systems at $E = 1.75$ V versus RHE is similar, i.e., $j = 1.03$ mA/cm² for LSMO and $j = 1.05$ mA/cm² for PCMO. These values are close to the activity of IrO₂ (110) films⁴⁹. However, upon cycling and chronoamperometric OER between cycle 3 and 4, the decrease for PCMO is much more pronounced than for LSMO. Comparing the pristine and post electrolysis structure of LSMO and PCMO after 50 electrochemical cycles (Supplementary Figs. 4–7) reveals significant differences. Whereas for LSMO the crystalline surface structure with flat terraces and unit cell height steps is fully preserved, PCMO displays an increase of surface roughness. Postmortem high-resolution scanning transmission electron microscopy (HRSTEM) combined with electron energy loss spectroscopy (EELS) of film surfaces shows a strong surface depletion of Mn for PCMO, leading to a 2–3 nm thick Pr-enriched surface. Emerging small peaks in XRD after 1 h of electrolysis are consistent with a thin cubic PrO_{2+x} layer. In contrast, the Mn concentration at the LSMO surface is only slightly reduced.

Surface termination of the manganite films in H₂O. The study of surface termination of epitaxial perovskite films using environmental high-resolution transmission electron microscopy (ETEM) was demonstrated by Roddatis et al.⁴² and requires careful TEM lamella preparation, as documented in the Supplementary Figs. 8–11 and the associated text. The changes of

surface termination of the LSMO and PCMO (001) oriented thin film electrodes in high vacuum (HV), O₂ and H₂O are shown in Fig. 2. For LSMO predominant A-terminated surfaces (La–Sr–O) are observed in O₂, whereas in high vacuum (HV), a mixed surface termination with disorder at the B-terminated (Mn–O) areas is developed. This is observed even after saturation of the surface in 1 mbar O₂. In H₂O vapor, the LSMO surface appears to be dominated by an A-site layer; however, Mn is still present as dynamic surface adatoms. For PCMO, a disordered surface develops in HV following the ordering of the surface in 1 mbar of O₂, where a mixed termination of an ordered surface is observed. In H₂O, a mixed surface termination emerges, where the A-terminated areas (Pr–Ca–O) show higher ordering compared to the B-terminated areas. Surface Mn adatoms as well as subsurface lattice Mn is highly mobile.

The determination of surface termination requires the comparison of the HRTEM images with simulated images (Fig. 2d, h). In these simulations, the lamella thickness t at the surface is estimated from measurement of the inelastic scattering intensity by EELS and fine-tuned by a fit of contrast of simulated to experimental images using a Monte-Carlo-based simulated least-squares optimization, yielding $t = 4.2$ (4.3) nm for LSMO (PCMO). The obtained electron optical parameters, such as defocus, spherical aberration, astigmatism, and axial coma, fit reasonably well to those estimated from tilt-tableau measurements via the Cs-corrector software. The different surface terminations can be clearly distinguished by the weaker contrast of the MnO columns. In the subsurface, A-site and B-site columns are separable from contrast due to different atomic numbers and octahedral tilt patterns of MnO₆ octahedra. Details of the image fitting and parameters used can be found in the Supplementary Fig. 12 and Supplementary Table 1.

Reversible Mn-adatom dynamics at the LSMO–H₂O interface.

Figure 3 shows a time sequence of HRTEM images for the LSMO $x = 0.4$ (001) surface in 0.5 Pa of H₂O. The full image series is compiled in Movie M01. The surface is well ordered and shows stable A-termination over more than 30 min. However, mobile Mn is, in fact, present on the surface. This is indicated by the sudden appearance and disappearance of atom contrast at B-layer surface positions on flat stable A layers (Fig. 3a). We define the detection limit of Mn atoms by the amplitude of the signal above the noise level 3σ , where σ is the standard deviation of the background fluctuations of the CCD signal at an area above the surface in the presence of the experimental gas. Image simulation and contrast quantification show that signal to noise ratio at the used frame rate of 4.4 fps does allow for detection of triple or higher occupancy of B-columns by Mn at a 4.2-nm thick lamella surface (Fig. 3b, c).

Closer inspection of image contrast in Fig. 3a reveal adatom contrast mainly appears at interstitial surface positions and rarely at the nominal octahedral positions of an ideal non-reconstructed surface. Contrast quantification of the columns of Mn adatoms is obtained by calibration of the experimental A-site contrast at the lamella surface to the simulated contrast, as shown in the Supplementary Figs. 13–15. Based on contrast simulations, the interpretation of dynamic adatom contrast other than Mn on a static A-layer is unlikely: O and OH species are below the contrast detection limit. La/Sr occupancy on B-terminated layers can be excluded from contrast. Fast La/Sr adatom dynamics on a stable A-terminated layer can be not entirely excluded from contrast. However, this would lead to an A-enriched surface with a Mn depleted layer, which is contrary to our observations for LSMO but in agreement to Mn surface leaching in PCMO reported below. Since all experiments in different environments

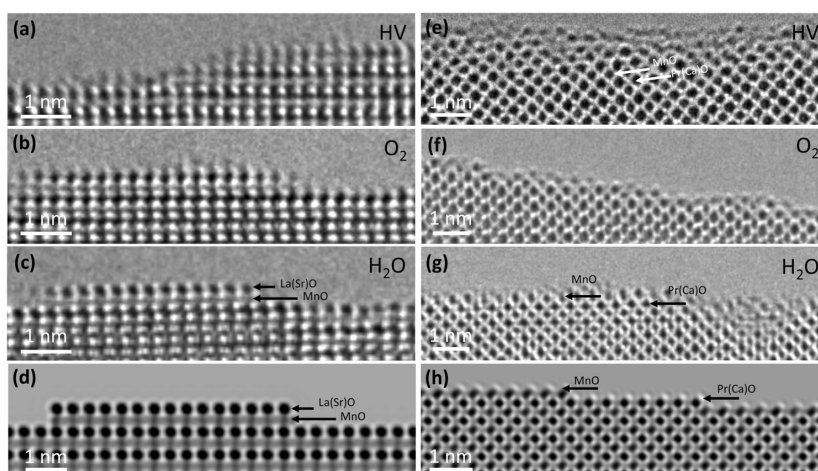


Fig. 2 HRTEM cross plane images of LSMO and PCMO (001) surfaces in different ambients. All images are taken at negative defocus, i.e., atomic columns appear as dark contrast, and with objective lens aberrations corrected up to 5th order. **a-d** LSMO is imaged in the pseudocubic [110] zone axis. **a** Mixed B- and A- termination in high vacuum (HV). **b** Dominant A-termination in 1 mbar O₂. **c** In 0.5 Pa H₂O, the surface consists of a stable A-layer with highly mobile Mn on top (see Fig. 3). **d** Simulated image with A-termination and surface step. **e-h** PCMO is imaged in the orthorhombic [110] zone axis. **e** Disordered surface structure in HV. **f** Highly ordered surface in 1 mbar of O₂ with a mixed termination. **g** In 0.5 Pa of H₂O, the B-terminated areas of PCMO exhibit pronounced disorder with mobile Mn. **h** Simulated image for PCMO with different surface terminations.

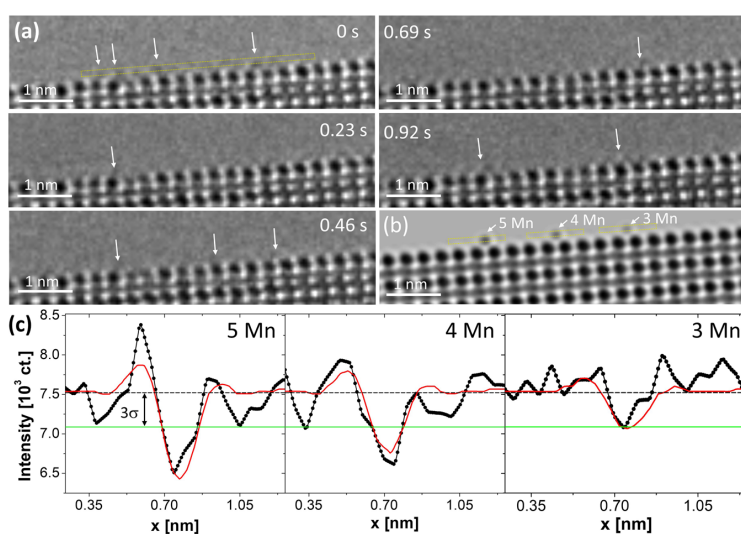


Fig. 3 Observation of dynamic Mn adatoms on a LSMO (001) surface in 0.5 Pa of H₂O at [110] zone axis. **a** Time sequence of HRTEM images taken at 4.4 fps at negative defocus. Mn-adatom contrast appears and disappears on a stable La(Sr)O surface layer as indicated by white arrows. **b** Simulated HRTEM image with Mn-adatom column occupation of 3, 4, and 5. The Mn columns are located at interstitial surface positions on an A-terminated sample. Lamella thickness is 4.2 nm. **c** Line profiles of simulated (red) and experimental (black with symbols) images of B-columns with 3, 4, and 5 Mn atom occupation. The 3σ threshold indicates the detection limit of Mn columns above noise level, i.e., triple Mn occupation at a B-layer column. The time sequence gives a lower limit of the Mn-adatom hopping rate of $r \geq 4 \text{ s}^{-1}$.

reveal that surface Mn is more mobile than A-type cations, our overall conclusion from image contrast and electrochemical behavior is that Mn adatoms are the highly mobile species on stable LSMO surfaces in H₂O.

The camera frame rate of around 4 fps is selected as a compromise between achieving sufficient signal to noise ratio and capturing some of the surface dynamics. Double Mn B-layer occupancy corresponds to the detection limit at 3σ of the noise level. Both triple Mn as well as higher Mn B-layer occupancy

contrast appears and disappears with the frame rate used. We can thus only determine a lower limit of the surface hopping rate, which is given by the frame rate of the images. If triple Mn occupation appears and disappears on the timescale of the frame rate, it may be attributed to one of the following events: (i) A single Mn atom hops to another site and the remaining double occupation contrast becomes invisible. (ii) Two or three Mn atoms coincidentally hop to another site and the B-site contrast on the original site disappears. Since (ii) has a lower probability

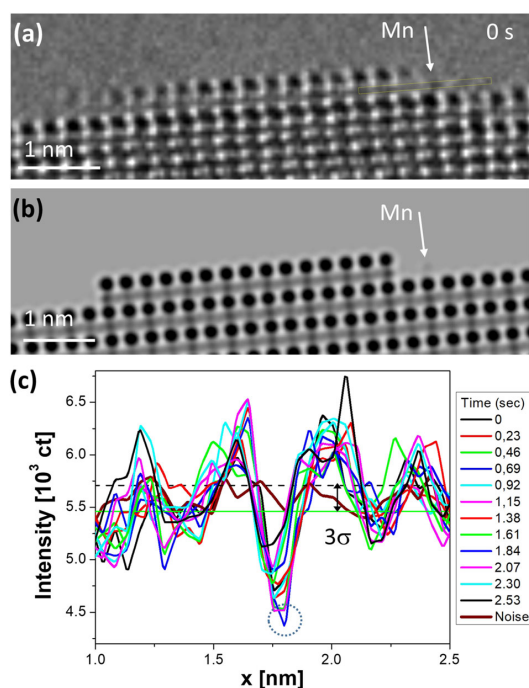


Fig. 4 Slowed down Mn surface mobility due to a unit cell height surface step at a LSMO (001) facet in 0.5 Pa of H₂O. **a** First HRTEM image of a time sequence taken at a frame rate of 4.4 fps with the surface step taken at the same conditions as in Fig. 3; see Movie M02. **b** Simulated HRTEM image with the step and 3 Mn occupation contrast on a slightly displaced B-site column. **c** Line profiles of the time sequence taken at the B-layer as indicated by the green box in **a**. It is showing an increased sticking time of a triple Mn column of 1.4 s near the step edge compared to ≤ 0.23 s at the flat surface, providing evidence for a locally increased surface barrier.

than (i) and represents the slowest process, it defines the minimum detectable hopping rate of $r \geq 4 \text{ s}^{-1}$.

The dynamic state with highly mobile Mn atoms on top of a more or less static A-terminated layer can be strongly affected by the presence of a surface step. Since the Mn surface mobility depends on the surface activation barrier, it can be strongly reduced at step edges due to an Erich-Schwöbel barrier. Figure 4 shows an increased contrast of mobile Mn atoms in the vicinity of step edges formed by a static A-terminated layer. The reduction of Mn mobility in the vicinity of the step edges can directly be observed in the Movie M02. The analysis of line profiles at the B-layer location in the vicinity of the step edge in Fig. 4 reveal a reduction of the Mn-adatom hopping rate from $r \geq 4 \text{ s}^{-1}$ to $r \approx 0.7 \text{ s}^{-1}$. Remarkably, the A-layer forming the step edge in Fig. 4 is quite stable and does not change on the timescale of the Movie M02 of 1 min 25; see also Supplementary Fig. 16.

Compared to H₂O, the Mn surface mobility on LSMO (001) in high vacuum (HV) and in other gases is strongly reduced at the same dose rate (Supplementary Figs. 17–19, Movies M03–M05). The surface with mixed termination shows contrast changes on the B-site columns with $r \leq 0.25 \text{ s}^{-1}$ in HV and $r \leq 0.2 \text{ s}^{-1}$ in 100 Pa O₂, where the highly ordered surface is predominantly A-site terminated. The high Mn surface mobility on LSMO (001) is thus a unique observation in H₂O and is visible in a pressure range of 0.01–5 Pa. At higher H₂O pressures, LSMO becomes unstable, possibly due to the impact of ions formed by beam-induced⁷² motion from the thermally induced motion, the momentum

ionization of H₂O. Despite the high mobility, the Mn leaching is rather slow, as confirmed by the post-ETEM stoichiometry analysis (Supplementary Fig. 20). Furthermore, the Mn valence state remains quite stable, indicating only a slight Mn reduction in increasing H₂O pressure and ruling out pronounced formation of oxygen vacancies.

Irreversible Mn-adatom dynamics at the PCMO–H₂O interface. Figure 5 shows a time series of HRTEM images of the (001) PCMO surface in 0.5 Pa H₂O, taken from Movie M06. After fully ordering in O₂ (Fig. 2f), the addition of H₂O causes the surface to form a disordered layer of highly mobile Mn atoms, visible as rapid fluctuation of B-site contrast. Similar to LSMO, the hopping rate of Mn atoms is above the frame rate of the camera, i.e., $r \leq 4 \text{ s}^{-1}$. In contrast to the disordered B-terminated surface, the A-subsurface layer remains highly ordered and static on the timescale of several seconds (Movie M06). In addition, an increase of contrast dynamics is observed at the B-site columns at the subsurface. Figure 5b, c shows the later stages of the PCMO (001) surface in 0.5 Pa H₂O. Three min after initiation, the fast Mn leaching has led to the formation of a Pr-rich surface bilayer (Movie M06) which further grows up to a thickness of 3–4 monolayers over the course of the in situ experiment (11 min). The growth of a cubic phase due to Mn leaching is directly visible in the surface structure. Postmortem EELS analysis of the surface area in Fig. 5f reveals Pr and O, whereas the Mn L-edge at 640 eV as well as Ca L-edge at 346 eV (not shown) are below the noise level. We thus associate the cubic oxide visible in HRTEM with PrO_x, with x close to 2. The growth speed of the PrO_x slows down over time, indicating self-passivation of the surface by the formed PrO_x layer. Post-ETEM EELS of the Mn L and O K edges at the PCMO surface region reveals a pronounced Mn depletion (Supplementary Fig. 21), which is accompanied by Mn reduction. Leaching out of subsurface Mn in PCMO (001) is only observed in H₂O and is absent in HV (Movie M07) and O₂ (Movie M08). In contrast, the Mn concentration at LSMO surfaces remains unmodified. This is fully consistent with the observation of different electrode behavior in electrochemical experiments described above.

Enhanced Mn mobility at (001) surface due to presence of adsorbed H₂O layer. The formation of a few monolayer thick water layer on oxide surfaces down to pressures of $\sim 10^{-5}$ Pa much below the equilibrium vapor pressure of water of $p_{\text{vap}} = 3.17 \text{ kPa}$ at $T = 25 \text{ }^\circ\text{C}$ has been previously demonstrated^{50–52}. It is driven by the large adsorption enthalpy of H₂O on oxide surfaces of the order of $\Delta H_{\text{ad,ox}} \sim 160 \text{ kJ/mol}$ ^{51,53}. Although this value might vary between different oxides, $\Delta H_{\text{ad,ox}} < \Delta H_{\text{ad}} = -44 \text{ kJ/mol}$ for H₂O on bulk water reflects exothermic water adsorption on oxide surface at much reduced pressures. In the HV of the ETEM ($p \geq 10^{-5}$ Pa), the effect of H₂O condensation on manganese surfaces can be only avoided by using a cold trap that is reducing the partial pressure of H₂O in HV by one order of magnitude⁴². The thickness of the adsorbed water layer in the ETEM experiments as a function of $p_{\text{H}_2\text{O}}$ is calculated by using the energy balance between surface energy γ_s of the oxide in HV, the surface energy $\gamma_{\text{H}_2\text{O}}$ of liquid H₂O to vapor and ΔH_{ad} (see Supplementary Fig. 22 and associated text). The liquid state of 2–4 monolayer H₂O is consistent with our observation of enhanced mobility of Mn on manganite (001) surfaces in a pressure range between 0.01 and 5 Pa of H₂O compared to HV.

Thermally induced versus electron beam-induced hopping. In order to separate out the effect of the electron beam on adatom motion from the thermally induced motion, the momentum

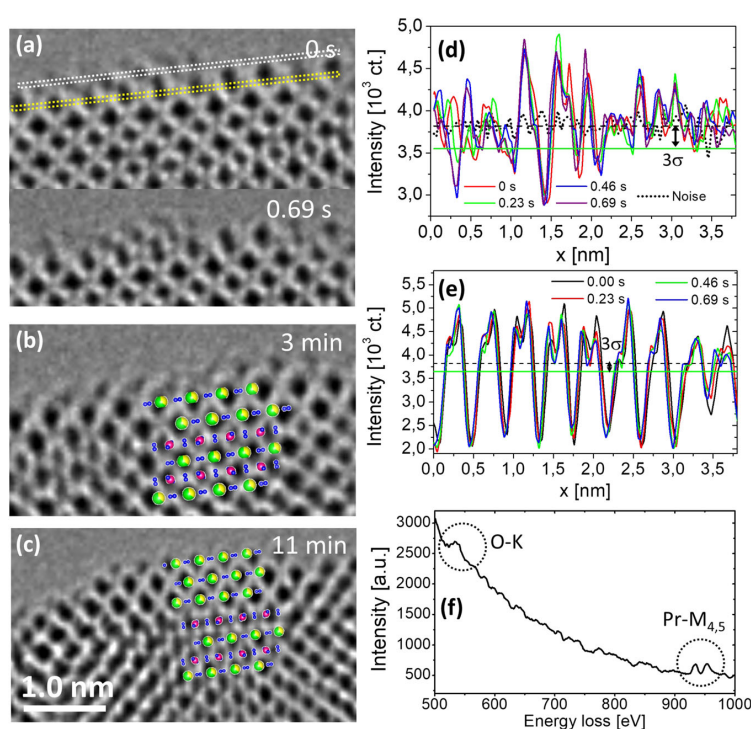


Fig. 5 Atomic surface dynamics of the PCMO (001) surface in 0.5 Pa H₂O. **a** HRTEM images taken from a time series taken at a rate of 4 fps at [110] zone axis and negative defocus, compiled in Movie M06. **b, c** Later stages of that surface area at same conditions. The line profiles are taken at the B-site (**d**) and A-site (**e**) columns. Whereas the A-site columns of the first subsurface layer remain ordered (**f**), the B-site columns transform into a dynamical highly disordered surface structure. The measured hopping rate of Mn adatoms is $r \geq 4 \text{ s}^{-1}$, from triple Mn coincidence occupation. In addition to surface movement, there is a pronounced leaching of Mn from the subsurface to the surface leading to the growth of a Pr-rich surface layer, where Mn L_{3,2} is below the detection limit (**f**).

transfer from scattering of the high energy primary electron beam on the adatoms is calculated. As pointed out by Egerton⁵⁴, for energies of primary electrons $E_0 \geq 10 \text{ keV}$, the interaction is dominated by elastic scattering of the incident electrons at the atomic nuclei, and momentum transfer due to inelastic scattering at the electron shell can be disregarded. This allows calculation of the momentum transfer using the Rutherford scattering equation. We consider the maximum momentum transfer perpendicular to the primary electron beam, which gives rise to transversal movement of adatoms on a surface parallel to the electron beam. Figure 6 compares the beam-induced hopping rates for O, Mn, Sr and La adatoms to the thermally activated hopping rate as a function of the surface activation energy E_a for an upper limit of used dose rates of $12.000 \text{ e}^-/\text{\AA}^2\text{s}$ (see method section). For $E_a \geq 0.2 \text{ eV}$, the calculated beam-induced hopping rate for Mn adatoms is below the experimentally observed hopping rate in HV, indicating that the slow Mn motion is thermally activated. The comparison of the calculated thermally activated hopping with the experimentally observed $r \text{ (HV)} \approx 0.25 \text{ s}^{-1}$ leads to an estimated $E_a \text{ (Mn)} \approx 0.75 \text{ eV}$ in HV. The increase of the Mn-adatom hopping in H₂O to $r \text{ (H}_2\text{O)} \geq 4 \text{ s}^{-1}$ thus can be interpreted as resulting from a reduction of the effective surface activation barrier in the presence of a H₂O layer to $E_a \text{ (Mn)} < 0.62 \text{ eV}$ most probably due to partial solvation of surface Mn in H₂O. Furthermore, the calculation of momentum transfer between the electron beam and H₂O shows that the adsorbed H₂O layer is only marginally affected by the beam since the beam-induced desorption rate is with $\approx 2.5 \cdot 10^{-3} \text{ s}^{-1}$ orders of magnitudes below

the impingement rate of H₂O molecules of around 10^3 s^{-1} at $p = 0.5 \text{ Pa}$.

Parallel trends in electrolysis and ETEM studies with respect to reversible and irreversible dynamics. For LSMO $x = 0.4$, the (001) interface to liquid H₂O is quite stable both in situ ETEM experiments as well as in cyclic voltammetry in alkaline conditions between +1.1 and 1.75 V vers. RHE. Only slow Mn leaching is observed in previous studies by postmortem XPS after 1 h of electrochemical OER, which can be further slowed down by choosing a Mn/A ratio ≥ 1 ref. ⁵⁵. In contrast to LSMO, the in situ ETEM study of PCMO shows pronounced irreversible surface dynamics of Mn, leaching into the liquid H₂O layer in parallel to fast drop of OER activity in electrolysis and observation of a Pr-rich surface layer in postmortem studies. The huge difference in reversibility of Mn-adatom motion at the interface between the more or less static A-site terminated layer and liquid H₂O must therefore be attributed to the different materials properties of LSMO and PCMO. Post-ETEM electron energy loss spectroscopy (EELS) of the Mn L edge at a $\approx 1\text{-nm}$ thick surface layer on PCMO demonstrates a change of Mn valence from 3.5 ± 0.1 after oxidation in O₂ to 3.2 ± 0.1 after ETEM study in 0.5 Pa and 3.1 ± 0.1 in 5 Pa of H₂O (Supplementary Fig. 21). Thus, Mn is reduced although the experiments are performed under anodic polarization. In contrast, for LSMO the pristine Mn valence of 3.5 ± 0.1 after oxidation in O₂ and 3.4 ± 0.1 after ETEM study in 0.5 Pa H₂O is preserved within the error of measurements (Supplementary Fig. 20). Previous post electrochemical XPS studies of

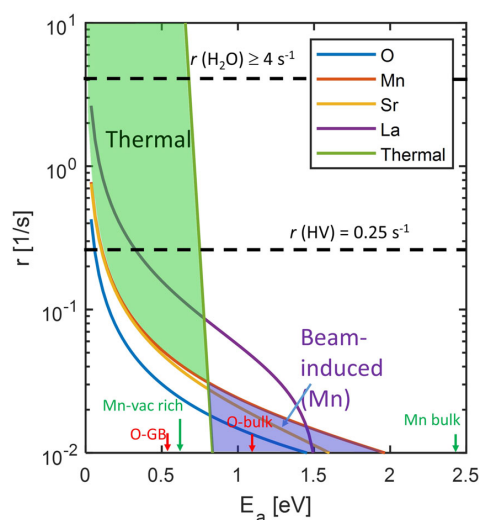


Fig. 6 Calculated beam-induced and thermally activated adatom hopping rate r at $T = 22\text{ }^{\circ}\text{C}$ as a function of the surface activation energy E_a .

Additionally, the experimentally observed Mn-adatom hopping rates in high vacuum $r(\text{HV})$ and $r(\text{H}_2\text{O})$ in 0.5 Pa H_2O are indicated. Colored areas mark the regimes for thermally and beam-induced hopping for Mn. The activation energy of O diffusion in bulk LMO is from ref. ⁶⁵ and for O in Sr-doped LMO grain boundaries from ref. ⁶⁶. For the activation energy of Mn the lower and upper limit of Mn diffusion in LMO are indicated, since it shows a broad range of values, depending on the La-off-stoichiometry of the sample⁶⁷. See method section for details of the calculations.

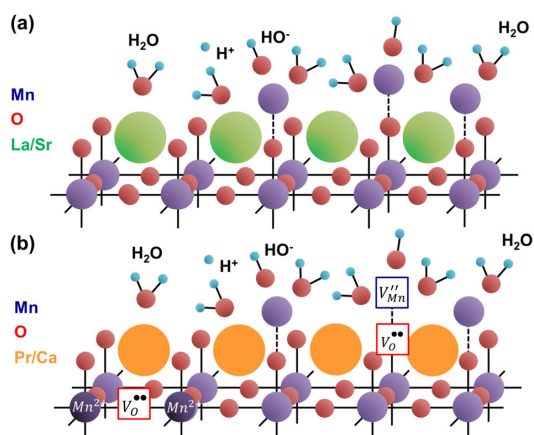


Fig. 7 Schematic representation of a snapshot of the dynamic manganite- H_2O interface. **a** For LSMO, the observed reversible Mn-adatom dynamics in liquid H_2O is connected to the absence of defect reactions and preservation of Mn oxidation state. **b** In contrast for PCMO, the reduced Mn^{2+} species are formed, due to surface and subsurface oxygen vacancy V_{O} formation.

LSMO (001) do not show surface loss of oxygen²⁹. As summarized in Fig. 7, these observations suggest that stabilization of high oxidation states of surface Mn is essential for a high reversibility of Mn-adatom movement and thus for the stability on the surface. Surface reduction and Mn^{2+} formation lead to irreversible Mn surface dynamics due to the higher solubility of Mn^{2+} in⁷⁴

H_2O compared to Mn^{3+} . Leaching of Mn^{2+} in H_2O is also predicted by a Pourbaix diagram of binary Mn-O compounds.

We attribute the different behavior of LSMO and PCMO to their different electronic properties, in particular covalency and charge localization (see Supplementary Figs. 23 and 24). Metallic LSMO exhibits spatially delocalized charge carriers, so called large polarons due to a larger Mn-O covalency and an electron-phonon coupling constant $\alpha \approx 1$ ⁵⁶. As long as the metallic state is preserved at the electrode surface, an extra charge acquired from water oxidation cannot change the valence state of a single atomic surface species. In contrast, PCMO $x = 0.33$ displays localized charge carriers, so called small polarons due a smaller Mn-O covalency and larger $\alpha \approx 3$ (see ref. ⁵⁷). They represent Zener polarons, which are located on Mn-O-Mn bridges⁵⁸⁻⁶⁰. From the chemical perspective, such a Zener polaron represents the formation of an O-oxo species, due to the presence of a localized hole charge and thus the oxidation of the lattice oxygen with a formal valence state of O^{2-} . Under anodic polarisation, hole type polarons can accumulate on the surface near Mn-O-Mn bridges and thus can easily induce oxidation of lattice oxygen to O^- as an intermediate step for subsequent formation of vacancies V_{O} . Formation of O^- and V_{O} thus can therefore reduce Mn and turn reversible adatom dynamics of oxidized metal species into irreversible processes of reduced metal species. Note that the different charge carriers may be also the origin of the different Tafel slopes b of both manganites. For LSMO, $b \approx 60\text{ mV/dec}$ fits to the theoretical prediction for a chemical rate-limiting step that follows an electrochemical pre-equilibrium, probably O-O bond formation. For PCMO, the higher $b \approx 90\text{--}120\text{ mV/dec}$ is consistent with electron transfer as the rate-limiting step and thus may reflect the lower intrinsic electric conductivity as well as limitations due to surface reduction.

Solvated dynamic Mn adatoms and impact on reaction mechanisms of oxygen evolution. The demonstrated parallel trends in in situ ETEM and electrolysis studies underpins that the observation of enhanced surface dynamics of Mn adatoms in H_2O is highly relevant for the real-world electrochemical behavior of the manganite electrodes. Clearly, there are differences in the properties of a Helmholtz layer in a liquid electrolyte with ion concentration of 10^{-1} M and the thin water layer adsorbed on top of oxide materials in ETEM. In particular, the ion concentration is much lower, with typically $10^{-6}\text{--}10^{-7}\text{ M}$ in the vapor⁴⁵ that is close to the ion concentration at neutral pH. However, the composition of ions generated by electron impact is different since positively charged ions such as H_2O^+ dominate over anions such as OH^- . Our ETEM studies are performed under positive electric potentials of $U = +2\text{ V}$ with respect to ground and thus under anodic polarization. Due to the high electric conductivity of the manganite lamella on highly conductive Nb-doped SrTiO_3 , beam-induced potentials can be disregarded⁴⁵. The comparison of hopping rates in different ambients clearly demonstrate that the observed $\geq 20\times$ increased Mn-adatom mobility in H_2O while other conditions of the experiment remain the same is not due to the electron beam. This is fully understandable from the calculation of beam-induced momentum transfer in Fig. 6. Therefore, the enhancement of thermally activated adatom motion in water is fully relevant for OER catalysis in ex situ electrochemical conditions. It can be attributed to a partial solvation of surface Mn in liquid H_2O . Such solvation effects thus do not only affect the adsorption energies of the reactants but also strongly modify the coordination and electronic properties of active sites.

The formation of a partial solvation shell of H_2O around chemisorbed Mn adatoms in OER thus has far-reaching consequences for understanding of the reaction pathways. First

of all, Mn can develop other, more flexible coordination to OH₂ and OH compared to a static octahedral Mn–O coordination of a frozen surface (Fig. 7). This would allow new configuration for the formation of the O–O double bond. Furthermore, the question is raised whether the Mn dynamics affect the OER. The electron transfer rate per surface Mn atom derived from RRDE measurements is between 0.2 s⁻¹ (1.6 V) and 10 s⁻¹ (1.74 V vers RHE), assuming a Faraday efficiency of 1 and a complete Mn surface coverage. Due to partial coverage, these numbers represent a lower limit of the electron transfer rate per Mn. Comparing these numbers with the observed lower limit of Mn-adatom hopping $r \approx 4 \text{ s}^{-1}$, shows that both are of the same order of magnitude or even higher. Consequently, Mn can move over several surface sites during a full O₂ evolution cycle.

In summary, our study reveals unexpectedly high Mn-adatom hopping rates implying that the understanding of OER mechanisms requires theoretical treatment beyond the frozen surface approximation. There is strong experimental evidence from ref. 21 that surface Mn species represent the catalytically active sites for LSMO. Fast Mn leaching at PCMO surfaces dramatically decreases OER activity. Although hopping rates and contrast of single Mn atoms are beyond the resolution of our experiments, the observation of dynamic multiple occupancy of surface sites by Mn moieties establishes a pronounced dynamical surface reconstruction of the catalyst-water interface with partial solvation of surface Mn atoms in H₂O. Mn-adatom contrast dominantly appears at interstitial surface sites rather than the nominal octahedral B sites of an unreconstructed ideal surface, suggesting a modified surface coordination. The implications of these findings are quite far-reaching. First of all, leaching of reduced transition metal species is observed for many transition metal oxides^{61,62}. Our results imply that the underlying transition from reversible dynamics of surface atoms to irreversible leaching of surface and subsurface metal species is controlled by charge localization and a related shift of the Fermi energy. Indeed, the recent results on self-gating of electrocatalysts evidences a modification of the Fermi level at the onset of an electrochemical reaction⁶³. The finding of pronounced reversible dynamics of partially solvated adatoms in the stationary state of OER implies that for the theoretical understanding of heterogeneous catalysis some aspects of homogeneous catalysis must be taken into account, such as modified metal coordination, different valence states, solvation shell reorganization during electron transfer, solvent thermal fluctuations and possibly Mn displacements during intermediate formation. Incorporating these effects into theoretical analysis will open new strategies of breaking scaling relations between adsorption energies and thus new perspectives in atomic scale design of efficient and stable electrode surfaces for OER.

Methods

Film fabrication and structure. La_{0.6}Sr_{0.4}MnO₃ and Pr_{0.33}Ca_{0.67}MnO₃ (001) films were prepared by ion-beam sputtering (IBS) on 0.5 wt% Nb-doped SrTiO₃ (STNO) substrates with (100)-orientation (CrysTec GmbH, Berlin, Germany). The La_{0.6}Sr_{0.4}MnO₃ (Pr_{0.33}Ca_{0.67}MnO₃) with thickness of 80 nm were grown at 800 °C (650 °C) in an oxygen atmosphere of 1.7 · 10⁻⁴ mbar. In order to avoid rectifying junction properties for PCMO, a 20-nm thick La_{0.6}Sr_{0.4}MnO₃ (LSMO) buffer layer was deposited without vacuum breaking. LSMO has a rhombohedral lattice, spacegroup R3c with a small rhombohedral tilt angle of 90.37°, lattice parameter $a = 5.47 \text{ \AA}$, which converts in a pseudocubic lattice constant $a_c = 3.87 \text{ \AA}$. PCMO is orthorhombic, spacegroup Pbnm, with ideal lattice parameters $a = 5.42 \text{ \AA}$, $b = 5.45 \text{ \AA}$ and $c = 7.67 \text{ \AA}$. Due to the larger lattice constant of STNO ($a = 3.92$), the films have in-plane tensile and out-of-plane compressive strain leading to $a_c = 3.83 \text{ \AA}$ (LSMO) and $c = 7.62 \text{ \AA}$ (PCMO). For LSMO, we use pseudocubic notation to facilitate the comparison of the (001) surface with the equivalent (001) surface of PCMO. The films show atomically flat surfaces with unit cell high steps. The temperature dependent electric resistivity of the films shows the expected metal-like (LSMO) and small polaron hopping like (PCMO) characteristics. See Supplementary Figs. 4–7 and 24 for more details.

Backside contacts for the STNO substrate consisted of 5 nm Ti and 100 nm Pt layers prepared by IBS at room temperature to ensure an ohmic contact. Carbon tape and InGa eutectic (Sigma–Aldrich, Munich, Germany, 99.99%) served as the flexible and adjustable conductive spacer. In the final assembly, only the thin film surface is exposed to the electrolyte after fixation with chemically stable, nonconductive epoxy (Omegabond 101).

Electrochemistry. The electrochemical measurements were carried out with two Interface 1000E potentiostats (Gamry Instruments Inc., Warminster, PA, USA) in a bipotentiostat setup and an RRDE-3A rotator (ALS Co. Ltd., Tokyo, Japan). The rotating ring electrode consists of a disk electrode of the assembled PCMO|LSMO|NSTO electrode with a diameter of 4 mm and a Pt ring electrode with an inner diameter of 5 mm and an outer diameter of 7 mm. All electrochemical measurements were performed in 0.1 M KOH electrolyte prepared by diluting KOH stock solution (Sigma–Aldrich, Munich, Germany) with deionized water (MilliQ, >16.5 MΩ). The electrolyte was saturated with Ar gas at least 30 min before measurements and continuously with Ar throughout the measurement. Electrode potentials were converted to the reversible hydrogen electrode (RHE) scale using $E_{\text{RHE}} = E_{\text{Applied}} + E_{\text{ref}}$, where $E_{\text{ref}} = 0.993 \text{ V}$ vs. SCE was obtained from the hydrogen evolution using a clean Pt disk. Cyclic voltammograms are measured at 10 mV/s with rotation of 1600 turns per minute. In Fig. 1b, between third and 4th cycle, chronoamperometric OER is measured at 1.5, 1.55, 1.6, 1.65, 1.7, 1.75, and 1.8 V vs RHE, each 60 s.

Environmental TEM experiments. Transmission Electron Microscopy (TEM) experiments were carried out using a FEI Titan ETEM G2 80–300, operated at 300 kV. The microscope is equipped with a Cs-corrector of the image forming lens for enhanced high-resolution TEM (HRTEM) imaging, and a Gatan Image Filter (GIF) Quantum 965ER. A Gatan UltraScan 1000XP CCD was used to collect all movies with rate of about 4 frames per second (fps) in 512 × 512 pixels. The microscope was used in the high vacuum (HV) mode (~10⁻⁵ Pa) with cold trap to reduce H₂O partial pressure, as well as in environmental mode using H₂O, O₂ and He in a pressure range between 0.01 and 100 Pa. The following movies are provided: M01 LSMO 0.5 Pa H₂O flat facet, M02 LSMO 0.5 Pa H₂O Schwoebel Barrier, M03 LSMO HV, M04 LSMO 0.5 Pa O₂, M05 LSMO 0.5 Pa N₂, M06 PCMO 0.5 Pa H₂O, M07 PCMO HV, M08 PCMO 0.5 Pa O₂, M09 LSMO 10 Pa O₂ recrystallization early state and M10 LSMO 10 Pa O₂ recrystallization late state. All time resolved HRTEM experiments were performed at a beam current of 4 nA and beam radius between 80 and 100 nm, resulting in a spatially inhomogeneous electron dose rate of 8000–12,000 e/Å⁻²s. Local electron dose rates at the location of TEM lamella surfaces are measured by calibrated CCD contrast with 0.136 electrons/counts, yielding ~10,000 e/Å⁻²s for the adatom hopping studies. This dose rate is two orders of magnitude below the damage threshold in HV. Imaging over a time of 10 min keeps the total electron dose ≤ 6 · 10³ As/cm², where no changes by electron irradiation are observed in HV, in good agreement with the studies of the intrinsic surface in ref. 41.

Electron energy loss spectroscopy (EELS). Was performed using Gatan Quantum 965ER post-column energy filter in the same FEI Titan ETEM. Spectra of the Mn L, O K, and Pr M edges were acquired. For analysis of the Mn L edge spectra, Hartree–Slater (HS) type cross-section functions from Gatan’s Digital Micrograph are used. The Mn valence state has been acquired from a C++ based LabTalk script using OriginLab software. EEL spectra are extracted from spectrum images at an area of vacuum and at different H₂O vapor pressure for postmortem analysis. Power-law background functions are fitted to a 50 eV wide window before each Mn L-edge and 25 eV for O K-edge for background subtraction. By using dual EELS acquisition, the ZLP is used to correct the drift of the energy shift.

TEM lamella preparation. TEM lamellae were prepared from epitaxially grown (001) oriented thin films by Focused Ion-Beam lift-out technique using a noble metal free protection layer and careful low energy ion milling for the preparation of ultrathin lamella with a thickness close to the surface between 4 and 10 nm. The loss of oxygen by Ar milling is compensated by a treatment in pure oxygen. Further details are described in the Supplementary information and Movies M09–M10.

Image simulations. Atomic models and the high-resolution TEM simulated images were calculated using the multislice method as established in the QSTEM package⁶⁴, where electron optical parameters were optimized by using a metropolis algorithm implementation to fit simulated to experimental images. Structure models for the image simulations are based on the Pbnm spacegroup for PCMO with lattice parameters $a = 5.42 \text{ \AA}$, $b = 5.45 \text{ \AA}$ and $c = 7.67 \text{ \AA}$ and R3c for LSMO with lattice $a_c = 3.87 \text{ \AA}$. Details and parameters used for image simulation are given in the SI.

Calculation of electron beam-induced and thermally activated hopping. Using the analytical solution given in ref. ⁵⁴, the adatom hopping rate is

$$R = \frac{J\sigma_0}{e} FZ^2 \left[\frac{1}{\sin^2(\vartheta_{\min}/2)} - \frac{1}{\sin^2(\vartheta_{\max}/2)} \right] \quad (1)$$

where ϑ is the scattering angle of the electrons. The limits

$$\vartheta_{\min} = \arcsin \left[2 \left(\frac{E_s}{E_{\max}} \right)^{0.5} \right] \text{ and } \vartheta_{\max} = \pi - \arcsin \left[2 \left(\frac{E_s}{E_{\max}} \right)^{0.5} \right] \quad (2)$$

are given by ratio of the captured surface energy E_s of the adatom to the maximum possible energy transfer E_{\max} , which would correspond to a 180° scattering, i.e.,

$$E_{\max}(\text{eV}) \approx \frac{1.1}{A} \left[2 + \frac{E_0}{511\text{keV}} \right] E_0(\text{keV}) \quad (3)$$

A is the atomic mass, Z the nuclear charge, e the elementary electron charge, J is the current density of the primary electron beam, $\sigma_0 = 1 \text{ barn} = 10^{-28} \text{ m}^2$ and $F = (1 - v^2/c^2)^{-0.5}$, where c is the velocity of light and v the velocity of the primary electrons. In order to calculate the hopping rate of an adatom on a surface, it is assumed that the kinetic energy transversal to the surface is equal to the surface activation energy E_a , i.e., $E_s = E_a$. In the Mn-adatom hopping studies, $E_0 = 300 \text{ keV}$ and for the current density an upper limit of the experimental values of $J = 2.0 \cdot 10^5 \text{ A/m}^2$ is chosen, corresponding to $12,000 \text{ e}/\text{\AA}^2\text{s}$.

The thermally activated hopping rate is given by

$$R_{\text{th}} = \nu_0 e^{-\frac{E_a}{k_B T}} \quad (4)$$

with adatom vibration frequency ν_0 and Boltzmann constant k_B . We have chosen $\nu_0 = 10^{12} \text{ s}^{-1}$, which for $E_a = 0 \text{ eV}$ results in a thermal velocity for Mn atoms matching the maximum of the Maxwell-Boltzmann distribution.

Data availability

All relevant data are available from the corresponding authors on request.

Received: 8 April 2020; Accepted: 30 July 2020;

Published online: 24 September 2020

References

- Wiechen, M., Berends, H. M. & Kurz, P. Water oxidation catalysed by manganese compounds: from complexes to 'biomimetic rocks'. *Dalton Trans.* **41**, 21–31 (2012).
- McCrorry, C. C. L., Jung, S., Peters, J. C. & Jaramillo, T. F. Benchmarking heterogeneous electrocatalysts for the oxygen evolution reaction. *J. Am. Chem. Soc.* **135**, 16977–16987 (2013).
- Hong, W. T. et al. Toward the rational design of non-precious transition metal oxides for oxygen electrocatalysis. *Energy Environ. Sci.* **8**, 1404–1427 (2015).
- Lyons, M. E. G. & Burke, L. D. Mechanism of oxygen reactions at porous oxide electrodes. Part 1.—oxygen evolution at RuO₂ and Ru_xSn_{1-x}O₂ electrodes in alkaline solution under vigorous electrolysis conditions. *J. Chem. Soc. Faraday Trans. 1 Phys. Chem. Condens. Phases* **83**, 299–321 (1987).
- Bockris, J. O'M. & Conway, B. E. Modern aspects series of chemistry. *Butterworths Sci. Publ. Lond.* **1**, 180 (1954).
- Conway, B. E. & Salomon, M. Electrochemical reaction orders: applications to the hydrogen- and oxygen-evolution reactions. *Electrochim. Acta* **9**, 1599 (1964).
- Lodi, G., Sivieri, E., De Battisti, A. & Trasatti, S. Ruthenium dioxide-based film electrodes—III. Effect of chemical composition and surface morphology on oxygen evolution in acid solutions. *J. Appl. Electrochem.* **8**, 135–143 (1978).
- Kobussen, A. G. C. & Broers, G. H. J. The oxygen evolution on La_{0.5}Ba_{0.5}CoO₃. Theoretical impedance behaviour for a multi-step mechanism involving two adsorbates. *J. Electroanal. Chem.* **126**, 221–240 (1981).
- Rossmel, J., Qu, Z. W., Zhu, H., Kroes, G. J. & Nørskov, J. K. Electrolysis of water on oxide surfaces. *J. Electroanal. Chem.* **607**, 83–89 (2007).
- Wohlfahrt-Mehrens, M. & Heitbaum, J. Oxygen evolution on Ru and RuO₂ electrodes studied using isotope labelling and on-line mass spectrometry. *J. Electroanal. Chem.* **237**, 251–260 (1987).
- Grimaud, A. et al. Double perovskites as a family of highly active catalysts for oxygen evolution in alkaline solution. *Nat. Commun.* **4**, 2439 (2013).
- Rong, X., Parolin, J. & Kolpak, A. M. A fundamental relationship between reaction mechanism and stability in metal oxide catalysts for oxygen evolution. *ACS Catal.* **6**, 1153–1158 (2016).
- Mierwaldt, D. et al. In situ XANES/XPS investigation of doped manganese perovskite Catalysts. *Catalysts* **4**, 129–145 (2014).
- Kuan-Yu Yeh & Michael J. Janik. In *Computational Catalysis* (ed. Aravind Asthagiri, M. J. J.) 116–156 (Royal Society of Chemistry, 2014).
- Blakemore, J. D., Crabtree, R. H. & Brudvig, G. W. Molecular catalysts for water oxidation. *Chem. Rev.* **115**, 12974–13005 (2015).
- Man, I. C. et al. Universality in oxygen evolution electrocatalysis on oxide surfaces. *ChemCatChem* **3**, 1159–1165 (2011).
- She, Z. W. et al. Combining theory and experiment in electrocatalysis: insights into materials design. *Science* **355**, eaad4998 (2017).
- Gono, P. & Pasquarello, A. Oxygen evolution reaction: bifunctional mechanism breaking the linear scaling relationship. *J. Chem. Phys.* **152**, 104712 (2020).
- Calle-Vallejo, F., Krabbe, A. & Garcia-Lastra, J. M. How covalence breaks adsorption-energy scaling relations and solvation restores them. *Chem. Sci.* **8**, 124–130 (2016).
- Zhang, B. et al. Homogeneously dispersed multimetal oxygen-evolving catalysts. *Science* **352**, 333–337 (2016).
- Arrigo, R. et al. In situ study of the gas-phase electrolysis of water on platinum by NAP-XPS. *Angew. Chem. Int. Ed.* **52**, 11660–11664 (2013).
- Bergmann et al. Reversible amorphization and the catalytically active state of crystalline Co₃O₄ during oxygen evolution. *Nat. Commun.* **6**, 8625 (2015).
- Risch, M. et al. Water oxidation by amorphous cobalt-based oxides: in situ tracking of redox transitions and mode of catalysis. *Energy Environ. Sci.* **8**, 661–674 (2015).
- Xia, X. et al. On the role of surface diffusion in determining the shape or morphology of noble-metal nanocrystals. *Proc. Natl. Acad. Sci. USA* **110**, 6669–6673 (2013).
- Chen, L. Y. & Ying, S. C. Adatoms on solid surfaces. *Phys. Rev. B* **49**, 838–847 (1994).
- Shiotari, A., Okuyama, H., Hatta, S., Aruga, T. & Hamada, I. Atomic-scale study of the formation of sodium-water complexes on Cu(110). *Phys. Chem. Chem. Phys.* **20**, 12210–12216 (2018).
- Wang, Y. G., Mei, D., Glezakou, V. A., Li, J. & Rousseau, R. Dynamic formation of single-atom catalytic active sites on ceria-supported gold nanoparticles. *Nat. Commun.* **6**, 6511 (2015).
- Raabe, S. et al. In situ electrochemical electron microscopy study of oxygen evolution activity of doped manganite perovskites. *Adv. Funct. Mater.* **22**, 3378–3388 (2012).
- Scholz, J. et al. Rotating ring-disk electrode study of oxygen evolution at a perovskite surface: Correlating activity to manganese concentration. *J. Phys. Chem. C* **120**, 27746–27756 (2016).
- Izgorodin, A., Winther-Jensen, O. & MacFarlane, D. R. On the stability of water oxidation catalysts: challenges and prospects. *Aust. J. Chem.* **65**, 638–642 (2012).
- Kötz, R., Stucki, S., Scherson, D. & Kolb, D. M. In-situ identification of RuO₄ as the corrosion product during oxygen evolution on ruthenium in acid media. *J. Electroanal. Chem.* **172**, 211–219 (1984).
- da Silva, G. C., Mayrhofer, K. J. J., Ticianelli, E. A. & Cherevko, S. Dissolution stability: the major challenge in the regenerative fuel cells bifunctional catalysis. *J. Electrochem. Soc.* **165**, F1376–F1384 (2018).
- Stoerzinger, K. A. et al. The role of Ru redox in pH-dependent oxygen evolution on rutile ruthenium dioxide. *Surfaces. Chem.* **2**, 668–675 (2017).
- Cherevko, S. Stability and dissolution of electrocatalysts: building the bridge between model and “real world” systems. *Curr. Opin. Electrochem.* **8**, 118–125 (2018).
- Kanan, M. W. & Nocera, D. G. In situ formation of an oxygen-evolving catalyst in neutral water containing phosphate and Co²⁺. *Science* **321**, 1072–1075 (2008).
- Handoko, A. D., Wei, F., Jenndy, Yeo, B. S. & Seh, Z. W. Understanding heterogeneous electrocatalytic carbon dioxide reduction through operando techniques. *Nat. Catal.* **1**, 922–934 (2018).
- Kasian, O., Grote, J. P., Geiger, S., Cherevko, S. & Mayrhofer, K. J. J. The common intermediates of oxygen evolution and dissolution reactions during water electrolysis on iridium. *Angew. Chem. Int. Ed.* **57**, 2488–2491 (2018).
- Yoshida, H. et al. Visualizing gas molecules interacting with supported nanoparticulate catalysts at reaction conditions. *Science* **335**, 317–319 (2012).
- Lin, Y., Wu, Z., Wen, J., Poepplmeier, K. R. & Marks, L. D. Imaging the atomic surface structures of CeO₂ nanoparticles. *Nano Lett.* **14**, 191–196 (2014).
- Bugnet, M., Overbury, S. H., Wu, Z. L. & Epicier, T. Direct visualization and control of atomic mobility at {100} surfaces of Ceria in the environmental transmission electron microscope. *Nano Lett.* **17**, 7652–7658 (2017).
- Kuwauchi, Y., Yoshida, H., Akita, T., Haruta, M. & Takeda, S. Intrinsic catalytic structure of gold nanoparticles supported on TiO₂. *Angew. Chem. Int. Ed.* **51**, 7729–7733 (2012).
- Roddatis, V., Lole, G. & Jooss, C. In situ preparation of Pr_{1-x}Ca_xMnO₃ and La_{1-x}Sr_xMnO₃ catalysts surface for high-resolution environmental transmission electron microscopy. *Catalysts* **9**, 751 (2019).
- Möbus, G. et al. Dynamics of polar surfaces on ceria nanoparticles observed in situ with single-atom resolution. *Adv. Funct. Mater.* **21**, 1971–1976 (2011).

44. Yuan, W. et al. Visualizing H₂O molecules reacting at TiO₂ active sites with transmission electron microscopy. *Science* **367**, 428–430 (2020).
45. Mildner, S. et al. Environmental TEM study of electron beam induced electrochemistry of Pr_{0.64}Ca_{0.36}MnO₃ catalysts for oxygen evolution. *J. Phys. Chem. C* **119**, 5301–5310 (2015).
46. Bakardjieva, S., Bezdička, P., Grygar, T. & Vorm, P. Reductive dissolution of microparticulate manganese oxides. *J. Solid State Electrochem.* **4**, 306 (2000).
47. Nemudry, A., Rudolf, P. & Schöllhorn, R. Topotactic electrochemical redox reactions of the defect perovskite SrCoO_{2.5+x}. *Chem. Mater.* **8**, 2232 (1996).
48. Köhler, L., Szabadics, L., Jooss, C. & Risch, M. Peroxide yield of the (001) La_{0.6}Sr_{0.4}MnO₃ surface as a bifunctional electrocatalyst for the oxygen reduction reaction and oxygen evolution reaction in alkaline media. *Batter. Supercaps* **2**, 364–372 (2019).
49. Stoerzinger, K. A., Qiao, L., Biegalski, M. D. & Shao-Horn, Y. Correction to “Orientation-Dependent Oxygen Evolution Activities of Rutile IrO₂ and RuO₂”. *J. Phys. Chem. Lett.* **5**, 1636–1641 (2015).
50. Kettler, G. et al. The nature of water nucleation sites on TiO₂(110) surfaces revealed by ambient pressure X-ray photoelectron spectroscopy. *J. Phys. Chem. C* **111**, 8278–8282 (2007).
51. Srinivasan, S. G. et al. Crystal structures, surface stability, and water adsorption energies of La-Bastnäsite via density functional theory and experimental studies. *J. Phys. Chem. C* **120**, 16767–16781 (2016).
52. Opitz, A., Scherge, M., Ahmed, S. I. U. & Schaefer, J. A. A comparative investigation of thickness measurements of ultra-thin water films by scanning probe techniques. *J. Appl. Phys.* **101**, 064310 (2007).
53. Drazin, J. W. & Castro, R. H. R. Water adsorption microcalorimetry model: deciphering surface energies and water chemical potentials of nanocrystalline oxides. *J. Phys. Chem. C* **118**, 10131–10142 (2014).
54. Egerton, R. F. Beam-induced motion of adatoms in the transmission electron microscope. *Microsc. Microanal.* **19**, 479–486 (2013).
55. Scholz, J. et al. Tailoring the oxygen evolution activity and stability using defect chemistry. *Catalysts* **7**, 139 (2017).
56. Hartinger, C., Mayr, F., Loidl, A. & Kopp, T. Polaronic excitations in colossal magnetoresistance manganite films. *Phys. Rev. B Condens. Matter Mater. Phys.* **73**, 024408 (2006).
57. Hoffmann, J. et al. Effects of interaction and disorder on polarons in colossal resistance manganite Pr_{0.68}Ca_{0.32}MnO₃ thin films. *Mater. Res. Express* **1**, 046403 (2015).
58. Daoud-Aladine, A., Rodríguez-Carvajal, J., Pinsard-Gaudart, L., Fernández-Díaz, M. T. & Revcolevschi, A. Zener polaron ordering in half-doped manganites. *Phys. Rev. Lett.* **89**, 097205 (2002).
59. Jooss, C. et al. Polaron melting and ordering as key mechanisms for colossal resistance effects in manganites. *Proc. Natl Acad. Sci. USA* **104**, 13597 (2007).
60. Sotoudeh, M. et al. Electronic structure of Pr_{1-x}Ca_xMnO₃. *Phys. Rev. B* **95**, 235150 (2017).
61. Najafpour, M. M., Sedigh, D. J., Pashaei, B. & Nayeri, S. Water oxidation by nano-layered manganese oxides in the presence of cerium(IV) ammonium nitrate: important factors and a proposed self-repair mechanism. *N. J. Chem.* **37**, 2448 (2013).
62. Chivot, J., Mendoza, L., Mansour, C., Pauporté, T. & Cassir, M. New insight in the behaviour of Co-H₂O system at 25–150 °C, based on revised Pourbaix diagrams. *Corros. Sci.* **50**, 62–69 (2008).
63. He, Y. et al. Self-gating in semiconductor electrocatalysis. *Nat. Mater.* **18**, 1098–1104 (2019).
64. Koch, C. *Determination of Core Structure Periodicity and Point Defect Along Dislocations*. Ph.D. Thesis, Arizona State University (2002).
65. Palcut, M., Wiik, K. & Grande, T. Cation self-diffusion and nonstoichiometry of lanthanum manganite studied by diffusion couple measurements. *J. Phys. Chem. C* **111**, 813–822 (2007).
66. Polfus, J. M., Yildiz, B. & Tuller, H. L. Origin of fast oxide ion diffusion along grain boundaries in Sr-doped LaMnO₃. *Phys. Chem. Chem. Phys.* **20**, 19142–19150 (2018).
67. Miyoshi, S. & Martin, M. B-Site cation diffusivity of Mn and Cr in perovskite-type LaMnO₃ with cation-deficit nonstoichiometry. *Phys. Chem. Chem. Phys.* **11**, 3063 (2009).

Acknowledgements

This work was financially supported by the DFG SFB 1073, projects C02, C03 and B02 and use of equipment in the “Collaborative Laboratory and User Facility for Electron Microscopy” (CLUE) at University of Goettingen are gratefully acknowledged. We thank Ch. Luderer and D. Busse for post electrochemical TEM analysis of LSMO films.

Author contributions

G.L. and V.R. carried out the ETEM experiments. T.M. and U.R. contributed to image analysis. J.G. and G.W. did manganite epitaxy and structural analysis as well as electrochemical measurements. M.R. contributed to analysis of electrochemical data. L.R. provided software for image simulation. P.B. contributed to theoretical analysis of the results. C.J. did calculations on beam effects and water adsorption and wrote the manuscript. All authors commented on, discussed and edited the manuscript.

Competing interests

The authors declare no competing interests.


Additional information

Supplementary information is available for this paper at <https://doi.org/10.1038/s43246-020-00070-6>.

Correspondence and requests for materials should be addressed to C.J.

Reprints and permission information is available at <http://www.nature.com/reprints>

Publisher's note Springer Nature remains neutral with regard to jurisdictional claims in published maps and institutional affiliations.

 **Open Access** This article is licensed under a Creative Commons Attribution 4.0 International License, which permits use, sharing, adaptation, distribution and reproduction in any medium or format, as long as you give appropriate credit to the original author(s) and the source, provide a link to the Creative Commons license, and indicate if changes were made. The images or other third party material in this article are included in the article's Creative Commons license, unless indicated otherwise in a credit line to the material. If material is not included in the article's Creative Commons license and your intended use is not permitted by statutory regulation or exceeds the permitted use, you will need to obtain permission directly from the copyright holder. To view a copy of this license, visit <http://creativecommons.org/licenses/by/4.0/>.

© The Author(s) 2020

Chapter 6

Contrasting $\text{Pr}_{1-x}\text{Ca}_x\text{MnO}_3$ OER catalyst with different valence and covalence: $x = 0.1$ and $x = 0.33$

Contrasting $\text{Pr}_{1-x}\text{Ca}_x\text{MnO}_3$ OER catalyst with different valence and covalence: $x=0.1$ and $x=0.33$

Gaurav Lole, Fatemeh Ebrahimi, Tobias Meyer, Daniel Mierwaldt, Vladimir Roddatis, Janis Geppert, Marcel Risch & Christian Jooss*

ABSTRACT: Perovskite oxides are promising materials for catalysing the oxygen evolution reaction (OER). However, the understanding of properties of active sites that enable high OER activity without corrosive electrode reduction is still elusive. In this work, we use combined electrochemical and Environmental Transmission Electron Microscopy (ETEM) studies to compare OER stability of (001) surfaces of $\text{Pr}_{1-x}\text{Ca}_x\text{MnO}_3$ perovskite films with doping of $x = 0.1$ and $x = 0.33$. Notably, electrochemical analysis in alkaline conditions as well as ETEM studies in H_2O vapour show parallel trends in stability of both systems: Mn leaching for the PCMO $x=0.33$ system due to oxygen vacancy formation at the surface and higher stability of PCMO $x=0.1$, where the oxygen vacancy redox peak is absent in cyclic voltammetry. Electron energy-loss spectroscopy reveals the preservation of Mn valence state in H_2O for the PCMO $x=0.1$ system, whereas for $x=0.3$ Mn is reduced. We interpret this enhanced stability for the low doped system in terms of a modified Mn 3d - O 2p hybridization, i.e. covalence. For a system with charge localization due to Jahn-Teller polarons, the covalence determines to what degree redox processes of lattice oxygen can arise that can finally lead to corrosive oxygen vacancy formation.

KEYWORDS: Thin films, oxygen evolution reaction, in-situ transmission electron microscopy, electron energy loss spectroscopy, covalence

1. INTRODUCTION

The electrochemical catalytic water splitting including oxygen evolution is an eco-friendly and sustainable approach to produce hydrogen with zero carbon emission¹. The electrocatalytic splitting of water includes the OER ($4\text{OH}^- \rightarrow \text{O}_2 + 2\text{H}_2\text{O} + 4\text{e}^-$) at the anode and the hydrogen evolution reaction (HER) ($2\text{H}_2\text{O} + 2\text{e}^- \rightarrow 2\text{OH}^- + \text{H}_2$) at the cathode. The OER incorporates a four electron transfer process, which needs a high electric potential to overcome rate limiting thermodynamic and kinetic energy barriers, depending on the reaction mechanism.¹⁻⁸ In particular, multiple transfers of electrons and protons during the OER result in a higher overpotential in

contrast to HER. The utilization of efficient OER electrocatalyst is, thus, crucial to significantly reduce the overpotential of the anodic reaction in water splitting for hydrogen generation.⁹

At present, the Ruthenium (Ru) or Ru-based catalysts have one of the lowest overpotential for OER under an acidic environment.^{10,11} Iridium (Ir) and Ru based perovskites are profoundly tuneable and distinct materials that assure OER electrocatalyst, with many modifications promoting high activities and stabilities in acidic environments. Thus, the noble metal oxides IrO₂ and RuO₂ are presently considered as the best catalysts for OER.¹² However, the high price and low abundance limit the practical utilization of these noble metal-based catalysts on a large scale. Therefore, searching for cost-effective and alternatives for noble metal catalysts is essential.^{1,3,13,14} Lately, 3d transition-metal oxides (TMO) have come forth as potential substitutes to RuO₂ and IrO₂ because of their notable activities and low cost in alkaline conditions.^{15–17} Amongst them, perovskites with ABO₃ formula have attracted particular attention because of their tuneable structure and properties.^{18–23} Substituting A and B cations alters the electronic structure, oxidation state, and catalytic properties. This substitution permits controlling the valence states of the B site transition metals and influences the formation of oxygen vacancies.¹ Sometimes, fast surface reconstruction appears after a few OER cycles, or even upon immersion in the electrolyte, before the initiation of the OER process.^{7,24–27} Even though many transition metal perovskite oxides initially show a high catalytic performance, the electrode surface-electrolyte interface reactions and catalyst stability are still difficult to interpret. The perovskite interface to water is typically dynamic, showing reversible as well as irreversible processes under OER conditions.²⁸ The most typical irreversible surface transformation occurs due to A-site and B-site transition metal cations leaching during OER which can be facilitated by oxygen vacancy formation and subsequent reduction of the metal species. Leaching of A-site or B-site elements at the electrode surface during the OER leads to the drastic change of OER activity.^{20,28} The underlying mechanisms that control whether the emerging surface processes are reversible or irreversible are however still elusive.

One important aspect is the participation of lattice oxygen in the formation of molecular oxygen in some perovskite systems, known as the lattice oxygen mechanism (LOM). This reaction pathway can decrease the energy barrier and leads to higher activity in some perovskite systems.^{20,29,30} On the other hand, the single site adsorbate evolution mechanism (AEM) typically involves four-step proton-electron transfer reactions occurring entirely on a single B- site metal ion. Based on a frozen surface approximation, a scaling relation between the adsorption energies of the different surface

intermediates was proposed.³¹ The DFT calculations reveal an adsorption process that involves antibonding e_g orbitals of TM hybridized with oxygen 2p bands of oxygen-containing intermediate chemical species. Involving lattice oxygen to couple O-O bond to produce an O_2 molecule could lower the energy barrier compared to the scaling relation predicted by the AEM, because LOM circumvents the formation of the HOO* intermediate. An increase of metal–oxygen covalence is considered as a tool to alter the OER mechanism from the AEM to the LOM.²³ Optimizing the e_g filling or increasing the TM 3d–O 2p covalence can booster the OER on the perovskite surface.^{32–35} Thus, optimizing both valence and covalence can induce a higher density of the TM 3d acceptor states near the Fermi level and so facilitate the electron transfer from the oxygen intermediates to the electrode surface.⁹ By an increase in covalence, the electron transfer between TM ions and oxygen is facilitated, and direct O–O bonding with the reversible formation of oxygen vacancy i.e., the LOM mechanism becomes favourable.³⁶

An increased covalence cannot only give rise to lattice oxygen redox activity but also to the irreversible formation of oxygen vacancies during OER, as observed in ref^{37,38} for PCMO. Oxygen vacancies modify the electrical conductivity of the surface, alter the electronic structure, transition metal valence as well as can modify the active sites for electrocatalytic reactions.²⁸ However, examples where oxygen vacancies improve OER activity without hampering the stability of the electrode are very rare. One example is the Ruddlesden Popper $La_{0.5}Sr_{1.5}Ni_{1-x}Fe_xO_{4-\delta}$, where a doping dependent oxygen vacancy formation energy and oxygen mobility together with the capability of in cooperation of excess oxygen may result in a stable LOM mechanism.³⁹ More frequently, a catalyst corrosion by oxygen vacancies is observed which can even lead to surface amorphization of perovskites.²⁶ Nevertheless, the impact of oxygen vacancies on the OER activity is still unresolved.

Environmental transmission electron microscopy (ETEM) is a versatile tool for the study of the surface changes by the formation of oxygen vacancies due to its high-spatial-resolution as well as the capability of applying electron energy loss spectroscopy (EELS) to the catalyst surface.⁴⁰ In differentially pumped systems, the reactive gas is allowed to flow over the surface. Aberration corrected ETEM studies offer the possibility to observe catalysts surface with real space atomic resolution in several millibars pressure of reactive gases.⁴¹ The latest advances of atomic resolution observations allow comparison of surface atomic dynamics in reactive and inert atmosphere.^{28,42} Developments towards controlling the electron beam-induced and applied electric potentials in

ETEM enable in situ studies of catalyst surfaces under OER relevant potentials.²⁸ The capability to regulate the gas pressure during ETEM observations is a beneficial way of exploring the changes in the structure and electronic properties.⁴³

In this work, we present an in-situ ETEM study of the $\text{Pr}_{1-x}\text{Ca}_x\text{MnO}_3$ (PCMO) manganite system with Ca doping of $x = 0.1$ and $x = 0.33$. We observe a pronounced difference of OER stability both in rotating ring disc electrode (RRDE) experiments as well as in ETEM. While PCMO $x = 0.33$ display a drastic decrease the OER activity even though it shows initially a high OER current density²⁸, PCMO $x=0.1$ has a lower activity but the decrease is less. EELS analysis shows that the $x=0.1$ system preserves Mn^{3+} valence state during OER, while the $x = 0.33$ system shows surface reduction due to oxygen vacancy formation and subsequent leaching of the formed Mn^{2+} species. For the PCMO $x=0.1$ system we also compare two different surfaces, i.e., the (001) and the (112) surface which both are stable but display quite different surface dynamics. These observations allow to derive conclusions on the impact of covalence and surface orientation on the dynamic states of the electrode interface to water.

2. RESULTS AND DISCUSSION

Electrochemistry. Cyclic voltammetry (CV) study in a rotating ring disc electrode (RRDE) setup was employed to study the current density with voltage cycling of epitaxial (001) oriented $\text{Pr}_{1-x}\text{Ca}_x\text{MnO}_3$ thin film at $x=0.1$ and $x = 0.33$. The structural characterisation of both films with AFM and XRD is shown in the supplementary information Figures S1 and S2. Figure 1a depicts the 2nd and 50th cycles of the CV for both doping in O_2 saturated 0.1 mol KOH. Both films show exponentially increasing currents that indicates electrocatalytic activity of OER. In order to qualitatively probe the produced oxygen by the PCMO thin films, additional measurements were performed in Ar-saturated 0.1 mol KOH, where a potential of 0.5 V vs. RHE is applied to the Pt ring electrode in order to drive the oxygen reduction reaction (ORR) in transport limitation.⁴⁴ The ring current densities show the same exponential trend as the disc current densities (supplementary Figure S3). This supports the assignment of the disc current to the evolution of oxygen. Clearly, for $x=0.33$ the onset of OER occurs at lower potential, demonstrating a higher activity compared to $x=0.1$ which decreases for both samples upon cycling.

Additionally, a cathodic redox transition peak is visible on PCMO for $x = 0.33$ at $E = 1.3$ V vs. RHE. During cycling, the corresponding anodic peak becomes visible (50th cycle, indicated by

arrow). The redox couple is related to reversible formation and annihilation of oxygen vacancies, which are electron donors and thus induce a surface reduction of the transition metal³⁷. The easy formation of oxygen vacancies in the PCMO film with $x = 0.33$ suggests that lattice oxygen is redox active, i.e., holes can be transferred between Mn 3d and O 2p states. They can oxidize O^{2-} to form O^- and $O_2(g)$.²⁸ This feature was not observed in for the PCMO film $x=0.1$. As a result, the CV of this film did not show any pre-catalytic redox peaks.

In order to study the stability of both doping levels, chronoamperometric measurement of the OER current have been performed. Figure 1b and c compares the time decay of the catalytic current density of both electrodes in Ar-saturated conditions. After an initial fast drop, the current remains more stable for the $x=0.1$ sample compared to $x=0.33$ which has a higher initial absolute current density (Figure 1b). The chronoamperometric measurements for higher applied potentials up to 1.8 V vs RHE and for O_2 -saturated conditions are shown in the supplementary Figures S4 and S5. Remarkably, at higher anodic polarization (Figure 1c) as well as for O_2 -saturation, the difference of the time decay of both doping levels almost disappears. This points to a loss of lattice oxygen and vacancy formation as a dominant corrosion mechanism for the $x=0.33$ films which is minor at higher anodic potentials and electrolyte oxygen concentration. AFM images of as grown epitaxial films before and after electrochemical measurement do not reveal significant changes in the microstructure of the surfaces after cycling (See supplementary Figure S1).

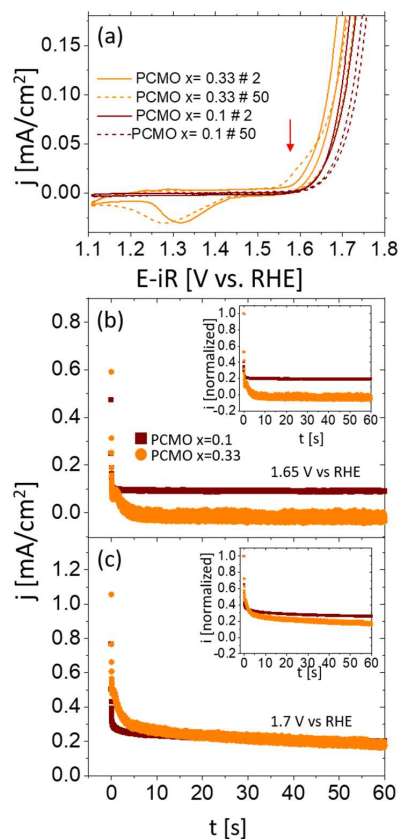


Figure 1. Electrochemical OER performance of epitaxial PCMO $x = 0.1$ and $x = 0.33$ (001) oriented thin films. (a) Cyclic voltammetry for both films at cycles #2 and #50. In addition to the OER, PCMO $x = 0.33$ shows a redox couple after 50 cycles as indicated by an arrow. Chronoamperometric measurements show current at two applied potentials 1.65 V vs RHE (b) and 1.7 V vs RHE (c) as a function of time in argon-saturated electrolyte. Inset shows normalized plots of (b-c) respectively.

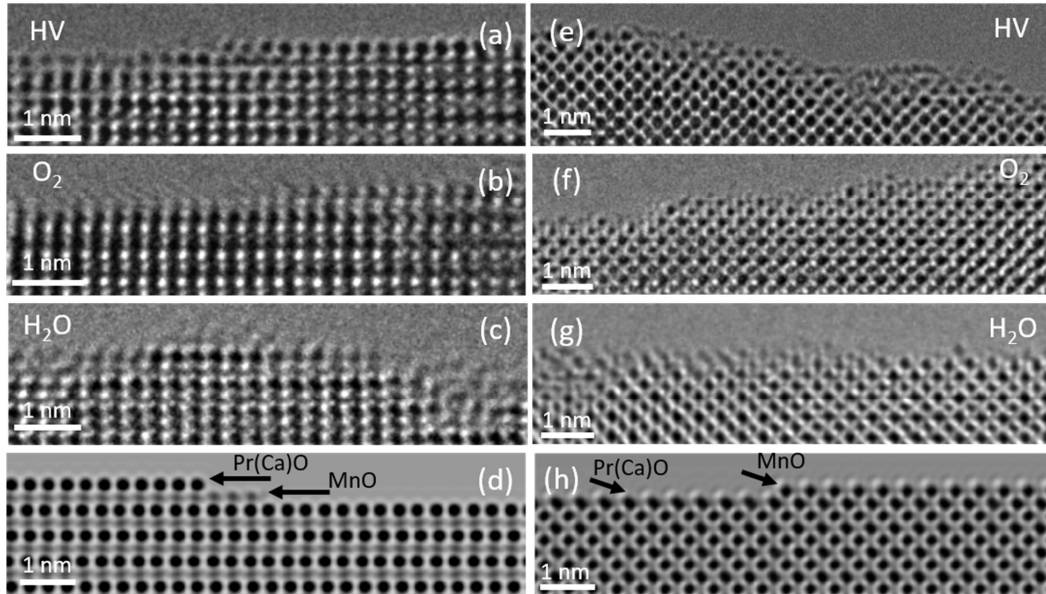


Figure 2. HRTEM images of PCMO (001) surfaces of $x=0.1$ and 0.33 in different environments. (a–c) PCMO $x=0.1$ is imaged in the [010] and (e–g) PCMO $x=0.33$ in the [110] zone axis, respectively. (a) Mixed A and B termination in high vacuum (HV). (b) Dominant A-termination in 1 mbar O_2 . (c) A-site terminated surface with a disordered layer in 0.8 Pa H_2O . (e) Disordered mixed A-site and B-site terminated surface in HV. (f) Highly ordered mixed terminated surface in 1 mbar of O_2 . (g) The B-site terminated areas of $x=0.33$ show a distinct disordered area in 0.5 Pa of H_2O . (d) and (h) Simulated images with mixed terminations for PCMO $x=0.1$ and $x=0.33$ surfaces, respectively.

Termination of PCMO $x=0.1$ and $x=0.33$ (001) surfaces. Surface termination of the (001) surfaces of PCMO $x=0.1$ and 0.33 are observed in the ETEM in different reactive (H_2O and O_2) and inert (high vacuum - HV) environments. The study of surface termination is performed on the HRTEM images recorded in negative defocus, i.e., all the atomic columns show black contrast. Such surface termination analysis is only possible if the TEM lamella are prepared with care including healing out of surface oxygen loss, as reported by ref28,42. The detailed procedure for TEM lamella preparation is summarized in the method section. All surfaces are studied after recrystallization in 1 mbar O_2 . The resulting trends in surface termination of PCMO $x=0.1$ and 0.33 epitaxially grown thin films in HV, O_2 and H_2O are shown in Figure 2.

In HV, a quite ordered surface with mixed A-site (Pr/Ca - O) and B-site (Mn-O) terminated facets are observed for PCMO $x=0.1$ (Figure 2a). In contrast, PCMO $x=0.33$ shows a strongly disordered surface (Figure 2e) in HV. In 1 mbar O_2 both PCMO $x=0.1$ and $x=0.33$ develop ordered surfaces with mixed A and B termination (Figure 2b and Figure 2f). In H_2O , the surfaces develop again a pronounced disordered structure for both doping levels (Figure 2c for $x=0.1$ at 0.8 Pa H_2O and Figure 2g for $x=0.33$ at 0.5 Pa of H_2O). For $x=0.1$, there is a tendency that the A-site terminated facets are more ordered compared to the B-terminated facets. Figures 2d and h show simulated images of PCMO $x=0.1$ and $x=0.33$ respectively. The simulated images refer to $[010]$ zone axis for PCMO $x=0.1$ and $[110]$ zone axis for PCMO $x=0.33$, both with $[001]$ surfaces. The comparison of experimental images to simulations allow to distinguish the contrast of A-terminated and B-terminated facets. The simulated images are obtained from multi-slice simulations using QSTEM⁴⁵ software. The sample thickness as well as lens aberrations, i.e., defocus, spherical aberration, two-fold astigmatism and axial coma, are fitted by minimizing the root mean square difference between experimental and simulated images as described in the method section.

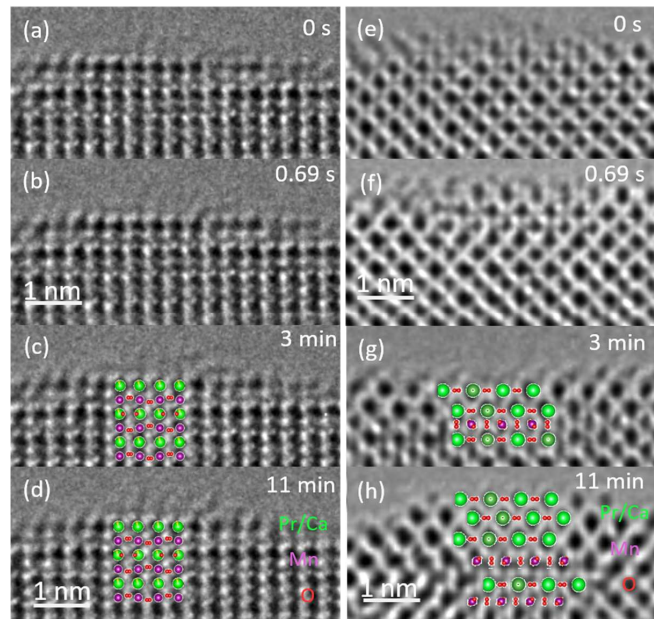


Figure 3. Time resolved series of HRTEM images of PCMO (001) $x=0.1$ and 0.33 surfaces at negative defocus that show atomic dynamics in H_2O . (a-d) HRTEM images captured from a movie M2 recorded at 4 frames per second (fps) at $[010]$ zone axis for PCMO $x=0.1$. The sequence shows stable A-site termination for a longer time in H_2O . The surface does not exhibit any structural

changes and retains perovskite structure even after 11 min. Mn adatoms show mobility on the surface from the beginning of the movie. (e) HRTEM images taken from a time series at a rate of 4 fps at [110] zone axis for PCMO $x = 0.33$, compiled in movies M3-M5. (f-h) Later stages of that surface area at the same conditions confirm Mn leaching from the topmost 3 atomic layers of the surface.

Dynamical disordered surface layer at the PCMO $x=0.1$ - H_2O interface. Figures 3a-d shows HRTEM images of PCMO $x=0.1$ recorded in 0.8 Pa H_2O in ETEM taken from the movie M2 at different times. The frame rate of CCD is adjusted to 4 frames per second (fps) which does not capture the entire surface dynamics but enables a sufficient signal to noise ratio to observe atomic contrast. The used frame rate gives only a lower limit to the adatom hopping rate on the surface, as demonstrated in our prior work²⁸. Before we start the in situ observations in H_2O , the surface is fully recrystallized in 1 mbar O_2 (movie M6 and supplementary Figure S7). Movie M1 shows an increased adatom dynamics on the PCMO $x=0.1$ (001) surface in 0.8 Pa H_2O (supplementary Figure S10) compared to O_2 (supplementary Figure S9 and movie M6) or HV (supplementary Figure S8 and movie M9). Interestingly, the disordered surface layer between two crystalline facets shows a more pronounced atom dynamics in the presence of H_2O compared to the ordered facets. This disordered layer does not grow over time. The two crystalline A-site terminated surface facets on each side of the disordered surface region remain stable and retain the perovskite structure even after 11 min. Consequently, PCMO $x=0.1$ does not show irreversible structural degradation in contact with H_2O during the time of observation.

Dynamic PCMO $x=0.33$ - H_2O interface with fast Mn leaching. Figures 3e-h represent a time sequence of HRTEM images of PCMO $x = 0.33$ (001) surface in 0.5 Pa H_2O in ETEM captured from the movies M3, M4, and M5 respectively. Before the study in H_2O , the lamella surface was completely recrystallized in 1 mbar O_2 (Figure 2f and movie M7). In H_2O , the fluctuating B-site atomic columns form a highly dynamic disordered layer on the surface, whereas the A-site subsurface layer remains ordered and stable (Figure 3e and movie M3). Figures 3g and h show the PCMO $x=0.33$ surface after 3 min (movie M4) and 11 min (movie M5) of observation. After 3 min, significant leaching of Mn is already visible by the formation of a cubic Pr-rich bilayer surface. This process continues until the Pr-rich cubic phase forms up to a thickness of 3-4 monolayers (Figure 3h). Previously reported post mortem EELS analysis reveals Pr and O edges, while the Mn L-edge at 640 eV vanished below the noise level.²⁸

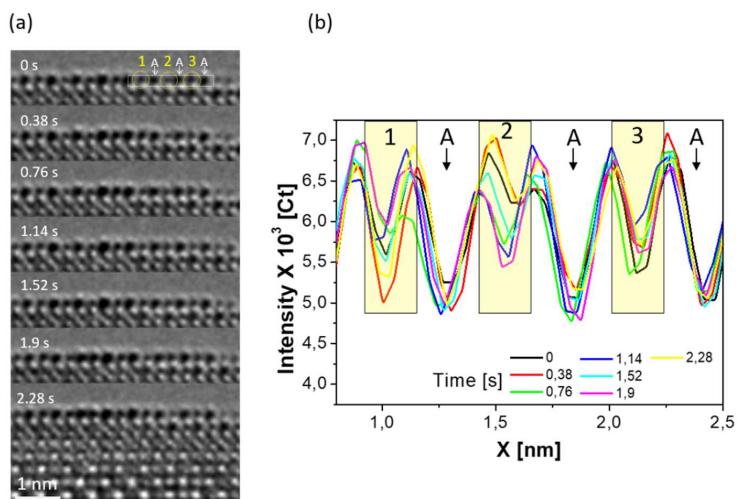


Figure 4. Time sequence of HRTEM images of the PCMO $x=0.1$ (112) surface imaged in [110] zone axis at negative defocus. (a) Series of HRTEM images captured at 3 fps from movie M8. The HRTEM images are recorded in 0.5 Pa of H_2O . At this surface orientation, alternating B and A site columns are observed at the surface. The B column show a temporally fluctuating contrast, whereas the A-column is more stable. (b) Line profile of the top layer at the surface marked by a white dotted rectangle in the 0s HRTEM image in (a). Yellow rectangles in the line profile graph indicate the marked three Mn atomic columns.

Dynamic (112) surface of PCMO 0.1 with oscillating Mn column occupation. Figure 4a shows a time sequence of HRTEM images with a temporally periodic surface reconstruction of a PCMO $x=0.1$ (112) surface facet in 0.5 Pa of H_2O , taken from movie M8. This surface orientation intrinsically has a termination of alternating A- and B-columns. The dynamic surface reconstruction consists of an oscillatory variation of the occupancy of Mn-O columns in [110] direction with Mn and O atoms, where columns become "less occupied" and "filled" again. In contrast, the A columns are more or less stable. Such an oscillatory behavior is absent in high vacuum.

Figure 4b shows the line profile for the area marked by dotted white rectangle in (a). Areas marked by three dotted yellow circles in the line profile indicate the 1, 2, and 3 B-site atomic columns that reveal an oscillating type of behavior in the line profile. Contrary to B-site, A-sites marked by arrow image (a) and in line profile are stable for the 10 min of observation. It is important to note

that we do not observe Mn leaching out of the (112) surface at $x=0.1$. Altogether, the PCMO $x=0.1$ (112) surface, although it is highly dynamic, shows remarkable stability and ordered structure on time scales of several minutes.

Movie M8 gives a larger overview area with mobile Mn atomic columns on the (112) surface. Here, additional dynamics of monolayer step edges of the (112) surface are observed. It displays two different types of atom dynamics: A temporally oscillating surface reconstruction close to the step edges as well as a jumping-like displacement of entire Mn-O atomic columns. Probably, this is related to the B-site atomic columns' fast oscillating behavior.

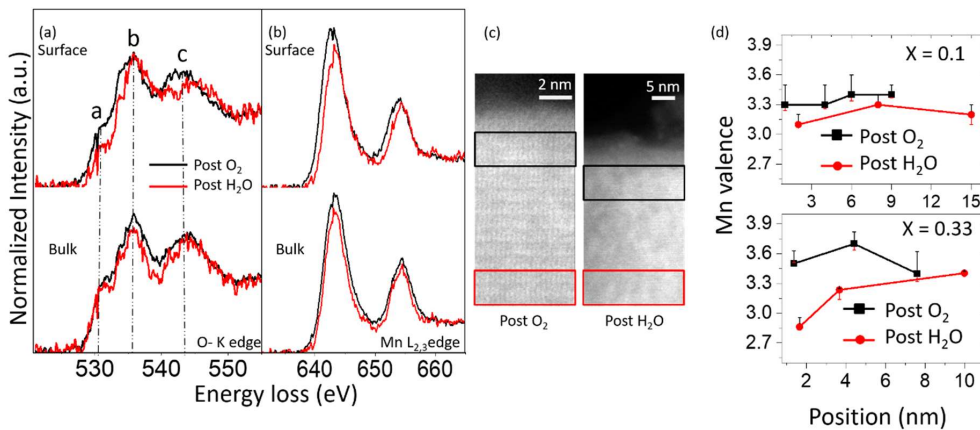


Figure 5. EELS analysis of the Mn L-edge and O K-edge of PCMO $x=0.1$ at the surface and in the bulk in HV imaged after atomic dynamic observations in 100 Pa O₂ and 0.8 Pa H₂O, respectively. The spectra of the oxygen K-edge (a) and Mn L-edge (b) are recorded in the area from the surface (black rectangle) and bulk (red rectangle) shown in the ADF-STEM images (c). Mn L edge show small change after the H₂O treatment at the surface. A slight decrease in the O K prepeak at 531 eV indicates a minor surface reduction. (d) shows that Mn³⁺ valence is retained after contact to the water for $x=0.1$ and significant decrease in Mn valence for $x=0.33$.

Change of the oxidation state close to the surface. Figure 5 shows the electron energy loss spectroscopy (EELS) analysis of the PCMO $x=0.1$ (001) surface. The O K and Mn L-edges are recorded post O₂ (100 Pa) and post H₂O in high vacuum (after removal of O₂ and H₂O from the ETEM). They are taken at the surface (black rectangle) and the bulk (red rectangle) of the TEM lamella, marked in the ADF-STEM image (Figure 5c). All the high loss spectra are energy

calibrated using the corresponding zero-loss peak and then background subtracted as described in the method section. Figure 5a shows the O K-edges that are mainly dominated by the three peaks labeled as a, b, and c and are typical for the perovskite structure. The prepeak at around 530 eV is attributed to the transition from the 1s oxygen core state to empty 2p states which hybridizes with Mn 3d orbitals. Peak b is associated to the A-site 5d orbitals/ B-site 4sp orbitals and peak c is related to transition in the vacuum or due to multiple scattering of electronic excitations.^{46,47}

Figure 5b compares the Mn L₃ and L₂ edges from the surface and bulk of the post O₂ and post H₂O measurements. The energy position of Mn-L edges as well as the intensity ratio of the L₂ and L₃ peaks reflect the Mn valence state in the PCMO x= 0.1 systems. The energy position of Mn-L edges for post O₂ and post H₂O show slight changes at the surface. The tiny shift in the Mn-L edges at the surface in post H₂O indicates decrease in the Mn valence state after the H₂O treatment in the ETEM. This is also demonstrated by calculating Mn valence using the integrated L₃/L₂ ratio as shown in reference.⁴⁸ Both PCMO systems show slightly higher Mn valence in contact to high partial pressure of O₂ (100 Pa) in ETEM. The resulting Mn valence is shown in Figure 5d (top). For x=0.1, it is stable in the bulk and shows a very slight valence decrease from Mn 3.3+ (± 0.26) to Mn 3.1+ (± 0.1) at the surface after contact to H₂O, however, within error range. EELS analysis thus suggests that the oxidation state of Mn is more or less maintained for the x=0.1 sample. This is in good agreement with the preservation of perovskite structure observed in HRTEM images in H₂O. Post mortem EELS analysis after 0.5 Pa H₂O for the PCMO x=0.33 is described in ref.²⁸ Here, the O K prepeak is substantially reduced after the 12 minutes of contact to H₂O. The change in the Mn L edge, L₃/L₂ intensity ratio and calculated Mn valence indicates a significant decrease in the Mn valence close to the surface (~ 2 nm) from 3.5+ (± 0.14) to 2.9+ (± 0.12) after 0.5 Pa H₂O (Figure 5d - bottom).

Figure 6 summarizes the Mn adatom and lattice Mn atomic column dynamics on (001) and (112) PCMO x=0.1 surfaces recorded in [010] and [110] zone axis, respectively. In Figure 6a, the fluctuating dynamics of Mn adatom columns is schematically depicted as suggested by the time series of HRTEM images of the (001) surface of PCMO x=0.1. This is derived from movie M2 and the two HRTEM figures at 0 and 0.7 s right to the scheme. These HRTEM images clearly show fluctuating B site contrast on a stable A site terminated surface. This is most probably due to dynamic Mn adatoms. Figure 6b shows the oscillation of the occupation of an entire lattice Mn atomic column on (112) surface as visible in Figure 4 and in the HRTEM images right to the

scheme in Figure 6b). Such a Mn atomic column dynamics is substantial in H₂O (see supplementary Figure S10) and decreases drastically in HV and O₂ environment (see supplementary Figs. S8 and S9). Both (001) and (112) surfaces thus show highly dynamic Mn species at the surface in the presence of H₂O. These dynamics are reversible in contrast to the leaching behavior of Mn for x=0.33.

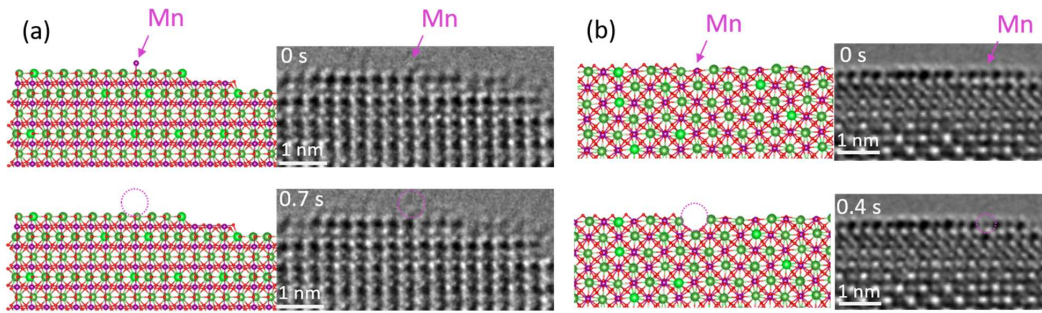


Figure 6. Atomic models and experimental images of the PCMO $x=0.1$ (001) and (112) surfaces, showing different type Mn dynamics, respectively. (a) Atomic model and experimental HRTEM images of (001) surface of PCMO $x=0.1$ in [010] zone axis. (b) (112) surface of PCMO $x=0.1$ in [110] zone axis. Appearance and disappearance of Mn atomic columns are indicated by the pink arrow and dotted circle for both surfaces, respectively.

In the following, we discuss the physical origin of the different behavior of PCMO 0.1 and 0.33. Figure 7a shows EELS spectra of O K edges for PCMO with Ca doping from 0, 0.1, 0.34, 0.5 and 0.95 respectively. There is a strong increase of prepeak ‘a’ intensity and shift to lower energy with increase in Ca doping. These trends are also seen in DFT calculations.⁴⁹ However, these changes cannot be solely attributed to the change of the e_g filling, i.e. Mn valence state. Furthermore, the degree of hybridization between Mn 3d states to O 2p states, i.e., covalence, is also modified. To analyze this effect, the prepeak area ‘a’ in Figure 7a is used to calculate the experimental covalence factor for all the doping levels. After proper background subtraction and normalization, prepeak ‘a’ is integrated from 529 eV to 532 eV and then divided by the change in the valence state.³⁵ All results are then normalized to the value at PCMO $x = 0.5$. Figure 7b shows the result, revealing an increase of hybridization with increasing in Mn valence. The covalence change calculated by the X-ray absorption near edge spectroscopy³⁸ (XANES) shows a similar trend (Figure 7b blue line).

PCMO shows Jahn-Teller polarons at both doping levels, i.e. small polarons that show hopping conductivity.^{50,51} Since acceptor states for electrons from water oxidation are formed by the Jahn-Teller split empty states, i.e., Mn 3d e_g antibonding states, we conclude that also these acceptor states have a small polaron type of character in the studied doping range. Consequently, electrons from water oxidation are rather localized and the degree of localization depends on the covalence. In PCMO $x=0.33$, the higher covalence, i.e., the higher hybridization of Mn 3d and O 2p gives rise to a pronounced Zener polaron physics. Here, Jahn-Teller polarons are ferromagnetically coupled via the oxygen bridge.^{49,52} This has the consequence, that additional electrons in Mn 3d acceptor states can easily reduce lattice oxygen, forming O^- , and even neutral O charge states, which can lead to $O_2(g)$ and pronounced oxygen vacancy formation. In contrast, for PCMO $x=0.1$, such Zener polaron physics is less pronounced, and the additional electrons in the 3d e_g acceptor states can only move between different Mn sites via thermally active polaron hopping.

Thus, despite of the change in the e_g filling, the main difference between the two doping levels is a change in the overlap of the Mn 3d e_g states to the O 2p states. This can be quantified by the covalence factor which is reduced for the $x=0.1$ system compared to $x = 0.33$. Although the atomic structure at the surface is different to the bulk, our argument is relevant, since the subsurface layer is important for acquisition the electrons from surface acceptor states. Furthermore, oxygen vacancy formation in the subsurface is essential for the observed irreversible processes of Mn reduction and leaching in the $x=0.33$ system.

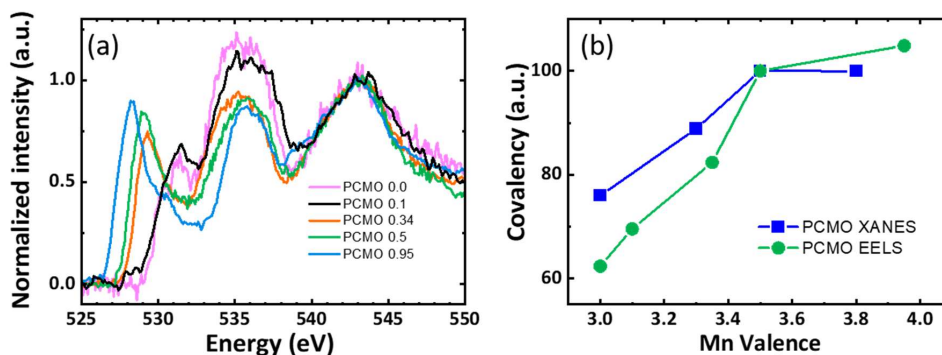


Figure 7. (a) EELS of the O K-edge of PCMO $x= 0 - 0.95$ thin film lamella, respectively. (b) Covalence analysis calculated from EELS analysis and X-ray absorption spectroscopy of the O K edge as a function of Mn valence.

3. CONCLUSION

In summary, we discovered distinct behaviour of manganite (001) surfaces for OER with different A-site doping. As more extensively analysed in previous work,²⁸ PCMO $x=0.33$ shows formation of Mn^{2+} species which can leach out of the electrode surface. This is due to subsurface oxygen vacancy formation. The resulting reduced Mn species have a high solubility in H_2O . In contrast, O K and Mn L edges in EELS analysis confirm the stable Mn valence at the PCMO $x=0.1$ (001) surface. We have repeated the experiments on the formation of Pr rich cubic phase at the subsurface of PCMO $x=0.33$ system which is fully consistent to the results in ref.²⁸

Similar to cobaltates, where the enhancement in the TM 3d – O 2p covalence facilitates the charge transfer between the occupied O 2p and unoccupied TM 3d states and increase OER activity^{34,53}, the PCMO $x=0.33$ system shows higher initial OER activity. However, it experiences fast corrosion on the surface and thus represents an unstable system for OER. In contrast, PCMO $x=0.1$ (001) and (112) surfaces show pronounced reversible Mn surface dynamics in H_2O . These surfaces possess a higher stability both in ETEM as well in RRDE studies under conditions that facilitate surface reduction, i.e., in O_2 -poor environments and at moderate anodic polarisation. In particular, the in-situ ETEM experiments do not reveal any hint of irreversible Mn leaching out of the PCMO $x=0.1$ interface to H_2O .

Even though PCMO does not belong to the top catalyst for OER, this study gives new insights about the role of covalence factor and charge localization. Charge localization in e_g acceptor states due to polaron formation is not itself detrimental to electrode stability, which depends on hybridisation to O 2p states. The latter facilitates lattice oxygen reduction and subsequent vacancy formation. Thus, this phenomenon can lead to the local reduction of the surface Mn. Remarkably, high stability and high activity is observed for the (La,Sr) MnO_3 system in the ferromagnetic metallic state, where acceptor states are delocalized to varying degrees.^{28,44} Here, electrons from H_2O oxidation form band-like carriers and lattice oxygen reduction is absent. This suggests that perovskite oxides with simultaneously high activity and stability are based on the requirement that oxidation of lattice oxygen due to a strong covalence of localized charges needs to be avoided. In the case of PCMO $x=0.1$, localized Mn 3d e_g charges due to small polaron formation have a lower overlap to the O 2p states reflected by the smaller covalency.

4. EXPERIMENTAL SECTION

4.1 Thin film fabrication: $\text{Pr}_{0.9}\text{Ca}_{0.1}\text{MnO}_3$ (and $\text{Pr}_{0.7}\text{Ca}_{0.3}\text{MnO}_3$) films were prepared by ion-beam sputtering (IBS). In a first step, a $\text{La}_{0.6}\text{Sr}_{0.4}\text{MnO}_3$ (LSMO) layer of 21(2) nm thickness was deposited at 750 °C onto disc-shaped 0.5 wt % Nb-doped SrTiO_3 (STNO) substrates with (100)-orientation (CrysTec GmbH, Berlin, Germany). In a second step, $\text{Pr}_{1-x}\text{Ca}_x\text{MnO}_3$ films were sputtered at 650 °C without exposing to air. The chamber contained 3×10^{-4} mbar Ar and 1.6×10^{-4} mbar O_2 as the reactive gas. Supplementary Figure 2 confirms the epitaxial growth of both films. Film thicknesses were measured by X-ray reflectometry (XRR).

4.2 Electrochemistry: The electrochemical measurements are performed in a bipotentiostat setup of Interface 1000E potentiostats (Gamry Instruments Inc., Warminster, PA, USA) and an RRDE-3A rotator (ALS Co. Ltd., Tokyo, Japan). The PCMO|NSTO electrodes are prepared for the RRDE disc electrode with a diameter of 4 mm and a Pt ring electrode with an inner diameter of 5 mm and an outer diameter of 7 mm. All electrochemical reactions are performed in 0.1 M KOH electrolyte. Electrolyte solution is prepared by diluting KOH stock solution (Sigma Aldrich, Munich, Germany) with deionized water (MilliQ, >16.5 M Ω). The 0.1 M KOH electrolyte was saturated with Argon (Ar) gas at least 30 min before measurements and continuously purged with Ar during the measurements. Electrode potentials were converted to the reversible hydrogen electrode (RHE) scale using $E_{\text{RHE}} = E_{\text{applied}} + E_{\text{ref}}$, where $E_{\text{ref}} = 0.993$ V vs. SCE is obtained from the hydrogen evolution using a clean Pt disc. The measured potentials are corrected for the ohmic resistance extracted from the impedance spectroscopy measurement prior to measurement. Cyclic voltammograms are measured at 10 mV/s with rotation of 1600 rpm.

4.3 Environmental TEM experiments: In-situ Environmental Transmission Electron Microscopy experiments are performed using FEI Titan ETEM G2, 80-300 kV. A Cs-corrector and Gatan Image filter (GIF) Quantum 965ER facilities are attached to the microscope for the superior HRTEM imaging and EELS spectroscopy respectively. A Gatan UltraScan 1000XP CCD was used to collect movies with frame rate between 3 and 4 frames per second (fps) in 512 x 512 pixels for PCMO $x=0.33$ and 1024 x 1024 pixels for PCMO $x=0.1$ respectively. ETEM is used to capture movies in HV (high vacuum $\sim 10^{-5}$ Pa) with cold trap to reduce H_2O partial pressure in the octagon, 100 Pa O_2 and 0.5 – 1 Pa of H_2O . All time sequenced HRTEM movies are recorded at a beam current of 4 nA and beam diameter between 80 and 100 nm, therefore local electron dose rates at the location of TEM lamella surfaces calculated by calibrated CCD contrast with 0.16696

electrons/counts yields in between 8,000 – 15,000 $e/\text{\AA}^2\text{s}$ for HV, O₂ and H₂O surface studies respectively.

4.4 Electron energy loss spectroscopy (EELS): The EELS analysis is carried out using Gatan Quantum 965ER post-column energy filter in the ETEM. Mn L and O K edges are recorded using 0.1 eV/ch dispersion in post 1 mbar O₂ and post 8 μbar H₂O. Background is subtracted using power-law background functions from Gatan's Digital Micrograph are fitted to a 50 eV wide window before each Mn L-edge and 25 eV for O K-edge respectively. EELS analysis and discussion for PCMO $x=0.33$ can be found in the ref.²⁸

4.5 Method of Mn Valence analysis: Mn valence is calculating by Mn L₃/L₂ integrated intensity ratio using the similar method described in detail by M. Varela et al.⁴⁸ A 50 eV wide window is used in power-law background (inbuilt Gatan DM function) to fit before each Mn L₃-edge. A Hartree-Slater (HS) type cross-section step function (in Gatan Digital Micrograph) is used for subtracting the background inside the L₃ and L₂ edges. The HS step function removes continuum background contribution of a 10 eV window immediately after the L₂ edge. The high loss spectra is calibrated using the energy calibration of the zero loss peak. The error bars are determined by performing the integration of L₃ and L₂ edges by shifting the integration windows by ± 1 eV.

4.6 TEM lamella preparation: TEM lamellae for PCMO $x=0.1$ is prepared from epitaxially grown (001) oriented thin films by Focused Ion Beam lift-out technique using a noble metal free protection layer and careful low energy ion milling for the preparation of ultrathin lamella. Supplementary Figure S6 shows the before and after thinning steps of PCMO $x=0.1$ TEM lamella. The lamella preparation is followed by the method explained for the lamella preparation of PCMO $x=0.33$ in ref.²⁸ The Ar ion milling (Precision Ion Polishing System (PIPS II) Gatan, Inc) is used for fine thinning and surface cleaning with 0.3 KeV beam energy and 24.13 μA beam current with only one stationary beam and stage rotation off (Stage tilt $\pm 5^\circ$). As reported earlier^{28, 42} the damaged perovskite structure by FIB and PIPS can be recrystallized in high partial pressure of O₂ in ETEM. The PCMO $x=0.1$ reduced surface is recrystallized in 1 mbar O₂ in the ETEM. Supplementary Figure 7 and movie M6 shows recrystallization process of PCMO $x=0.1$ (001) surface.

4.7 Image simulations: The multi-slice HRTEM image simulation for both PCMO system shown in Figure 2 d and h is performed with QSTEM⁴⁵ using a crystal model in which the placement of the mixed A-site atoms, i.e., Pr and Ca, is done column by column. For each atomic site, a Pr atom

is set if the fraction of all previously set atoms exceeds the doping concentration x . A Ca atom is placed otherwise. This way, agglomeration of A-site atoms of the same kind are avoided in each column and the resulting A-site contrasts are rather homogeneous matching the experimental observations.

To approximate the experimental conditions for PCMO $x=0.33$, a small image section is extracted from the experimental data close to the surface and the sample thickness as well as the lens aberrations (including defocus, spherical aberration, two-fold astigmatism and axial coma) are fitted by minimizing the root mean square difference between experimental and simulated images. The Metropolis method is employed as minimization algorithm and the virtual temperature is decreased exponentially as a function of the iteration step. PCMO $x = 0.33$ crystal model creation as well as fitting procedure were already reported and used in ref.²⁸

The main goal of this work is to understand the contrast difference between A and B site atomic columns. Therefore, only thickness and defocus parameters are used for the PCMO $x = 0.1$ system. The (001) surface is simulated without lens aberrations parameters (Figure 2d). The resultant image adequately provides a contrast difference between A-site (Pr/Ca - O) and B-site (Mn-O) atomic columns. The resulting electron optical parameters and sample thickness are noted in table 1.

Parameters	Fit PCMO ($x=0.33$)	Fit PCMO ($x=0.1$)
C1 -Defocus	-63 Å	-40 Å
A1-Two fold Astigmatism	68.09 Å	0 Å
A1 angle	2.41 rad	0 rad
Cs -spherical aberration	-15817.58 Å	0 Å
B2-Axial coma	8639 Å	0 Å
Thickness	4.3 nm	4.3 nm
Focal spread	100 Å	100 Å

Table 1: Electron optical parameters as obtained by fitting of simulated to experimental images.

ASSOCIATED CONTENT

Supporting Information

AFM images of as grown epitaxial PCMO $x=0.1$ (001) and (b) PCMO $x=0.3$ (001) thin films; Logarithmically plotted XRD of epitaxially grown PCMO $x=0.1$ and $x=0.3$ thin films; Cyclic voltammograms of thin films disc and the corresponding ring current; Chronoamperometric measurements at different applied potentials as a function of time in Argon saturated electrolyte; Chronoamperometric measurements at different applied potentials as a function of time in O_2 saturated electrolyte; TEM lamella preparation; HRTEM images of the as prepared and recrystallized surface; Time sequenced HRTEM frames in HV; Time sequenced HRTEM frames in O_2 ; Time sequenced HRTEM frames in H_2O

Supporting movies

Movie	Material	Environment	Pressure (Pascal)	Frame rate (fps)	What can be seen in the movie
M01	$Pr_{0.9}Ca_{0.1}MnO_3$	H_2O	0.8	4	Dynamic surface in contact to H_2O
M02	$Pr_{0.9}Ca_{0.1}MnO_3$	H_2O	0.8		Mn adatoms fluctuations on stable A-site terminated surface
M03	$Pr_{0.67}Ca_{0.33}MnO_3$	H_2O	0.5		Perovskite structure in the beginning
M04	$Pr_{0.67}Ca_{0.33}MnO_3$	H_2O	0.5		Slow Mn leaching from top layer
M05	$Pr_{0.67}Ca_{0.33}MnO_3$	H_2O	0.5		Pronounced leaching of Mn from the surface.
M06	$Pr_{0.9}Ca_{0.1}MnO_3$	O_2	100		Highly ordered surface
M07	$Pr_{0.67}Ca_{0.33}MnO_3$	O_2	100		Highly ordered surface
M08	$Pr_{0.9}Ca_{0.1}MnO_3$	H_2O	0.5		Oscillatory behavior of Mn atomic columns
M09	$Pr_{0.9}Ca_{0.1}MnO_3$	High vacuum	2×10^{-5}		Mixed surface termination

AUTHOR INFORMATION

Corresponding Author

Christian Jooss - Institute of Materials Physics, University of Goettingen, Friedrich-Hund-Platz 1, 37077 Goettingen, Germany; International Center for Advanced Studies of Energy Conversion (ICASEC), University of Goettingen, D-37077 Goettingen, Germany; <https://orcid.org/0000-0002-8762-9359>

Email: cjooss@gwdg.de

Authors

Gaurav Lole - Institute of Materials Physics, University of Goettingen, Friedrich-Hund-Platz 1, 37077 Goettingen, Germany; International Center for Advanced Studies of Energy Conversion (ICASEC), University of Goettingen, D-37077 Goettingen, Germany; <https://orcid.org/0000-0001-9227-8752>

Fatemeh Ebrahimi - Institute of Materials Physics, University of Goettingen, Friedrich-Hund-Platz 1, 37077 Goettingen, Germany; <https://orcid.org/0000-0002-2532-5691>

Tobias Meyer - Institute of Materials Physics, University of Goettingen, Friedrich-Hund-Platz 1, 37077 Goettingen, Germany; <https://orcid.org/0000-0003-3191-0376>

Daniel Mierwaldt - Institute of Materials Physics, University of Goettingen, Friedrich-Hund-Platz 1, 37077 Goettingen, Germany

Vladimir Roddatis - Institute of Materials Physics, University of Goettingen, Friedrich-Hund-Platz 1, 37077 Goettingen, Germany; present adress: Helmholtz-Zentrum Potsdam Deutsches GeoForschungsZentrum GFZ, Telegrafenberg 14473, Potsdam, Germany; <https://orcid.org/0000-0002-9584-0808>

Janis Geppert - Institute of Materials Physics, University of Goettingen, Friedrich-Hund-Platz 1, 37077 Goettingen, Germany; present address: Institute for Applied Materials – Electrochemical Technologies, Karlsruhe Institute of Technology, Adenauerring 20b, 76131 Karlsruhe; <https://orcid.org/0000-0002-9991-2725>

Marcel Risch - Institute of Materials Physics, University of Goettingen, Friedrich-Hund-Platz 1, 37077 Goettingen, Germany; Helmholtz-Zentrum Berlin für Materialien und Energie GmbH, Young Investigator Group Oxygen Evolution Mechanism Engineering, 14109 Berlin, Germany; <https://orcid.org/0000-0003-2820-7006>

Notes

All relevant data are available from the corresponding author on request.

The authors declare no competing interests.

Acknowledgements

This work is financially funded by the DFG 217133147/SFB 1073 project C02. The "Collaborative Laboratory and User Facility for Electron Microscopy" (CLUE) at the University of Goettingen is acknowledged for the instrument's support.

References

- (1) Liu, D.; Zhou, P.; Bai, H.; Ai, H.; Du, X.; Chen, M.; Liu, D.; Fai Ip, W.; Ho Lo, K.; Tat Kwok, C.; Chen, S.; Wang, S.; Xing, G.; Wang, X.; Pan, H.; Liu, D.; Zhou, P.; Bai, H.; Chen, M.; Chen, S.; Wang, S.; Xing, G.; Pan, H.; Ai, H.; Du, X.; Lo, K. H.; Kwok, C. T.; Ip, W. F.; Wang, X. Development of Perovskite Oxide-Based Electrocatalysts for Oxygen Evolution Reaction. *Small* **2021**, *17* (43), 2101605. <https://doi.org/10.1002/SMLL.202101605>.
- (2) She, S.; Zhu, Y.; Tahini, H. A.; Hu, Z.; Weng, S.-C.; Wu, X.; Chen, Y.; Guan, D.; Song, Y.; Dai, J.; Smith, S. C.; Wang, H.; Zhou, W.; Shao, Z. A Molecular-Level Strategy to Boost the Mass Transport of Perovskite Electrocatalyst for Enhanced Oxygen Evolution. *Appl. Phys. Rev.* **2021**, *8* (1), 011407. <https://doi.org/10.1063/5.0033912>.
- (3) Edgington, J.; Schweitzer, N.; Alayoglu, S.; Seitz, L. C. Constant Change: Exploring Dynamic Oxygen Evolution Reaction Catalysis and Material Transformations in Strontium Zinc Iridate Perovskite in Acid. *Cite This J. Am. Chem. Soc* **2021**, *143*, 9961–9971. <https://doi.org/10.1021/jacs.1c04332>.
- (4) Fu, G.; Li, W.; Zhang, J.-Y.; Li, M.; Li, C.; Li, N.; He, Q.; Xi, S.; Qi, D.; MacManus-Driscoll, J. L.; Cheng, J.; Zhang, K. H. Facilitating the Deprotonation of OH to O through Fe⁴⁺-Induced States in Perovskite LaNiO₃ Enables a Fast Oxygen Evolution Reaction. *Small* **2021**, *17* (12), 2006930. <https://doi.org/10.1002/SMLL.202006930>.
- (5) Man, I. C.; Su, H. Y.; Calle-Vallejo, F.; Hansen, H. A.; Martínez, J. I.; Inoglu, N. G.; Kitchin, J.; Jaramillo, T. F.; Nørskov, J. K.; Rossmeisl, J. Universality in Oxygen Evolution Electrocatalysis on Oxide Surfaces. *ChemCatChem* **2011**, *3*, 1159–1165. <https://doi.org/10.1002/cctc.201000397>.
- (6) Porokhin, S. V.; Nikitina, V. A.; Aksyonov, D. A.; Filimonov, D. S.; Pazhetnov, E. M.; Mikheev, I. V.; Abakumov, A. M. Mixed-Cation Perovskite La_{0.6}Ca_{0.4}Fe_{0.7}Ni_{0.3}O_{2.9} as a Stable and Efficient Catalyst for the Oxygen Evolution Reaction. **2021**. <https://doi.org/10.1021/acscatal.1c00796>.
- (7) Retuerto, M.; Pascual, L.; Piqué, O.; Kayser, P.; Salam, M. A.; Mokhtar, M.; Alonso, J. A.; Peña, M.; Calle-Vallejo, F.; Rojas, S. How Oxidation State and Lattice Distortion Influence the Oxygen Evolution Activity in Acid of Iridium Double Perovskites. *J. Mater. Chem. A* **2021**, *9* (5), 2980–2990. <https://doi.org/10.1039/D0TA10316K>.
- (8) Quinn Carvalho, O.; Adiga, P.; Wang, L.; Liu, J.; Jia, E.; Du, Y.; Nemšák, S.;

- Stoerzinger, K. A. Probing Adsorbates on La $1-x$ Sr x NiO $3-\delta$ Surfaces under Humid Conditions: Implications for the Oxygen Evolution Reaction. *J. Phys. D Appl. Phys. J. Phys. D Appl. Phys.* **2021**, *54* (13pp), 274003. <https://doi.org/10.1088/1361-6463/abf674>.
- (9) Yun, T. G.; Heo, Y.; Bin Bae, H.; Chung, S.-Y. Elucidating Intrinsic Contribution of D-Orbital States to Oxygen Evolution Electrocatalysis in Oxides. *Nat. Commun. 2021 121* **2021**, *12* (1), 1–11. <https://doi.org/10.1038/s41467-021-21055-0>.
- (10) Lin, Y.; Tian, Z.; Zhang, L.; Ma, J.; Jiang, Z.; Deibert, B. J.; Ge, R.; Chen, L. Chromium-Ruthenium Oxide Solid Solution Electrocatalyst for Highly Efficient Oxygen Evolution Reaction in Acidic Media. *Nat. Commun.* **2019**, *10* (1). <https://doi.org/10.1038/s41467-018-08144-3>.
- (11) Reier, T.; Nong, H. N.; Teschner, D.; Schlögl, R.; Strasser, P. Electrocatalytic Oxygen Evolution Reaction in Acidic Environments – Reaction Mechanisms and Catalysts. *Advanced Energy Materials.* 2017. <https://doi.org/10.1002/aenm.201601275>.
- (12) Escalera-López, D.; Czióska, S.; Geppert, J.; Boubnov, A.; Röse, P.; Saraçi, E.; Krewer, U.; Grunwaldt, J. D.; Cherevko, S. Phase- And Surface Composition-Dependent Electrochemical Stability of Ir-Ru Nanoparticles during Oxygen Evolution Reaction. *ACS Catal.* **2021**, *11* (15), 9300–9316. <https://doi.org/10.1021/acscatal.1c01682>.
- (13) Ledendecker, M.; Geiger, S.; Hengge, K.; Lim, J.; Cherevko, S.; Mingers, A. M.; Göhl, D.; Fortunato, G. V.; Jalalpoor, D.; Schüth, F.; Scheu, C.; Mayrhofer, K. J. J. Towards Maximized Utilization of Iridium for the Acidic Oxygen Evolution Reaction. *Nano Res.* **2019 129** **2019**, *12* (9), 2275–2280. <https://doi.org/10.1007/S12274-019-2383-Y>.
- (14) She, Z. W.; Kibsgaard, J.; Dickens, C. F.; Chorkendorff, I.; Nørskov, J. K.; Jaramillo, T. F. Combining Theory and Experiment in Electrocatalysis: Insights into Materials Design. *Science (80-)*. **2017**, *355* (6321). <https://doi.org/10.1126/science.aad4998>.
- (15) Song, F.; Bai, L.; Moysiadou, A.; Lee, S.; Hu, C.; Liardet, L.; Hu, X. Transition Metal Oxides as Electrocatalysts for the Oxygen Evolution Reaction in Alkaline Solutions: An Application-Inspired Renaissance. *J. Am. Chem. Soc.* **2018**, *140* (25), 7748–7759. <https://doi.org/10.1021/JACS.8B04546>.
- (16) Roger, I.; Shipman, M. A.; Symes, M. D. Earth-Abundant Catalysts for Electrochemical and Photoelectrochemical Water Splitting. *Nat. Rev. Chem.* **2017 11** **2017**, *1* (1), 1–13. <https://doi.org/10.1038/s41570-016-0003>.
- (17) Zhao, J.-W.; Shi, Z.-X.; Li, C.-F.; Gu, L.-F.; Li, G.-R. Boosting the Electrocatalytic Performance of NiFe Layered Double Hydroxides for the Oxygen Evolution Reaction by Exposing the Highly Active Edge Plane (012). *Chem. Sci.* **2021**, *12* (2), 650–659. <https://doi.org/10.1039/D0SC04196C>.
- (18) Yin, W.-J.; Weng, B.; Ge, J.; Sun, Q.; Li, Z.; Yan, Y. Oxide Perovskites, Double Perovskites and Derivatives for Electrocatalysis, Photocatalysis, and Photovoltaics. *Energy Environ. Sci.* **2019**, *12* (2), 442–462. <https://doi.org/10.1039/C8EE01574K>.
- (19) Wang, W.; Xu, M.; Xu, X.; Zhou, W.; Shao, Z. Perovskite Oxide Based Electrodes for High-Performance Photoelectrochemical Water Splitting. *Angew. Chemie Int. Ed.* **2020**, *59* (1), 136–152. <https://doi.org/10.1002/ANIE.201900292>.
- (20) Zhao, J.-W.; Shi, Z.-X.; Li, C.-F.; Ren, Q.; Li, G.-R. Regulation of Perovskite Surface Stability on the Electrocatalysis of Oxygen Evolution Reaction. **2021**. <https://doi.org/10.1021/acsmaterialslett.1c00018>.
- (21) Dong, F.; Li, L.; Kong, Z.; Xu, X.; Zhang, Y.; Gao, Z.; Dongyang, B.; Ni, M.; Liu, Q.; Lin, Z. Materials Engineering in Perovskite for Optimized Oxygen Evolution Electrocatalysis in Alkaline Condition. *Small* **2021**, *17* (2). <https://doi.org/10.1002/SMLL.202006638>.

- (22) Nguyen, T. X.; Liao, Y.-C.; Lin, C.-C.; Su, Y.-H.; Ting, J.-M. Advanced High Entropy Perovskite Oxide Electrocatalyst for Oxygen Evolution Reaction. *Adv. Funct. Mater.* **2021**, *31* (27), 2101632. <https://doi.org/10.1002/ADFM.202101632>.
- (23) Peng, M.; Huang, J.; Zhu, Y.; Zhou, H.; Hu, Z.; Liao, Y.-K.; Lai, Y.-H.; Chen, C.-T.; Chu, Y.-H.; Zhang, K. H. L.; Fu, X.; Zuo, F.; Li, J.; Sun, Y. Structural Anisotropy Determining the Oxygen Evolution Mechanism of Strongly Correlated Perovskite Nickelate Electrocatalyst. **2021**. <https://doi.org/10.1021/acssuschemeng.1c00596>.
- (24) Chen, Y.; Li, H.; Wang, J.; Du, Y.; Xi, S.; Sun, Y.; Sherburne, M.; Ager, J. W.; Fisher, A. C.; Xu, Z. J. Exceptionally Active Iridium Evolved from a Pseudo-Cubic Perovskite for Oxygen Evolution in Acid. *Nat. Commun.* **2019**, *10* (1), 1–10. <https://doi.org/10.1038/s41467-019-08532-3>.
- (25) Risch, M.; Grimaud, A.; May, K. J.; Stoerzinger, K. A.; Chen, T. J.; Mansour, A. N.; Shao-Horn, Y. Structural Changes of Cobalt-Based Perovskites upon Water Oxidation Investigated by EXAFS. *J. Phys. Chem. C* **2013**, *117* (17), 8628–8635. <https://doi.org/10.1021/JP3126768>.
- (26) May, K. J.; Carlton, C. E.; Stoerzinger, K. A.; Risch, M.; Suntivich, J.; Lee, Y. L.; Grimaud, A.; Shao-Horn, Y. Influence of Oxygen Evolution during Water Oxidation on the Surface of Perovskite Oxide Catalysts. *J. Phys. Chem. Lett.* **2012**, *3* (22), 3264–3270. <https://doi.org/10.1021/JZ301414Z>.
- (27) Fabbri, E.; Nachttegaal, M.; Binniger, T.; Cheng, X.; Kim, B. J.; Durst, J.; Bozza, F.; Graule, T.; Schäublin, R.; Wiles, L.; Pertoso, M.; Danilovic, N.; Ayers, K. E.; Schmidt, T. J. Dynamic Surface Self-Reconstruction Is the Key of Highly Active Perovskite Nano-Electrocatalysts for Water Splitting. *Nat. Mater.* **2017**, *16* (9), 925–931. <https://doi.org/10.1038/nmat4938>.
- (28) Lole, G.; Roddatis, V.; Ross, U.; Risch, M.; Meyer, T.; Rump, L.; Geppert, J.; Wartner, G.; Blöchl, P.; Jooss, C. Dynamic Observation of Manganese Adatom Mobility at Perovskite Oxide Catalyst Interfaces with Water. *Commun. Mater.* **2020**, *1* (1), 68. <https://doi.org/10.1038/s43246-020-00070-6>.
- (29) Yoo, J. S.; Rong, X.; Liu, Y.; Kolpak, A. M. Role of Lattice Oxygen Participation in Understanding Trends in the Oxygen Evolution Reaction on Perovskites. *ACS Catal.* **2018**, *8* (5), 4628–4636. <https://doi.org/10.1021/ACSCATAL.8B00612>.
- (30) Grimaud, A.; Diaz-Morales, O.; Han, B.; Hong, W. T.; Lee, Y.-L.; Giordano, L.; Stoerzinger, K. A.; Koper, M. T. M.; Shao-Horn, Y. Activating Lattice Oxygen Redox Reactions in Metal Oxides to Catalyze Oxygen Evolution. *Nat. Chem.* **2017**, *9* (5), 457–465. <https://doi.org/10.1038/nchem.2695>.
- (31) Man, I. C.; Su, H. Y.; Calle-Vallejo, F.; Hansen, H. A.; Martínez, J. I.; Inoglu, N. G.; Kitchin, J.; Jaramillo, T. F.; Nørskov, J. K.; Rossmeisl, J. Universality in Oxygen Evolution Electrocatalysis on Oxide Surfaces. *ChemCatChem* **2011**, *3* (7), 1159–1165. <https://doi.org/10.1002/CCTC.201000397>.
- (32) Suntivich, J.; May, K. J.; Gasteiger, H. A.; Goodenough, J. B.; Shao-Horn, Y. A Perovskite Oxide Optimized for Oxygen Evolution Catalysis from Molecular Orbital Principles. *Science (80-.)*. **2011**, *334* (6061), 1383–1385. <https://doi.org/10.1126/SCIENCE.1212858>.
- (33) Zhang, Y.; Sun, Y.-F.; Luo, J.-L.; Kim, B.; Fabbri, E.; Antipin, D.; Risch, M. Trends of Epitaxial Perovskite Oxide Films Catalyzing the Oxygen Evolution Reaction in Alkaline Media. *J. Phys. Energy* **2020**, *2* (3), 032003. <https://doi.org/10.1088/2515-7655/AB812F>.
- (34) Heymann, L.; Weber, M. L.; Wohlgemuth, M.; Risch, M.; Dittmann, R.; Baeumer, C.; Gunkel, F. Separating the Effects of Band Bending and Covalency in Hybrid Perovskite

- Oxide Electrocatalyst Bilayers for Water Electrolysis. *ACS Appl. Mater. Interfaces* **2022**, *14* (12), 14129–14136. <https://doi.org/10.1021/ACSAMI.1C20337>.
- (35) Abrishami, M. E.; Risch, M.; Scholz, J.; Roddatis, V.; Osterthun, N.; Jooss, C. Oxygen Evolution at Manganite Perovskite Ruddlesden-Popper Type Particles: Trends of Activity on Structure, Valence and Covalence. *Mater. 2016, Vol. 9, Page 921* **2016**, *9* (11), 921. <https://doi.org/10.3390/MA9110921>.
- (36) Song, J.; Wei, C.; Huang, Z.-F.; Liu, C.; Zeng, L.; Wang, X.; Xu, Z. J. A Review on Fundamentals for Designing Oxygen Evolution Electrocatalysts. *2196 | Chem. Soc. Rev* **2020**, *49*, 2196. <https://doi.org/10.1039/c9cs00607a>.
- (37) Raabe, S.; Mierwaldt, D.; Ciston, J.; Uijtewaal, M.; Stein, H.; Hoffmann, J.; Zhu, Y.; Blöchl, P.; Jooss, C. In Situ Electrochemical Electron Microscopy Study of Oxygen Evolution Activity of Doped Manganite Perovskites. *Adv. Funct. Mater.* **2012**, *22*, 3378–3388.
- (38) Mierwaldt, D.; Mildner, S.; Arrigo, R.; Knop-Gericke, A.; Franke, E.; Blumenstein, A.; Hoffmann, J.; Jooss, C. In Situ XANES/XPS Investigation of Doped Manganese Perovskite Catalysts. *Catalysts* **2014**, *4* (2), 129–145. <https://doi.org/10.3390/catal4020129>.
- (39) Forslund, R. P.; Hardin, W. G.; Rong, X.; Abakumov, A. M.; Filimonov, D.; Alexander, C. T.; Mefford, J. T.; Iyer, H.; Kolpak, A. M.; Johnston, K. P.; Stevenson, K. J. Exceptional Electrocatalytic Oxygen Evolution via Tunable Charge Transfer Interactions in $\text{La}_{0.5}\text{Sr}_{1.5}\text{Ni}_{1-x}\text{Fe}_x\text{O}_{4\pm\delta}$ Ruddlesden-Popper Oxides. *Nat. Commun.* **2018**, *9* (1), 1–11. <https://doi.org/10.1038/s41467-018-05600-y>.
- (40) Crozier, P. A.; Hansen, T. W. In Situ and Operando Transmission Electron Microscopy of Catalytic Materials. *MRS Bull.* **2015**, *40* (1), 38–45. <https://doi.org/10.1557/MRS.2014.304>.
- (41) Mildner, S.; Beleggia, M.; Mierwaldt, D.; Hansen, T. W.; Wagner, J. B.; Yazdi, S.; Kasama, T.; Ciston, J.; Zhu, Y.; Jooss, C. Environmental TEM Study of Electron Beam Induced Electrochemistry of $\text{Pr}_{0.64}\text{Ca}_{0.36}\text{MnO}_3$ Catalysts for Oxygen Evolution. *J. Phys. Chem. C* **2015**, *119*, 5301–5310.
- (42) Roddatis, V.; Lole, G.; Jooss, C. In Situ Preparation of $\text{Pr}_{1-x}\text{Ca}_x\text{MnO}_3$ and $\text{La}_{1-x}\text{Sr}_x\text{MnO}_3$ Catalysts Surface for High-Resolution Environmental Transmission Electron Microscopy. *Catalysts* **2019**, *9*(9), 751.
- (43) Crozier, P. A.; Chenna, S. In Situ Analysis of Gas Composition by Electron Energy-Loss Spectroscopy for Environmental Transmission Electron Microscopy. *Ultramicroscopy* **2011**, *111* (3), 177–185. <https://doi.org/10.1016/J.ULTRAMIC.2010.11.005>.
- (44) Scholz, J.; Risch, M.; Stoerzinger, K. A.; Wartner, G.; Shao-Horn, Y.; Jooss, C. Rotating Ring-Disk Electrode Study of Oxygen Evolution at a Perovskite Surface: Correlating Activity to Manganese Concentration. *J. Phys. Chem. C* **2016**, *120* (49), 27746–27756. <https://doi.org/10.1021/ACS.JPCC.6B07654>.
- (45) Koch, C. Determination of Core Structure Periodicity and Point Defect Along Dislocations. **2002**, Ph.D. Thesis, Arizona State University, Tempe, AZ,.
- (46) Kurata, H.; Colliex, C. Electron-Energy-Loss Core-Edge Structures in Manganese Oxides. *Phys. Rev. B* **1993**. <https://doi.org/10.1103/PhysRevB.48.2102>.
- (47) Du, G. H.; Yuan, Z. Y.; Van Tendeloo, G. Transmission Electron Microscopy and Electron Energy-Loss Spectroscopy Analysis of Manganese Oxide Nanowires. *Appl. Phys. Lett.* **2005**, *86* (6). <https://doi.org/10.1063/1.1861963>.
- (48) Varela, M.; Oxley, M. P.; Luo, W.; Tao, J.; Watanabe, M.; Lupini, A. R.; Pantelides, S. T.; Pennycook, S. J. Atomic-Resolution Imaging of Oxidation States in Manganites. *Phys.*

- Rev. B - Condens. Matter Mater. Phys.* **2009**, *79*, 085117.
<https://doi.org/10.1103/PhysRevB.79.085117>.
- (49) Sotoudeh, M.; Rajpurohit, S.; Blöchl, P.; Mierwaldt, D.; Norpoth, J.; Roddatis, V.; Mildner, S.; Kressdorf, B.; Iffland, B.; Jooss, C. Electronic Structure of Pr_{1-x}Ca_xMnO₃. *Phys. Rev. B* **2017**, *95*, 235150.
- (50) Hoffmann, J.; Moschkau, P.; Mildner, S.; Norpoth, J.; Jooss, C.; Wu, L.; Zhu, Y. Effects of Interaction and Disorder on Polarons in Colossal Resistance Manganite Pr_{0.68}Ca_{0.32}MnO₃ Thin Films. *Mater. Res. Express* **2014**, *1*, 46403. <https://doi.org/10.1088/2053-1591/1/4/046403>.
- (51) Kressdorf, B.; Meyer, T.; Brink, M.; Seick, C.; Melles, S.; Ottinger, N.; Titze, T.; Meer, H.; Weisser, A.; Hoffmann, J.; Mathias, S.; Ulrichs, H.; Steil, D.; Seibt, M.; Blöchl, P. E.; Jooss, C. Orbital-Order Phase Transition in $\text{Pr}_{1-x}\text{Ca}_x\text{MnO}_3$. *Phys. Rev. B* **2021**, *103* (23), 235122. <https://doi.org/10.1103/PhysRevB.103.235122>.
- (52) Raiser, D.; Mildner, S.; Iffland, B.; Sotoudeh, M.; Blöchl, P.; Techert, S.; Jooss, C. Evolution of Hot Polaron States with a Nanosecond Lifetime in a Manganite Perovskite. *Adv. Energy Mater.* **2017**, *7* (12), 1602174. <https://doi.org/10.1002/AENM.201602174>.
- (53) Zhou, Y.; Sun, S.; Song, J.; Xi, S.; Chen, B.; Du, Y.; Fisher, A. C.; Cheng, F.; Wang, X.; Zhang, H.; Xu, Z. J.; Zhou, Y.; Sun, S.; Song, J.; Chen, B.; Zhang, H.; Xu, Z. J.; Xi, S.; Du, Y.; Fisher, A. C.; Cheng, F.; Wang, X. Enlarged Co-O Covalency in Octahedral Sites Leading to Highly Efficient Spinel Oxides for Oxygen Evolution Reaction. *Adv. Mater.* **2018**, *30* (32), 1802912. <https://doi.org/10.1002/ADMA.201802912>.

Chapter 7

Atomistic insights into activation
and degradation of
 $\text{La}_{0.6}\text{Sr}_{0.4}\text{CoO}_{3-\sigma}$ electrocatalysts
under oxygen evolution conditions

Atomistic insights into activation and degradation of $\text{La}_{0.6}\text{Sr}_{0.4}\text{CoO}_{3-\delta}$ electrocatalysts under oxygen evolution conditions

Moritz L. Weber^{a,f,*}, Gaurav Lole^{b,c}, Attila Kormanyos^d, Alexander Schwiers^{a,§}, Lisa Heymann^a, Florian D. Speck^{d,e}, Tobias Meyer^b, Regina Dittmann^a, Serhiy Cherevko^d, Christian Jooss^{b,c}, Christoph Baeumer^{a,f} and Felix Gunkel^{a,*}

^aPeter Grünberg Institute (PGI-7) and JARA-FIT, Forschungszentrum Jülich GmbH, Jülich, 52425, Germany; Institute of Materials Physics, ^bUniversity of Göttingen, Göttingen, 37077, Germany; ^cInternational Center for Advanced Studies of Energy Conversion (ICASEC), University of Göttingen, Göttingen, 37077, Germany; ^dHelmholtz-Institute Erlangen-Nürnberg for Renewable Energy (IEK-11), Forschungszentrum Jülich GmbH, Erlangen, 91058, Germany; ^eDepartment of Chemical and Biological Engineering, Friedrich-Alexander-Universität Erlangen-Nürnberg, Erlangen, 91058, Germany; ^fMESA+ Institute for Nanotechnology, University of Twente, Faculty of Science and Technology, Enschede, 7500 AE, The Netherlands

*Email: mo.weber@fz-juelich.de; f.gunkel@fz-juelich.de

ABSTRACT: The stability of perovskite oxide catalysts for the oxygen evolution reaction (OER) plays a critical role for their applicability in water splitting concepts. Decomposition of perovskite oxides under applied potential is typically linked to cation leaching and amorphization of the material. However, structural changes and phase transformations at the catalyst surface were also shown to govern the activity of several perovskite electrocatalysts under applied potential. Hence, it is crucial for the rational design of durable perovskite catalysts to understand the interplay between the formation of active surface phases and stability limitations under OER conditions. In the present study, we reveal a surface-dominated activation and deactivation mechanism of the prominent electrocatalyst $\text{La}_{0.6}\text{Sr}_{0.4}\text{CoO}_{3-\delta}$ under steady-state OER conditions. Using a multi-scale microscopy and spectroscopy approach, we identify evolving Co-oxyhydroxide as catalytically active surface species and La-hydroxide as inactive species involved in the transient degradation behavior of the catalyst. While the leaching of Sr results in the formation of mixed surface phases, that can be considered as a part of the active surface, the gradual depletion of Co from a self-assembled active $\text{CoO}(\text{OH})$ phase and the relative enrichment of passivating $\text{La}(\text{OH})_3$ at the electrode surface results in the failure of the perovskite catalyst under applied potential.

INTRODUCTION

Active and durable energy materials are key to establish a sustainable energy management based on efficient devices for the production, conversion and storage of chemical fuels based on renewable energy, much needed to abandon climate-damaging fossil fuels.¹⁻³ Essentially, the sluggish oxygen evolution reaction (OER) thwarts the implementation of water splitting concepts for the production of hydrogen. To overcome this limitation, the exceptional catalytic activity of perovskite oxides for the OER has stimulated the discussion about the intrinsic properties responsible for the high catalytic performance of this material class for many years.⁴⁻⁷ Here, the attention increasingly lies on the processes at the topmost surface

and in the near-surface region of the oxide catalysts, which influence the catalytic activity of perovskite materials.⁸⁻¹² Besides activity, the stability of perovskite electrocatalysts in alkaline media and under applied potential is highly debated since high robustness is crucial for their applicability in energy devices.^{4,10,11,13,14} Numerous studies have indicated that electrocatalysts undergo surface reconstructions and chemical transformations under OER conditions, that may be related to the transformation of the perovskite surface toward an active, dynamic state but also to detrimental processes leading to irreversible degradation. Here, leaching of cations^{11,15-20} as well as structural modifications such as amorphization^{11,15,17,18,21-25} and even complete decomposition of oxide catalysts^{26,27} were observed and linked to

changes in the catalysts' activity. At the same time, recent studies have shown that surface-near phase transitions may play a key role in the catalytic process.^{8,12,28}

Hence it is apparent that surface phase transformations can trigger catalytic activity, but also are involved in the aging of catalysts. The link between these processes however remains unresolved to date. Therefore, a holistic view on both, activity and stability of perovskite OER catalysts, with respect to dynamic surface processes involved in the oxygen evolution reaction is needed, to develop strategies to overcome the stability limitations of active perovskite electrocatalysts. Epitaxial model catalysts offer a high level of control in material properties and thus attracted much attention for the study of catalytic processes at well-defined perovskite surfaces.^{11,12,14,26,29-32} In the present study, we identify active species at the surface of LSCO at the atomic scale and provide a detailed understanding of the potential-driven, dynamic processes at the solid-liquid interface under OER conditions that result in the formation of Co-oxhydroxide as active surface species and La-hydroxide as inactive passivation layer. Our findings link the transformation of the crystalline perovskite catalyst towards mixed chemical phases in the near-surface region to the degradation behavior of LSCO during operation in alkaline media.

RESULTS

Catalyst efficacy and lifetime at increased OER reaction rates. The electrochemical performance of the 20 nm thick epitaxial LSCO electrocatalysts was characterized in 0.1 M KOH using a rotating disk setup. Details on the sample preparation can be found in the experimental section and reference (26). Figure 1a shows representative cyclic voltammetry data, where an iR corrected potential of $E = 1.66 \pm 0.01$ V vs. RHE was determined at a current density of $j = 1.0$ mA·cm⁻² based on the average value obtained from three different samples. A representative Nyquist-plot, obtained by electrochemical impedance spectroscopy (EIS) at open circuit potential is shown as inset image. Furthermore, Tafel analysis was performed by consecutive steady-state galvanostatic holds at different current densities as displayed in Figure 1b. The Tafel plot derived from averaged values obtained from three samples is given in Figure 1c with a Tafel slope of $\partial V/\partial \log(j) \sim 88$ mV/dec which is in

good agreement with the literature.^{33,34} All LSCO layers hence show high OER activity comparable to the best-in-class perovskite catalyst.

To evaluate the stability, i.e. the lifetime, of the LSCO electrocatalysts during OER operation, chronopotentiometry was performed at different current densities. Here, the oxygen evolution reaction is driven under steady-state conditions (constant reaction rate) until the deactivation of the LSCO thin film electrodes is evident from a rapid increase in overpotential. All samples used for lifetime testing experienced equal electrochemical treatment before the respective galvanostatic measurements. A detailed description of the measurement protocol is given in the experimental section. The end of lifetime represents a sudden loss of the OER activity. Increasing lifetimes are observed for decreasing current densities, ranging between 0.6 - 19.5 hours in the current density range between $j = 1.0$ - 10.0 mA·cm⁻² (Figure 1d). Notably, the lifetime measurement of epitaxial LSCO at $j = 0.1$ mA·cm⁻² remained stable for >200 h and did not reach the end of its lifetime during the measurement time (denoted by asterisk). The investigation of the potential-dependent catalyst lifetime reveals substantial, though considerably varying stability of the epitaxial thin film electrodes of only 20 nm thickness. As can be seen, the lifetime shows a pronounced non-linear trend for LSCO catalysts operated at different current densities (Figure 1e, left). Similarly, the total charge Δq , indicative of the total amount of oxygen generated during the catalyst life, strongly depends on the applied potential (Figure 1e, right). This results in pronounced differences in the efficiency of the catalysts depending on the operation conditions, where low reaction rates at the catalyst surface lead to higher stability, while high current densities and high potentials result in rapid catalyst deactivation. Consequently, dynamic processes need to be considered to gain fundamental understanding of the degradation behavior of LSCO electrocatalysts.

Surface-dominated catalyst deactivation under steady-state OER operation. After steady-state operation of the epitaxial LSCO model electrodes until the end of lifetime, the formation of island-like structures is visible at the initially smooth surface, which exhibits a distinct step terrace structure in the pristine state (Figure 2a). In spite of the severe morphologic changes, X-ray diffraction analysis (XRD) in 2θ - ω measurement geometry reveals only minor changes in the bulk properties of the thin film catalysts, reflected by a slight broadening of the thin film diffrac-

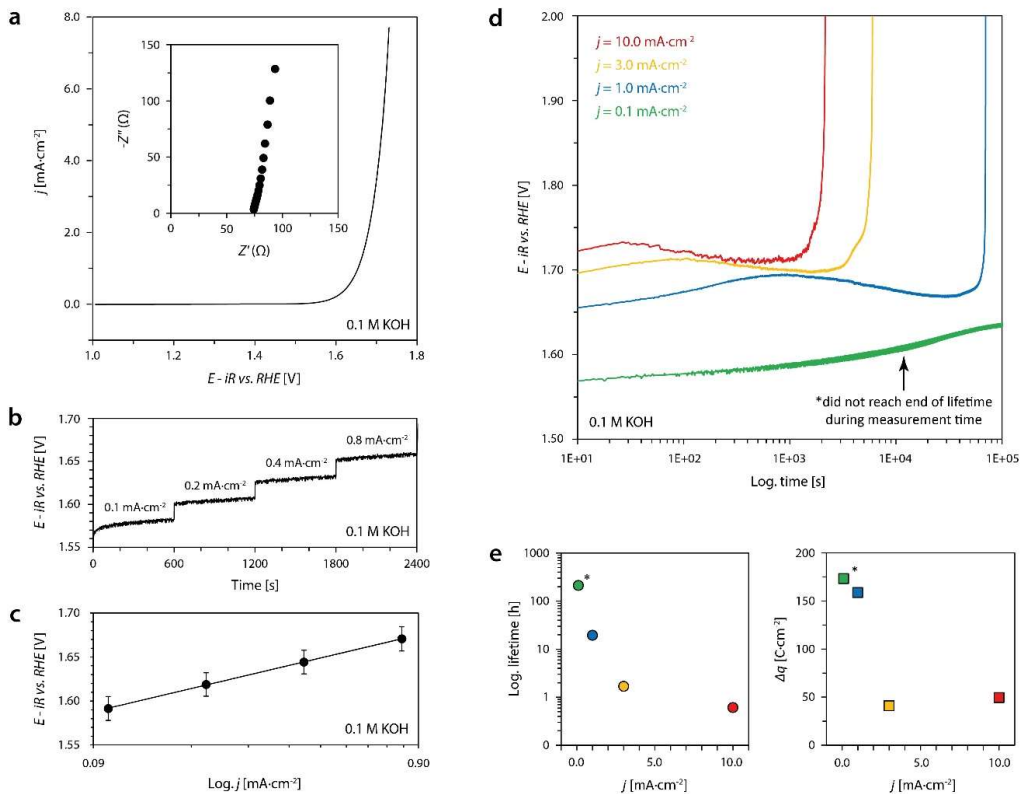


Figure 1. Electrochemical performance of 20 nm epitaxial (001) LSCO thin films catalyzing the oxygen evolution reaction (OER). (a) Averaged forward and reverse scans of the second cycle of cyclic voltammetry measurements; the inset image shows the Nyquist-plot obtained by electrochemical impedance spectroscopy. (b) Steady-state measurement of four consecutive galvanostatic holds. (c) Tafel-plot obtained from steady-state galvanostatic measurements; error bars represent the standard deviation of average values obtained by the measurement of three different samples. (d) Chronopotentiometric measurements for the characterization of the LSCO stability on the basis of the catalyst lifetimes at different applied current densities. Abrupt increase of potential denotes the end of lifetime. (e) Plot of the lifetimes (left) and the respective transferred charge (right) depending on the applied current density determined based on the data shown in (d), visualizing a strong non-linearity i.e. potential dependence of the catalyst deactivation.

tion peak and a slight shift of the peak position towards lower diffraction angles (Figure 2b). Reciprocal space mapping confirms a slight expansion of the *c*-lattice parameter, while the strain state is preserved as evident from the constant *a*-lattice parameter (Figure 2c).

These rather marginal changes in the bulk properties however, are unlikely to explain the complete deactivation of the catalysts. In fact, it demonstrates the high dissolution stability of the epitaxial thin film catalysts in steady-state operation mode. Nevertheless, a slight decrease in thickness of the crystalline LSCO layer can be observed from the XRD analysis that indicates a loss of the structural order of the perovskite

material in the near-surface region. The degradation zone can be estimated to be about ~ 1 nm in depth for thin film electrodes operated at high current densities of $j = 10.0 \text{ mA}\cdot\text{cm}^{-2}$ based on the periodicity of the thickness oscillations. After operation at lower current densities, the degradation depth was found to be slightly increased to several nanometers, which is consistent with an increased amount of transferred charge in the low potential regime (cf. Figure 1e). The lifetime of LSCO electrocatalysts under steady-state operation at increased current densities, therefore, might be rather determined by a surface-dominated deactivation mechanism than a bulk process.

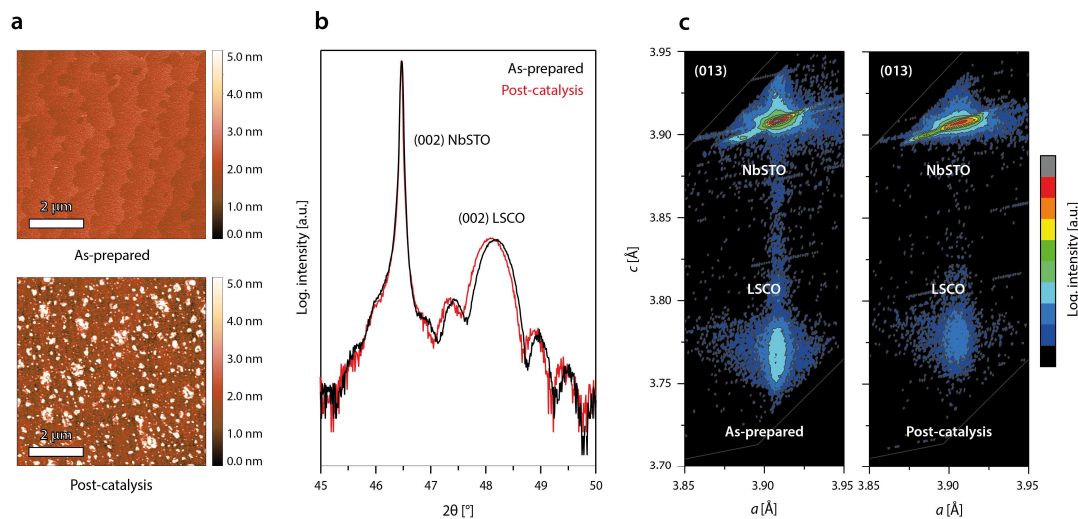


Figure 2. (a) Representative atomic force microscopy (AFM) images of a LSCO thin film comparing the morphology in the as-prepared state and after the end of lifetime (operated at $j = 10.0 \text{ mA}\cdot\text{cm}^{-2}$). (b) X-ray diffraction 2θ - ω analysis reveals a high crystallinity and similar thickness of the catalyst layers in the as-prepared and the post-catalysis state. (c) X-ray diffraction in reciprocal space mapping geometry around the asymmetric (013) reflections confirms minor expansion in the thin film c -lattice parameter, while epitaxial strain is found to be preserved after electrochemical operation (constant a -lattice parameter).

In contrast, bulk degradation and amorphization of the entire catalytic thin films was reported under repeated dynamic cycling.²⁶ The decreased amorphization rate under steady-state operation conditions in comparison to dynamic operation conditions during commonly applied potential cycling like cyclic voltametry is consistent with the observations of May et al.¹⁵ However, the limitation of structural changes to the topmost surface during steady-state operation at relatively increased current densities associated with the accelerated failure of the electrocatalysts is surprising.

Surface mobility of cobalt moieties promotes activity and surface disorder. To elucidate the atomistic details of the catalytic OER process, we investigated the LSCO samples under near-OER conditions using environmental transmission electron microscopy (ETEM), which allows to study the catalyst surface in direct contact to water adsorbates. The experimental details and the lamella preparation procedure followed the routines established in references^{35,36} and are described in the methods section. After a recrystallization procedure of the FIB lamella in O_2 atmosphere (cf. Figure S1), an atomically sharp surface is obtained, ideal for atomic-resolution studies of surface processes at the solid-liquid interface (Figure 3a). The surface is well ordered and exhibits

a sharp A-site termination, which remains stable in O_2 environment (cf. Figure S2 and movie M1 attached in the SI). Here, the experimentally observed atomic ordering is well-comparable to a simulated image of the LSCO surface structure (Figure 3b), which indicates a predominant A-site termination of the as-prepared (001) perovskite electrocatalyst, consistent with a typically observed A-site enriched surface. In order to investigate the LSCO surface structure under near-OER conditions, the imaging environment is switched from O_2 to H_2O conditions, which results in the condensation of a thin water layer at the perovskite surface. In addition, the incident electron beam induces an anodic potential to the sample, leading to effective near-OER conditions. A time sequence of HR-ETEM images of the interface recorded in 0.5 Pa of H_2O is shown in Figure 3c, which reveals dynamical changes of the surface structure that occur within the timespan of seconds to minutes after exposure to the water environment. Here, the presence of dynamic adatoms on top of the ordered A-site terminated surface is observed (white arrows at $t = 0.5 \text{ s}$). Based on the emerging contrast and their location at specific B-sites of the extended perovskite lattice, they are attributed as Co species. They can form dynamic active sites at the solid-liquid interface under anodic

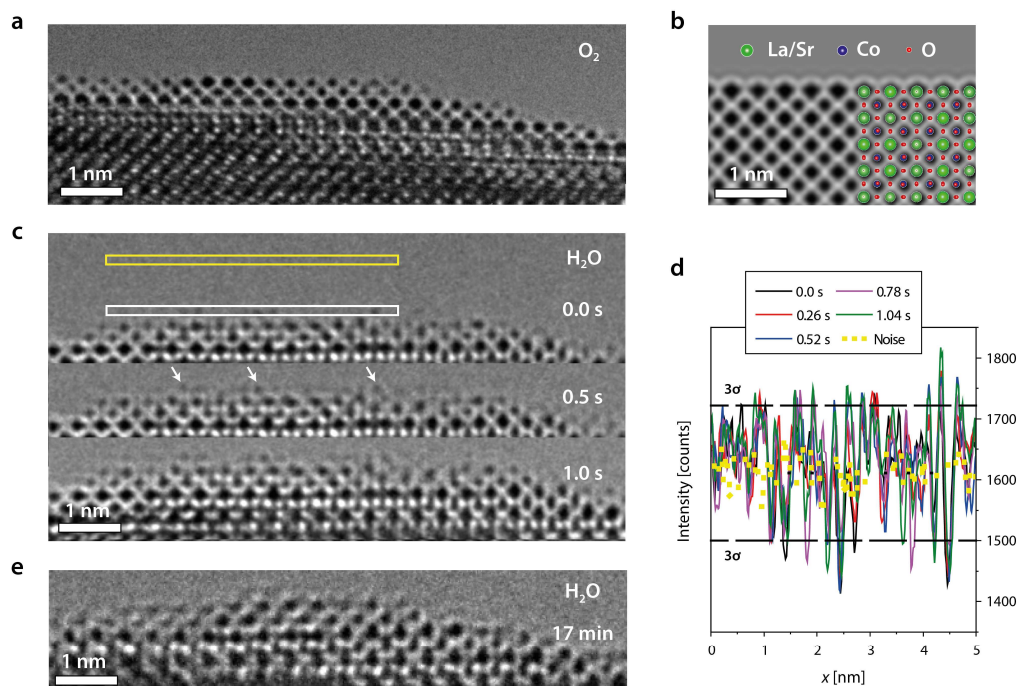


Figure 3. Observation of the dynamic LSCO (001) surface by ETEM. (a) The surface of the as-prepared LSCO lamella is atomically sharp and exhibits A-site termination in O_2 environment. (b) A simulated image of a LSCO (001) surface shows atomic contrast, that is consistent with the experimentally obtained HRTEM image. A superimposed structural model illustrates the atomic positions of Sr, La, Co and O. (c) Representative images of a time sequence (4 fps) demonstrate the LSCO surface dynamics in 0.5 Pa of H_2O . Highly mobile adatoms are detected at the solid-liquid interface under near-OER conditions, which appear at the B-site positions of the extended perovskite surface. White arrows highlight several exemplary Co adatoms. (d) Line profiles are recorded close above the A-site terminated surface as indicated by the white rectangle in (c) to quantitatively evaluate the hopping events. The noise level is determined above the sample (yellow rectangle) and the 3σ threshold is calculated from the noise signal, which indicates the detection limit of Co adatoms. Intensity fluctuations above 3σ level indicate the presence of highly mobile adatoms at the interface between the electrocatalysts and the condensed water layer. (e) A structural transformation of the crystalline LSCO surface region towards a disordered layer is detected under near-OER conditions. The image was recorded after imaging under anodic polarization for 17 min in 7 Pa of H_2O .

polarization of the OER catalyst. As these ionic processes occur on very short timescales in comparison to the catalysts lifetimes they are likely to play a key role for the catalyst activity. At the same time, they might affect the atomistic processes responsible for catalyst degradation.

The high mobility of the adatoms is further illustrated by line profiles shown in Figure 3d, extracted right above the topmost A-site column at the solid-liquid interface. The background fluctuations of the CCD signal are recorded in the vacuum region above the surface as a reference and yields the standard deviation 3σ which defines the noise level of the measurements. Each signal above the 3σ -level hence indicates the appearance and disappearance of dynamic Co

moieties at the catalyst surface. The hopping rate, i.e. the presence of active Co species at the LSCO surface was detected to be increased in H_2O environment by a factor of eight (cf. Figure S2). The increased mobility of Co cations results in transient changes of the surface structure, indicative of the degradation process associated to the evolution of the initially atomically sharp surface towards a disordered and Co-rich surface layer at the catalyst-electrolyte interface as can be seen in Figure 3e (cf. movie M3). The surface reconstruction that includes displacements and mixing of A- and B-site cations along the disordered surface was observed to be accelerated by higher partial pressures of H_2O . Consistently, imaging in 0.5 Pa of

H₂O results in a slow formation of a disordered surface layer (Figure S3a), while at 11 Pa of H₂O, a fast formation of the disordered surface is observed (Figure S3b and movie M4). Here, the disordered surface layer exhibits a thickness of about ~1 nm, well-comparable to the degradation zone detected by XRD after OER operation at high current densities (cf. Figure 2b, c).

OER activity is typically directly linked to the local electronic structure at the active catalyst surface. Therefore, electron energy-loss spectroscopy (EELS) is performed to investigate the evolution of the electronic structure of the LSCO catalysts under near-OER conditions. The O-K-edge and Co-L-edge spectra are acquired in the surface region of the catalyst as well as in the bulk (Figure 4a). The formation of a disordered surface layer under near-OER conditions is associated to gradual changes in the electronic signature towards the surface (Figure 4b,c). The O-K-edge exhibits three characteristic peaks denoted as (1), (2), and (3). Here, the pre-peak (1) is attributed to the hybridization of the O 2*p* states with the Co 3*d* states and indicates the presence of O 2*p* holes, while the peaks (2) and (3) represent transitions into hybridized O 2*p* - Co 4*sp* states.^{37,38} The decrease in the height of the pre-peak (1) obtained in the topmost atomic layers after operation of the sample at near-OER conditions indicates the decrease in the average Co valence state³⁹,

which furthermore is in good agreement with the apparent shift in the Co-L-edge towards lower energies.

This observation is consistent with the change in the intensity ratio of the Co-L₃/Co-L₂ signals, that is sensitive to the valence state of transition metals, where the average cation valence decreases with an increasing Co-L₃/Co-L₂ intensity ratio.³⁷ As can be seen, the ratio is generally increased after treatment at near-OER conditions, which indicates a reduction of the average oxidation state of Co cations.⁴⁰ Moreover, a distinct increase of the Co-L₃/Co-L₂ intensity ratio is visible with decreasing distance to the topmost surface (Figure 4c), which further emphasizes that the electronic changes evident by EELS appear to be interrelated to the surface processes driven under near-OER conditions. In comparison, only a small decrease in the intensity but no change in the spectral shape or shift in the peak position is detected for the La-M-edge spectra in the surface region (Figure S4).

Evolution of the surface chemistry from perovskite towards mixed phases. To link the structural evolution and electronic changes at the perovskite electrode surface upon OER operation with compositional changes in the near-surface region, a combined approach of on-line inductively coupled plasma mass spectrometry (ICP-MS) for the investigation of the leaching behavior and angle-dependent X-ray photoelectron spectroscopy (XPS) analysis for probing the electrode surface region is applied (Figure 5). On-line

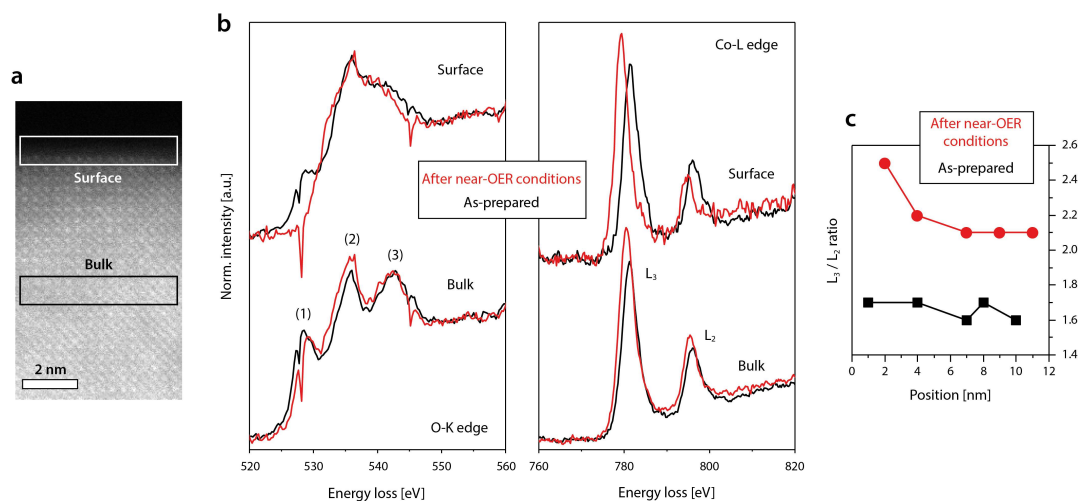


Figure 4. Electron energy loss spectroscopy. EELS analysis is performed in the as-prepare state (O₂) and after near-OER conditions after transfer to vacuum (1 x 10⁻⁵ Pa) of the LSCO catalyst. (a) The measurement position is varied between the surface and the subsurface region of the lamella as highlighted by the white (surface) and the black (bulk) rectangles denoted in the ADF-STEM image. (b) O-K-edge and Co-L-edge spectra recorded by EELS. (c) Plot of the Co-L₃/Co-L₂ intensity ratio versus the sampling position, where 1 corresponds to the topmost surface. A systematic increase in the Co-L₃/Co-L₂ ratio after near-OER conditions indicates a decrease of the average oxidation state of Co towards the catalyst surface. The spectra are background subtracted and energy calibrated using the corresponding zero-loss peak.

ICP-MS is performed to determine the rate of cation dissolution under electrochemical bias in real-time, enabling immediate tracking of dissolved catalyst constituents. The contact between the LSCO thin film electrodes and the scanning flow cell (SFC) setup was established under 1.0 V vs. RHE applied potential, followed by a first galvanostatic hold at different current densities of $j_1 = 0.1 \text{ mA}\cdot\text{cm}^{-2}$, $j_1 = 0.3 \text{ mA}\cdot\text{cm}^{-2}$ or $j_1 = 1.0 \text{ mA}\cdot\text{cm}^{-2}$. The duration of each galvanostatic hold was set to yield identical charge passed (1800 s, 600 s and 180 s, respectively, $\Delta q = 0.18 \text{ C}$). Each measurement protocol was finished with a second galvanostatic hold at $j_2 = 2.25 \text{ mA}\cdot\text{cm}^{-2}$. This protocol was chosen to test the electrochemical stability under different potentials and to correlate chemical leaching rates with the respective OER reaction rates (via j).

Throughout the measurements, only the dissolution of strontium was detected with generally low dissolution rates, which indicates a selective leaching of Sr cations from the A-sites. Here, the first significant dissolution feature is typically observed during the potentiostatic hold prior to switching to the galvanostatic holds. This feature is related to the dissolution of minor Sr-rich secondary phases, which are commonly present at the LSCO surface and is visible when the contact between the scanning flow cell is established with the LSCO electrode surface (cf. Figure S5).^{41,42} Figure 5a compares the detected Sr dissolution rate for the three different measurement protocols. Here, a small transient decay in Sr dissolution is observed independent from applied potential owing to a long tail of the initial contact peak, while dis-

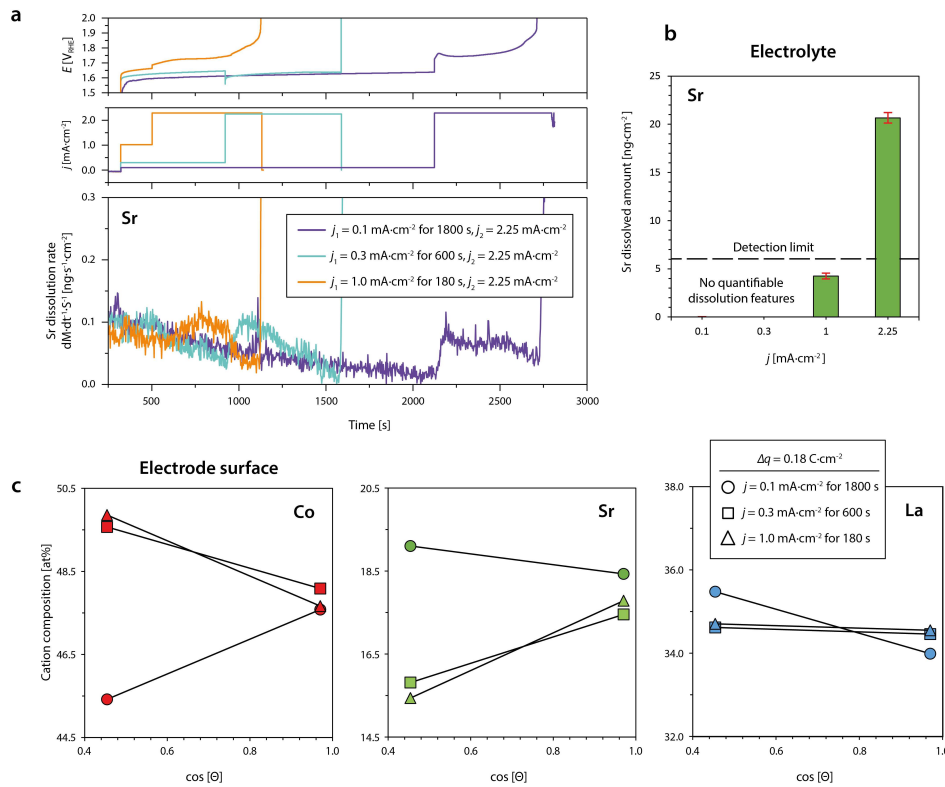


Figure 5. Investigation of stoichiometric changes of LSCO electrocatalysts during steady-state OER operation. (a) Chemical analysis of the electrolyte by on-line ICP-MS measurements. The dissolution rate of Sr is monitored during three different measurement protocols. For the systematic investigation of Sr dissolution at different current densities, two galvanostatic holds are applied during each measurement protocol, respectively ($j_1 = 0.1 \text{ mA}\cdot\text{cm}^{-2}$, $j_1 = 0.3 \text{ mA}\cdot\text{cm}^{-2}$ or $j_1 = 1.0 \text{ mA}\cdot\text{cm}^{-2}$ and $j_2 = 2.25 \text{ mA}\cdot\text{cm}^{-2}$). (b) The dissolved amounts of Sr is determined for the galvanostatic holds at different current densities. Error bars represent the standard deviation of average values obtained from three measurements, each performed on a fresh catalyst surface. (c) Angle-dependent XPS analysis of the surface stoichiometry after OER operation in the low potential regime similar to the conditions used during on-line ICP-MS. The depletion of strontium and the enrichment of cobalt is detected for catalysts operated at $j = 0.3 \text{ mA}\cdot\text{cm}^{-2}$ and $j = 1.0 \text{ mA}\cdot\text{cm}^{-2}$. XPS analysis was performed at a photoemission angle $\Theta = 15^\circ$ (less surface-sensitive) and $\Theta = 64^\circ$ (more surface-sensitive).

tinct dissolution features are only visible for potential steps that result in increased current densities. Interestingly, a potential-dependent leaching behavior is evident as summarized in Figure 5b, where Sr dissolution is only detectable during OER operation at a current density $j_1 \geq 1.0 \text{ mA}\cdot\text{cm}^{-2}$ yielding around $4.3 \text{ ng}\cdot\text{cm}^{-2}$. Here, the dissolution rate increases in a transient manner and slowly decays until the end of the hold. While qualitatively a dissolution feature can be observed at $j_1 = 1.0 \text{ mA}\cdot\text{cm}^{-2}$, the calculated dissolved amount of Sr needs to be taken with care at these operation conditions since the value is below the nominal detection limit of the on-line ICP-MS system.

Galvanostatic holds at a current density of $j_2 = 2.25 \text{ mA}\cdot\text{cm}^{-2}$ however, are accompanied with increased Sr dissolution rates and a total amount of dissolved Sr of about $20.7 \pm 0.5 \text{ ng}\cdot\text{cm}^{-2}$, $25.1 \pm 5.0 \text{ ng}\cdot\text{cm}^{-2}$ and $21.7 \pm 5.8 \text{ ng}\cdot\text{cm}^{-2}$. Similarly to the dissolution feature detected at lower current density ($j_1 = 1.0 \text{ mA}\cdot\text{cm}^{-2}$), Sr dissolution rapidly increases during the potential step. Each experiment was finished when the contact was lost due to vigorous bubble formation at the working electrode surface, blocking the channels of the SFC. Independent from the specific measurement protocol, the deactivation of the LSCO sample (contact loss) occurred when similar amounts of Sr (approx. $25 \text{ ng}\cdot\text{cm}^{-2}$) leached from the crystal lattice for all measurement protocols applied. Our results are consistent with precedent literature data, where the authors observed increased Sr leaching with increasing Sr-substitution at the A-site of the perovskite lattice. Remarkably, the authors found that Sr dissolution in LSCO is coupled to the dissolution of small amounts of cobalt.⁴³

The again non-linear dependence of the dissolution rate on the applied current density indicates that OER catalysis driven at higher current densities promotes the preferential leaching of A-site strontium cations with a higher rate, consistent with the non-linear behavior of lifetime and charge (Figure 1e). To further characterize the degradation of the LSCO electrocatalyst samples, stability-numbers (S numbers) were calculated, which directly correlate to the amount of dissolved metal species (here strontium) with the passed anodic current (the amount of evolved O_2 ²⁰). The obtained S-numbers (1.59×10^5 , 1.26×10^5 , 1.54×10^5 for the holds at $2.25 \text{ mA}\cdot\text{cm}^{-2}$ and 9.62×10^4 for the galvanostatic hold at $1 \text{ mA}\cdot\text{cm}^{-2}$) are in the range of 10^5 , which is close to the values observed for example, for metallic Ir²⁰ (1.0×10^5), Ir_{0.7}Sn_{0.3}O_x⁴⁴ (1.6×10^5) and SrIrO₃ thin films²⁰ (8.0×10^4), investigated in acidic media. Overall, the high S-number of our LSCO thin films indicate high stability of the investigated LSCO

perovskite electrocatalyst sample in the $j = 1.0 - 2.25 \text{ mA}\cdot\text{cm}^{-2}$ current density range similar to the chemical stability of the most common oxide catalysts applied in acidic media.

To correlate the dissolution behavior with stoichiometric changes at the electrode surface, angle-dependent XPS analysis is performed (Figure 5c). Here, the relative cation composition of the electrode surface is determined after transfer of an equal amount of charge during OER at different current densities of $j = 0.1 \text{ mA}\cdot\text{cm}^{-2}$, $j = 0.3 \text{ mA}\cdot\text{cm}^{-2}$ and $j = 1.0 \text{ mA}\cdot\text{cm}^{-2}$. Large photoemission angles Θ allow for the detection of surface-near signals (mean escape depth $d \sim 0.6 \text{ nm}$ for Co $2p_{3/2}$) while smaller photoemission angles result in the detection of photoelectrons originating from larger information depth (mean escape depth $d \sim 1.3 \text{ nm}$ for Co $2p_{3/2}$). As can be seen, the surface of the LSCO model electrodes remain predominantly A-site terminated when operated at low current densities of $j = 0.1 \text{ mA}\cdot\text{cm}^{-2}$ (cf. Figure S6 for as-prepared state). After operation at higher current densities of $j = 0.3 \text{ mA}\cdot\text{cm}^{-2}$ and $j = 1.0 \text{ mA}\cdot\text{cm}^{-2}$ we observe a relative increase of the cobalt signal and decrease of the strontium signal for small Θ while the lanthanum signal exhibits only minor changes. In contrast, the relative cation composition appears to remain unchanged in the (buried) near-surface region of the perovskite catalyst (large Θ).

Consistent with our on-line ICP-MS measurements Sr depletion is promoted at high current densities, which evidently is accompanied by an enrichment of cobalt at the LSCO surface. The XPS investigations reveal, however, that stoichiometric changes at the electrode surface are induced even at low current densities $j < 1.0 \text{ mA}\cdot\text{cm}^{-2}$, while Sr dissolution was detected by on-line ICP-MS only during operation at $j \geq 1.0 \text{ mA}\cdot\text{cm}^{-2}$. Here, the small dissolution rate of Sr may prevent its detection by time-resolved ICP-MS analysis.

Identification of mixed surface phases. To understand the nature of the chemical changes at the LSCO surface during steady-state OER conditions, galvanostatic holds at $j = 1.0 \text{ mA}\cdot\text{cm}^{-2}$ and $j = 10.0 \text{ mA}\cdot\text{cm}^{-2}$ are applied and XPS core-level spectra of the as prepared LSCO surface and the operated catalysts are recorded (Figure 6). Both operated catalysts were still active after OER operation and transferred to the vacuum of the XPS within $\sim 2 \text{ min}$ to limit post-experimental aging.

The Sr $3d$ spectrum of the as-prepared sample, exhibits a shoulder at high binding energies, which is typically related to Sr-rich surfaces phases, frequently observed for LSCO (Figure 6a).^{34,41,42,45,46} After operation

of the catalyst, the high binding energy component is vanished, which is consistent with the on-line ICP-MS investigations presented above. The La $3d_{5/2}$ spectrum exhibits distinct multiplet-splitting with a magnitude of $\Delta B.E. = 4.1$ eV for the as-prepared perovskite oxide. In the operated state, the magnitude of the multiplet-splitting is decreased to $\Delta B.E. = 3.8$ eV (Figure 6b). Furthermore, a shift in binding energy is evident by comparison to the as-prepared state. Both observations indicate the formation of La(OH)₃ at the surface upon OER operation.⁴⁷ The observed dissolution of strontium and the formation of lanthanum hydroxide is in accordance with the high solubility of Sr(OH)₂ and the low solubility of La(OH)₃ at pH = 13 (0.1 M KOH).⁴⁸ In

addition, changes in the chemistry of the transition metal can be observed. The Co $2p_{3/2}$ signature is composed of an asymmetric peak and a pronounced tail towards higher binding energies, where the tail feature originates from a set of satellite peaks (Figure 6c). In the operated state, a main peak of decreased width and increased symmetry is visible, indicating a loss in the metallic character of the catalyst surface. Furthermore, a separation between the main peak and the remaining tail structure, now composed of a single satellite peak becomes apparent.

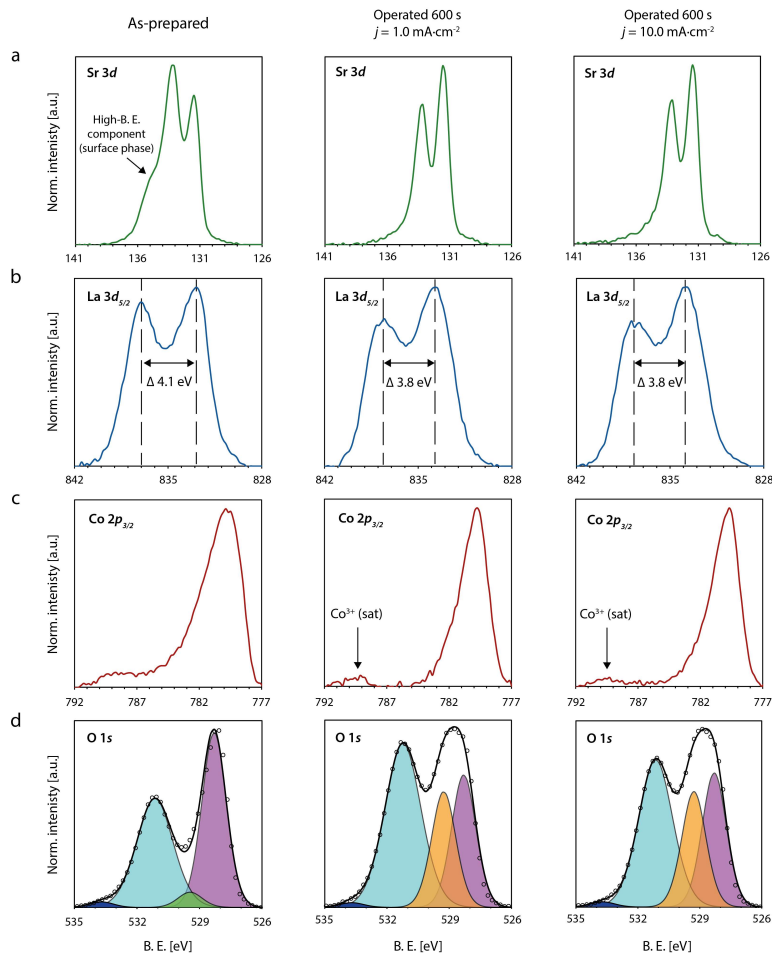


Figure 6. X-ray photoelectron spectroscopy investigations of the LSCO surface chemistry. Sr $3d$ (a), La $3d_{5/2}$ (b), Co $2p_{3/2}$ (c) and O $1s$ (d) XPS core-level spectra of LSCO catalysts in the as-prepared state (first column), and the operated (but still active) state after OER catalysis for 600s at $j = 1.0$ mA·cm⁻² (second column) and the operated (but still active) state after OER catalysis for 600s at $j = 10.0$ mA·cm⁻² (third column). The respective spectra are displayed for each sample state after subtraction of a Tougaard background. The O $1s$ spectra are deconvoluted by data fitting of five different components (ABO₃ lattice oxygen (purple), surface termination component (green), oxyhydroxide lattice oxygen (orange), mixed hydroxide groups (cyan), organic components (blue)). XPS analysis was performed at a photoemission angle $\theta = 46$.

The changes in the relative weight of the satellite features gives evidence about the formation of a new surface component at the operated catalysts which exhibits an oxidation state of Co(III), reflected by the pronounced satellite peak around ~ 790 eV.^{49,50}

Further insights on the chemical nature of the cobalt surface phase are gained based on the O 1s core-level signature (Figure 6d). Deconvolution of the O 1s core-level spectrum is based on five different chemical states which can be assigned to the lattice oxygen of the LSCO perovskite oxide, a termination layer component or, after OER operation, a (Co)oxyhydroxide lattice oxygen component, a mixed hydroxide component and a small amount of organic compounds.

The O 1s signature exhibits clear changes in the relative intensity of the different components after electrochemical operation, in particular visible in form of a decreased perovskite signal. The changes in the O 1s signature, are most likely associated to a change in the cobalt chemistry. Most likely, the correlated changes in the spectroscopic signature of the Co $2p_{3/2}$ and the O 1s core-level regions, indicate the presence of cobalt-oxyhydroxide at the catalyst surface. The evolution of a Co(III)-signature is accompanied by the emergence of an additional peak contributing to the O 1s signal, which is in accordance with the two different chemical states of oxygen (single bond and double bond) within the CoO(OH) compound. While the signal of the CoO(OH) hydroxide groups contribute to the mixed hydroxide component, the newly evolved component (orange peak in Figure 6), visible only for the operated state, likely reflects the CoO(OH) lattice oxygen contribution.⁵⁰ The presence of a lanthanum oxyhydroxide compound can be excluded due to its inherent instability in aqueous solution.⁵¹

The phase transition of the perovskite surface of mixed cobalt valency of nominally (III)/(IV) character towards a Co-oxyhydroxide phase with an oxidation state of Co(III) is consistent with the EELS results presented above, that have indicated a reduction of the average Co oxidation state of the operated catalyst surface. Furthermore, the observation of CoO(OH) formation is consistent with recent reports for LSCO OER electrocatalysts.⁵² Interestingly, the cobalt oxyhydroxide component was vanished after the end of lifetime, leaving behind a Co $2p_{3/2}$ and O 1s signature similar to the initial state, while a clear La(OH)₃ signature remains visible (cf. Figure S7). However, it cannot be ruled out that these post-mortem changes result from the rapidly increasing potential at the end

of the catalysts lifetime in galvanostatic measurements.

Our findings emphasize the particular importance of dynamic surface transformations at the surface of perovskite OER catalyst. These processes are accompanied with severe changes of the catalyst surface properties, which occur within the initial phase of OER catalysis at the solid-liquid interface.

DISCUSSION

In summary, we demonstrate that under OER conditions an active state of the LSCO catalyst surface rapidly evolves where highly mobile Co species dominate the surface chemistry, while additional irreversible processes result in an altered surface chemistry associated with a surface-dominated degradation process on longer time scales. The clear interrelation between the applied potential and the chemical changes of the perovskite surface may support the hypothesis that the process is driven by the potential-induced LOER.^{53,54} Here, the evolution of molecular oxygen, which originates from oxygen anions of the perovskite lattice, results in the decomposition of the perovskite structure and the release of Sr, La and Co cations. The subsequent stoichiometric evolution of the catalyst surface under applied potential appears to be mostly determined by the solubility of the involved cations in the investigated potential-pH-window⁴⁸, resulting in a complex evolution of mixed oxide phases at the catalyst surface. The catalyst surface becomes depleted from highly soluble strontium cations, while cobalt of finite solubility is enriched at the surface under initial OER operation as illustrated in Figure 7a. In contrast, lanthanum is insoluble under the given conditions and consistently, the lanthanum stoichiometry appears to be widely unchanged across the near-surface region. The topmost surface of operated LSCO electrocatalysts is found to be composed of La(OH)₃ and CoO(OH) (Figure 7a).

While Co-oxyhydroxide was reported to actively catalyze the OER⁸, lanthanum hydroxide may play a particular role in the deactivation mechanism of LSCO electrocatalysts, since it does not participate in oxidation reactions⁵⁵ and is highly stable under OER conditions.⁴⁸ Therefore, the compound may have a passivating character and likely blocks parts of the active catalyst surface. After the assembly of an active Co-oxyhydroxide layer as well as an inert lanthanum-hydroxide phase under applied potential, OER catalysis will be widely determined by the equilibrium between the dynamic dissolution of CoO(OH) and its reposition.⁸

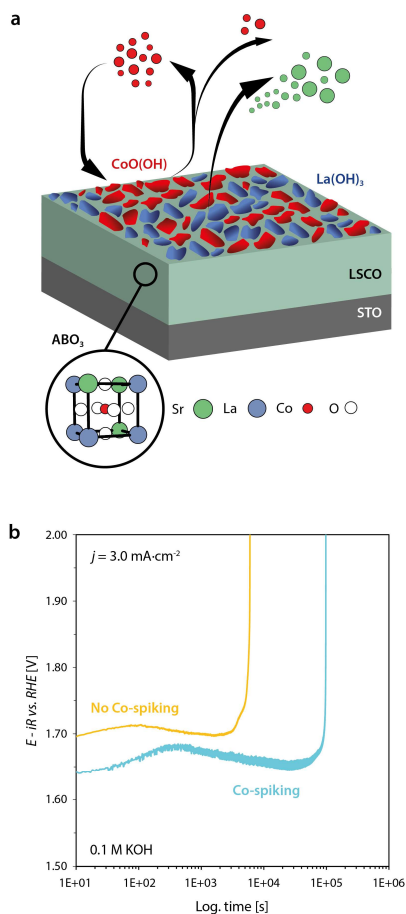


Figure 7. (a) Schematic illustration of the dynamic surface transformations induced under OER conditions. Strontium leaching and Co hopping during in the initial phase of OER results in the formation of mixed phases at the catalyst surface. A dynamically evolving and catalytically active CoO(OH) phase as well as a highly insoluble and catalytically inactive La(OH)₃ phase is formed. (b) Chronopotentiometric measurements for the characterization of the LSCO stability on the basis of the catalyst lifetimes at an applied current density of $j = 3.0 \text{ mA}\cdot\text{cm}^{-2}$ comparing the lifetime of LSCO in 0.1 M KOH and Co-spiked 0.1 M KOH. Abrupt increase of potential denotes the end of lifetime. The catalyst lifetime is considerably increased by Co-spiking of the electrolyte.

Considering the dynamic processes at the catalyst surface, we propose that the dynamic equilibrium successively shifts towards Co dissolution with increasing potentials which results in the gradual loss of cobalt from the active oxyhydroxide layer to the electrolyte over the course of many completed oxygen evolution reaction cycles. Thus, the depletion of Co-oxyhydroxide from the self-assembled surface

layer is accelerated at high OER rates, which may result in a failure of the catalyst when a critical ratio between CoO(OH) / La(OH)₃ coverage of the surface is reached. In addition, agglomeration of the CoO(OH) surface phase may result in a decrease of the catalytically active surface area. As shown in Figure 7b, this process can be delayed by spiking the electrolyte by cobalt, following the report of Chung et al.⁵⁶ In this way the balance between Co-oxyhydroxide and La-hydroxide can be manipulated by shifting the equilibrium between Co dissolution and re-deposition towards the precipitation of the solid Co-oxyhydroxide phase, which yields a 16-fold increase in lifetime.

Our findings suggest that not only the activity of the LSCO catalysts is determined by the assembly of active surface phases, but that the overall lifetime of the electrocatalysts is mainly determined by the stability of the active Co-oxyhydroxide surface layer. Here, it is crucial to maintain the balance between dissolution and re-deposition of Co, strongly influenced by the operation conditions, in order to preserve the active Co-oxyhydroxide phase. Potential-dependent surface processes hence may result in the successive degradation of the catalytically active surface layer under steady-state operation conditions, which may inherently limit the lifetime of perovskite electrocatalysts at increased, technically relevant current densities.

CONCLUSION

Under steady-state OER operation, an active surface state of LSCO electrocatalysts rapidly evolves which is characterized by Co-oxyhydroxide species which coincides with high ion dynamics at the solid-liquid interface. On longer timescales, degradation of the LSCO electrocatalysts is observed. While the catalyst bulk remains mostly unaffected at constant load, the catalyst lifetime is critically limited by the dynamic transformations of the topmost perovskite surface towards mixed phases. The degradation behavior hence considerably differs from dynamic conditions, where excessive amorphization and dissolution processes typically result in a loss of the catalytic performance over time. The surface transformation is potential-induced and results in a limited efficacy of the LSCO electrocatalysts in the high potential regime. We show that dynamic hopping of Co species across the LSCO surface is facilitated in presence of an aqueous electrolyte i.e. at the solid-liquid interface, which most likely plays an important role in the dynamic structural and chemical evolution of the catalyst surface. While Sr readily dissolves in the electrolyte at

relevant OER potentials, La remains stable at the surface in form of $\text{La}(\text{OH})_3$ and Co enriches at the surface in form of $\text{CoO}(\text{OH})$ during the early stage of steady-state OER operation. We propose that the interplay of the catalytically active and dynamically evolving $\text{CoO}(\text{OH})$ and a highly stable and catalytically inactive $\text{La}(\text{OH})_3$ surface phase results in potential-induced deactivation of the catalyst. Here the gradual dissolution of Co in the electrolyte, i.e. successive passivation of the LSCO surface by $\text{La}(\text{OH})_3$ causes the catalyst failure. The dynamic transformations in the surface chemistry that are driven under OER conditions are therefore key to understand not only activity trends, but also stability limitations of perovskite electrocatalysts.

EXPERIMENTAL

Thin film fabrication. Epitaxial $\text{La}_{0.6}\text{Sr}_{0.4}\text{CoO}_{3-\delta}$ thin film model electrodes of 20 nm thickness were deposited on single-crystalline, epi-polished (001) SrTiO_3 (STO) and (001) $\text{Nb}(0.5\text{wt}\%):\text{SrTiO}_3$ (NbSTO) substrates (Shinkosha Co. Ltd., Yokohama, Japan) with a size of $0.5 \times 10 \times 10$ mm in [001] orientation. The deposition process was performed by reflection high energy electron diffraction-controlled pulsed laser deposition at an oxygen partial pressure of $p(\text{O}_2) = 0.053$ mbar. The growth temperature was $T = 650^\circ\text{C}$ and the laser fluence $F = 2.19 \text{ J}\cdot\text{cm}^{-2}$ using a repetition rate of $f = 5$ Hz. The distance between the ceramic target and the heated substrate was $d = 60$ mm and a nanosecond KrF-excimer laser with a wavelength of $\lambda = 248$ nm was used to operate the PLD system. Platinum electrodes with a thickness of 50 nm were sputtered at the edges of the oxide thin film surface to provide for sufficient contact with the potentiostat. Furthermore, the backside and the sides of the substrates were covered with 50 nm of Pt forming a contact with the front Pt pads. Conductive Nb:STO substrates were applied to provide for an additional pathway for charge transfer through the Nb:STO/LSCO interface to improve measurement geometry for individual probing techniques when required (as indicated on the figure captions respectively). Please note, that the use of undoped and Nb-doped STO substrates may result in slight differences in the potential drop within the sample, and hence was only applied when an influence on the consistency of data interpretation can be excluded.

Thin film characterization. The surface morphology of the thin film electrodes was investigated using atomic force microscopy (AFM, Cypher, Oxford Instruments Asylum Research Inc., Santa Barbara, USA) operated with a tip with a curvature of ~ 8 nm. The

crystal structure of the thin films was characterized by X-ray diffraction (XRD, D8 Discover, Bruker AXS GmbH, Karlsruhe, Germany) by symmetric 2θ - ω scans around the (002) reflections as well as reciprocal space mapping (RSM) using asymmetric scans around the (013) reflections in grazing exit geometry. The diffractometer was equipped with a goebel mirror, a Cu K_α monochromator, a centric eulerian cradle and a Lynxeye XE detector. To provide for lateral resolution a pinhole adapter of 2 mm in diameter was applied. X-ray photoelectron spectroscopy (XPS, Phi 5000 VersaProbe, ULVAC Phi, Physical Electronics Inc.) was applied to study the surface chemistry, using the Al $K\alpha_1$ line ($E_\lambda = 1486.6$ eV, $FWHM = 0.26$ eV) of a monochromized X-ray source and constant pass energy ($E_0 = 29.35$ eV) in fixed analyzer transmission mode. To vary between different information depths of the detected photoelectrons, photoemission angles of $\Theta = 15^\circ$, and $\Theta = 64^\circ$ (cf. Figure 5c and Figure S6) were applied for the XPS analysis, while the XPS spectra presented in Figure 6 and Figure S7 were recorded at $\Theta = 46^\circ$. To calculate the cation stoichiometry, relative sensitivity factors (RSF) were referenced to the ceramic target material. For peak fitting, the full width half maximum ($FWHM$) of the components were constrained to exhibit an equal value and the components have a fixed position on the $B.E.$ scale for the comparison of different samples. However, the mixed hydroxide component is based on the sum of various overlapping signals of hydroxide groups with slightly varying binding energy due to differences in the chemical environment. Consequently, broadening of the multi-component peak compared to the other involved (single-component) chemical states requires a larger $FWHM$ applied for peak fitting. For data evaluation, a Shirley-type background was subtracted and the binding energies of all spectra were aligned to the C 1s signal. The inelastic mean free path ($1/\lambda$ IMPF) was calculated by the QUASES-IMPF software using the TPP2M formula⁵⁷ on the basis of the material properties of as-prepared LSCO. The mean escape depth was determined as indicator for the angle-dependent information depth of the XPS core-level.⁵⁸ The energy scale was periodically calibrated to the Au 4f core-level spectrum of a reference sample. XPS analysis of the operated samples was performed after rapid transfer ($t \sim 2$ min) to UHV subsequent to electrochemical operation and after gently patting the sample dry with a clean room swipe under N_2 -atmosphere.

TEM sample preparation. Three ultrathin TEM lamellae were prepared from epitaxial (LSCO) (001) thin films with a thickness of 100 nm deposited on a

single-crystalline NdGaO₃ (NGO) substrate in orthorhombic (110) surface orientation. The lamellae were prepared using an Alkali Resistant Positive Photoresist X AR-P 5900/4 protection layer by means of focused ion beam (FIB) on a DENS solutions heating and basing chip for in situ TEM measurements. Here, each lamella is attached to one of the electrical contact of chip with +20° offset. Platinum (1 μm thickness) is deposited to establish an electrical contact with the thin film in order to measure the beam-induced potential. Here, Pt is deposited far from the region of interest, so there is no possibility of interference of Pt in the in-situ ETEM catalytic investigations. Figure S1 shows the region of interest for the in-situ ETEM observations. Primary electron beam induced secondary electron emission results in a potential of 1.5 ± 0.2 V, which is close to relevant OER potentials. In order to remove a minor amorphous layer that forms on the surface upon FIB preparation an electron beam induced surface recrystallization procedure is performed in situ under 1 mbar oxygen partial pressure at $T = 400^\circ\text{C}$. Additional lamellae were prepared on a Cu grid for EELS analysis.

Environmental transmission electron microscopy. To evaluate the processes at the catalyst surface over time, several ETEM movies are recorded with a small negative defocus that results in a dark contrast of all atomic columns. In addition, a through focus series was acquired in O₂ gas for contrast simulation. The in-situ ETEM experiments are carried out using a FEI Titan ETEM G2 80–300 at operating voltage of 300 kV, equipped with a Cs-corrector. All in-situ movies are recorded using a Gatan UltraScan 1000XP at a beam current of 4 nA. The movie in O₂ is recorded with a cold trap to decrease the H₂O partial pressure. Local electron dose rates at the location of TEM lamella surfaces are measured by calibrated CCD contrast with 0.16696 electrons/counts, yielding 19.955 and 35.654 e/Å⁻²s⁻¹ for O₂ and H₂O environments respectively. A careful analysis of beam effects excludes that observed increase in Co mobility is induced by the momentum transfer during scattering of the high energetic primary electrons and give strong evidence for thermally induced surface hopping, that is enhanced by H₂O. The electron beam induced potential was measured via the electronic contact to the LSCO film and the DENS solutions holder as well as a FIB-Pt bridge across the substrate to be 1.5 (±0.2) V with respect to the ground (i.e. TEM column). An impedance converter was used to maintain nearly open circuit conditions during the voltage measurement.

Electron energy-loss spectroscopy. The EELS analysis are performed using Gatan Quantum 965ER post-column energy filter in the ETEM. Spectra of the

Co-L-, O-K-, and L-M-edges are acquired using 0.25 eV/ch dispersion in 1 mbar O₂ and post 5 μbar H₂O. Power-law background functions from Gatan’s Digital Micrograph are fitted to a 50 eV wide window before each Co L-edge, 25 eV for O-K-edge and 23 eV for La-M-edge for background subtraction respectively. Python based code is used for the precise calculation of the L₃/L₂ ratio. The spectra are background subtracted and energy calibrated using the corresponding zero-loss peak.

Image simulation. Multislice simulations of HRTEM images are conducted with QSTEM⁵⁹ following the procedure described in reference (35). For this purpose, the sample thickness as well as relevant electron-optical parameters are determined by minimizing the root mean square difference between experimental and simulated images of a single unit cell using the Metropolis algorithm. The multislice image simulations were performed using a sample thickness of 1.53 nm, a defocus of -14.5 nm and a focal spread of 9 nm. The two-fold astigmatism as well as the spherical aberration are found to have only a small influence on the image contrast within their experimental uncertainty and thus set to zero to avoid overfitting. In a second step, the obtained parameters are used during the simulation of a larger supercell including an A-site terminated surface.

Electrochemical characterization. The electrochemical characterization of the thin film electrodes was performed in a rotating disc electrode (RDE) setup (Pine Research) in O₂-saturated 0.1 molar KOH with a rotation rate of 1600 rpm using a custom-made adapter for 0.5 x 10 x 10 mm sized thin film samples. A chemically resistant Teflon beaker was applied as electrochemical cell and O₂-saturated (continuous purging) 0.1 M KOH was applied as electrolyte, which was prepared by dissolution of KOH pellets (Sigma Aldrich, 99.99 %) in deionized water (Milli-Q, >18.2 MΩcm). The potentiostat (BioLogic SP-150, Bio-Logic Science Instruments, France) was connected to the platinum contact sputtered at the backside of the substrate via a Pt stamp, providing for facile charge transfer to the thin film working electrode, while using a Pt-coil counter electrode. The center of the perovskite catalyst was sealed from the platinum contacts by an o ring with a diameter of $d = 7.5$ mm. The measurements were performed in reference to an Hg/HgO electrode (CHI Instruments), which was experimentally calibrated to the RHE (HydroFlex) for each batch of electrolyte. Electrochemical testing was conducted by electrochemical impedance spectroscopy, scan-rate dependent cyclic voltametry in the pseudocapacitive redox phase change region, cyclic

voltametry in the OER potential region (two cycles respectively). For Tafel analysis, chronopotentiometric (staircase) measurements were performed at different potentials in the range of $j = 0.1 \text{ mA}\cdot\text{cm}^{-2}$ - $j = 0.8 \text{ mA}\cdot\text{cm}^{-2}$ with galvanostatic holds of 10 min respectively. For lifetime testing LSCO thin film electrodes were operated in the OER region using chronopotentiometry at different current densities between $j = 0.1 \text{ mA}\cdot\text{cm}^{-2}$ - $j = 10.0 \text{ mA}\cdot\text{cm}^{-2}$. The entire setup was stored in a glove box, which was continuously purged with nitrogen gas. All potentials were *iR*-corrected by the uncompensated series resistance R_s of the electrode setup, that is typically in the range between $R_s = 75 - 100 \Omega$, as determined using the high frequency intersect of the Nyquist-plot determined by electrochemical impedance spectroscopy.

On-line ICP-MS measurements. To investigate the stability of the LSCO thin-film samples the outlet of a custom-designed and manufactured polycarbonate scanning flow cell (SFC) was coupled to the inlet of an inductively-coupled-plasma mass spectrometer (ICP-MS, Perkin-Elmer NexION 350X). The micro flow cell setup allows to probe electrochemical performance and dissolution behavior at several locations of the same thin film sample. A glassy carbon rod (SIGRADUR) was used as the counter- and an Ag/AgCl/3 M KCl (Metrohm) as the reference electrode, respectively. The counter electrode was channeled in the SFC from the inlet side via a T-connector, while the reference electrode was connected through a capillary channel from the outlet side (to avoid Cl⁻ contamination). The LSCO thin-films served as the working electrode (measured working electrode surface was $7.85 \times 10^{-3} \text{ cm}^2$). All electrochemical protocols during on-line stability measurements were performed using a potentiostat (Gamry, Reference 600). The working electrode was placed on an XYZ translation stage (Physik Instrumente M-403) allowing the rapid screening of multiple spots along the same LSCO sample. Electrochemical protocols were performed in 0.05 M KOH electrolyte solution (salt/organic matter content should be less than 2 w/w% for ICP-MS) saturated with Ar. Three different protocols were carried out as follows: contact with the working electrode was established at 1 V vs. RHE and the electrode was held at this potential for 5 min. This was followed by either a galvanostatic hold at $j = 0.1 \text{ mA}\cdot\text{cm}^{-2}$ for $t = 30$ min or $j = 0.3 \text{ mA}\cdot\text{cm}^{-2}$ for $t = 10$ min or $j = 1 \text{ mA}\cdot\text{cm}^{-2}$ for $t = 3$ min. All measurements were finished with a galvanostatic hold at $j = 2.25 \text{ mA}\cdot\text{cm}^{-2}$ for $t = 30$ min. An *iR* correction of 1 k Ω was applied during all measurements. The total Sr loss during OER operation is quantified by integration of the dissolution features,

detected by ICP-MS during the respective galvanostatic holds. The ICP-MS was calibrated daily by a four-point calibration slope made from standard solutions (Merck Certipur, Sr, La, In, Nb, Y, Ti, Sc, Co, Ge 1000 mg \cdot l⁻¹) containing the metals of interest in a given concentration in 0.05 M KOH. ¹¹⁵In (for ⁸⁸Sr, ¹³⁹La), ⁸⁹Y (for ⁹³Nb), ⁴⁵Sc (for ⁴⁷Ti), and ⁷⁴Ge (for ⁵⁹Co) served as internal standards. Internal standard solutions were prepared in 1% HNO₃. The electrolyte flow-rate was controlled by the peristaltic pump of the ICP-MS; the average flow-rate was $3.46 \pm 0.03 \mu\text{l}\cdot\text{s}^{-1}$.

ASSOCIATED CONTENT

Supporting Information. Recrystallization procedure of the FIB lamella, ETEM investigation in O₂ environment, Investigation of the LSCO surface dynamics in 0.5 Pa of H₂O, EELS analysis of the La-M-edge, On-line ICP-MS analysis including contact peak, Angle-dependent XPS analysis of as-prepared LSCO, XPS analysis of the surface chemistry of LSCO after the end of the catalyst lifetime. This material is available free of charge via the Internet at <http://pubs.acs.org>.

AUTHOR INFORMATION

Corresponding Authors

*Moritz L. Weber and Felix Gunkel - Peter Grünberg Institute (PGI-7) and JARA-FIT, Forschungszentrum Jülich GmbH, Jülich, 52425, Germany

Present Addresses

† Advanced Light Source, Lawrence Berkeley National Laboratory, Berkeley, California 94720, Peter Gruenberg Institute (PGI-7), Forschungszentrum Juelich, D-52425 Juelich GmbH, Germany, Juelich-Aachen Research Alliance (JARA-FIT)

§ IEK-1, Forschungszentrum Juelich GmbH, D-52425 Juelich, Germany

Author Contributions

M.L.W., A.S. and L.H. synthesized the samples. M.L.W. A.S. and C.B. performed and analyzed the rotating disc electrochemical measurements. M.L.W performed and analyzed AFM surface imaging, XRD and XPS. G.L. and T.M. performed and analyzed the electrochemical transmission electron microscopy experiments. A.K. and F.S. performed and analyzed the on-line ICP-MS experiments. F.G., C.B., C. J. and S. C. supervised the research and conceived the experiments. M.V.K., M.L.W. wrote the manuscript with contributions from all authors. All authors have given approval to the final version of the manuscript.

Funding Sources

Any funds used to support the research of the manuscript should be placed here (per journal style).

ACKNOWLEDGMENT

The authors thank René Borowski, Grigory Potemkin, Sylvia de Waal, Clemens Wiedenhöft and Astrid Besmehn for their experimental support.

ABBREVIATIONS

AFM, atomic force microscopy; CCD, charge-coupled device; EELS, electron energy loss spectroscopy; EIS, electrochemical impedance spectroscopy; ETEM, environmental transmission electron microscopy; FIB, focused ion beam; ICP-MS, Inductively coupled plasma mass spectrometry; LOER, lattice oxygen evolution reaction; LSCO, $\text{La}_{0.6}\text{Sr}_{0.4}\text{CoO}_{3-\delta}$; OER, oxygen evolution reaction; RSM, reciprocal space mapping; SFC, scanning flow cell; XRD, X-ray diffraction; XPS, X-ray photoelectron spectroscopy,

REFERENCES

- (1) Davis, S. J.; Lewis, N. S.; Shaner, M.; Aggarwal, S.; Arent, D.; Azevedo, I. L.; Benson, S. M.; Bradley, T.; Brouwer, J.; Chiang, Y.-M.; *et al.* Net-zero emissions energy systems. *Science (New York, N.Y.)* **2018**, *360*.
- (2) Rogelj, J.; Schaeffer, M.; Meinshausen, M.; Knutti, R.; Alcamo, J.; Riahi, K.; Hare, W. Zero emission targets as long-term global goals for climate protection. *Environ. Res. Lett.* **2015**, *10*, 105007.
- (3) Rogelj, J.; Luderer, G.; Pietzcker, R. C.; Kriegler, E.; Schaeffer, M.; Krey, V.; Riahi, K. Energy system transformations for limiting end-of-century warming to below 1.5 °C. *Nature Clim Change* **2015**, *5*, 519–527.
- (4) Bockris, J. O.; Otagawa, T. The Electrocatalysis of Oxygen Evolution on Perovskites. *J. Electrochem. Soc.* **1984**, *131*, 290–302.
- (5) Grimaud, A.; May, K. J.; Carlton, C. E.; Lee, Y.-L.; Risch, M.; Hong, W. T.; Zhou, J.; Shao-Horn, Y. Double perovskites as a family of highly active catalysts for oxygen evolution in alkaline solution. *Nature communications* **2013**, *4*, 2439.
- (6) Vojvodic, A.; Nørskov, J. K. Chemistry. Optimizing perovskites for the water-splitting reaction. *Science (New York, N.Y.)* **2011**, *334*, 1355–1356.
- (7) Suntivich, J.; May, K. J.; Gasteiger, H. A.; Goodenough, J. B.; Shao-Horn, Y. A perovskite oxide optimized for oxygen evolution catalysis from molecular orbital principles. *Science (New York, N.Y.)* **2011**, *334*, 1383–1385.
- (8) Fabbri, E.; Nachttegaal, M.; Binninger, T.; Cheng, X.; Kim, B.-J.; Durst, J.; Bozza, F.; Graule, T.; Schäublin, R.; Wiles, L.; *et al.* Dynamic surface self-reconstruction is the key of highly active perovskite nano-electrocatalysts for water splitting. *Nature materials* **2017**, *16*, 925–931.
- (9) Stoerzinger, K. A.; Comes, R.; Spurgeon, S. R.; Thevuthasan, S.; Ihm, K.; Crumlin, E. J.; Chambers, S. A. Influence of LaFeO_3 Surface Termination on Water Reactivity. *J. Phys. Chem. Lett.* **2017**, *8*, 1038–1043.
- (10) Seitz, L. C.; Dickens, C. F.; Nishio, K.; Hikita, Y.; Montoya, J.; Doyle, A.; Kirk, C.; Vojvodic, A.; Hwang, H. Y.; Nørskov, J. K.; *et al.* A highly active and stable $\text{IrO}_3/\text{SrIrO}_3$ catalyst for the oxygen evolution reaction. *Science (New York, N.Y.)* **2016**, *353*, 1011–1014.
- (11) Wan, G.; Freeland, J. W.; Kloppenburg, J.; Petretto, G.; Nelson, J. N.; Kuo, D.-Y.; Sun, C.-J.; Wen, J.; Diulus, J. T.; Herman, G. S.; *et al.* Amorphization mechanism of SrIrO_3 electrocatalyst: How oxygen redox initiates ionic diffusion and structural reorganization. *Science advances* **2021**, *7*.
- (12) Baeumer, C.; Li, J.; Lu, Q.; Liang, A. Y.-L.; Jin, L.; Martins, H. P.; Duchoň, T.; Glöß, M.; Gericke, S. M.; Wohlgenuth, M. A.; *et al.* Tuning electrochemically driven surface transformation in atomically flat LaNiO_3 thin films for enhanced water electrolysis. *Nat. Mater.* **2021**, *20*, 674–682.
- (13) Katsounaros, I.; Cherevko, S.; Zeradjanin, A. R.; Mayrhofer, K. J. J. Oxygen electrochemistry as a cornerstone for sustainable energy conversion. *Angewandte Chemie (International ed. in English)* **2014**, *53*, 102–121.
- (14) Akbashev, A. R.; Zhang, L.; Mefford, J. T.; Park, J.; Butz, B.; Luftman, H.; Chueh, W. C.; Vojvodic, A. Activation of ultrathin SrTiO_3 with subsurface SrRuO_3 for the oxygen evolution reaction. *Energy Environ. Sci.* **2018**, *11*, 1762–1769.
- (15) May, K. J.; Carlton, C. E.; Stoerzinger, K. A.; Risch, M.; Suntivich, J.; Lee, Y.-L.; Grimaud, A.; Shao-Horn, Y. Influence of Oxygen Evolution during Water Oxidation on the Surface of Perovskite Oxide Catalysts. *J. Phys. Chem. Lett.* **2012**, *3*, 3264–3270.
- (16) Bak, J.; Heo, Y.; Yun, T. G.; Chung, S.-Y. Atomic-Level Manipulations in Oxides and Alloys for Electrocatalysis of Oxygen Evolution and Reduction. *ACS nano* **2020**, *14*, 14323–14354.
- (17) Bick, D. S.; Kindsmüller, A.; Staikov, G.; Gunkel, F.; Müller, D.; Schneller, T.; Waser, R.; Valov, I. Stability and Degradation of Perovskite Electrocatalysts for Oxygen Evolution Reaction. *Electrochimica Acta* **2016**, *218*, 156–162.
- (18) Raman, A. S.; Patel, R.; Vojvodic, A. Surface stability of perovskite oxides under OER operating conditions: A first principles approach. *Faraday Discuss.* [Online early access]. DOI: 10.1039/C9FD00146H.
- (19) Schalenbach, M. A Perspective on Low-Temperature Water Electrolysis – Challenges in Alkaline and Acidic Technology. *Int. J. Electrochem. Sci.* **2018**, 1173–1226.
- (20) Geiger, S.; Kasian, O.; Ledendecker, M.; Pizzutilo, E.; Mingers, A. M.; Fu, W. T.; Diaz-Morales, O.; Li, Z.; Oellers, T.; Fruchter, L.; *et al.* The stability number as a metric for electrocatalyst stability benchmarking. *Nat Catal* **2018**, *1*, 508–515.
- (21) Bergmann, A.; Martinez-Moreno, E.; Teschner, D.; Chernev, P.; Gliech, M.; Araújo, J. F. de; Reier, T.; Dau, H.; Strasser, P. Reversible amorphization and the catalytically active state of crystalline Co_3O_4 during oxygen evolution. *Nature communications* **2015**, *6*, 8625.
- (22) Risch, M.; Grimaud, A.; May, K. J.; Stoerzinger, K. A.; Chen, T. J.; Mansour, A. N.; Shao-Horn, Y. Structural Changes of Cobalt-Based Perovskites upon Water Oxidation Investigated by EXAFS. *J. Phys. Chem. C* **2013**, *117*, 8628–8635.
- (23) Bick, D. S.; Krebs, T. B.; Kleimaier, D.; Zurhelle, A. F.; Staikov, G.; Waser, R.; Valov, I. Degradation Kinetics during Oxygen Electrocatalysis on Perovskite-Based Surfaces in

- Alkaline Media. *Langmuir : the ACS journal of surfaces and colloids* **2018**, *34*, 1347–1352.
- (24) Grimaud, A.; Carlton, C. E.; Risch, M.; Hong, W. T.; May, K. J.; Shao-Horn, Y. Oxygen Evolution Activity and Stability of $\text{Ba}_6\text{Mn}_5\text{O}_{16}$, $\text{Sr}_4\text{Mn}_2\text{CoO}_9$, and $\text{Sr}_6\text{Co}_5\text{O}_{15}$: The Influence of Transition Metal Coordination. *J. Phys. Chem. C* **2013**, *117*, 25926–25932.
- (25) Almeida, T. P.; McGrouther, D.; Pivak, Y.; Perez Garza, H. H.; Temple, R.; Massey, J.; Marrows, C. H.; McVitie, S. Preparation of high-quality planar FeRh thin films for in situ TEM investigations. *J. Phys.: Conf. Ser.* **2017**, *903*, 12022.
- (26) Weber, M. L.; Baeumer, C.; Mueller, D. N.; Jin, L.; Jia, C.-L.; Bick, D. S.; Waser, R.; Dittmann, R.; Valov, I.; Gunkel, F. Electrolysis of Water at Atomically Tailored Epitaxial Cobaltite Surfaces. *Chem. Mater.* **2019**, *31*, 2337–2346.
- (27) Song, F.; Bai, L.; Moysiadou, A.; Lee, S.; Hu, C.; Liardet, L.; Hu, X. Transition Metal Oxides as Electrocatalysts for the Oxygen Evolution Reaction in Alkaline Solutions: An Application-Inspired Renaissance. *Journal of the American Chemical Society* **2018**, *140*, 7748–7759.
- (28) Samira, S.; Hong, J.; Camayang, J. C. A.; Sun, K.; Hoffman, A. S.; Bare, S. R.; Nikolla, E. Dynamic Surface Reconstruction Unifies the Electrocatalytic Oxygen Evolution Performance of Nonstoichiometric Mixed Metal Oxides. *JACS Au* [Online early access]. DOI: 10.1021/jacsau.1c00359.
- (29) Antipin, D.; Risch, M. Trends of epitaxial perovskite oxide films catalyzing the oxygen evolution reaction in alkaline media. *J. Phys. Energy* **2020**, *2*, 32003.
- (30) Weber, M. L.; Gunkel, F. Epitaxial catalysts for oxygen evolution reaction: model systems and beyond. *J. Phys. Energy* **2019**, *1*, 31001.
- (31) Scholz, J.; Risch, M.; Stoerzinger, K. A.; Wartner, G.; Shao-Horn, Y.; Jooss, C. Rotating Ring–Disk Electrode Study of Oxygen Evolution at a Perovskite Surface: Correlating Activity to Manganese Concentration. *J. Phys. Chem. C* **2016**, *120*, 27746–27756.
- (32) Liu, J.; Jia, E.; Stoerzinger, K. A.; Le Wang; Wang, Y.; Yang, Z.; Shen, D.; Engelhard, M. H.; Bowden, M. E.; Zhu, Z.; *et al.* Dynamic Lattice Oxygen Participation on Perovskite LaNiO_3 during Oxygen Evolution Reaction. *J. Phys. Chem. C* **2020**, *124*, 15386–15390.
- (33) Mefford, J. T.; Rong, X.; Abakumov, A. M.; Hardin, W. G.; Dai, S.; Kolpak, A. M.; Johnston, K. P.; Stevenson, K. J. Water electrolysis on $\text{La}(1-x)\text{Sr}(x)\text{CoO}(3-\delta)$ perovskite electrocatalysts. *Nature communications* **2016**, *7*, 11053.
- (34) Boucly, A.; Fabbri, E.; Artiglia, L.; Cheng, X.; Pergolesi, D.; Ammann, M.; Schmidt, T. J. Surface Segregation Acts as Surface Engineering for the Oxygen Evolution Reaction on Perovskite Oxides in Alkaline Media. *Chem. Mater.* **2020**, *32*, 5256–5263.
- (35) Lole, G.; Roddatis, V.; Ross, U.; Risch, M.; Meyer, T.; Rump, L.; Geppert, J.; Wartner, G.; Blöchl, P.; Jooss, C. Dynamic observation of manganese adatom mobility at perovskite oxide catalyst interfaces with water. *Commun Mater* **2020**, *1*.
- (36) Roddatis; Lole; Jooss. In Situ Preparation of $\text{Pr}_{1-x}\text{Ca}_x\text{MnO}_3$ and $\text{La}_{1-x}\text{Sr}_x\text{MnO}_3$ Catalysts Surface for High-Resolution Environmental Transmission Electron Microscopy. *Catalysts* **2019**, *9*, 751.
- (37) Zhao, Y.; Feltes, T. E.; Regalbutto, J. R.; Meyer, R. J.; Klie, R. F. In situ electron energy loss spectroscopy study of metallic Co and Co oxides. *Journal of Applied Physics* **2010**, *108*, 63704.
- (38) Mueller, D. N.; Machala, M. L.; Bluhm, H.; Chueh, W. C. Redox activity of surface oxygen anions in oxygen-deficient perovskite oxides during electrochemical reactions. *Nature communications* **2015**, *6*, 6097.
- (39) Stemmer, S. Characterization of oxygen-deficient SrCoO_3 by electron energy-loss spectroscopy and Z-contrast imaging. *Solid State Ionics* **2000**, *130*, 71–80.
- (40) Wang, Z. L.; Yin, J. S.; Jiang, Y. D. EELS analysis of cation valence states and oxygen vacancies in magnetic oxides. *Micron* **2000**, *31*, 571–580.
- (41) Kubicek, M.; Rupp, G. M.; Huber, S.; Penn, A.; Opitz, A. K.; Bernardi, J.; Stöger-Pollach, M.; Hutter, H.; Fleig, J. Cation diffusion in $\text{La}_{(0.6)}\text{Sr}_{(0.4)}\text{CoO}_{(3-\delta)}$ below 800 °C and its relevance for Sr segregation. *Physical chemistry chemical physics : PCCP* **2014**, *16*, 2715–2726.
- (42) Koo, B.; Kim, K.; Kim, J. K.; Kwon, H.; Han, J. W.; Jung, W. Sr Segregation in Perovskite Oxides: Why It Happens and How It Exists. *Joule* **2018**, *2*, 1476–1499.
- (43) Lopes, P. P.; Chung, D. Y.; Rui, X.; Zheng, H.; He, H.; Farinazzo Bergamo Dias Martins, P.; Strmcnik, D.; Stamenkovic, V. R.; Zapol, P.; Mitchell, J. F.; *et al.* Dynamically Stable Active Sites from Surface Evolution of Perovskite Materials during the Oxygen Evolution Reaction. *Journal of the American Chemical Society* **2021**, *143*, 2741–2750.
- (44) Kasian, O.; Geiger, S.; Schalenbach, M.; Mingers, A. M.; Savan, A.; Ludwig, A.; Cherevko, S.; Mayrhofer, K. J. J. Using Instability of a Non-stoichiometric Mixed Oxide Oxygen Evolution Catalyst As a Tool to Improve Its Electrocatalytic Performance. *Electrocatalysis* **2018**, *9*, 139–145.
- (45) Jung, W.; Tuller, H. L. Investigation of surface Sr segregation in model thin film solid oxide fuel cell perovskite electrodes. *Energy Environ. Sci.* **2012**, *5*, 5370–5378.
- (46) Li, Y.; Zhang, W.; Wu, T.; Zheng, Y.; Chen, J.; Yu, B.; Zhu, J.; Liu, M. Segregation Induced Self-Assembly of Highly Active Perovskite for Rapid Oxygen Reduction Reaction. *Adv. Energy Mater.* **2018**, *8*, 1801893.
- (47) Sunding, M. F.; Hadidi, K.; Diplas, S.; Løvrvik, O. M.; Norby, T. E.; Gunnæs, A. E. XPS characterisation of in situ treated lanthanum oxide and hydroxide using tailored charge referencing and peak fitting procedures. *Journal of Electron Spectroscopy and Related Phenomena* **2011**, *184*, 399–409.
- (48) Schweitzer, G. K.; Pesterfield, L. L. *The aqueous chemistry of the elements*; Oxford University Press: Oxford, New York, 2010.
- (49) Biesinger, M. C.; Payne, B. P.; Grosvenor, A. P.; Lau, L. W.; Gerson, A. R.; Smart, R. S. Resolving surface chemical states in XPS analysis of first row transition metals, oxides

- and hydroxides: Cr, Mn, Fe, Co and Ni. *Applied Surface Science* **2011**, *257*, 2717–2730.
- (50) Yang, J.; Liu, H.; Martens, W. N.; Frost, R. L. Synthesis and Characterization of Cobalt Hydroxide, Cobalt Oxyhydroxide, and Cobalt Oxide Nanodiscs. *J. Phys. Chem. C* **2010**, *114*, 111–119.
- (51) Samata, H.; Kimura, D.; Saeki, Y.; Nagata, Y.; Ozawa, T. C. Synthesis of lanthanum oxyhydroxide single crystals using an electrochemical method. *Journal of Crystal Growth* **2007**, *304*, 448–451.
- (52) Boucly, A.; Artiglia, L.; Fabbri, E.; Palagin, D.; Aegerter, D.; Pergolesi, D.; Novotny, Z.; Comini, N.; Diulus, J. T.; Huthwelker, T.; *et al.* Direct evidence of cobalt oxyhydroxide formation on a La_{0.2}Sr_{0.8}CoO₃ perovskite water splitting catalyst. *J. Mater. Chem. A* [Online early access]. DOI: 10.1039/D1TA04957G.
- (53) Binninger, T.; Mohamed, R.; Waltar, K.; Fabbri, E.; Levecque, P.; Kötz, R.; Schmidt, T. J. Thermodynamic explanation of the universal correlation between oxygen evolution activity and corrosion of oxide catalysts. *Scientific reports* **2015**, *5*, 12167.
- (54) Fabbri, E.; Schmidt, T. J. Oxygen Evolution Reaction—The Enigma in Water Electrolysis. *ACS Catal.* **2018**, *8*, 9765–9774.
- (55) Therese, G. H. A.; Kamath, P. V. Electrochemical Synthesis of Metal Oxides and Hydroxides. *Chem. Mater.* **2000**, *12*, 1195–1204.
- (56) Chung, D. Y.; Lopes, P. P.; Farinazzo Bergamo Dias Martins, P.; He, H.; Kawaguchi, T.; Zapol, P.; You, H.; Tripkovic, D.; Strmcnik, D.; Zhu, Y.; *et al.* Dynamic stability of active sites in hydr(oxy)oxides for the oxygen evolution reaction. *Nat Energy* **2020**, *5*, 222–230.
- (57) Tanuma, S.; Powell, C. J.; Penn, D. R. Calculations of electron inelastic mean free paths. V. Data for 14 organic compounds over the 50–2000 eV range. *Surf. Interface Anal.* **1994**, *21*, 165–176.
- (58) Powell, C. J. Practical guide for inelastic mean free paths, effective attenuation lengths, mean escape depths, and information depths in x-ray photoelectron spectroscopy. *Journal of Vacuum Science & Technology A* **2020**, *38*, 23209.
- (59) C. Koch. *Determination of core structure periodicity and point defect density along dislocations*, 2002.

Chapter 8

Discussion and Summary

In the following, the outline of the main accomplishments of this thesis and a critical conclusion are discussed. An essential requirement for atomic-scale in-situ ETEM observations of catalyst behavior in H_2O is a careful specimen thinning procedure that preserves the surface as much as possible. Conventional TEM lamella preparation constantly forms amorphous material due to the Ga ion beam damage. The thickness of the damaged surface ranges between subnanometer to several tens of nanometer depending on the final thinning steps in the FIB. Such a surface cannot provide information about atomic insights of the H_2O -catalyst dynamical interface. An advanced approach of the FIB system is reported to prepare high-quality, single-crystalline TEM cross-section lamella of the perovskite thin films. Catalytically inactive surface protection of polymer-based positive photoresist materials is used, which can be removed with the help of PIPS and plasma cleaning. Although it is challenging to obtain a surface without damage, an advanced approach is used to recrystallize this damaged surface under the electron beam influence in high partial pressure of oxygen. ETEM observations show that the surface termination of a single-crystalline ordered surface depends on the gas environment. The modification of the surface stoichiometry depends on the reactive, inert gas or in high vacuum (HV) conditions. The presence of a trace amount of residual H_2O also affects the surface chemical composition in the perovskite structure. The irreversible formation of polycrystalline structures on $\text{Pr}_{1-x}\text{Ca}_x\text{MnO}_3$ surface from the amorphous layer has been reported if the partial pressure of H_2O is raised in ETEM. Detailed EELS analysis suggests an increase in Mn^{3+} states is associated with the healing of the damaged surface due to electron beam-induced electrochemical oxidation of the $\text{Pr}_{1-x}\text{Ca}_x\text{MnO}_3$ surface. This process is high in high partial pressure of oxygen and slows in an inert atmosphere of He or N_2 due to residual oxygen. In HV conditions, this electrochemical oxidation is almost negligible. The single controlled crystalline ordered perovskite oxide surface in O_2 , inert environment, and reactive conditions like H_2O is an essential desired com-

ponent for revealing the surface in situ reactions. These findings are essential for the in-situ observation of active states of heterogeneous catalytic reaction as well as in battery research of complex oxide materials.

Electrochemical OER experiments provide information about stability and increase or decrease in catalyst activity. Comparison of catalyst surface before and after the electrochemical studies provide valuable information on structural changes. However, ETEM observations demonstrate atomic mobility at the H₂O-catalyst interface, local structural and TM valence changes compared to electrochemical experiments. A combination of electrochemical and ETEM experiments could help to disclose the mechanism of OER activity and the stability of complex catalysts. Electrochemical studies of La_{0.6}Sr_{0.4}MnO₃ show good OER activity and stability while ETEM observations reveal Mn adatoms on the surface. Mn adatom hopping rate in contact to condensed H₂O is at least 20 times higher than in high vacuum and inert gasses. It certainly indicates that the fast dynamics of Mn adatom is related to the interaction with H₂O and not due to the influence of electron beam. The calculated electron beam-induced Mn adatom hopping rate is way beneath the hopping rate observed experimentally in HV. The fast mobility of Mn adatoms can be evaluated as emerging from a surface activation barrier reduction in contact with the H₂O layer, which is apparently due to partial solvation of surface Mn in H₂O. The earlier described OER mechanism AER and LOM does not comply with our findings; even the thermodynamic calculation for the OER descriptor has far-reaching repercussions for understanding such OER mechanism. Theoretical calculations are much desired beyond frozen surface approximation; the flexible valence of partially solvated Mn is a fundamental factor that needs to be considered for the evolution of new OER reaction pathways. Both perovskite system La_{0.6}Sr_{0.4}MnO₃ and Pr_{0.67}Ca_{0.33}MnO₃ shows similar current density $j = 1.03 \text{ mA/cm}^2$ and $j = 1.05 \text{ mA/cm}^2$ respectively at $E = 1.75 \text{ V}$ vers. RHE. However, Pr_{0.67}Ca_{0.33}MnO₃ shows a drastic decrease in OER activity immediately after the third cycle. The sudden OER activity decrease is associated with irreversible formation of surface oxygen vacancies (V_O). V_O donates an electron to the surface Mn atoms, promoting Mn³⁺ to Mn²⁺ reduction and Mn leaching. Pr_{1-x}Ca_xMnO₃ system shows distinct performance by the change in A-site doping. Detailed electrochemical and ETEM studies are shown in chapter 5, show the leaching of surface Mn atoms with the formation of Mn²⁺ species due to formation of surface V_O and reduction of Mn species with high solubility in H₂O. EELS analysis of the Pr_{1-x}Ca_xMnO₃ (x=0.1 and 0.33) system for the O k and Mn L edges implies stable Mn valence at the x=0.1 surface. Pr_{0.67}Ca_{0.33}MnO₃ system shows high OER activity initially, but it undergoes corrosion on the surface and hence is not a stable OER system. EELS analysis of Pr_{0.67}Ca_{0.33}MnO₃ shows the reduction in O K edge prepeak after interaction with H₂O, and change in the

L_3/L_2 intensity ratio confirms Mn reduction. $\text{Pr}_{0.9}\text{Ca}_{0.1}\text{MnO}_3$ system shows high reversible Mn fluctuation dynamics at the interface to H_2O . Surprisingly, it delivers stable behavior for OER-like conditions in ETEM and actual electrochemical conditions in RRDE compared to the $\text{Pr}_{0.67}\text{Ca}_{0.33}\text{MnO}_3$ system. ETEM observations confirm the absence of Mn leaching for the $\text{Pr}_{0.9}\text{Ca}_{0.1}\text{MnO}_3$ system in contact with H_2O . Though the $\text{Pr}_{0.9}\text{Ca}_{0.1}\text{MnO}_3$ system is not a suitable OER catalyst, it shows how change in covalency can drastically change OER activity and stability, which will help in constructing future OER catalysts.

Electrochemical and X-rays studies confirm the change in the activity and stability of the $\text{La}_{0.6}\text{Sr}_{0.4}\text{CoO}_3$ surface due to the formation of the active phase of the Cobalt-oxyhydroxide type layer. ETEM observations are in good agreement with the active phase formation on the surface, which strongly determines the OER activity of the $\text{La}_{0.6}\text{Sr}_{0.4}\text{CoO}_3$. In-situ ETEM studies show mobile Co adatoms on the $\text{La}_{0.6}\text{Sr}_{0.4}\text{CoO}_3$ surface interfaces to H_2O ; however, an increase in partial pressure of H_2O in ETEM shows the formation of a disordered layer. EELS analysis confirmed Co valence changes after interaction with H_2O , indicating flexible valence of Co, which could be related to the formation of an active phase of Co on the surface.

In summary, ETEM observations suggest that partially solvated Mn species are mobile on the $\text{La}_{0.6}\text{Sr}_{0.4}\text{MnO}_3$ surface and act as an active catalytic site due to their flexible coordination. The flexible valence and fast mobility of transition metal without leaching might be a critical factor in breaking the scaling relation of adsorption energies of the intermediate oxygen species and decreasing the overpotential of the catalyst. The current studies also suggest that this flexible coordination increases the stability of the $\text{La}_{0.6}\text{Sr}_{0.4}\text{MnO}_3$ catalyst, which is essential to consider along with the high OER activity. The transition metal-oxygen covalency in the $\text{Pr}_{1-x}\text{Ca}_x\text{MnO}_3$ system also plays a critical role in the OER activity and changes the reaction mechanism. ETEM observation showed how transition metal is mobile on the perovskite surface under the OER-like conditions. These new insights do not rely on the classical AEM and LOM mechanism and open new possibilities for developing highly active catalysts suggesting a new approach for the OER mechanism. Atomically resolved observations open opportunities for developing highly active catalysts by considering catalyst-electrolyte dynamic interface, surface transformation, and defect reactions.

Appendix A

Supplementary Information

A.1 In-situ surface preparation

Supporting Information

In situ Preparation of Catalyst Surface for High Resolution Environmental Transmission Electron Microscopy

Vladimir Roddatis*, Gaurav Lole, and Christian Jooss**

Institute of Materials Physics, University of Goettingen, D-37077, Goettingen, Germany;

* Correspondence: vroddatis@ump.gwdg.de; Tel.: +49-551-39-25026 (V.R.);

** Correspondence: cjooss@gwdg.de; Tel.: +49-551-39-25303 (C.J.);

Received: date; Accepted: date; Published: date

Supporting Figures

Figure S1 - The PCMO ($x=0.33$) after electron beam treatment in He at 50 μ bars.

Figure S2 - The PCMO ($x=0.33$) after electron beam treatment in O₂ at 50 μ bars.

Figure S3 - HRTEM image and rotationally averaged profiles of PCMO in O₂ and in He ($x=0.33$).

Figure S4 - HRTEM image and rotationally averaged profiles of PCMO in He ($x=0.33$).

Figure S5- Analysis of broadening of spots in FFTs, lattice disorder in PCMO ($x=0.1$)

Figure S6-1. Through focus series of HRTEM images of PCMO ($x=0.33$) for the thickness of 10 nm.

Figure S6-2. Experimental and calculated HRTEM images of PCMO ($x=0.33$) for the thickness of 3 nm.

Figure S7 - The PCMO ($x=0.1$) after electron beam treatment in He at 50 μ bars.

Figure S8 - HRSTEM image and EELS spectrum of PrO_x particle at the surface of PCMO ($x=0.33$).

Figure S9 - An example of multiple ion detection scan in Quadera™ software.

Supporting Tables

Table S1. Summary of the Mn valence PCMO ($x=0.33$) after electron beam treatment in He at 50 μ bars.

Table S2. Summary of the Mn valence of PCMO ($x=0.33$) after electron beam treatment in O₂ at 50 μ bars.

Table S3-1. Simulation parameters for the through focus series.

Table S3-2. Simulation parameters for individual experimental images.

Table S4. Summary of the Mn valence of PCMO ($x=0.1$) after electron beam treatment in He at 50 μ bars.

The PCMO ($x=0.33$) after electron beam treatment in He at 50 μbars .

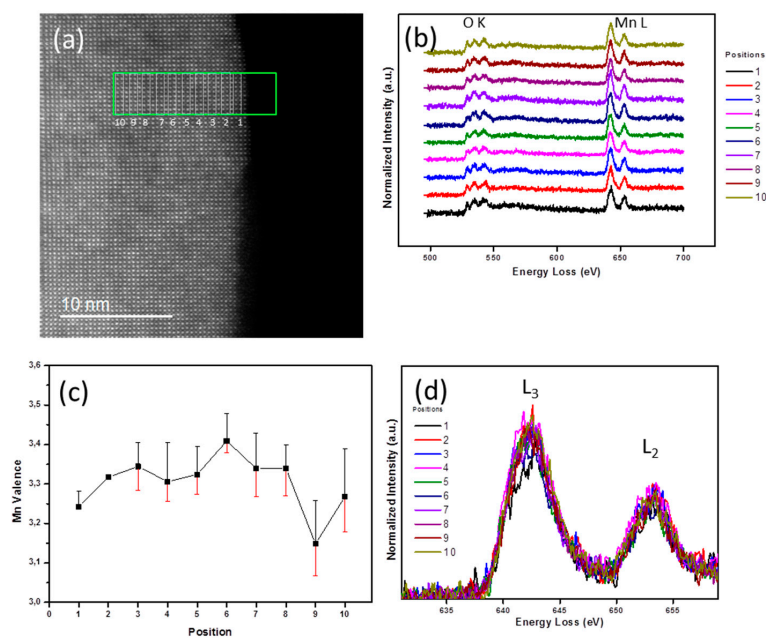


Figure S1. The PCMO ($x=0.33$) after electron beam treatment in He at 50 μbars . (a) HAADF image; (b) EELS spectra; (c) Mn valence plot; (d) $L_{2,3}$ -edge of Mn at each point.

Table S1. Summary of the Mn valence PCMO ($x=0.33$) after electron beam treatment in He at 50 μbars . The average value is 3.30 ± 0.06 .

Position	1	2	3	4	5	6	7	8	9	10
Mn valence	3.24	3.31	3.34	3.31	3.32	3.41	3.34	3.34	3.15	3.27
Error (-)	0	0	-0.06	-0.05	-0.05	-0.03	-0.07	-0.07	-0.08	-0.09
Error (+)	0.04	0	0.06	0.1	0.07	0.07	0.09	0.06	0.11	0.12

The PCMO ($x=0.33$) after electron beam treatment in O_2 at 50 μ bars.

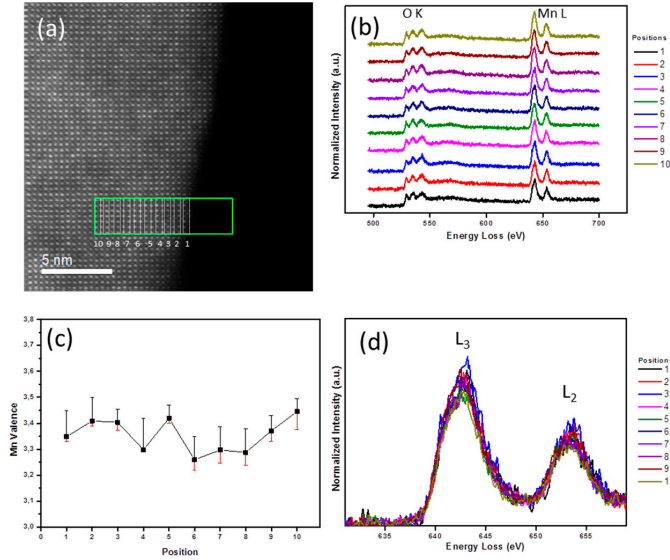


Figure S2. The PCMO ($x=0.33$) after electron beam treatment in O_2 at 50 μ bars. (a) HAADF image; (b) EELS spectra; (c) Mn valence plot; (d) $L_{2,3}$ -edge of Mn at each point.

Table S2. Summary of the Mn valence of PCMO ($x=0.33$) after electron beam treatment in O_2 at 50 μ bars. Average value is 3.36 ± 0.06 .

Position	1	2	3	4	5	6	7	8	9	10
Mn valence	3.35	3.41	3.40	3.30	3.42	3.26	3.30	3.29	3.37	3.45
Error (-)	-0.02	-0.02	-0.03	0.0	-0.02	-0.04	-0.05	-0.05	-0.04	-0.07
Error (+)	0.10	0.09	0.05	0.12	0.05	0.09	0.09	0.09	0.06	0.05

Method of Valence analysis used:

Mn valence state is determined by calculating Mn L_3/L_2 integrated intensity ratio using method demonstrated by M. Varela *et al* (see Ref. 37 in the main text) for $La_xCa_{1-x}MnO_3$ yielding a valence $V = -0.73(11) \times \text{Mn } L_3/L_2 \text{ intensity ratio} + 5.0(4)$. All our EELS spectra are extracted from spectrum images at area of vacuum and at different gas pressure for post-mortem analysis as visible in Figures S1 and 2. A power-law background functions is fit to 50 eV wide windows before each Mn L_3 -edge. A Hartree-Slater (HS) type cross-section step function from Gatan Digital Micrograph is used for correcting the background within the L_3 and L_2 peaks. The HS step function removes continuum contribution by placing a 10 eV window exactly after L_2 edge. The energy axis is calibrated by using the zero loss peak. The error bars are determined by changing the position of integration windows of L_3 and L_2 edges by ± 1 eV. The relative thickness of the lamella region, where the spectra is extracted is $t/\lambda < 0.5$, where $\lambda \approx 50$ nm represents the inelastic scattering length.

Analysis of broadening of spots in FFTs, lattice disorder in PCMO ($x=0.33$)

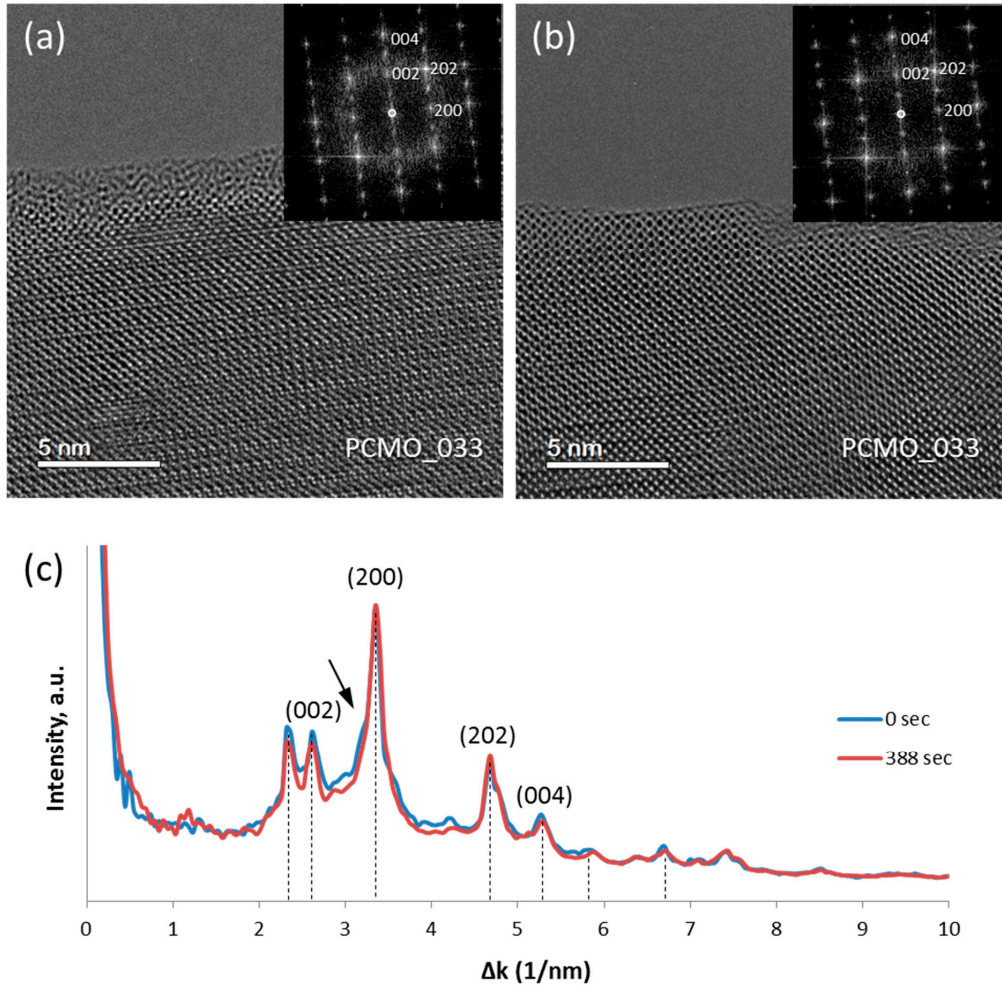


Figure S3. Analysis of broadening of spots in FFTs, lattice disorder in PCMO ($x=0.33$) in O_2 . (a) HRTEM image of PCMO ($x=0.33$) at the beginning and (b) after 388 seconds of electron irradiation in O_2 . (c) The rotationally averaged profiles of corresponding FFTs. The intensities of peaks remain almost unchanged. A shoulder marked with the black arrow originates from the amorphous phase and disappears after 388 seconds.

HRTEM image and rotationally averaged profiles of PCMO in He ($x=0.33$)

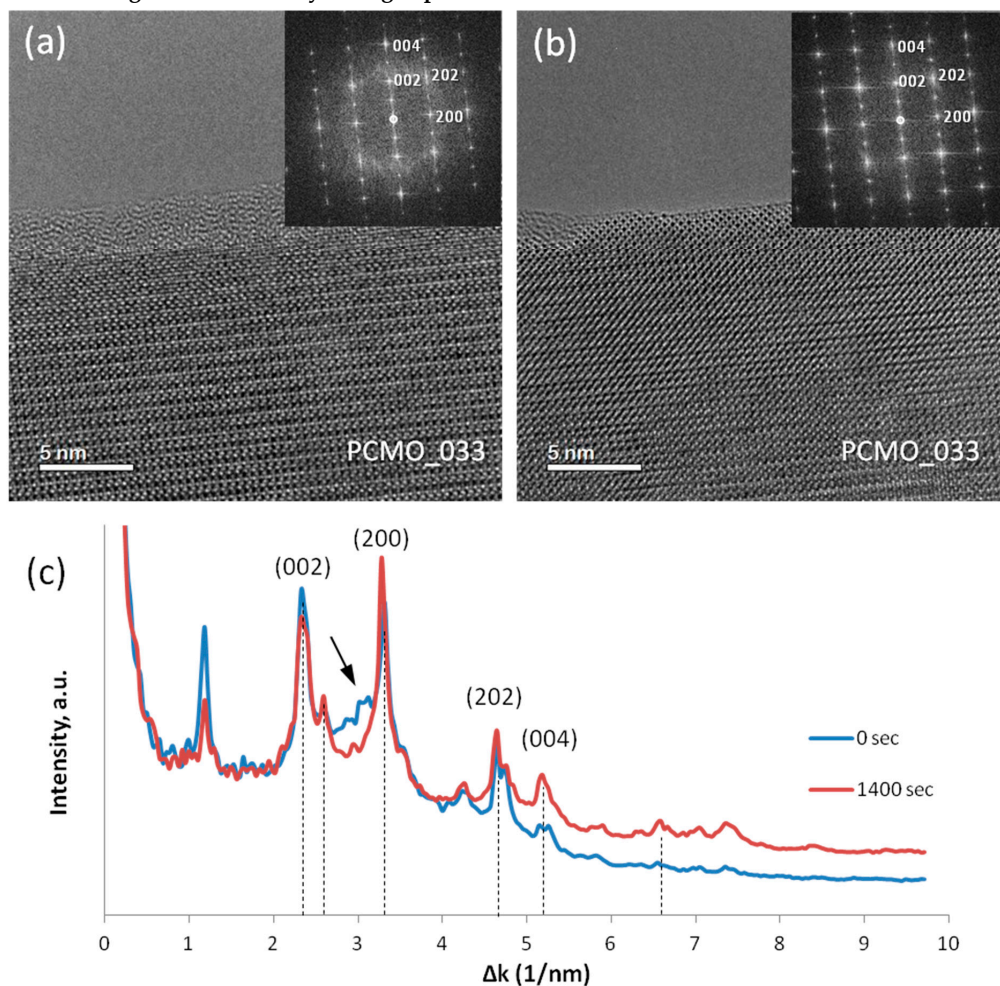


Figure S4. HRTEM image and rotationally averaged profiles of PCMO in He ($x=0.33$). (a) HRTEM image of PCMO ($x=0.33$) at the beginning and (b) after 1400 seconds of electron irradiation in He. (c) The rotationally averaged profiles of corresponding FFTs. The broadening of peaks and change their intensity is visible, revealing the increase of structural disorder. The broad peak marked with the black arrow originates from the amorphous phase and disappears after 1400 seconds.

Analysis of broadening of spots in FFTs, lattice disorder in PCMO ($x=0.1$)

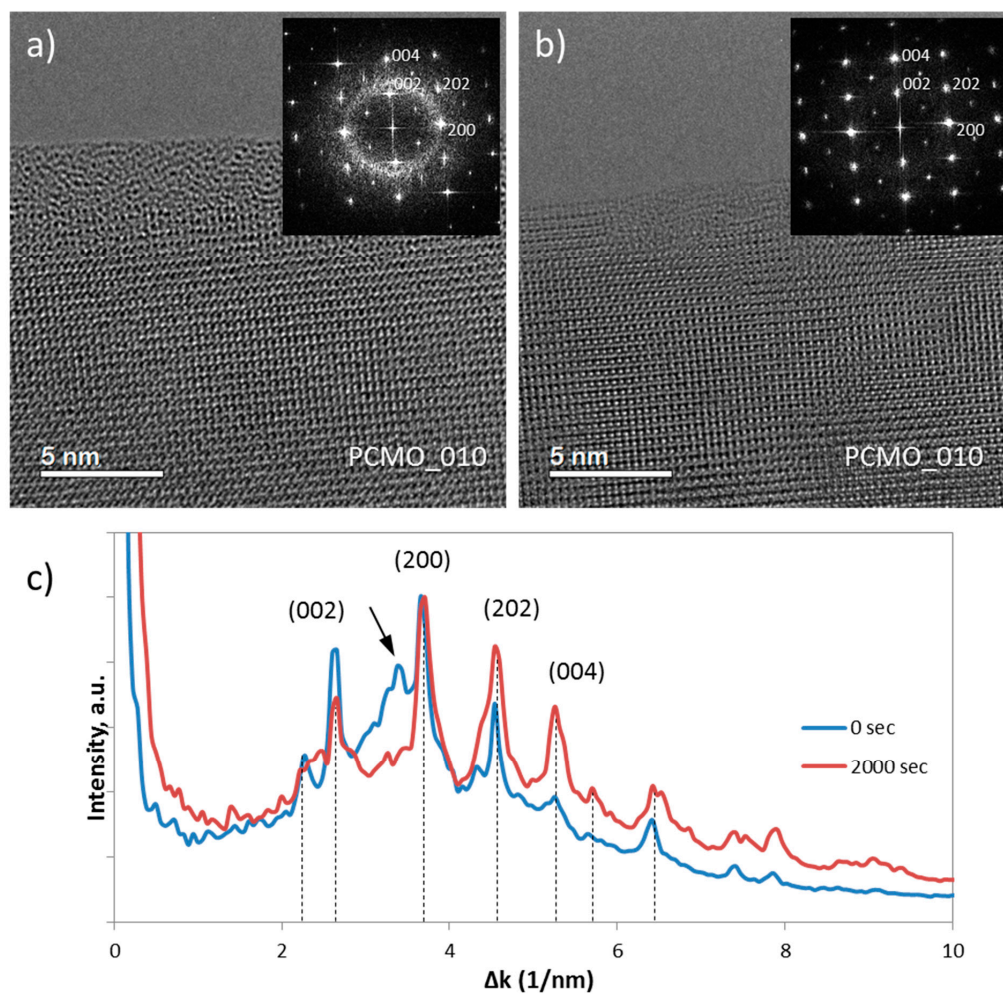


Figure S5. (a) HRTEM image of PCMO ($x=0.1$) at the beginning and (b) after 2000 seconds of electron irradiation. (c) The rotationally averaged profiles of corresponding FFTs. The broadening of peaks and change their intensity is clearly visible, revealing the increase of structural disorder. The broad peak marked with the black arrow originates from the amorphous phase and disappears after 2000 seconds.

HRTEM image simulations and atomic models

Detailed analysis of image conditions in the ETEM was reported by Bugnet et al. (see Ref. [29] in the main text). We followed similar procedure of the microscope tuning to achieve the spherical aberration coefficient (C_s) to a positive value of $10 \pm 5 \mu\text{m}$ when atoms appear in black at the Scherzer defocus. The thickness of edge was estimated from low-loss EELSS spectra yielding a value of less than 10 nm. HRTEM images were calculated using QSTEM software. Parameters of simulations are listed in Table S5-1 and Table S5-2.

Table S3-1: Simulation parameters for the through focus series

Acceleration voltage	300 kV
Defocus C_1	-20 nm - +20 nm
Spherical aberration constant C_3	10 μm
Specimen thickness	10 nm
Emitter energy spread	1 eV

An example of seria of images corresponding to this thickness is shown in the following Figure S5-1. The individual Mn atomic columns are revealed in the narrow interval of defocus values from -12 to -8 nm (marked with the orange frame).

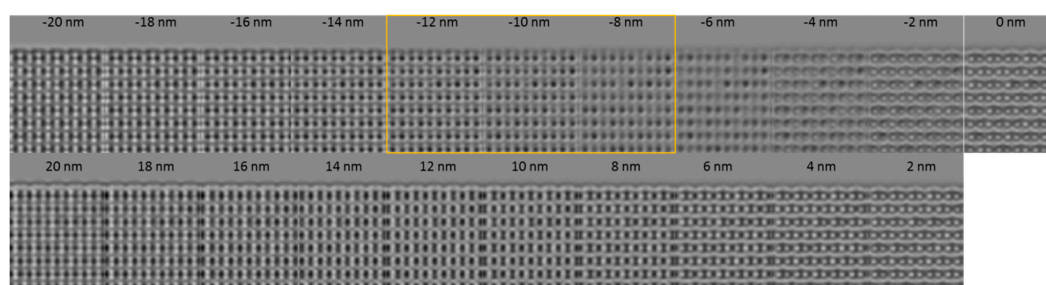


Figure S6-1. Calculated image of B-terminated surface of PCMO ($x=0.33$) projected along [010] corresponding to the thickness of 10 nm

Taking into account the sputtering of material by electron beam the real thickness could be even less than 9 nm. Figure S5-2 shows calculated images of PCMO ($x=0.33$) along [010] and [001] crystallographic directions.

Table S3-2: Simulation parameters for individual experimental images

Acceleration voltage	300 kV
Defocus C_1	-2 nm
Spherical aberration constant C_3	10 μm
Specimen thickness	3 nm
Emitter energy spread	1 eV

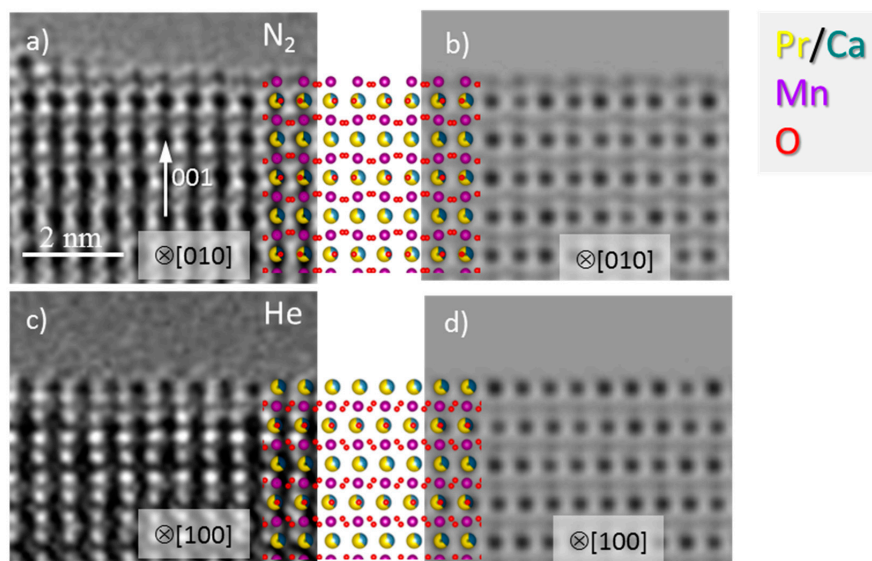


Figure S6-2. (a) Experimental HRTEM image and (b) corresponding calculated image of B-terminated surface of PCMO ($x=0.33$) projected along [010]. (c) Experimental HRTEM image and (d) corresponding calculated image of A-terminated surface of PCMO projected along [100]. The atomic models are shown in between.

The PCMO ($x=0.1$) after electron beam treatment in He at 50 μ bars.

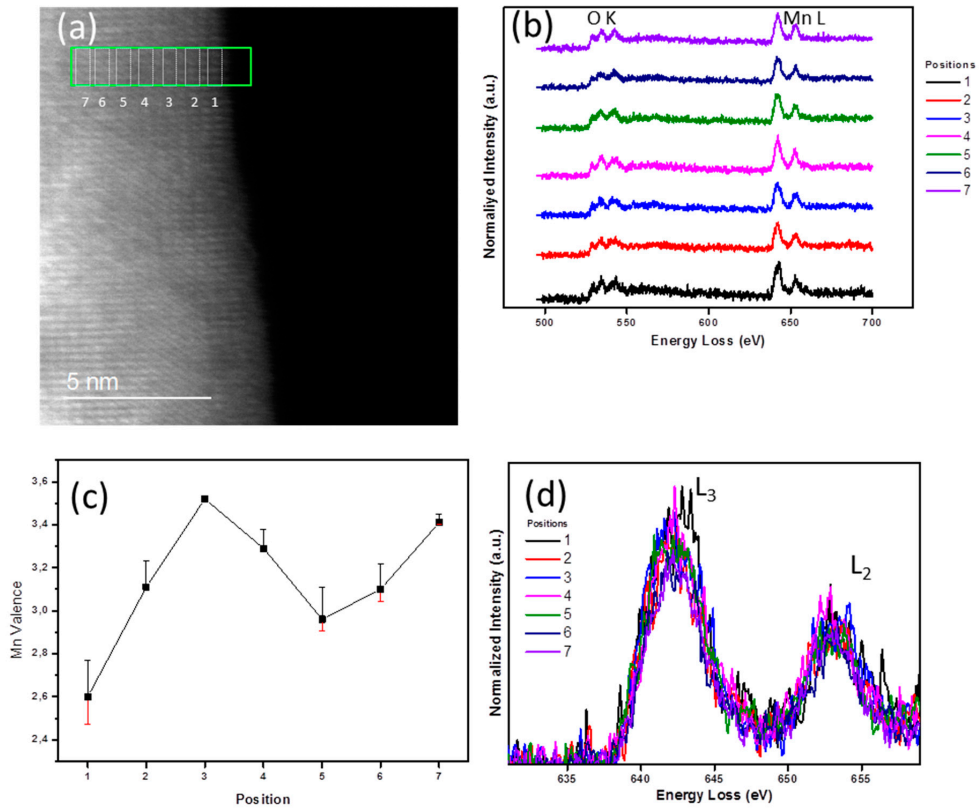


Figure S7. The PCMO ($x=0.1$) after electron beam treatment in He at 50 μ bars. (a) HAADF image; (b) EELS spectra; (c) Mn valence plot; (d) $L_{2,3}$ -edge of Mn at each point.

Table S4. Summary of the Mn valence of PCMO ($x=0.1$) after electron beam treatment in He at 50 μ bars.

The average value is 3.14 ± 0.06

Position	1	2	3	4	5	6	7
Mn valence	2.6	3.11	3.52	3.29	2.96	3.10	3.41
Error (-)	-0.13	0	0	0	-0.054	-0.058	-0.01
Error (+)	0.17	0.12	0	0.09	0.15	0.12	0.04

Verification of structure and chemistry of particles formed at the amorphous edge.

The structure of nanoparticles formed at the amorphous edge of PCMO ($x=0.1$; 0.33) was identified using FFT analysis individually (Fig. S7) and by averaging over many particles similar to reported earlier (see Ref. 18 in the main text). The structure fits to the fcc cubic fluorite structure (Fm3m, $a=0.5393$ nm) of PrO_2 . Moreover, several particles were also analyzed using EELSS. One of spectra is shown in Fig. S7b. Only O-K and Pr-M edges are present.

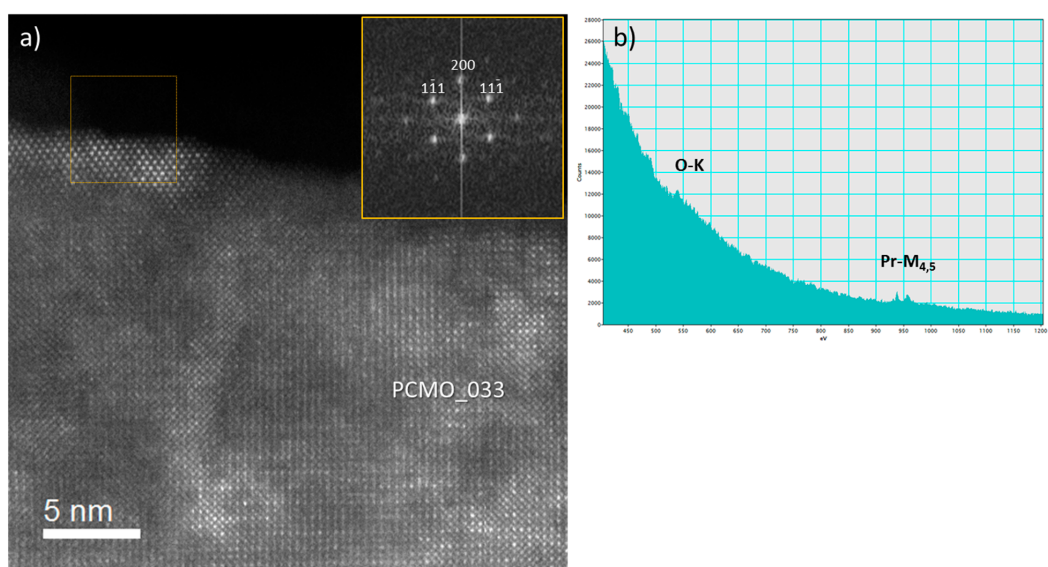


Figure S8. (a) HRSTEM image of PCMO ($x=0.33$) the corresponding FFTs is shown in the inset. (b) EELS spectrum taken from the particle shown in (a). The only O-K and Pr-M_{4,5} edges are present.

Control over the composition and purity of a gas before exposing the sample to the gas.

The mass spectrometry measurements with the rest gas analyzer (RGA) are controlled by the software program Quadera™.

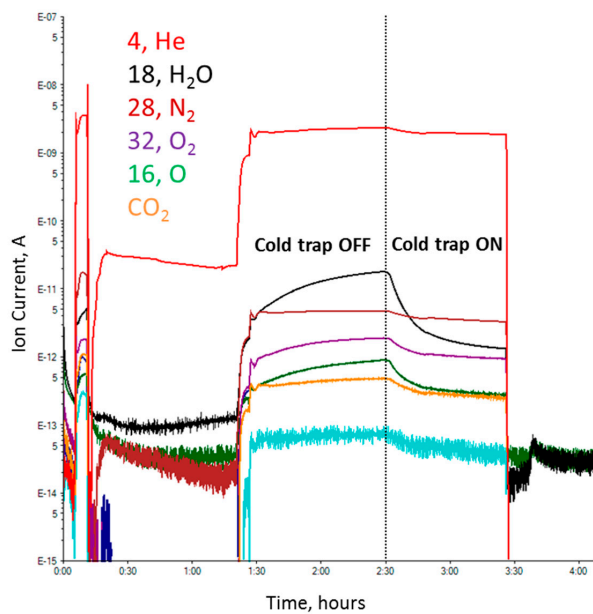


Figure S9 An example of multiple ion detection scan in Quadera™ for the experiment in He with and without using of cold trap.

A.1.1 Supporting Movies

<https://owncloud.gwdg.de/index.php/s/CaypVIYcpbjzUWM>

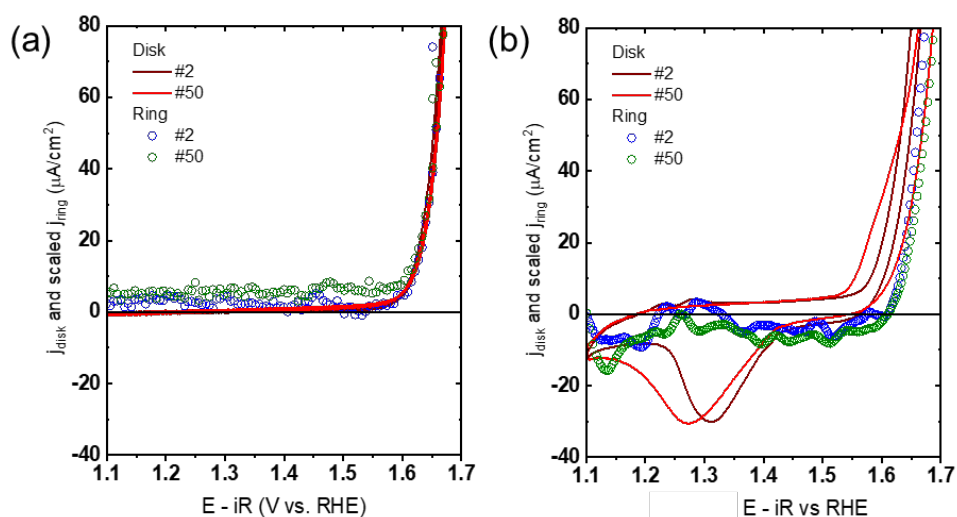
A.2 Dynamic observation of manganese adatom mobility

Supplementary Information

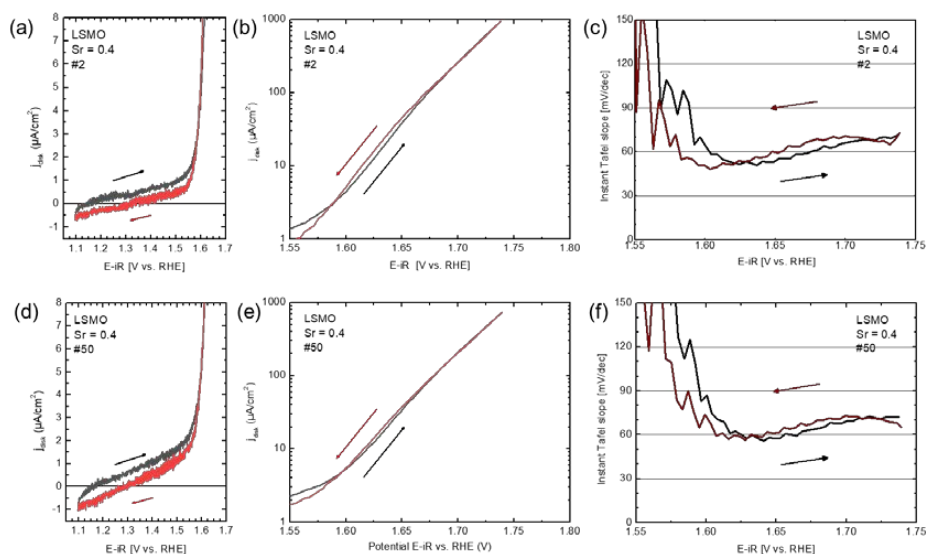
Dynamic observation of Mn-atom mobility at perovskite oxide catalyst interfaces with water.

G. Lole et al.

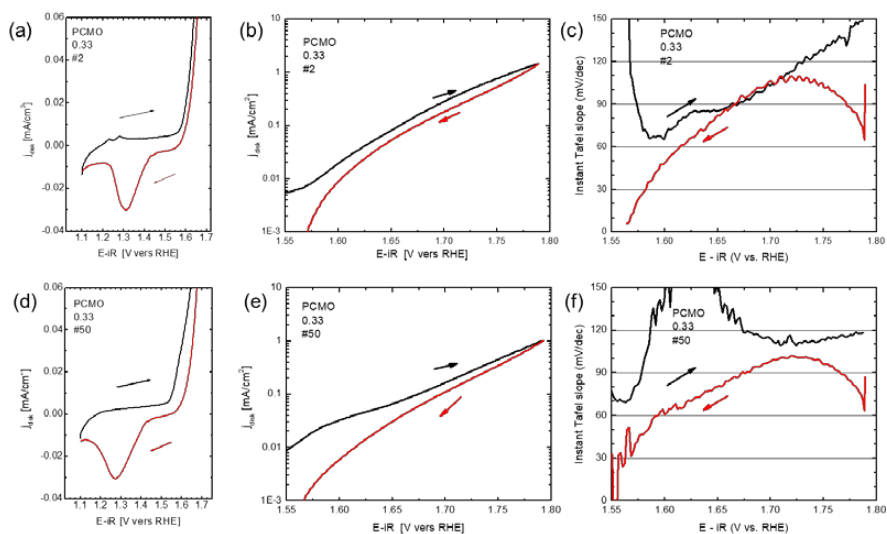
1. Electrochemical characterization of epitaxial (001) oriented LSMO and PCMO electrodes



Supplementary Figure 1: Oxygen evolution of the LSMO $x=0.4$ (a) and PCMO $x=0.33$ (b) films in aqueous 0.1 M Ar-saturated 0.1 M KOH measured by rotating ring disk electrode (RRDE) cyclic voltammetry. The ring current density (circles) is measured at 0.5 V vs. RHE and only the anodic scan is shown. Electrodes were swept at 10 mV/s and rotated at 1600 rpm. For PCMO, the shift of the onset of the ring current compared to the disk current is due to the shoulder in the anodic OER scan caused by oxygen intercalation.

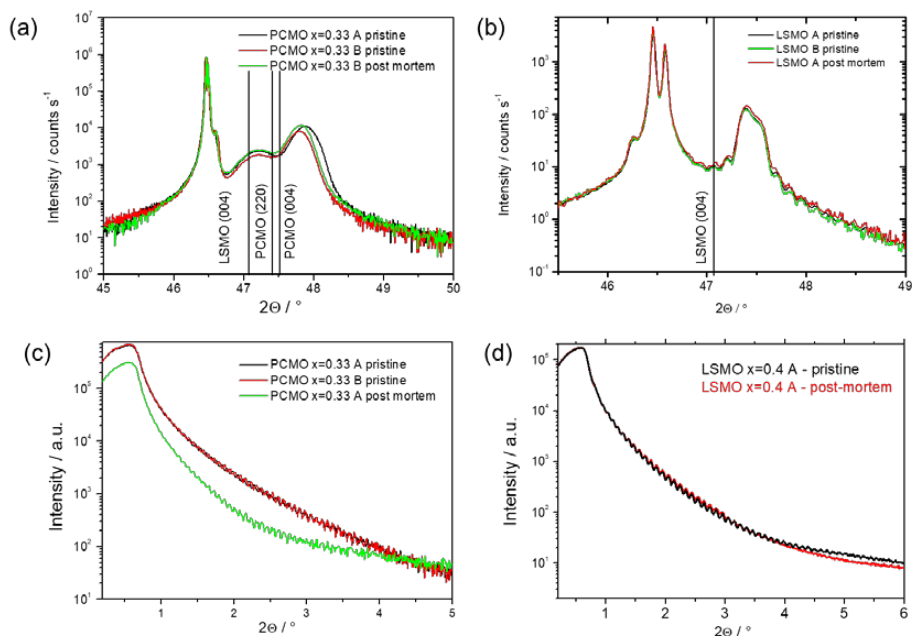


Supplementary Figure 2: Tafel analysis of the LSMO $x=0.4$ thin film in 0.1 M aqueous KOH solution for cycle #2 (a-c) and #50 (d-f). (a,d) Cyclic voltammogram (b,e) Tafel plot and (c,f) instant Tafel slope taken for the disk current. Above 1.6 V vers RHE, the transition from capacitive to catalytic currents sets in, giving a Tafel slope of $b \approx 60$ -70 mV/dec. The voltage resolution of the data in panels b,c,e,f was reduced from 1 mV to 4 mV by averaging before the analysis.

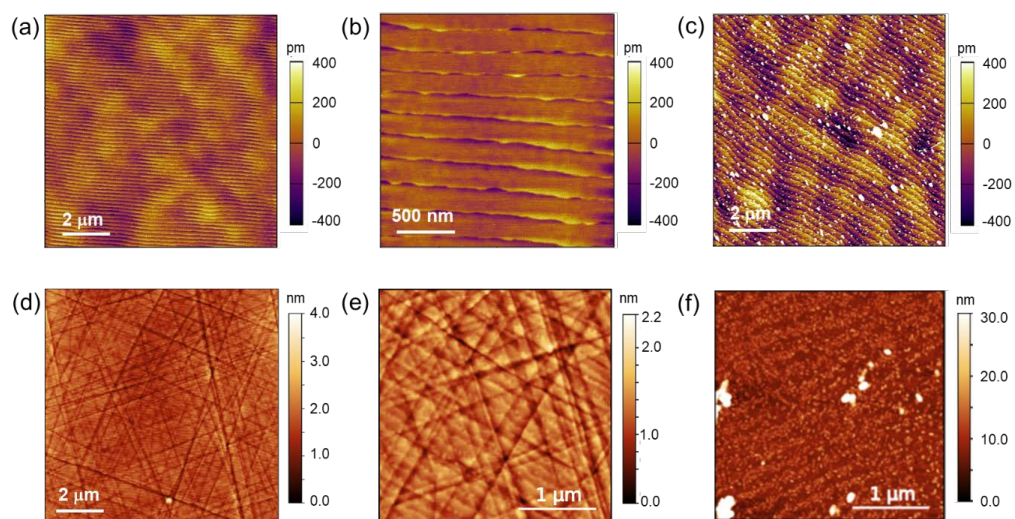


Supplementary Figure 3: Tafel analysis of the PCMO $x=0.33$ thin film in 0.1 M aqueous KOH solution for cycle #2 (a-c) and #50 (d-f). (a,d) Cyclic voltammogram (b,e) Tafel plot and (c,f) instant Tafel slope taken for the disk current. The transition from capacitive to catalytic current above 1.6 V vers RHE is superimposed by pronounced surface redox process, leading to a peak in the Tafel slope of the anodic current at 1.6-1.65 V vers RHE for cycle #2 and at 1.58-1.68 vers RHE for cycle #50. The Tafel slope related to OER of PCMO (001) surface is strongly potential dependent and ranges between 90-120 mV/dec. Tafel slopes for potentials above 1.75 V vers RHE are not further considered because of the large hysteresis of the current.

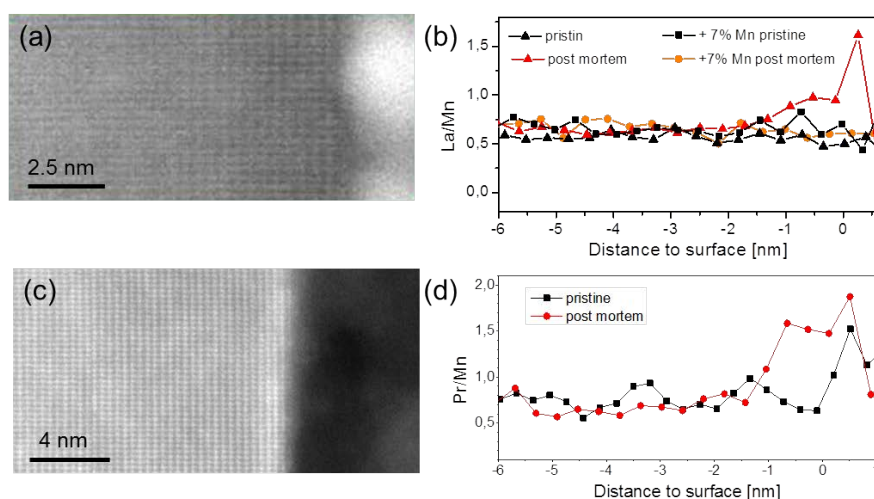
2. Structural characterization of epitaxial (001) oriented LSMO and PCMO electrodes in pristine state and post electrolysis



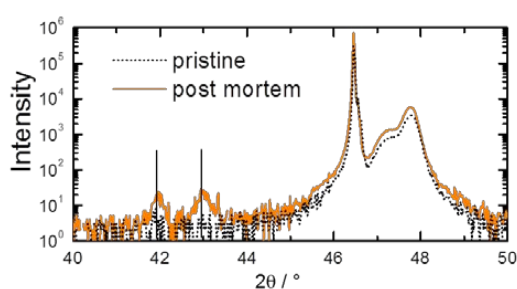
Supplementary Figure 4: X-ray diffraction and x-ray reflectivity of PCMO $x=0.33$ and LSMO $x=0.4$ epitaxial thin films, pristine and after 1 h of OER at 1.7 V vers RHE. (a) Detailed 2θ XRD scan on the (004)/(220) PCMO reflex as well as the (004) reflex of the LSMO buffer layer for two different films. (b) Detailed 2θ XRD scan on the (004) LSMO reflex for two different films. All films show out of plane compressive strain which is consistent to the in-plane tensile strain due to the misfit to the Nb:SrTiO₃ substrate. Peak position is not changed after electrolysis. (c,d) Reflectometry of the PCMO and LSMO films giving a thickness of 104 and 85 nm, respectively. The comparison of pristine and post mortem measurements demonstrates the high stability of the LSMO film, whereas the PCMO films shows changes in thickness and density.



Supplementary Figure 5: Exemplary AFM images of as grown epitaxial LSMO $x=0.4$ (001) (a-b) and PCMO $x=0.33$ (001) (d-e) thin films. (c) and (f) show the surface after 50 cycles of OER between 1.1 and 1.75 V vers RHE and 7 min CA between cycle 3 and 4. Particles are reminiscent of the aqueous electrolyte containing 0.1 M KOH. The thickness of all films is 80 nm.



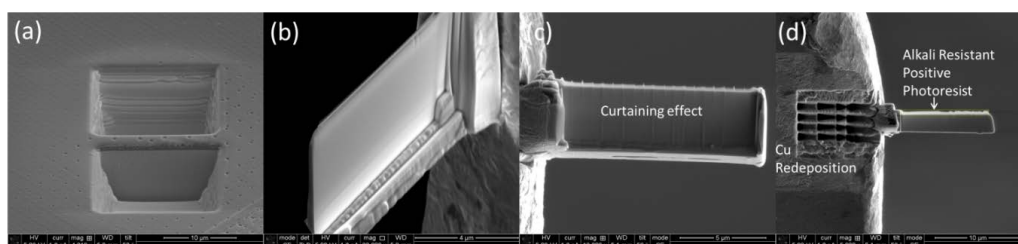
Supplementary Figure 6: Post mortem study of the surface of LSMO (001) (a,b) and PCMO (001) (c,d) films after 1h of electrolysis at a potential of 1.7 V vers RHE. a) STEM HAADF image of a post mortem LSMO film in cross section. The lamella was prepared by FIB using a PtC protection layer, where a Pt particle at the surface of LSMO is visible as a bright area on the right side of the image. (b) Line profiles of the La/Mn ratio as a function of the distance to the surface determined by STEM EELS of a pristine LSMO film, and the same film after electrolysis. Mn depletion is visible for a region of ≈ 1 nm below the surface. In addition, data for a Mn enriched off-stoichiometric film is shown before and after electrolysis, in order to demonstrate reliability of our method. (c) STEM HAADF image of a post mortem PCMO film in cross section. The lamella was prepared by using an epoxy protection layer, visible as the dark region above the surface. (b) Line profiles of the Pr/Mn ratio as a function of the distance to the surface determined by STEM EELS of a pristine PCMO film, and the same film after electrolysis. Strong Mn depletion is visible for a region of ≈ 2 nm below the surface. The Pr/Mn ratio is also somewhat enhanced over the full length of the line profiles in the electrolyzed sample, due to the leaching at the two PCMO-water interfaces normal to the electron beam.



Supplementary Figure 7: Comparison of a PCMO (001) film before and after 3 cycles of voltammetry between 1.1 and 1.8 V vers RHE and 7x1 min of electrolysis at 1.5, 1.55, 1.6, 1.65, 1.7, 1.75 and 1.8 V vers RHE. The new peaks after electrolysis correspond the lattice spacings of 2.15Å and 2.1Å, respectively. The peak at 42° is close to (002) of the cubic PrO₂ structure with $a=0.539$ nm.

4. TEM Lamella/Sample preparation and subsequent surface characterization

For in-situ atomic scale reactions we have fabricated ultrathin TEM lamella by a special technique based on focused ion beam (FIB) and further ion milling, avoiding damaged amorphous surface layers, as well as catalytic protection layers such as Pt¹. Wedge shaped lamella with dimensions of 14 X 2 X 7 μm^3 were cut out of the (001) oriented PCMO and LSMO thin films using FEI Nova NanoLab 600 Dual Beam instrument.

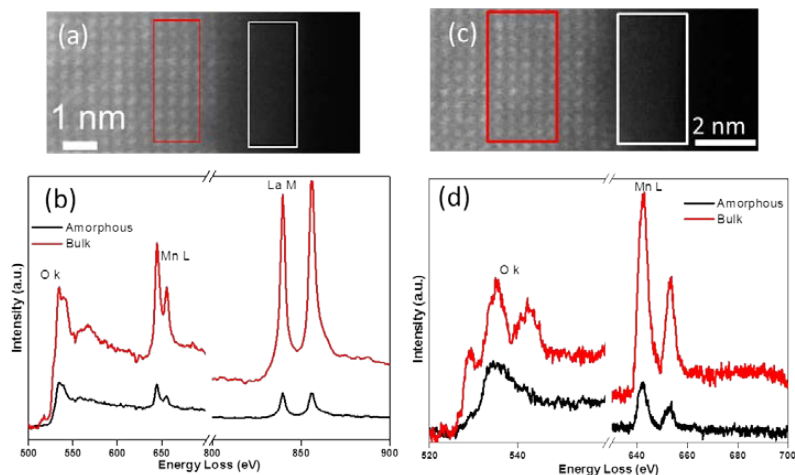


Supplementary Figure 8: SEM-FIB snapshot images of lamella preparation procedure. (a) Cut of a plate-like cross-section lamella using Alkali Resistant Positive Photoresist X AR-P 5900/4 protection layer on the LSMO surface. (b) TEM lamella after thinning procedure in FIB. (c) TEM lamella after glueing to a Cu grid using Cu redeposition technique. Because of inhomogeneous thickness of photoresist, a curtaining-like pattern is observed. (d) Finally thinned lamella with a few hundreds nm photoresist layer is still present on top of the film surface in order to protect the lamella from beam damage.

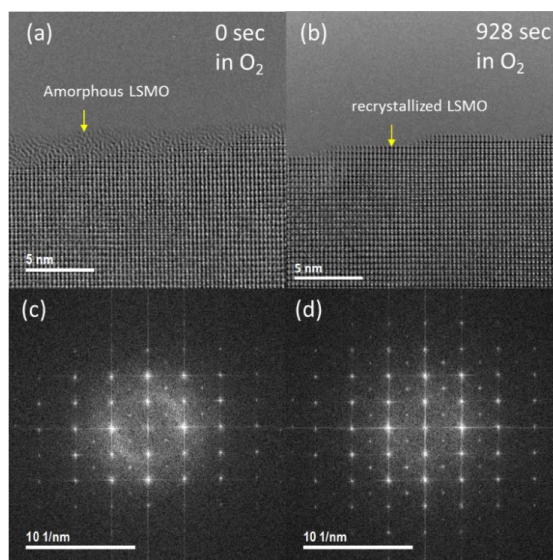
We have used a commercially available Alkali Resistant Positive Photoresist X-AR-P5900/4 (Photoresist) (<http://www.allresist.de/photoresists-xar-p5900-4>), deposited uniformly on the sample surface with a spin coater at 4000 rpm, during 60 sec. The coating was dried for 30 min in the oven (circulating air) at 100 ° C and then, a mask was placed in the center of the sample and exposed for 6 minutes using the UV lamp 360-450 nm. The sample was etched for 20 seconds with 10% NaOH and rinsed well in distilled H₂O, finally 20 sec H₂O in ultrasonic bath. A FIB lamella was then cut and lifted out of the protected area (Supplementary Figure 8). To avoid contamination of platinum in any aspect, TEM lamella is attached to Cu grid carefully by using Cu redeposition technique (Fig S8d). Copper is redeposited from Cu grid to attach the lamella using 30 kV accelerating voltage and 1 nA ion beam current with 1 ms dwell time. The last thinning step was done at 5 kV at ion beam current of 29 pA. Afterwards, the thickness of photoresist protective layer was about 30 nm along the whole surface of the lamella which was removed by a final Ar ion milling step by a Gatan Precision Ion Polishing System 691 (PIPS). We used 100 eV Argon ions and ion current of 0.42 μA for 20 minutes. Before inserting the lamella into the TEM, plasma etching in pure oxygen plasma was performed.

Even after the final Ar ion milling step and oxygen plasma etching we still observed a 2 nm thick amorphous layer on the top of bulk LSMO (Supplementary Figure 9). In order to confirm whether it is a damaged surface during sample preparation, residual photoresist or any kind of contamination, we have investigated this surface by electron energy loss spectroscopy (EELS) analysis. The EEL spectra is recorded with two different energy dispersions. Presence of Mn L and O K edges are clearly seen in the both spectra. In the amorphous areas, the shape of the O k edge is different from typical perovskite

oxide spectra and absence of O K prepeak indicates that reduced LSMO was formed during sample preparation. This is confirmed by the presence of Lanthanum M edge in the amorphous layer.



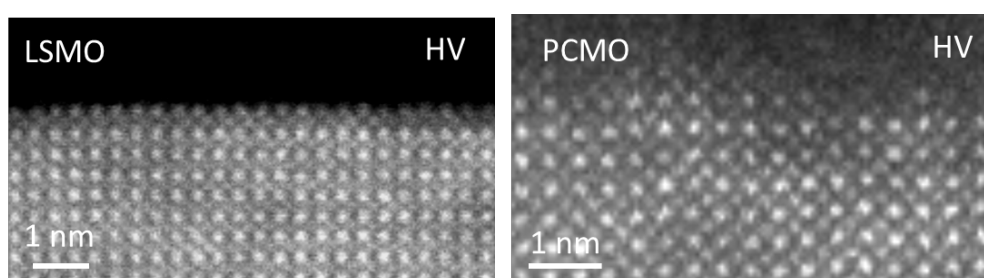
Supplementary Figure 9: Typical surface structure of a LSMO lamella after removal of photoresist by plasma cleaning with a 2 nm thick amorphous layer analyzed by STEM-HAADF (a & c) and EELS (b & d). Red rectangle marks fully crystalline bulk LSMO and white amorphous surface area, where EELS of O K-, Mn L- and La M-edges were recorded, respectively. Absence of the typical 3-fold structure of the O K- edge including the prepeak in amorphous area shows a reduced LSMO state due to preferential sputtering of oxygen by Ar ion milling.



Supplementary Figure 10: HRTEM images of the pristine and recrystallized surface and their corresponding FFT's in 1 mbar O₂. (a) Thin amorphous layer at the top of LSMO surface after final thinning steps of the TEM lamella. (b) Recrystallized surface after 15 min electron beam exposure in 100 Pa of O₂. The absence of amorphous rings in (d) compared to (c) indicates complete recrystallization of amorphous LSMO on all lamella-surfaces.

Similar to the procedure for PCMO $x=0.33^2$, we performed an electron beam induced surface recrystallization and oxidation process of amorphous LSMO under oxygen partial pressure of 1 mbar at room temperature in the ETEM. After continuous exposure to an electron-beam for about 15 minutes, amorphous LSMO was fully recrystallized with nice atomically flat surface facets showing some unit cell height step edges at the top of the surface (Supplementary Figure 10).

Following the recrystallization process, it is found that surface oxidation initially started at the amorphous edge with atomic steps or small pyramids which grows slowly. After a few minutes of exposure to an electron beam with dose rate of $13100 \text{ e}/\text{\AA}^2\text{s}$ in 100 Pa of O_2 single crystalline facets are formed which are served to study in-situ atomic dynamics in H_2O . The recrystallization of the amorphous layer to the crystalline flat facet after few hundred seconds is visible in Movies M08 and M09.



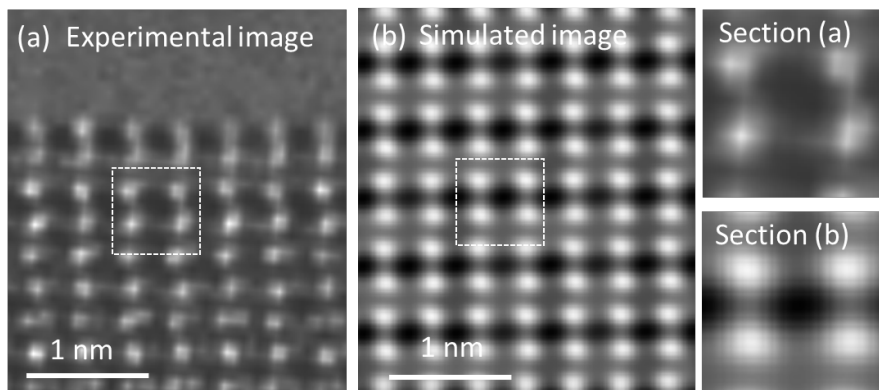
Supplementary Figure 11: STEM HAADF images of the (001) surfaces of LSMO and PCMO after imaged under HV conditions. Whereas LSMO shows a crystalline surface structure dominated by A-layer terminated areas, PCMO exhibits a disordered surface in HV, even after full crystallization in 100 Pa O_2 was achieved. LSMO is imaged in the pseudocubic [010] and PCMO in the orthorhombic [110] zone axis.

5. HRTEM image simulation by the multislice method

Multislice simulations of high-resolution TEM exit wave functions were performed using QSTEM software developed by Christoph Koch³. Subsequently, the aberration parameters were optimized by using a metropolis algorithm implementation to minimize the RMS of the difference between a simulated and an excerpt of the experimental image beneath the surface⁴. Finally, the optimal aberration parameters (see Supplementary Table 1) were used for the image simulations including Mn adatoms.

Parameter	Fit LSMO	Fit PCMO
C1-Defocus	-30 Å	- 63 Å
C3-Cs	-106439.86 Å	- 15817.58 Å
A1-Two fold Astigmatism	20.23 Å	68.09 Å
A1- angle	1.18 rad	2.41 rad
B2-Axial coma	0 Å	8639 Å
Thickness	42 Å	43 Å
Focal spread	100 Å	100 Å
Contrast calibration factor (Sim/Exp) from first A-layer	24	-

Supplementary Table 1: Electron optical parameters determined by fitting simulated contrast to the experimental images.

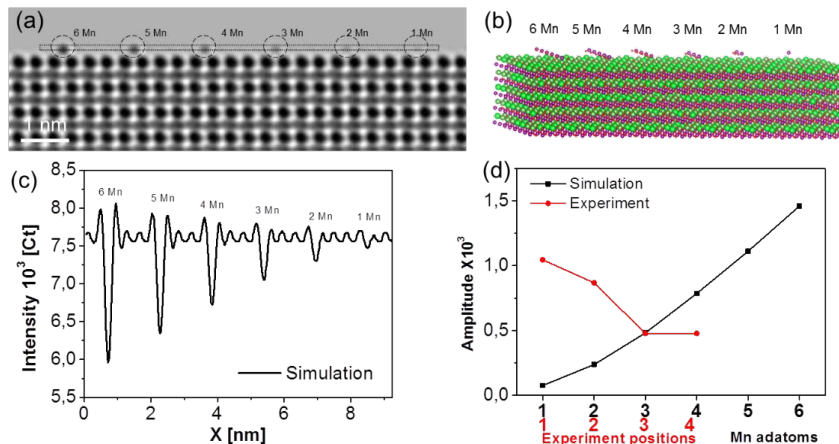


Supplementary Figure 12: Experimental image of LSMO (a) with marked section that was used for image simulation. (b) Simulated image, using the obtained fit parameters of Table S1. Left column: Cut out of the experimental image in (a) and the corresponding simulated image section of (b).

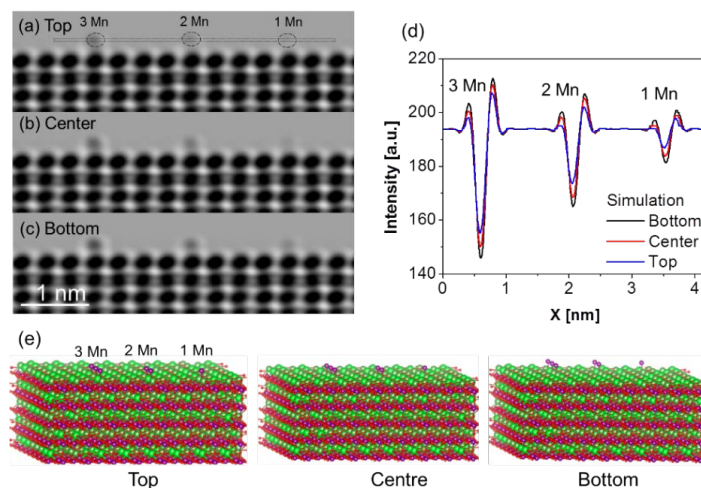
The atomic models of the simulated supercells were created with a custom python script based on the spacegroup $P6mm$ for PCMO with lattice parameters $a = 5.42 \text{ \AA}$, $b = 5.45 \text{ \AA}$ and $c = 7.67 \text{ \AA}$ ⁵, and spacegroup $R\bar{3}c$ for LSMO with a small rhombohedral tilt angle of 90.37° and a pseudocubic lattice constant $a_c = 3.87 \text{ \AA}$ ⁶. We use pseudocubic notation for LSMO in order to facilitate the comparison to PCMO. I.e. the pseudocubic $[110]$ zone axis and (001) surface refers to $[100]$ zone axis and (011) surface in the rhombohedral space group. This is used for image simulation, taking the related octahedral tilting pattern into account. In order to simulate the experimentally established, homogenized occupation of A sites by La/Sr, the A-site atoms were set column by column and chosen to be Sr if the concentration of already set atoms falls below x and La otherwise. For the fitting, a cut out of an experimental image was used for the first subsurface unitcell as shown in Supplementary Figure 12. The same approach is chosen for PCMO with Pr/Ca on the A sites. This leads to a stronger local homogeneity of A-site atoms in comparison to a simple random number generation approach while still preserving the global doping concentration. We justify this local homogeneity with the absence of strong A-site contrast fluctuations in the experimental images which one would observe in the simulations in the case of a random number generated structure.

The models for both materials are constructed with the illuminating beam taken to be incident parallel to the $[110]$ direction of the PCMO and LSMO, respectively. Different numbers of Mn adatoms occupation on the surface B sites at the upper, center and bottom edge were simulated by variation of number of Mn atoms parallel to the electron beam as well as their position. The models are exported in VESTA software for visualization.

6. Single and multiple adatom contrast (LSMO)

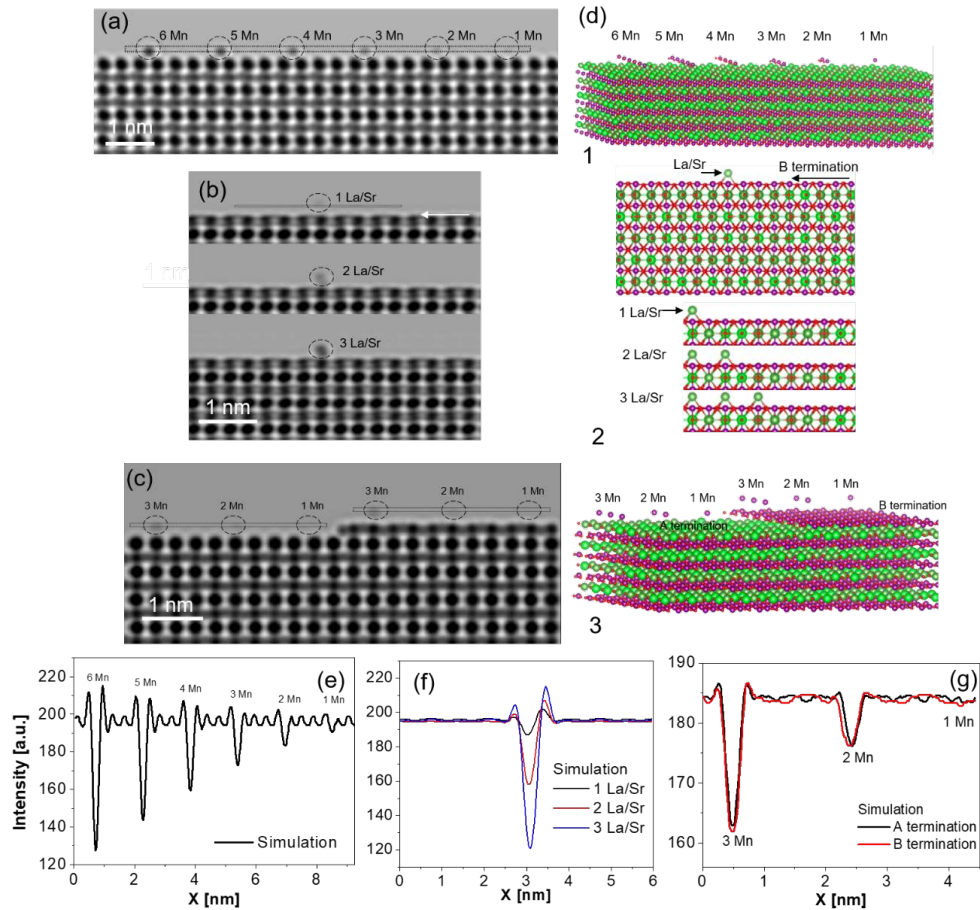


Supplementary Figure 13: Single and multiple adatom contrast. (a) Calculated image of LSMO (001) surface with bulk thickness of 4.2 nm. Black dotted circles show the positions of Mn adatom columns. (b) Visualization of the used surface structure model indicating the position of Mn adatoms columns and number of Mn adatoms at interstitial sites in a surface B-layer. (c) The corresponding line intensity profile (black dotted rectangle marked in Fig (a) for columns with 1-6 Mn adatoms. (d) Amplitude of Mn-contrast for the simulated line profiles, where the scaling factor of the simulated image was determined from the A-site contrast of the surface columns (last line in table Supplementary Table 1). In the experimentally measured contrast amplitudes for the three line profiles in Figure 3 in the main text are shown.



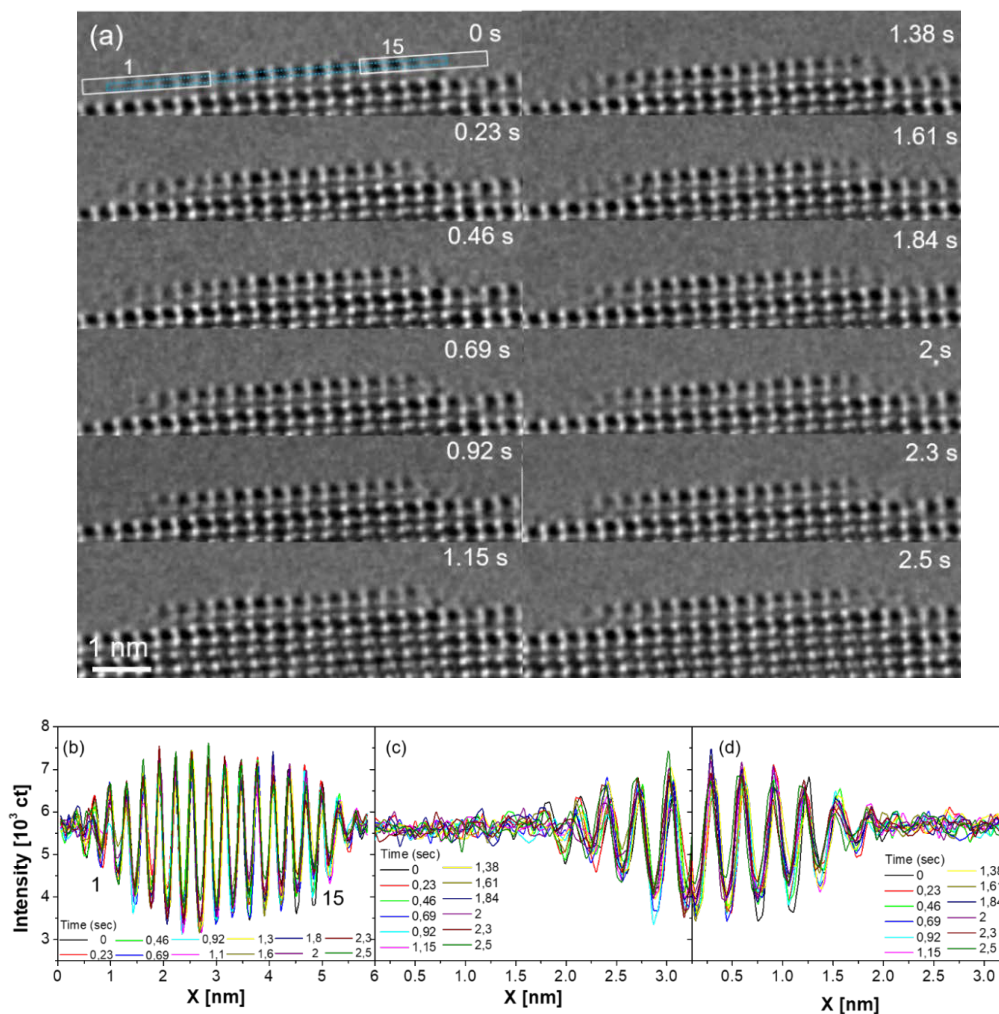
Supplementary Figure 14: Simulated images of LSMO (001) surface with a bulk thickness = 4.2 nm and 1, 2 and 3 Mn adatom per column at the top edge (a), center (b) and bottom edge (c) position at the surface. Black marked areas shows intensity of 1, 2 and 3 Mn adatoms. (d) Line profile at the dotted rectangle marked in (a) for top, center and bottom position of Mn adatoms. (e) Visualization of the surface structure with different positions of the Mn columns with respect to the upper edge of the TEM lamella.

7. Mn adatoms on Mn and La/Sr terminated surfaces (LSMO)



Supplementary Figure 15: Simulated image contrast of A-layer (a), Mn-layer (b) and mix layer terminated (c) LSMO (001) surfaces with a thickness of 4.2 nm and different adatoms at the surface, respectively. (d) Visualization of the crystal models used in (a,b and c) with different adatom configurations. (e) Line profiles of 1-6 Mn adatoms at interstitial positions on an A-terminated surface in (a). (f) 1-3 La/Sr adatoms on a B terminated surface marked in (b). (g) Line profiles of 1-3 Mn adatoms at octahedral positions contrast on A- and B-terminated surfaces in (c).

8. Stability of a unit cell height surface step in H₂O



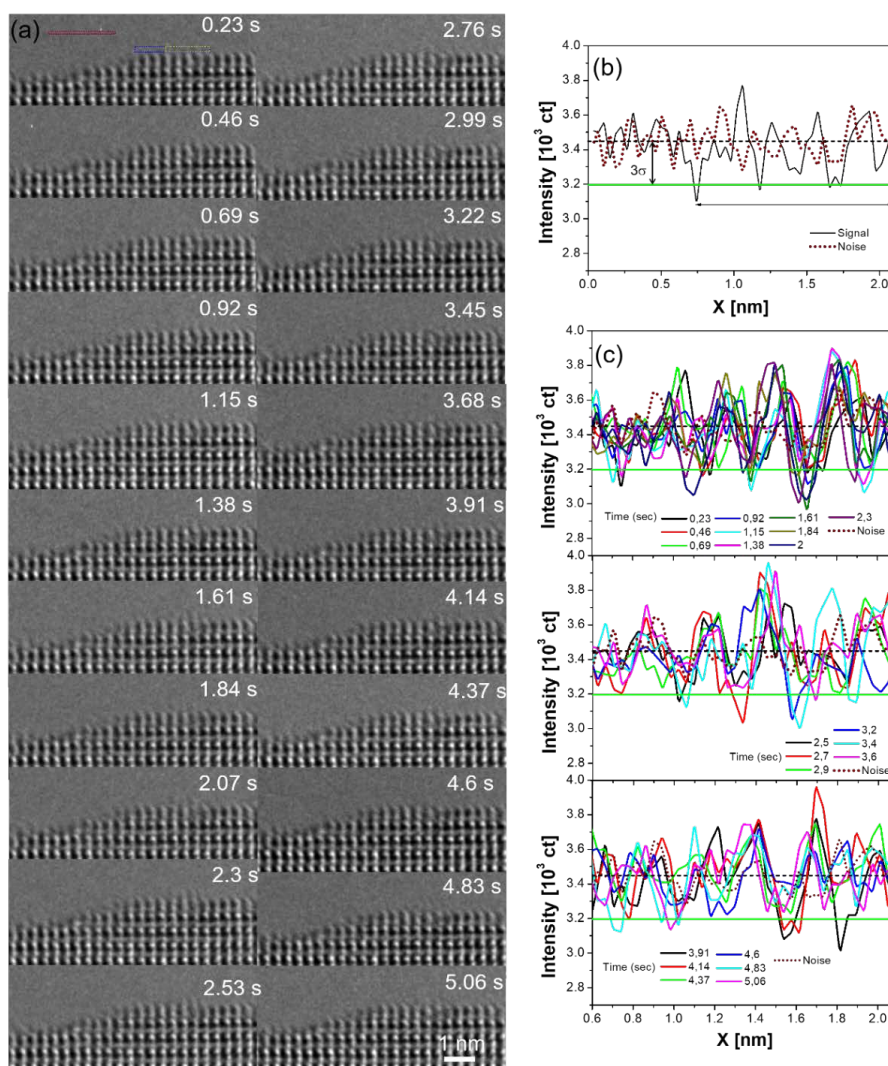
Supplementary Figure 16: Temporal sequence of HRTEM images, showing the A-site terminated LSMO 0.4 (001) surface in 0.5 Pa of H₂O (a). A static A-site terminated surface is formed, where reversible A-site dynamics is only visible at atomic step edges in the real time Movie M02. (b) The corresponding line intensity profiles for the complete unit cell height surface step at the A-site columns marked with blue rectangle in (a). (c and d) shows line profiles for left and right corners of the A-site columns at the step edge marked with white rectangles in (a).

Stable A-site cation atoms termination is observed at room temperature in the in-situ reaction in the controlled water pressure. The disordered LSMO (001) surface formed crystalline edge that is followed by stable A-termination. The HRTEM images Supplementary Figure 16 (a) are extracted with the time difference of 0.23s/frame from the Movie M02. Time resolved image sequence (a) and the corresponding line intensity profile (b) of the atomic step edge suggest that A-terminated surface is remarkably single crystalline ordered and shows atomic mobility. Line profile analysis suggests that

the atomic contrast is fluctuating on a time scale of several seconds on the same position, which can be attributed to the stable of AO terminated (001) surface in H₂O.

9. Mn surface mobility in HV

In order to compare the mobility of adatoms on the (001) surface of LSMO in absence of a liquid water layer, we continued our experiments with in-situ imaging under high vacuum conditions. Supplementary Figure 17 shows a time sequence of HRTEM images (0.23s-5.06s) of the crystalline LSMO surface at an octagon pressure of 2×10^{-5} Pa with a cold trap in the octagon, in order to further reduce the water partial pressure.

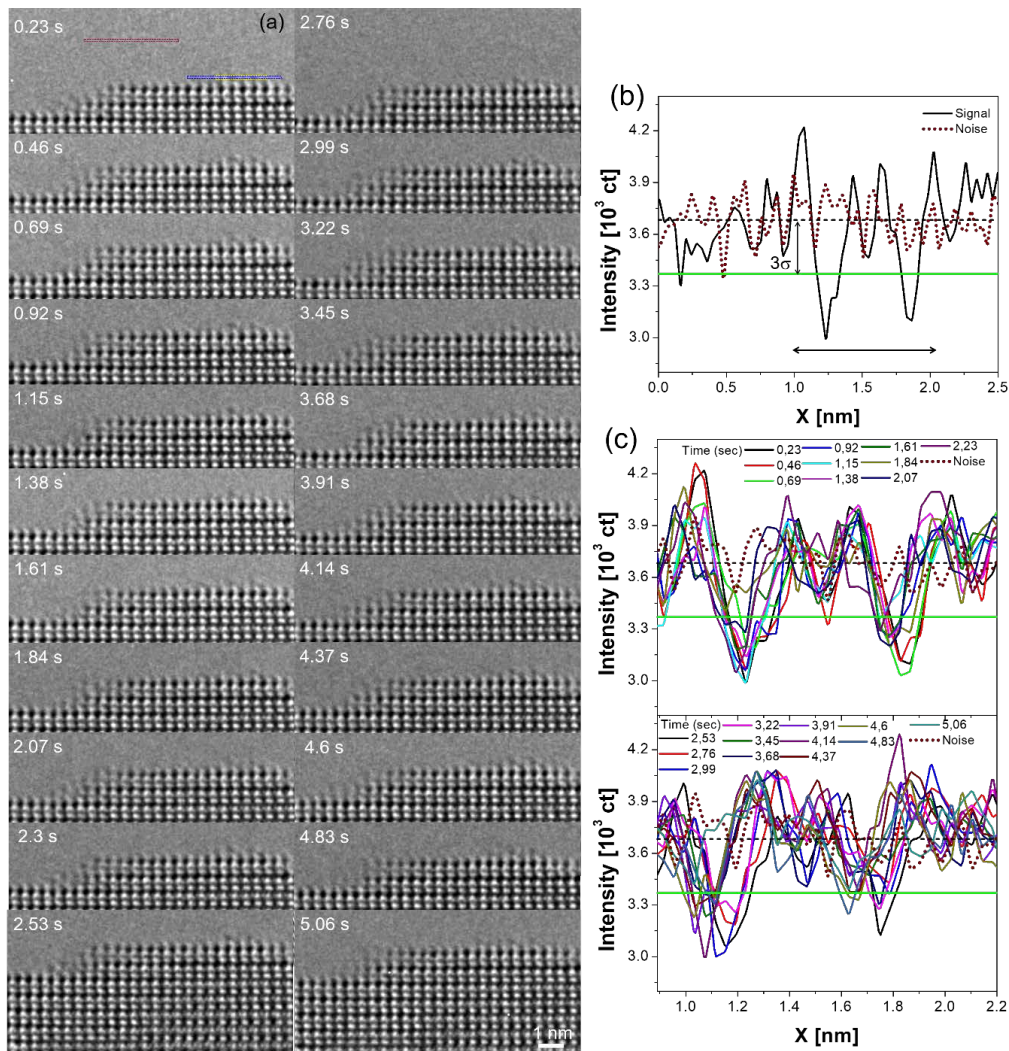


Supplementary Figure 17: (a) Time sequence (0.23s – 5.06 s) of HRTEM images of the LSMO (001) surface in high vacuum. A single crystalline LSMO (001) surface facet was prepared in O₂ and was subsequently used to study atomic dynamics in HV. The crystalline surface in HV shows mixed surface termination and is less mobile as compared to in H₂O. (b) Shows line profile at a B site position

marked as blue rectangle in the image at 0.23s. (c) Line profile of B site position (yellow rectangle) for time sequence from 0.23s-2.3s, 2.5s-3.6s and 3.9s-5.06s, respectively, where most Mn is visible. The Mn terminated areas display a more pronounced disorder compared to A site terminated areas.

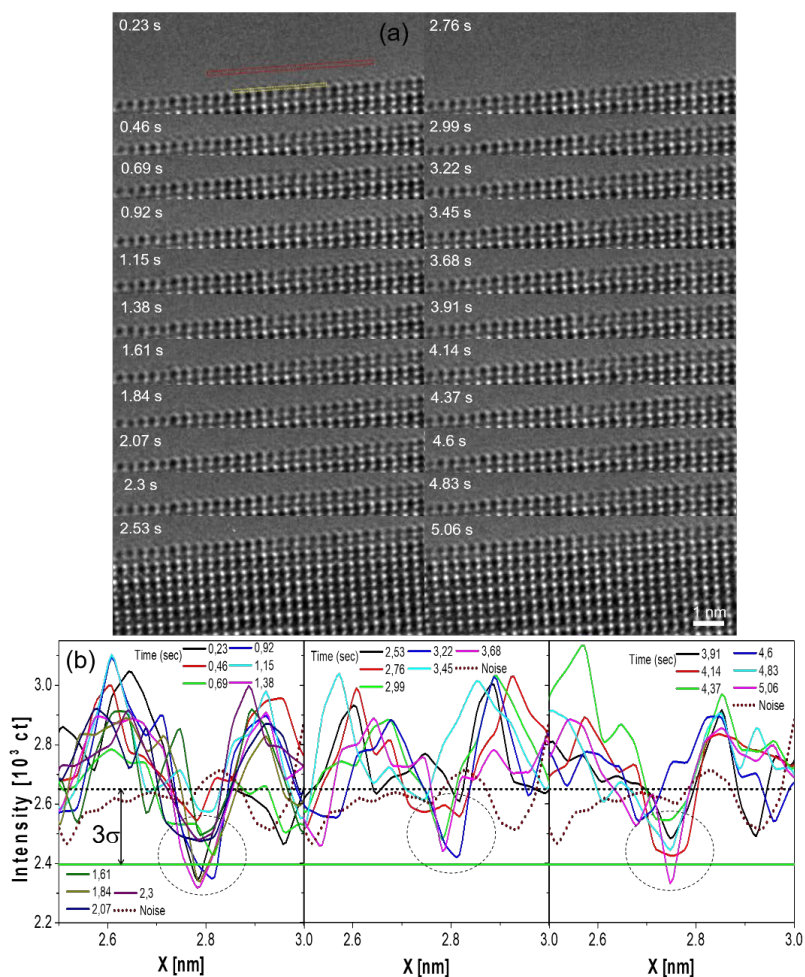
The study of surface stability and atom dynamics of the LSMO (001) surface in HV are presented in Supplementary Figure 17. A stable LSMO (001) surface with mixed surface termination and a higher disorder at the Mn terminate regions is observed in HV. The surface is not changed during 10 min of e beam exposure at approximate $10,000 \text{ e}^-/\text{\AA}^2\text{s}$. For the comparison of Mn surface mobility we have selected a time sequence of HRTEM images from 0.23s-5.06s from the Movie M03 with 4 fps. Supplementary Figure 17 b shows a line profile of a surface area at the B-site positions marked with blue rectangle. The 3σ deviation from the average taken from the noise profile at the brown rectangle in the image at 0.23s is shown. The line profiles in (c) show line are taken from the images at 0.23s-2.3s, 2.5s-3.6s and 3.9s-5.06s, respectively, suggesting that Mn occupation of B site columns can be stable for more than 2 seconds. This also confirms that the rate of Mn surface hopping is with $r < 0.5 \text{ s}^{-1}$ considerably slower in HV. Long-time observation of perovskite structure of LSMO under electron beam in HV for 12 minutes shows no visible structural changes.

10. Mn surface mobility on LSMO (001) in O₂



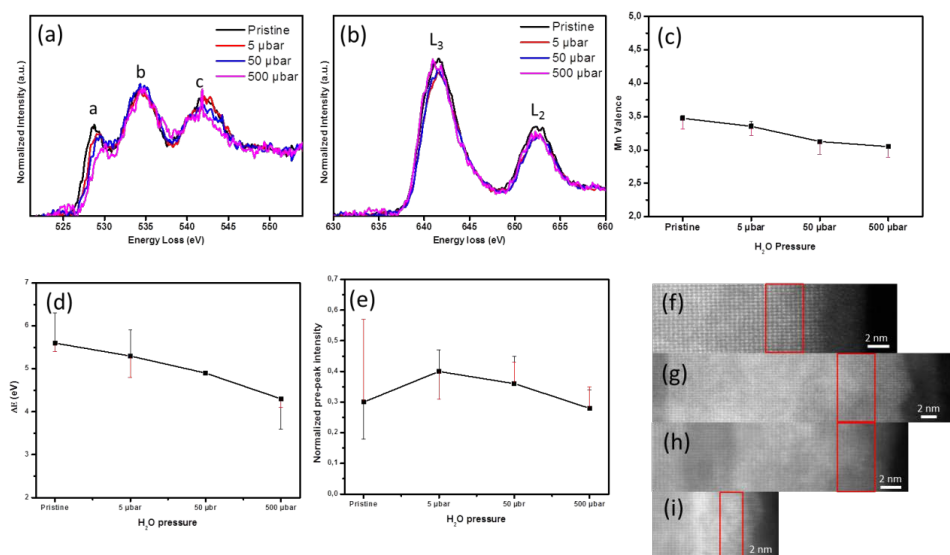
Supplementary Figure 18: (a) Time sequence of HRTEM images of a (001) LSMO surface taken at 0.23 s – 5 s in 100 Pa of O₂ (Movie M04). The surface is predominantly A-site terminated. (b) shows line profile at a B site position (yellow rectangle) and noise with a 3σ line calculated from noise profile in brown rectangle in images 0.23s. (c) Line profiles at a B site position (yellow rectangle) for time sequence from 0.23s-2.3s and 2.5s-5.06s, respectively. Mn adatom sticking time is more than 3 s, i.e. hopping rate is $r \leq 0.33 \text{ s}^{-1}$

11. Mn surface mobility in N₂



Supplementary Figure 19: (a) Time sequence of HRTEM images 0.23s – 5.06 s of a (001) LSMO surface in 10 Pa N₂. The surface is predominantly B-terminated (Movie M05). (b) Line profiles at a B-layer position (yellow rectangle) for time sequence from 0.23s-2.3s, 2.5s-3.6s and 3.9s-5s, respectively. The sticking time is close to 4s, i.e. $r \approx 0.25 \text{ s}^{-1}$. Noise 3σ is calculated from the noise profile taken at the brown rectangle in image at time 0.23s and shown as a dotted line in (b).

12. Post ETEM analysis of the Mn L and O K edges close to the surface of LSMO and PCMO



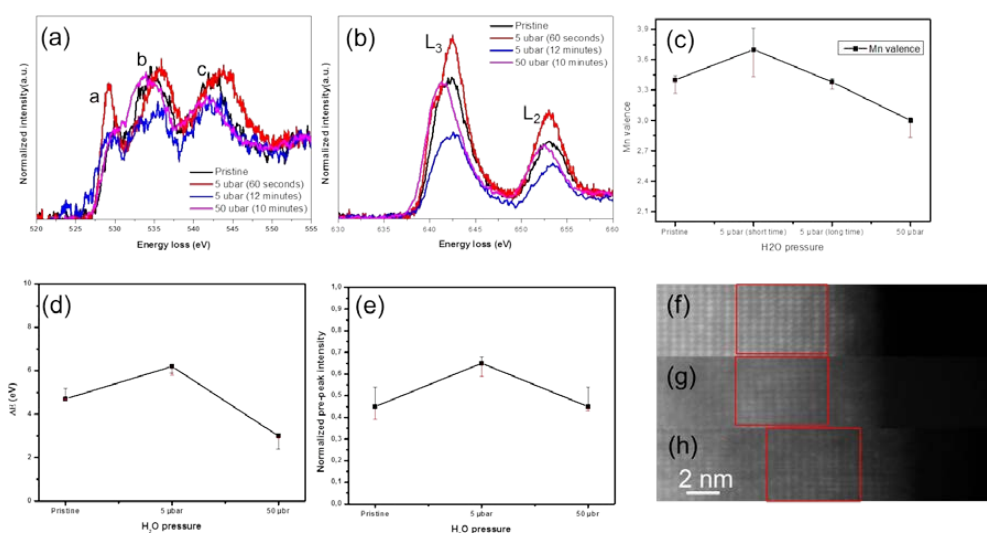
Supplementary Figure 20: Post ETEM EELS analysis at the Mn L-edge and O K-edge of LSMO film after removal of water. The O K (a) and Mn L_{2,3} –edges (b) spectra are taken from the area with red colored rectangles in HAADF-STEM image (f-i) for pristine and $p_{\text{H}_2\text{O}} = 0.5$ Pa, 5 Pa & 50 Pa, respectively. (b) The Mn L₃ edge maximum shows very small noticeable shift for post mortem spectra in water. The close to surface Mn valence change is shown for the pristine sample and different water pressures. (f-i) HAADF-STEM image showing the rectangles, where EELS spectra were recorded. Amorphous areas at the top of the surface which forms after switching back from H₂O to HV state of the octagon is strictly excluded from the analysis due to high amount of Carbon. (d) Energy separation calculated as the difference between pre-peak positions of the second peak ‘b’ and the pre-peak ‘a’ of the O K edge as a function of increase in water pressure. (e) Normalized pre-peak intensity versus water pressure.

We have carried out an extensive investigation of the LSMO (001) surface with high resolution Scanning transmission electron microscopy – electron energy loss spectroscopy (STEM-EELS). The EELS edges shapes and chemical shifts are very sensitive towards crystal field interaction and gives information about 3d occupancy and the valence state of transition metal. Supplementary Figure 20 (a & b) shows O K and Mn L_{3,2} edges corresponding to pristine LSMO surface as well as after reacted with water with pressures of 0.5 Pa, 5 Pa & 50 Pa, respectively. The Mn L edges spectra (b) exhibits two edges L₃ (641-641.5 eV) and L₂ (652-652.5 eV) which are the consequence of the splitting of Mn 2p states in two 2p_{3/2} and 2p_{1/2} due to spin orbit coupling. The Mn valence state in Supplementary Figure 20c is analysed by calculating the L₃ to L₂ ratio and calibration to the data of Varela et al⁷. Whereas there is no change between pristine and 0.5 Pa H₂O within error, a slight reduction of Mn close to the surface is observed at higher pressures.

Supplementary Figure 20 (a) shows O K edge spectra at various water pressures. O K edge spectra is the governed by the excitation of O1s electrons to the O2p unoccupied states (prepeak a), A site d states

(b) and vacuum levels (c)⁸. Empty states in the O2p band are formed due to hybridization with Mn 3d orbitals. As shown in Supplementary Figure 20e, compared to the pristine state, the pre-peak 'a' to O K edge ratio increases at 0.5 Pa and then further decreases at higher water pressure. The latter can be attributed to an increase of the filling of the O 2p states due to electron donors, such as oxygen vacancies or due to Sr leaching. It is consistent to the slight trend of Mn reduction obtained from L3/L2 ratio analysis.

The same post ETEM analysis after H₂O is performed for the PCMO (001) surface is shown in Supplementary Figure 21. Here, a pronounced Mn reduction is observed at 0.5 Pa H₂O. This is consistently obtained from analysis of L3/L2 ratio, energy separation between positions of the second peak 'b' and the pre-peak 'a' of the O K edge and normalized O K pre-edge intensity ratio. Due to the fast Mn leaching in PCMO, the interpretation of the correlation between changes in the L3 and L2 edges compared to the O K edge is not trivial.



Supplementary Figure 21: Post ETEM EELS analysis of the Mn L- and O K-edges of close to surface region of the PCMO (001) film after removal of water. The spectra in O K (a) and Mn L_{2,3} -edges (b) are taken from the area with red colored rectangles in HAADF-STEM image (f-h) for pristine and p_{H₂O} = 0.5 Pa and 5 Pa, respectively. (c) Mn valence change from the pristine to 5 Pa water pressure. (d) Energy separation calculated as the difference between positions of the second peak 'b' and the pre-peak 'a' of the O K edge as a function of increase in water pressure. (e) Normalized pre-peak intensity versus water pressure. (f-h) HAADF-STEM image showing the rectangles where EELS spectra were recorded.

13. Formation of a condensed H₂O layer on oxide surfaces at $p \leq p_{\text{vap}}$

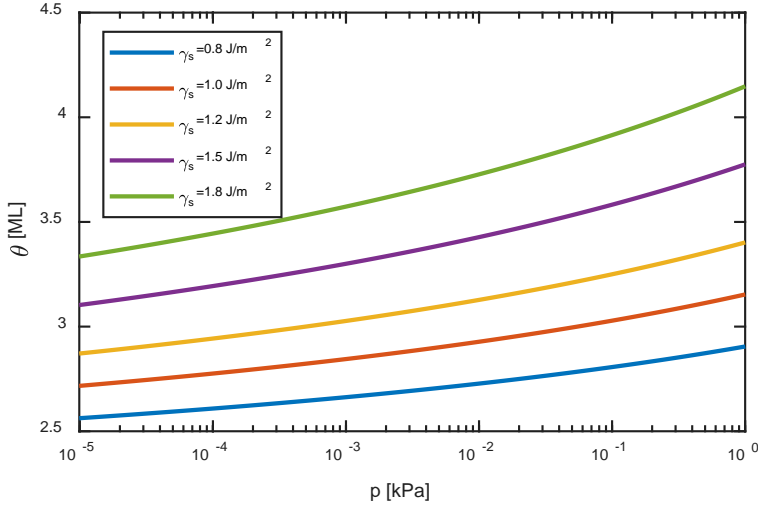
The thickness of a liquid water layer on a metal-oxide surface in the ETEM experiments is calculated as a function of water partial pressure $p_{\text{H}_2\text{O}}$ by using energy balance between the surface energy of the oxide γ_s in HV, the surface energy $\gamma_{\text{H}_2\text{O}}$ of liquid H₂O to H₂O vapor and the adsorption enthalpy of H₂O on the oxide surface, ΔH_{ad} . This results in

$$(1) \quad \gamma_{\text{H}_2\text{O}}(\theta) - \gamma_s = \theta \Delta H_{ad}(\theta, p)$$

For the formation of the first 1-2 monolayers of liquid water, both $\gamma_{\text{H}_2\text{O}}(\theta)$ as well as $\Delta H_{ad}(\theta, p)$ may depend on the coverage θ . Since experiments show that the formation of the first 2-4 monolayers of liquid water on the surface is completed for $p_{\text{H}_2\text{O}} \geq 10^{-5} \text{ Pa}$ ^{9,10,11}, we restrict the calculations to the growth of liquid H₂O on a pre-formed 2ML thick water layer and approximate the water surface energy for $\theta \geq 2$ as a bulk water surface i.e. $\gamma_{\text{H}_2\text{O}}(\theta = 2) = \gamma_{\text{H}_2\text{O},b} = 0.76 \text{ J/m}^2$. For the pressure dependence of the adsorption energy of water on a liquid water surface, we use

$$(2) \quad \Delta H_{ad}(\theta = 2, p) = \Delta H_{ad,b}(p) = \Delta H_{ad,b}(p_{\text{vap}}) + RT \ln\left(\frac{p}{p_{\text{vap}}}\right)$$

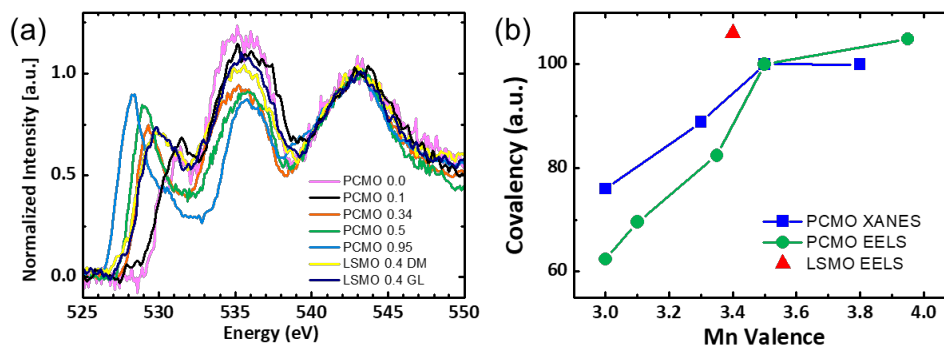
following from the Clausius Clapeyron equation and using the ideal gas law which is a good approximation for $p \leq p_{\text{vap}}$.



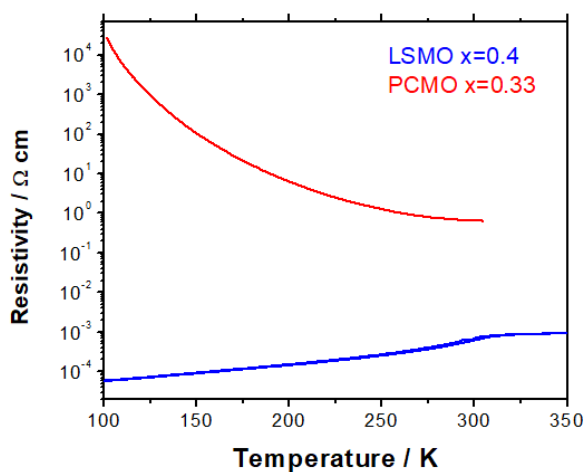
Supplementary Figure 22: Calculated coverage of oxide films with liquid water as a function of the water pressure at 25° C. The driving force for the condensation of water is the large adsorption enthalpy of H₂O on metal oxide surfaces, modified by difference between the surface energy γ_s of the oxide and that of a water surface $\gamma_{\text{H}_2\text{O},b} = 0.76 \text{ J/m}^2$.

Supplementary Figure 22 shows the surface coverage of liquid water following from Eq. (1) for different surface energies γ_s . The surface energy of perovskite oxides strongly depends on the surface termination¹². A theoretical calculation of a (001) LaMnO₃ surface yields $\gamma_s \approx 0.9 \text{ J/m}^2$ [ref¹³]. Independently of the choice of γ_s , the thermodynamic model shows that liquid H₂O can be condensed on top of a preformed condensed H₂O layer.

14. Covalency factor and electric transport of PCMO and LSMO



Supplementary Figure 23: a) Electron energy loss spectra (EELS) of the O K-edge PCMO $x=0$, 0.1, 0.34, 0.5 & 0.95 and LSMO $x=0.4$, respectively. Background is subtracted by polynomial fitting and intensity is normalized to the OK_c peak at energy of 543 eV. b) Covalency analysis with respect to Manganese valence. The covalency factor is obtained by integrating the OK pre-edge peak in an energy range between 525-532 eV and dividing the integral by the Mn valence. Afterwards all covalency factors are normalized to that of PCMO $x=0.5$, in order to visualize the trend upon doping.



Supplementary Figure 24: Typical temperature dependent resistivity of the epitaxial (001) LSMO and PCMO films of thickness of 80 nm and 100 nm, respectively. The hopping type conductivity of PCMO $x=0.33$ is due to the formation of small polaron quasiparticles with an electron-phonon coupling constant of $\alpha \approx 3$ and a binding energy of about 370 meV¹⁴. In contrast, the metal like conductivity of LSMO $x=0.4$ is due to a large polaron with an electron-phonon coupling constant of $\alpha \approx 1-1.5$ resulting a binding energy of around 100 meV at room temperature¹.

References

1. Mierwaldt, D. *et al.* Environmental TEM Investigation of Electrochemical Stability of Perovskite and Ruddlesden-Popper Type Manganite Oxygen Evolution Catalysts. *Adv. Sustain. Syst.* **1**, 1700109 (2017).
2. Roddatis, V., Lole, G. & Jooss, C. In situ preparation of $\text{Pr}_{1-x}\text{Ca}_x\text{MnO}_3$ and $\text{La}_{1-x}\text{Sr}_x\text{MnO}_3$ catalysts surface for high-resolution environmental transmission electron microscopy. *Catalysts* **9**(9), 751 (2019).
3. Koch, C. Determination of Core Structure Periodicity and Point Defect Along Dislocations. Ph.D. Thesis, Arizona State University, Tempe, AZ, (2002).
4. Rump, L. Determination of Electron Optical Aberrations by Image Matching : Implementation of a Simulated Annealing Approach. Bachelor 's Thesis, Georg-August-Universität, Göttingen. (2018).
5. Collado, J. A. *et al.* Room temperature structural and microstructural study for the magneto-conducting $\text{La}_{5/8-x}\text{Pr}_x\text{Ca}_{3/8}\text{MnO}_3$ ($0 \leq x \leq 5/8$) series. *Chem. Mater.* **15**, 167–174 (2003).
6. Zemni, S. *et al.* The effect of a cation radii on structural, magnetic and electrical properties of doped manganites $\text{La}_{0.6-x}\text{Pr}_x\text{Sr}_{0.4}\text{MnO}_3$. *J. Solid State Chem.* **177**, 2387–2393 (2004).
7. Varela, M. *et al.* Atomic-resolution imaging of oxidation states in manganites. *Phys. Rev. B - Condens. Matter Mater. Phys.* **79**, 085117 (2009).
8. Sotoudeh, M. *et al.* Electronic structure of $\text{Pr}_{1-x}\text{Ca}_x\text{MnO}_3$. *Phys. Rev. B* **95**, 235150 (2017).
9. Ketteler, G. *et al.* The nature of water nucleation sites on $\text{TiO}_2(110)$ surfaces revealed by ambient pressure X-ray photoelectron spectroscopy. *J. Phys. Chem. C* **111**(23), 8278–8282 (2007).
10. Srinivasan, S. G. *et al.* Crystal structures, surface stability, and water adsorption energies of La-Bastnäsita via density functional theory and experimental studies. *J. Phys. Chem. C* **120**, 16767–16781 (2016).
11. Opitz, A., Scherge, M., Ahmed, S. I. U. & Schaefer, J. A. A comparative investigation of thickness measurements of ultra-thin water films by scanning probe techniques. *J. Appl. Phys.* **101**, 064310 (2007).
12. Liang Y. & Demkov A. *Interfacial Properties of Epitaxial Oxide/Semiconductor Systems*. In: Demkov A.A., Navrotsky A. (eds) *Materials Fundamentals of Gate Dielectrics*. Page-341. (Springer, Dordrecht, 2005).
13. Mantz, Y. A. New LaMnO_3 surface energy results obtained from density-functional theory. *Surf. Sci.* **695**, (2020).
14. Hoffmann, J. *et al.* Effects of interaction and disorder on polarons in colossal resistance manganite $\text{Pr}_{0.68}\text{Ca}_{0.32}\text{MnO}_3$ thin films. *Mater. Res. Express* **1**, 046403 (2015).

A.2.1 Supporting Movies

<https://www.nature.com/articles/s43246-020-00070-6#Sec19>

A.3 Contrasting $\text{Pr}_{1-x}\text{Ca}_x\text{MnO}_3$ OER catalysis

Supplementary Information

Contrasting $\text{Pr}_{1-x}\text{Ca}_x\text{MnO}_3$ OER catalyst with different valence and covalence: $x=0.1$ and $x=0.33$

Gaurav Lole^{1,2}, Fatemeh Ebrahimi¹, Tobias Meyer¹, Daniel Mierwaldt¹, Vladimir Roddatis^{1,3},
Janis Geppert^{1,4}, Marcel Risch^{1,5} & Christian Jooss^{1,2} *

¹Institute of Materials Physics, University of Goettingen, Friedrich-Hund-Platz 1, 37077
Goettingen, Germany

²International Center for Advanced Studies of Energy Conversion (ICASEC), University of
Goettingen, D-37077 Goettingen, Germany.

³Present address: Helmholtz-Zentrum Potsdam Deutsches GeoForschungsZentrum GFZ,
Telegrafenberg 14473, Potsdam, Germany.

⁴Present address: Institute for Applied Materials – Electrochemical Technologies, Karlsruhe
Institute of Technology, Adenauerring 20b, 76131 Karlsruhe

⁵Helmholtz-Zentrum Berlin für Materialien und Energie GmbH, Young Investigator Group
Oxygen Evolution Mechanism Engineering, 14109 Berlin, Germany.

* Corresponding author.

Email: Christian Jooss: cjooss@gwdg.de

Structural characterization of epitaxial (001) oriented PCMO

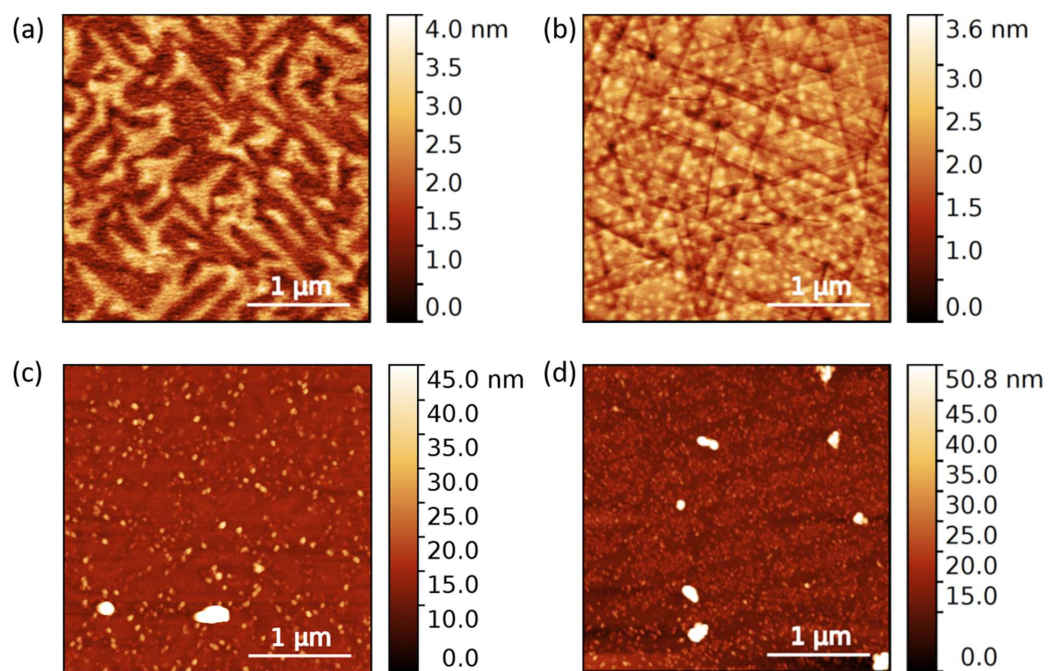


Figure S1. AFM images of (a) as grown epitaxial PCMO $x=0.1$ (001) and (b) PCMO $x=0.3$ (001) (c) the surface of PCMO $x=0.1$ after 50 cycles of OER and (d) the surface of PCMO $x=0.3$ after 50 cycles of OER. Particle on the surfaces are residue of the 0.1 M KOH aqueous electrolyte.

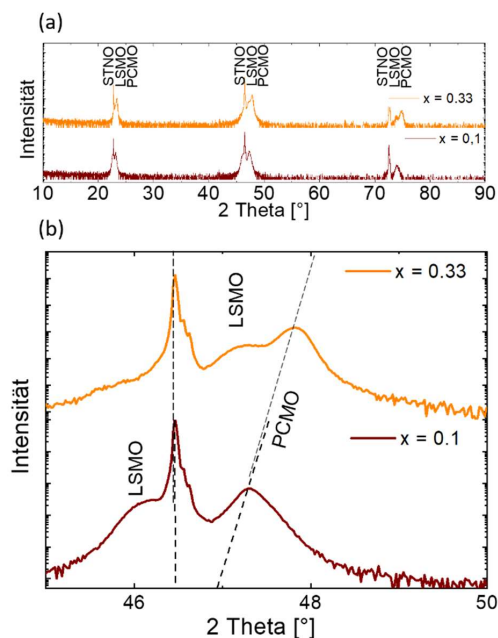


Figure S2. Logarithmically plotted XRD of epitaxially grown PCMO $x=0.1$ and $x=0.33$ thin films. (a) STNO substrate peaks and the intensity of the X-rays diffraction at the LSMO and PCMO lattice planes confirms the epitaxial growth. (b) Trend of STNO, LSMO, PCMO in the PCMO $x=0.1$ (001) and $x=0.33$ thin films.

Electrochemical measurement and characterization of epitaxial (001) oriented LSMO and PCMO electrodes

In order to prepare electrodes for electrochemical investigation, a layer of a 5-nm Ti and 100-nm Pt was prepared by IBS as backside contacts for the STNO substrate. This back contact ensures an ohmic contact. Furthermore, In Ga eutectic (Sigma-Aldrich, Munich, Germany, 99.99%) were served as a conductive material to assemble the film on a stainless steel cylinder with the help of carbon tape. As a result, only the thin film surface was exposed to the electrolyte in the final assembly after fixation with chemically stable, nonconductive epoxy (Omegabond 101).

The electrochemical measurements were carried out using two Interface 1000E (Gamry Instruments Inc., Warminster, PA, USA) and an RRDE-3A rotator (ALS Co. Ltd., Tokyo, Japan). The rotating ring electrode consists of a disk electrode of the assembled thin film with a diameter of 4 mm ($A = 0.126 \text{ cm}^2$) and a Pt ring electrode with an inner diameter of 5 mm and an outer diameter of 7 mm. The electrochemical investigations were done in 0.1 M KOH electrolyte prepared by diluting KOH solution (Sigma Aldrich, Munich, Germany) with deionized water (MilliQ, $>16.5 \text{ M}\Omega$). The electrolyte was saturated with Ar gas at least 30 min before measurements and continuously purged with Ar on top of the electrolyte during the measurement. Electrode

potentials were converted to the reversible hydrogen electrode (RHE) scale using $E_{\text{RHE}} = E_{\text{appl}} + E_{\text{ref}}$.

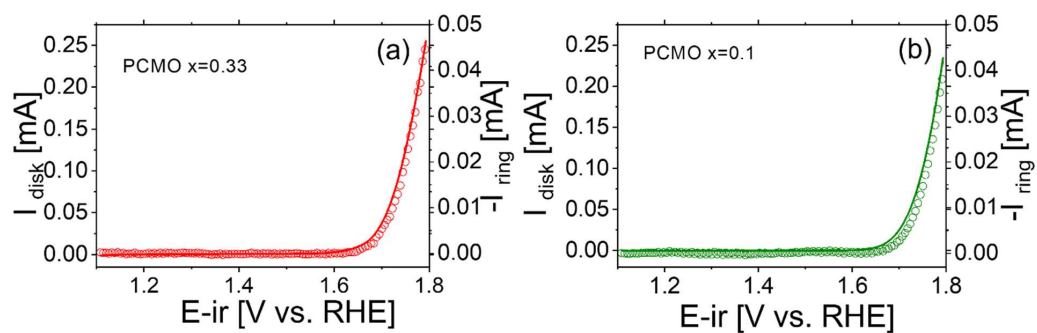


Figure S3. Cyclic voltammograms of (a) PCMO $x=0.33$ (solid red line) and (b) PCMO $x=0.1$ (solid green line) thin films discs and the corresponding ring current (open red and green circles) for oxygen detection at the ring electrode respectively. The voltage was corrected for electrolyte resistance.

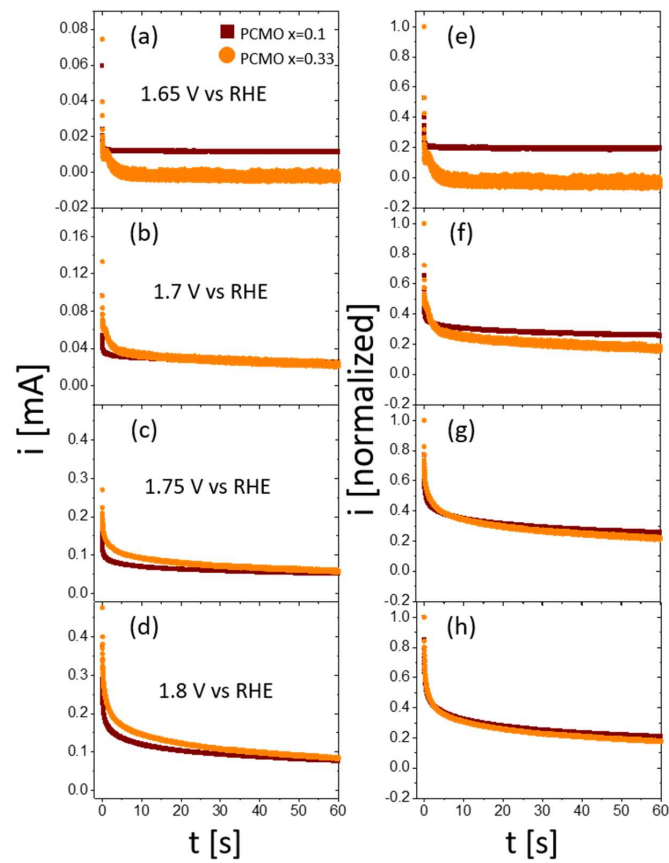


Figure S4. Chronoamperometric measurements (a-d) show current at different applied potentials as a function of time in Argon saturated electrolyte. (e-h) shows normalized plots of (a-d) respectively.

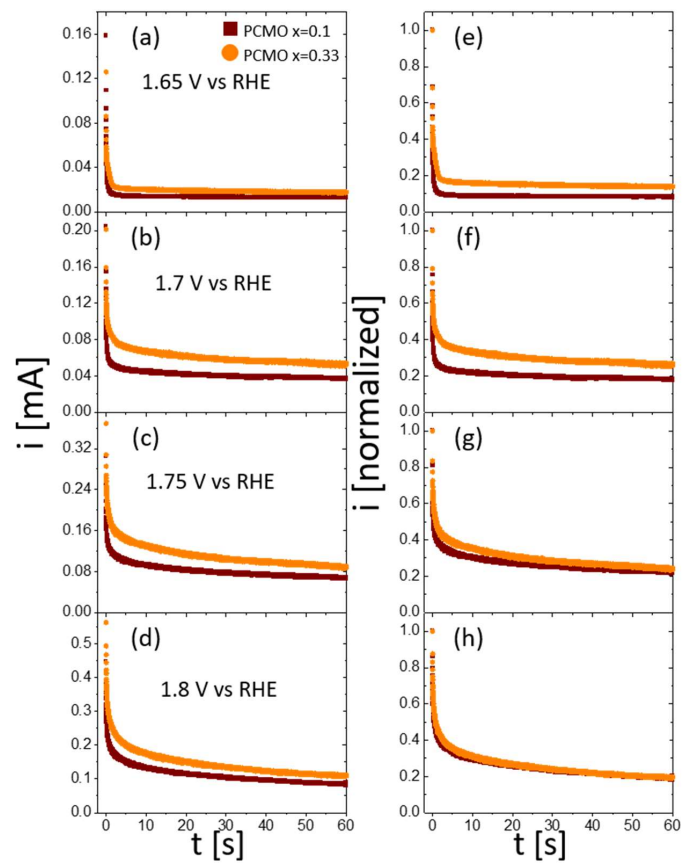


Figure S5. Chronoamperometric measurements (a-d) show current at different applied potentials as a function of time in Oxygen saturated electrolyte. (e-h) shows normalized plots of (a-d) respectively.

TEM Lamella/Sample preparation

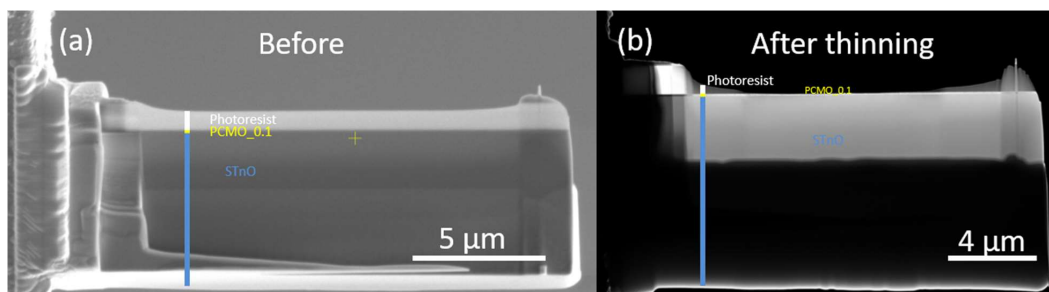


Figure S6. (a) A cross-section lamella of PCMO $x=0.1$ before thinning. (b) TEM lamella after careful thinning procedure in FIB. Lamella preparation is followed from the ref¹.

Surface recrystallization

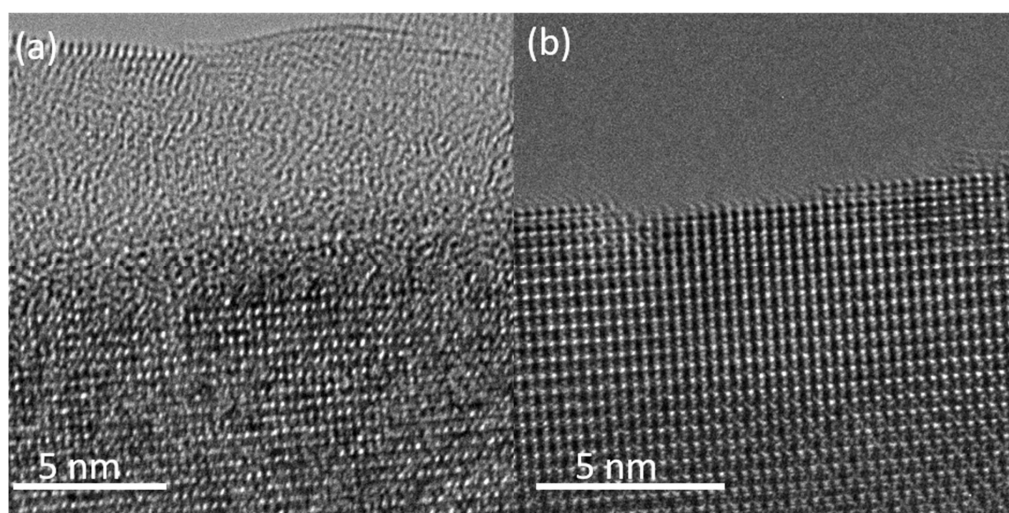


Figure S7. HRTEM images of the as prepared and recrystallized surface in 100 Pa of O_2 . (a) Thin amorphous layer at the top of PCMO $x=0.1$ surface after thinning in FIB. (b) Recrystallized surface after ≈ 12 min of electron beam exposed in ETEM at 100 Pa of O_2 .

Surface dynamics in HV

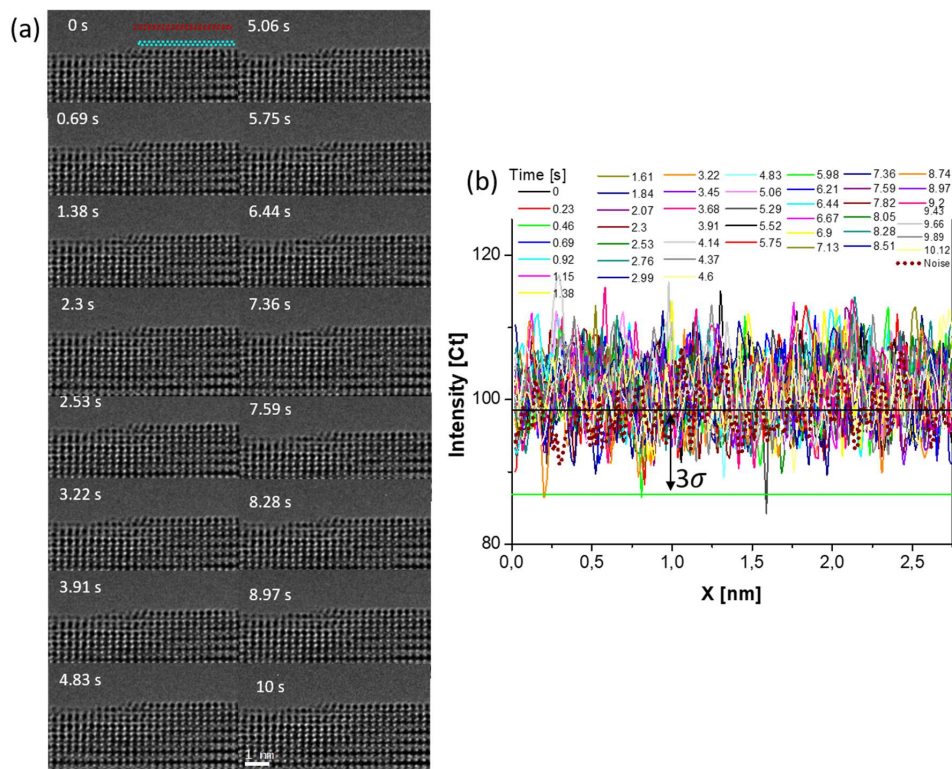


Figure S8. (a) Time sequence (0s – 10 s) of HRTEM frames of the PCMO $x=0.1$ (001) surface in high vacuum (Movie M9). The (001) recrystallized surface in 100 Pa of O_2 is used to study atomic dynamics in HV. The single crystalline atomically flat surface in HV shows mixed A-site and B-site surface termination and is less active as compared to in H_2O . (b) Line profile at top of A-site terminated position marked as blue rectangle in the image at 0s. Surface shows almost no Mn mobility in HV.

Surface dynamics in 1 mbar O₂

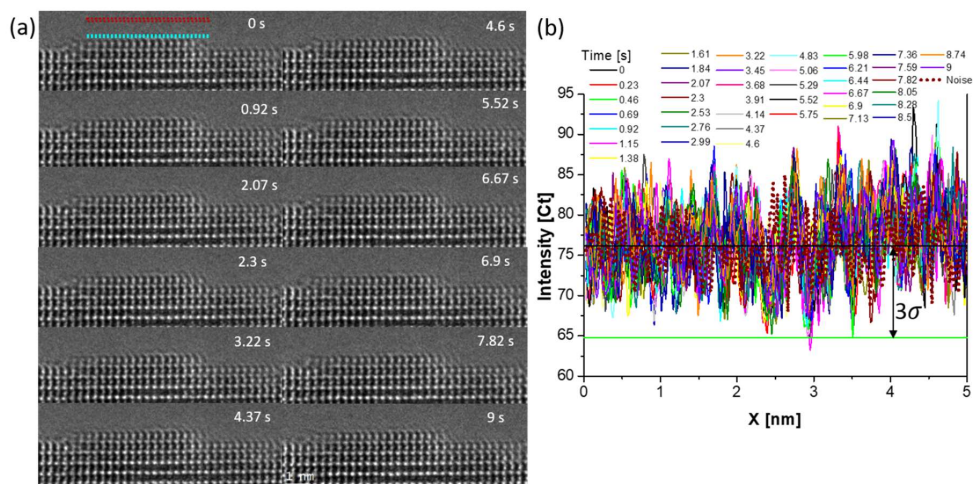


Figure S9. (a) Time sequence of HRTEM images of PCMO $x=0.1$ (001) surface recorded at 0s – 9 s in 100 Pa of O₂ (Movie M6). The surface is dominantly A terminated in O₂. (b) shows line profile at a B site position above the A-site terminated surface (blue rectangle) and noise (brown rectangle) with a 3σ line calculated from noise profile in images 0s.

Surface dynamics in H₂O

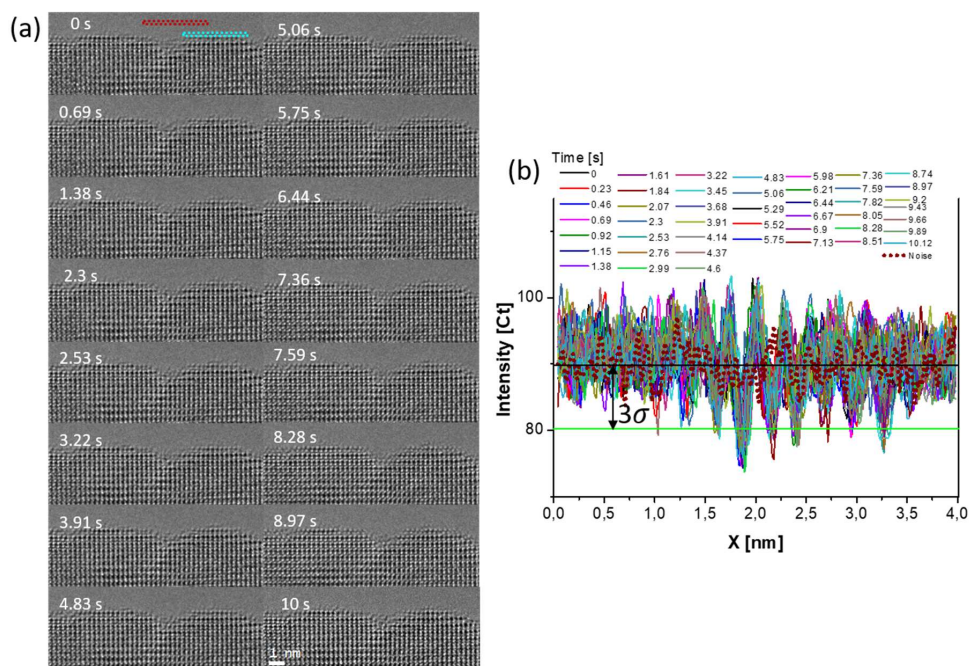


Figure S10. (a) Time sequence of HRTEM images of PCMO x=0.1 (001) surface in 0.8 Pa of H₂O (Movie M1). b shows line profile above A-site terminated surface (blue rectangle) and noise (brown rectangle) with a 3σ line calculated from noise profile shown in images 0s. Fluctuating/blinking type behaviour at same position of Mn atomic columns is clearly visible in the line profile.

References

- (1) Lole, G.; Roddatis, V.; Ross, U.; Risch, M.; Meyer, T.; Rump, L.; Geppert, J.; Wartner, G.; Blöchl, P.; Jooss, C. Dynamic Observation of Manganese Adatom Mobility at Perovskite Oxide Catalyst Interfaces with Water. *Commun. Mater.* **2020**, *1* (1), 68. <https://doi.org/10.1038/s43246-020-00070-6>.

A.3.1 Supporting Movies

<https://owncloud.gwdg.de/index.php/s/j20MXuukhogNBhP>

A.4 $\text{La}_{0.6}\text{Sr}_{0.4}\text{CoO}_3$ surface dynamics

SUPPORTING INFORMATION

Atomistic insights into activation and degradation of $\text{La}_{0.6}\text{Sr}_{0.4}\text{CoO}_{3-\delta}$ electrocatalysts under oxygen evolution conditions

Moritz L. Weber^{a,*}, Gaurav Lole^{b,c}, Attila Kormanyos^d, Alexander Schwiers^a, Lisa Heymann^a, Florian D. Speck^{d,e}, Tobias Meyer^b, Regina Dittmann^a, Serhiy Cherevko^d, Christian Jooss^{b,c}, Christoph Baeumer^{a,f} and Felix Gunkel^{a,*}

^aPeter Grünberg Institute (PGI-7) and JARA-FIT, Forschungszentrum Jülich GmbH, Jülich, 52425, Germany; Institute of Materials Physics, ^bUniversity of Göttingen, Göttingen, 37077, Germany; ^cInternational Center for Advanced Studies of Energy Conversion (ICASEC), University of Göttingen, Göttingen, 37077, Germany; ^dHelmholtz-Institute Erlangen-Nürnberg for Renewable Energy (IEK-11), Forschungszentrum Jülich GmbH, Erlangen, 91058, Germany; ^eDepartment of Chemical and Biological Engineering, Friedrich-Alexander-Universität Erlangen-Nürnberg, Erlangen, 91058, Germany; ^fMESA+ Institute for Nanotechnology, University of Twente, Faculty of Science and Technology, Enschede, 7500 AE, The Netherlands

*Email: mo.weber@fz-juelich.de; f.gunkel@fz-juelich.de

Figure S1. Recrystallization of the FIB lamella for ETEM investigations.

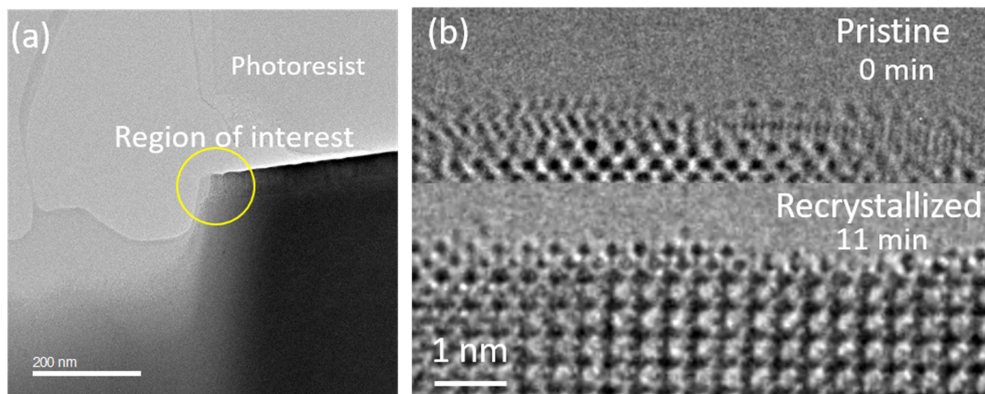


Figure S1. Lamella and surface preparation. (a) TEM image of region of interest (ROI). The photoresist protection layer is removed during lamella thinning procedure in FIB. (b) HRTEM images of the pristine and recrystallized LSCO surface. The thin amorphous layer at the top of LSCO surface formed during ion milling procedure in FIB can be recrystallized by electron irradiation of the surface. The image shows the result after 11 min in 100 Pa of O₂ (dose rate – 10320 e/A²s).

To reduce beam damage during FIB preparation of the LSCO lamella for ETEM investigations, a photoresist protection layer is applied. After removal of the protection layer by FIB thinning, only minor amorphization of the topmost surface is evident (Fig. S1, above). To reconstruct the perovskite structure in order to provide for an atomically sharp interface region, the LSCO surface recrystallized by electron irradiation (Fig. S1, below). For detailed information about the recrystallization procedure, we refer to reference (1).

Figure S2. Observation of a well-ordered and stable surface in O₂

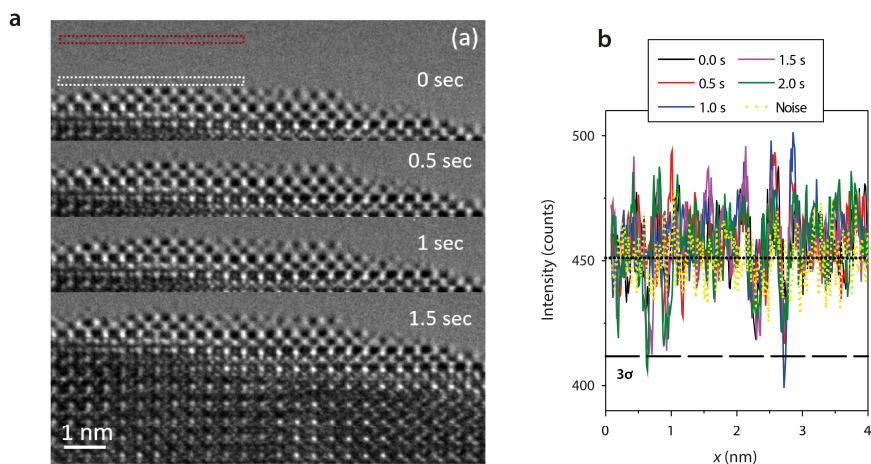


Figure S2. (a) Time sequence of HRTEM images of a (001) LSCO surface from 0 s – 1.5 s recorded in a 2.7 Pa O₂ atmosphere with a frame rate of 2 fps (Movie M1). The surface shows an ordered A-site termination. (b) Line profiles are recorded close above the A-site terminated surface as indicated by the white rectangle in the first image of the time series to quantitatively evaluate the hopping events under oxygen environment. The noise level is determined above (red rectangle) and the 3 σ threshold is calculated from the noise signal, which indicates the detection limit of Co adatoms.

After recrystallization of the LSCO surface, a sharp A-site terminated surface is visible, which remains stable in O₂ environment. Notably, the thin film deposition is carried out under oxidizing conditions and hence may result in a similar surface termination. A time series shown in Fig. S2 reveals no considerable contrast fluctuations associated to Co hopping events taking place at the surface under O₂ exposure. The statistically significant detection of transition metal atoms requires triple occupation, i.e. three adatoms lined up in the direction of the incident electron beam on the A-terminated surface. Hence, intensity fluctuations above 3 σ reflect the appearance and disappearance of adatom contrast, correlated to the hopping processes of cobalt moieties from the subsurface region onto the surface and vice versa. Only few signals above the 3 σ level are evident by line profiles acquired at the interface (white rectangle). The noise level i.e. the background fluctuations of the CCD signal is recorded in the vacuum region above the surface (red rectangle). Given the required triple occupation for the statistically significant detection of Co adatoms and considering the limited frame rate of the CCD detector, a lower limit of the surface adatom hopping rate of 0.5 s⁻¹ can be determined for O₂ conditions. In comparison, the lower limit of the surface adatom hopping rate during H₂O exposure was found to be 4.0 s⁻¹, which emphasizes the high mobility of Co species at the LSCO-H₂O interface, under near-OER conditions of the perovskite electrocatalyst.

Figure S3. Investigation of the LSCO surface dynamics in 0.5 Pa of H₂O.

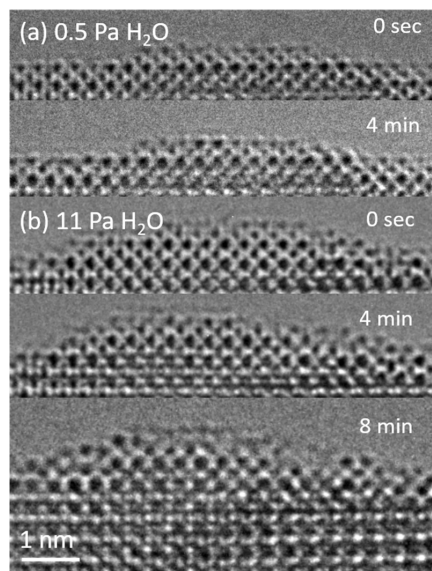


Figure S3. (a) HRTEM frames at 0 sec and 4 min recorded in 0.5 Pa of H₂O showing very slow formation of disordered layer on the surface in low H₂O pressure. (b) HRTEM frames with the time interval in 11 Pa of H₂O taken from the movie M4. Fast formation of a highly dynamical disordered surface in high partial pressure of H₂O.

Fig. S3a shows a series of HRTEM images acquired at the LSCO-H₂O interface over the time of several minutes at equal conditions to Fig. 3c of the main manuscript (0.5 Pa H₂O). Here, the formation of a disordered surface layer proceeds slow in comparison to investigations at increased partial pressures of 11 Pa H₂O (Fig. 3b), where the disordered surface layer forms during a comparably short time imaging time.

Figure S4. EELS analysis of the La-M-edge.

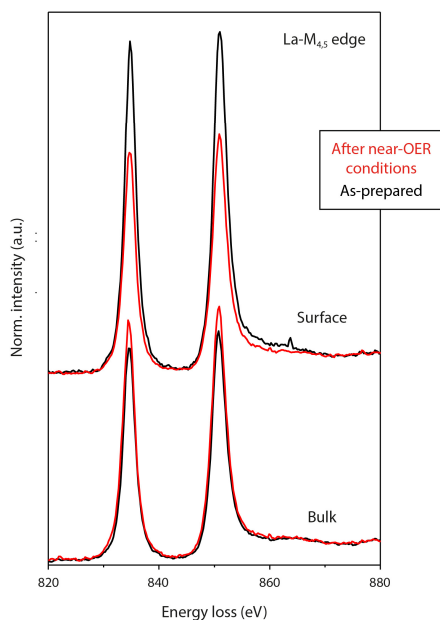


Figure S4. Electron energy loss spectroscopy. EELS analysis of the La-M-edge spectra is performed in the as-prepared state (O_2) and after near-OER conditions after transfer to vacuum (1×10^{-5} Pa) of the LSCO catalyst comparing the surface and the bulk region.

Fig. S4 shows the La-M-edge recorded in the as-prepared state and after near-OER conditions and comparing the bulk and surface region of the catalyst. In comparison to the O-K-edge and Co-L-edge only a small differences are visible for the different ample states. Here, a decrease in the intensity but no change in the spectral shape or shift in the peak position is visible for the surface region. No significant shift observed for La M-edge confirms high precision of the energy calibration by zero loss peak and the observed shift in Co L-edge in Fig. 4 of the main text is due to the interaction with H_2O .

Figure S5. On-line ICP-MS analysis of strontium dissolution.

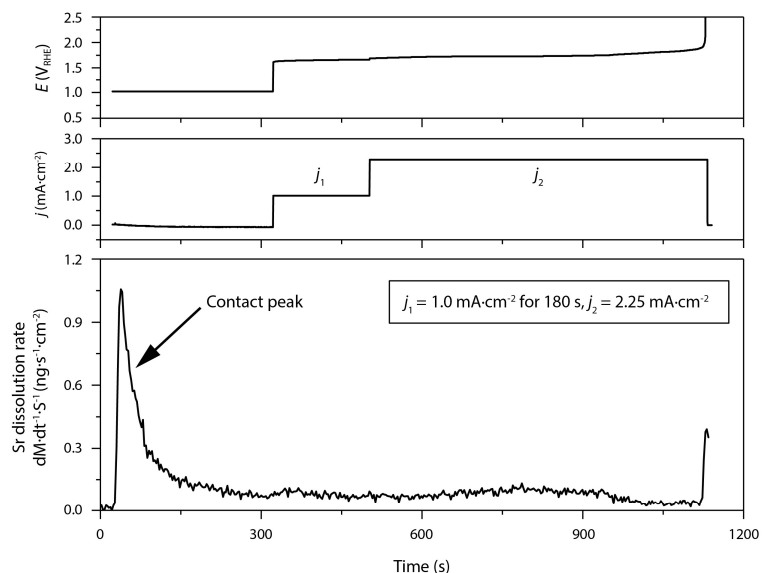


Figure S5. Chemical analysis of the electrolyte by *on-line* ICP-MS measurements. A representative dissolution measurement is shown including the region of increased Sr dissolution due to the leaching of minor Sr-rich surface phases during the first contact of the scanning flow cell with the LSCO electrode (contact peak). To investigate Sr dissolution under OER conditions, two consecutive galvanostatic holds are applied ($j_1 = 1.0 \text{ mA}\cdot\text{cm}^{-2}$ and $j_2 = 2.25 \text{ mA}\cdot\text{cm}^{-2}$) while the dissolution behavior is monitored.

Fig. S5 shows the dissolution behavior of LSCO during two consecutive galvanostatic holds in analogy to Fig. 5 of the main manuscript but including the initial contact peak.

Figure S6. Angle-dependent XPS analysis of the as-prepared LSCO.

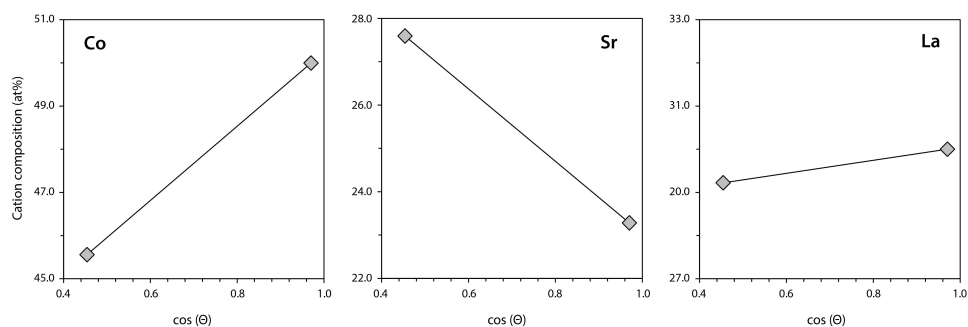


Figure S6. Angle-dependent XPS analysis of the surface stoichiometry of epitaxial LSCO electrodes in the as-prepared state. The surface is enriched by strontium and depleted from cobalt.

The as-prepared surface of the epitaxial LSCO electrodes are enriched by strontium, while cobalt is depleted from the surface. In comparison to the operated samples, discussed in the main manuscript (Fig. 5), the strontium enrichment is enhanced due to the presence of additional Sr-rich surface phases that typically dissolve during the first contact the alkaline electrolyte.

Figure S7. Surface chemistry of LSCO after the end of the catalyst lifetime.

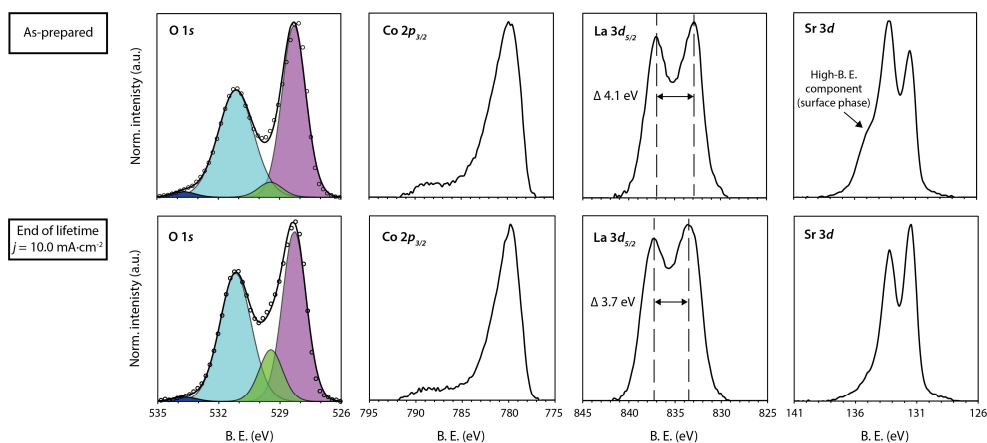


Figure S7. X-ray photoelectron spectroscopy investigations of the LSCO surface chemistry. O 1s, Co 2p_{3/2}, La 3d_{5/2} and Sr 3d XPS core-level spectra of LSCO catalysts in the as-prepared state (first row), and the operated (but still active) state after OER catalysis for 600s at $j = 1.0 \text{ mA}\cdot\text{cm}^{-2}$ (second row) and the operated (but still active) state after OER catalysis for 600 s at $j = 10.0 \text{ mA}\cdot\text{cm}^{-2}$ (third row). The respective spectra are displayed for each sample state after subtraction of a Tougaard background. The O 1s spectra is deconvoluted by data fitting of four different components (ABO₃ lattice oxygen (purple), surface termination component (green), oxyhydroxide lattice oxygen (orange), mixed hydroxide groups (cyan), organic components (blue)). XPS analysis was performed at a photoemission angle $\theta = 46^\circ$.

The as-prepared surface of the epitaxial LSCO electrodes are enriched by strontium, while cobalt is depleted from the surface. In comparison to the operated samples, discussed in the main manuscript (Fig. 5), the strontium enrichment is enhanced due to the presence of additional Sr-rich surface phases that typically dissolve during the first contact the alkaline electrolyte.

REFERENCES

- (1) Roddatis, V., Lole, G. & Jooss, C. In situ preparation of $\text{Pr}_{1-x}\text{Ca}_x\text{MnO}_3$ and $\text{La}_{1-x}\text{Sr}_x\text{MnO}_3$ catalysts surface for high-resolution environmental transmission electron microscopy. *Catalysts* **9**, 751 (2019).

A.4.1 Supporting Movies

<https://owncloud.gwdg.de/index.php/s/18KgZlIpdraToxJ>

Bibliography

- [1] Mikael Höök and Xu Tang. Depletion of fossil fuels and anthropogenic climate change—a review. *Energy policy*, 52:797–809, 2013.
- [2] N. Abas, A. Kalair, and N. Khan. Review of fossil fuels and future energy technologies. *Futures*, 69:31–49, 2015.
- [3] Zhijie Chen, Wei Wei, and Bing-Jie Ni. Cost-effective catalysts for renewable hydrogen production via electrochemical water splitting: Recent advances. *Current Opinion in Green and Sustainable Chemistry*, 27:100398, 2021.
- [4] Tapas K Mandal and Duncan H Gregory. Hydrogen: a future energy vector for sustainable development. *Journal of mechanical engineering science*, 224(3):539–558, 2010.
- [5] Xiao Li, Lili Zhao, Jiayuan Yu, Xiaoyan Liu, Xiaoli Zhang, Hong Liu, and Weijia Zhou. Water splitting: from electrode to green energy system. *Nano-Micro Letters*, 12(1):1–29, 2020.
- [6] Eugene D Coyle and Richard A Simmons. *Understanding the global energy crisis*. Purdue University Press, 2014.
- [7] Manish Kumar Singla, Parag Nijhawan, and Amandeep Singh Oberoi. Hydrogen fuel and fuel cell technology for 61a cleaner future: 61a review. *Environmental Science and Pollution Research*, pages 1–20, 2021.
- [8] Robert JH Dunn, Diane M Stanitski, Nadine Gobron, Kate M Willett, M Ades, R Adler, Rob Allan, RP Allan, J Anderson, Anthony Argüez, et al. Global climate. *Bulletin of the American Meteorological Society*, 101(101(8)):S9–S127, 2020.
- [9] Susan M Natali, John P Holdren, Brendan M Rogers, Rachael Treharne, Philip B Duffy, Rafe Pomerance, and Erin MacDonald. Permafrost carbon feedbacks threaten global climate goals. *Proceedings of the National Academy of Sciences*, 118(21), 2021.

- [10] RS Vose, B Huang, X Yin, D Arndt, DR Easterling, JH Lawrimore, MJ Menne, A Sanchez-Lugo, and HM Zhang. Implementing full spatial coverage in noaa’s global temperature analysis. *Geophysical Research Letters*, 48(4):e2020GL090873, 2021.
- [11] Wolfgang Lubitz and William Tumas. Hydrogen: an overview. *Chemical reviews*, 107(10):3900–3903, 2007.
- [12] National Centers for Environmental Information. Annually global land and ocean temperature correlation to the 20th-century aggregate from 1880–2021. <https://www.ncdc.noaa.gov/sotc/global/202109>. Accessed November 2, 2021.
- [13] UK SGN. Electrocatalytic water splitting uses electricity to produce hydrogen. <https://rb.gy/ir58bk>. Accessed November 3, 2021.
- [14] Sengeni Anantharaj and Suguru Noda. Amorphous catalysts and electrochemical water splitting: an untold story of harmony. *Small*, 16(2):1905779, 2020.
- [15] Maximilian Schalenbach, Geert Tjarks, Marcelo Carmo, Wiebke Lueke, Martin Mueller, and Detlef Stolten. Acidic or alkaline? towards a new perspective on the efficiency of water electrolysis. *Journal of The Electrochemical Society*, 163(11):F3197, 2016.
- [16] Isabela C Man, Hai-Yan Su, Federico Calle-Vallejo, Heine A Hansen, José I Martínez, Nilay G Inoglu, John Kitchin, Thomas F Jaramillo, Jens K Nørskov, and Jan Rossmeisl. Universality in oxygen evolution electrocatalysis on oxide surfaces. *ChemCatChem*, 3(7):1159–1165, 2011.
- [17] Hainan Sun, Xiaomin Xu, Yufei Song, Wei Zhou, and Zongping Shao. Designing high-valence metal sites for electrochemical water splitting. *Advanced Functional Materials*, year=2021, volume=31, number=16, pages=2009779, publisher=Wiley Online Library,.
- [18] J. Rossmeisl, Z.-W. Qu, H. Zhu, G.-J. Kroes, and J.K. Nørskov. Electrolysis of water on oxide surfaces. *Journal of Electroanalytical Chemistry*, 607(1):83–89, 2007. Theoretical and Computational Electrochemistry.
- [19] Jian Zhang, Qiuyu Zhang, and Xinliang Feng. Support and interface effects in water-splitting electrocatalysts. *Advanced Materials*, 31(31):1808167, 2019.

- [20] Fei Lu, Min Zhou, Yuxue Zhou, and Xianghua Zeng. First-row transition metal based catalysts for the oxygen evolution reaction under alkaline conditions: basic principles and recent advances. *Small*, 13(45):1701931, 2017.
- [21] Fang Song, Lichen Bai, Aliko Moysiadou, Seunghwa Lee, Chao Hu, Laurent Liardet, and Xile Hu. Transition metal oxides as electrocatalysts for the oxygen evolution reaction in alkaline solutions: an application-inspired renaissance. *Journal of the American Chemical Society*, 140(25):7748–7759, 2018.
- [22] Ju Seong Kim, Byunghoon Kim, Hyunah Kim, and Kisuk Kang. Recent progress on multimetal oxide catalysts for the oxygen evolution reaction. *Advanced Energy Materials*, 8(11):1702774, 2018.
- [23] C Angelinetta, S Trasatti, Lj D Atanasoska, ZS Minevski, and RT Atanasoski. Effect of preparation on the surface and electrocatalytic properties of $\text{RuO}_2 + \text{IrO}_2$ mixed oxide electrodes. *Materials chemistry and physics*, 22(1-2):231–247, 1989.
- [24] A Di Blasi, C D’urso, V Baglio, V Antonucci, AS Arico, R Ornelas, F Matteucci, G Orozco, D Beltran, Y Meas, et al. Preparation and evaluation of $\text{RuO}_2 - \text{IrO}_2$, $\text{IrO}_2 - \text{Pt}$ and $\text{IrO}_2 - \text{Ta}_2\text{O}_5$ catalysts for the oxygen evolution reaction in an SPE electrolyzer. *Journal of Applied Electrochemistry*, 39(2):191–196, 2009.
- [25] Fabio Dionigi and Peter Strasser. NiFe-based (oxy) hydroxide catalysts for oxygen evolution reaction in non-acidic electrolytes. *Advanced Energy Materials*, 6(23):1600621, 2016.
- [26] Jian Jiang, Fanfei Sun, Si Zhou, Wei Hu, Hao Zhang, Jinchao Dong, Zheng Jiang, Jijun Zhao, Jianfeng Li, Wensheng Yan, et al. Atomic-level insight into super-efficient electrocatalytic oxygen evolution on iron and vanadium co-doped nickel (oxy) hydroxide. *Nature communications*, 9(1):1–12, 2018.
- [27] Michaela S Burke, Shihui Zou, Lisa J Enman, Jaclyn E Kellon, Christian A Gabor, Erica Pledger, and Shannon W Boettcher. Revised oxygen evolution reaction activity trends for first-row transition-metal (oxy) hydroxides in alkaline media. *The journal of physical chemistry letters*, 6(18):3737–3742, 2015.
- [28] Michaela S Burke, Lisa J Enman, Adam S Batchellor, Shihui Zou, and Shannon W Boettcher. Oxygen evolution reaction electrocatalysis on transition metal oxides and (oxy) hydroxides: activity trends and design principles. *Chemistry of Materials*, 27(22):7549–7558, 2015.

- [29] Sengeni Anantharaj, Sivasankara Rao Ede, Kuppan Sakthikumar, Kanimithu Karthick, Soumyaranjan Mishra, and Subrata Kundu. Recent trends and perspectives in electrochemical water splitting with an emphasis on sulfide, selenide, and phosphide catalysts of fe, co, and ni: a review. *Acs Catalysis*, 6(12):8069–8097, 2016.
- [30] Yanmei Shi and Bin Zhang. Recent advances in transition metal phosphide nanomaterials: synthesis and applications in hydrogen evolution reaction. *Chemical Society Reviews*, 45(6):1529–1541, 2016.
- [31] Menny Shalom, Debora Ressnig, Xiaofei Yang, Guylhaine Clavel, Tim Patrick Fellingner, and Markus Antonietti. Nickel nitride as an efficient electrocatalyst for water splitting. *Journal of Materials Chemistry A*, 3(15):8171–8177, 2015.
- [32] Bingfei Cao, Gabriel M Veith, Joerg C Neufeind, Radoslav R Adzic, and Peter G Khalifah. Mixed close-packed cobalt molybdenum nitrides as non-noble metal electrocatalysts for the hydrogen evolution reaction. *Journal of the American Chemical Society*, 135(51):19186–19192, 2013.
- [33] Min Zeng, Hao Wang, Chong Zhao, Jiake Wei, Kuo Qi, Wenlong Wang, and Xuedong Bai. Nanostructured amorphous nickel boride for high-efficiency electrocatalytic hydrogen evolution over a broad ph range. *ChemCatChem*, 8(4):708–712, 2016.
- [34] Liang Ma, Louisa Rui Lin Ting, Valerio Molinari, Cristina Giordano, and Boon Siang Yeo. Efficient hydrogen evolution reaction catalyzed by molybdenum carbide and molybdenum nitride nanocatalysts synthesized via the urea glass route. *Journal of Materials Chemistry A*, 3(16):8361–8368, 2015.
- [35] Jhih-Fong Lin, Olli Pitkänen, Jani Mäklin, Robert Puskas, Akos Kukovecz, Aron Dombovari, Geza Toth, and Krisztian Kordas. Synthesis of tungsten carbide and tungsten disulfide on vertically aligned multi-walled carbon nanotube forests and their application as non-pt electrocatalysts for the hydrogen evolution reaction. *Journal of Materials Chemistry A*, 3(28):14609–14616, 2015.
- [36] Jinwhan Joo, Taekyung Kim, Jaeyoung Lee, Sang-Il Choi, and Kwangyeol Lee. Morphology-controlled metal sulfides and phosphides for electrochemical water splitting. *Advanced Materials*, 31(14):1806682, 2019.
- [37] Hao Wan, Xiaohe Liu, Haidong Wang, Renzhi Ma, and Takayoshi Sasaki. Recent advances in developing high-performance nanostructured electrocat-

- alysts based on 3d transition metal elements. *Nanoscale Horizons*, 4(4):789–808, 2019.
- [38] Francisco Zaera. Surface chemistry at the liquid/solid interface. *Surface science*, 605(13-14):1141–1145, 2011.
- [39] Olle Bjoernehalm, Martin H Hansen, Andrew Hodgson, Li-Min Liu, David T Limmer, Angelos Michaelides, Philipp Pedevilla, Jan Rossmeisl, Huaze Shen, Gabriele Tocci, et al. Water at interfaces. *Chemical reviews*, volume=116, (13):7698–7726, 2016.
- [40] Mengning Ding, Qiyuan He, Gongming Wang, Hung-Chieh Cheng, Yu Huang, and Xiangfeng Duan. An on-chip electrical transport spectroscopy approach for in situ monitoring electrochemical interfaces. *Nature communications*, 6(1):1–9, 2015.
- [41] Peiyao Wang, Mengyu Yan, Jiashen Meng, Gengping Jiang, Longbing Qu, Xuelei Pan, Jefferson Zhe Liu, and Liqiang Mai. Oxygen evolution reaction dynamics monitored by an individual nanosheet-based electronic circuit. *Nature communications*, 8(1):1–7, 2017.
- [42] Francisco Zaera. Probing liquid/solid interfaces at the molecular level. *Chemical reviews*, volume=112, (5):2920–2986, 2012.
- [43] Hemma Mistry, Ana Sofia Varela, Stefanie Kühn, Peter Strasser, and Beatriz Roldan Cuenya. Nanostructured electrocatalysts with tunable activity and selectivity. *Nature Reviews Materials*, 1(4):1–14, 2016.
- [44] Holger Dau, Christian Limberg, Tobias Reier, Marcel Risch, Stefan Roggan, and Peter Strasser. The mechanism of water oxidation: from electrolysis via homogeneous to biological catalysis. *ChemCatChem*, 2(7):724–761, 2010.
- [45] Alexis Grimaud, Oscar Diaz-Morales, Binghong Han, Wesley T Hong, Yueh-Lin Lee, Livia Giordano, Kelsey A Stoerzinger, Marc TM Koper, and Yang Shao-Horn. Activating lattice oxygen redox reactions in metal oxides to catalyze oxygen evolution. *Nature Chemistry*, 9(5):457–465, 2017.
- [46] Tuan Anh Pham, Yuan Ping, and Giulia Galli. Modelling heterogeneous interfaces for solar water splitting. *Nature materials*, 16(4):401–408, 2017.
- [47] Olaf M Magnussen and Axel Groß. Toward an atomic-scale understanding of electrochemical interface structure and dynamics. *Journal of the American Chemical Society*, 141(12):4777–4790, 2019.

- [48] Grazia Gonella, Ellen HG Backus, Yuki Nagata, Douwe J Bonthuis, Philip Loche, Alexander Schlaich, Roland R Netz, Angelika Kühnle, Ian T McCrum, Marc Koper, et al. Water at charged interfaces. *Nature Reviews Chemistry*, 5(7):466–485, 2021.
- [49] Ken Sakaushi, Tomoaki Kumeda, Sharon Hammes-Schiffer, Marko M Melander, and Osamu Sugino. Advances and challenges for experiment and theory for multi-electron multi-proton transfer at electrified solid–liquid interfaces. *Physical Chemistry Chemical Physics*, 22(35):19401–19442, 2020.
- [50] Hui-Ying Qu, Xiwen He, Yibo Wang, and Shuai Hou. Electrocatalysis for the oxygen evolution reaction in acidic media: Progress and challenges. *Applied Sciences*, 11(10):4320, 2021.
- [51] Hugh Stott Taylor. A theory of the catalytic surface. *Proceedings of the Royal Society of London. Series A, Containing Papers of a Mathematical and Physical Character*, 108(745):105–111, 1925.
- [52] JF Young, JA Osborn, FH Jardine, and G Wilkinson. Hydride intermediates in homogeneous hydrogenation reactions of olefins and acetylenes using rhodium catalysts. *Chemical Communications (London)*, (7):131–132, 1965.
- [53] SL Bernasek, WJ Siekhaus, and GA Somorjai. Molecular-beam study of hydrogen-deuterium exchange on low-and high-miller-index platinum single-crystal surfaces. *Physical Review Letters*, 30(24):1202, 1973.
- [54] RJ Gale, M Salmeron, and GA Somorjai. Variation of surface reaction probability with reactant angle of incidence: A molecular beam study of the asymmetry of stepped platinum crystal surfaces for hh bond breaking. *Physical Review Letters*, 38(18):1027, 1977.
- [55] M Salmeron, RJ Gale, and GA Somorjai. Molecular beam study of the h₂-d₂ exchange reaction on stepped platinum crystal surfaces: Dependence on reactant angle of incidence. *The Journal of Chemical Physics*, 67(11):5324–5334, 1977.
- [56] GA Somorjai, KR McCrea, and J Zhu. Active sites in heterogeneous catalysis: development of molecular concepts and future challenges. *Topics in Catalysis*, 18(3):157–166, 2002.
- [57] Marcel Risch, Alexis Grimaud, Kevin J May, Kelsey A Stoerzinger, Tina J Chen, Azzam N Mansour, and Yang Shao-Horn. Structural changes of cobalt-based perovskites upon water oxidation investigated by exafs. *The Journal of Physical Chemistry C*, 117(17):8628–8635, 2013.

- [58] Diego González-Flores, Irene Sánchez, Ivelina Zaharieva, Katharina Klingan, Jonathan Heidkamp, Petko Chernev, Prashanth W Menezes, Matthias Driess, Holger Dau, and Mavis L Montero. Heterogeneous water oxidation: surface activity versus amorphization activation in cobalt phosphate catalysts. *Angewandte Chemie International Edition*, 54(8):2472–2476, 2015.
- [59] Arno Bergmann, Elias Martinez-Moreno, Detre Teschner, Petko Chernev, Manuel Gliech, Jorge Ferreira De Araújo, Tobias Reier, Holger Dau, and Peter Strasser. Reversible amorphization and the catalytically active state of crystalline Co_3O_4 during oxygen evolution. *Nature communications*, 6(1):1–9, 2015.
- [60] Rodney DL Smith, Chiara Pasquini, Stefan Loos, Petko Chernev, Katharina Klingan, Paul Kubella, Mohammad Reza Mohammadi, Diego Gonzalez-Flores, and Holger Dau. Spectroscopic identification of active sites for the oxygen evolution reaction on iron-cobalt oxides. *Nature communications*, 8(1):1–8, 2017.
- [61] Xiaozhi Su, Yu Wang, Jing Zhou, Songqi Gu, Jiong Li, and Shuo Zhang. Operando spectroscopic identification of active sites in nife prussian blue analogues as electrocatalysts: activation of oxygen atoms for oxygen evolution reaction. *Journal of the American Chemical Society*, 140(36):11286–11292, 2018.
- [62] Feng Li, Gao-Feng Han, Hyuk-Jun Noh, Seok-Jin Kim, Yalin Lu, Hu Young Jeong, Zhengping Fu, and Jong-Beom Baek. Boosting oxygen reduction catalysis with abundant copper single atom active sites. *Energy & Environmental Science*, 11(8):2263–2269, 2018.
- [63] Jiantao Li, Wenzhong Huang, Manman Wang, Shibo Xi, Jiashen Meng, Kangning Zhao, Jun Jin, Wangwang Xu, Zhaoyang Wang, Xiong Liu, et al. Low-crystalline bimetallic metal–organic framework electrocatalysts with rich active sites for oxygen evolution. *ACS Energy Letters*, 4(1):285–292, 2018.
- [64] Yelena Gorlin, Benedikt Lassalle-Kaiser, Jesse D Benck, Sheraz Gul, Samuel M Webb, Vittal K Yachandra, Junko Yano, and Thomas F Jaramillo. In situ x-ray absorption spectroscopy investigation of a bifunctional manganese oxide catalyst with high activity for electrochemical water oxidation and oxygen reduction. *Journal of the American Chemical Society*, 135(23):8525–8534, 2013.

- [65] Arno Bergmann, Travis E Jones, Elias Martinez Moreno, Detre Teschner, Petko Chervnev, Manuel Gliech, Tobias Reier, Holger Dau, and Peter Strasser. Unified structural motifs of the catalytically active state of co (oxyhydr) oxides during the electrochemical oxygen evolution reaction. *Nature Catalysis*, 1(9):711–719, 2018.
- [66] Zhu Chen, Li Cai, Xiaofang Yang, Coleman Kronawitter, Liejin Guo, Shaohua Shen, and Bruce E Koel. Reversible structural evolution of nickel hydroxide during the oxygen evolution reaction and identification of the catalytically active phase. *ACS Catalysis*, 8(2):1238–1247, 2018.
- [67] Chengyi Hu, Qiuyu Ma, Sung-Fu Hung, Zhe-Ning Chen, Daohui Ou, Bin Ren, Hao Ming Chen, Gang Fu, and Nanfeng Zheng. In situ electrochemical production of ultrathin nickel nanosheets for hydrogen evolution electrocatalysis. *Chem*, 3(1):122–133, 2017.
- [68] Hui Ding, Hongfei Liu, Wangsheng Chu, Changzheng Wu, and Yi Xie. Structural transformation of heterogeneous materials for electrocatalytic oxygen evolution reaction. *Chemical Reviews*, 2021.
- [69] Christoph Baeumer, Jiang Li, Qiyang Lu, Allen Yu-Lun Liang, Lei Jin, Henrique Perin Martins, Tomáš Duchoň, Maria Glöß, Sabrina M Gericke, Marcus A Wohlgemuth, et al. Tuning electrochemically driven surface transformation in atomically flat lanio 3 thin films for enhanced water electrolysis. *Nature materials*, 20(5):674–682, 2021.
- [70] Ying Pan, Hangjuan Ren, Haiwei Du, Fuyang Cao, Yifeng Jiang, Haojin Du, and Dewei Chu. Active site engineering by surface sulfurization for a highly efficient oxygen evolution reaction: a case study of co 3 o 4 electrocatalysts. *Journal of Materials Chemistry A*, 6(45):22497–22502, 2018.
- [71] Xin Bo, Rosalie K Hocking, Si Zhou, Yibing Li, Xianjue Chen, Jincheng Zhuang, Yi Du, and Chuan Zhao. Capturing the active sites of multimetallic (oxy) hydroxides for the oxygen evolution reaction. *Energy & Environmental Science*, 13(11):4225–4237, 2020.
- [72] Pietro P Lopes, Dong Young Chung, Xue Rui, Hong Zheng, Haiying He, Pedro Farinazzo Bergamo Dias Martins, Dusan Strmcnik, Vojislav R Stamenkovic, Peter Zapol, JF Mitchell, et al. Dynamically stable active sites from surface evolution of perovskite materials during the oxygen evolution reaction. *Journal of the American Chemical Society*, 143(7):2741–2750, 2021.
- [73] Emiliana Fabbri, Maarten Nachtegaal, Tobias Binninger, Xi Cheng, Bae-Jung Kim, Julien Durst, Francesco Bozza, Thomas Graule, Robin Schäublin,

- Luke Wiles, et al. Dynamic surface self-reconstruction is the key of highly active perovskite nano-electrocatalysts for water splitting. *Nature materials*, 16(9):925–931, 2017.
- [74] Song Jin. Are metal chalcogenides, nitrides, and phosphides oxygen evolution catalysts or bifunctional catalysts?, 2017.
- [75] Hongliang Jiang, Qun He, Xiyu Li, Xiaozhi Su, Youkui Zhang, Shuangming Chen, Shuo Zhang, Guozhen Zhang, Jun Jiang, Yi Luo, et al. Tracking structural self-reconstruction and identifying true active sites toward cobalt oxychloride precatalyst of oxygen evolution reaction. *Advanced Materials*, 31(8):1805127, 2019.
- [76] Yi Jia, Kun Jiang, Haotian Wang, and Xiangdong Yao. The role of defect sites in nanomaterials for electrocatalytic energy conversion. *Chem*, 5(6):1371–1397, 2019.
- [77] Alexandra Zagalskaya and Vitaly Alexandrov. Role of defects in the interplay between adsorbate evolving and lattice oxygen mechanisms of the oxygen evolution reaction in ruo₂ and iro₂. *ACS Catalysis*, 10(6):3650–3657, 2020.
- [78] Dawei Chen, Man Qiao, Ying-Rui Lu, Li Hao, Dongdong Liu, Chung-Li Dong, Yafei Li, and Shuangyin Wang. Preferential cation vacancies in perovskite hydroxide for the oxygen evolution reaction. *Angewandte Chemie International Edition*, 57(28):8691–8696, 2018.
- [79] David N Mueller, Michael L Machala, Hendrik Bluhm, and William C Chueh. Redox activity of surface oxygen anions in oxygen-deficient perovskite oxides during electrochemical reactions. *Nature communications*, 6(1):1–8, 2015.
- [80] Ahmed Badreldin, Aya E Abusrafa, and Ahmed Abdel-Wahab. Oxygen-deficient perovskites for oxygen evolution reaction in alkaline media: A review. *Emergent Materials*, pages 1–24, 2020.
- [81] Guruprasad S Hegde, Arpita Ghosh, Rajashekar Badam, Noriyoshi Matsumi, and Ramaprabhu Sundara. Role of defects in low-cost perovskite catalysts toward orr and oer in lithium–oxygen batteries. *ACS Applied Energy Materials*, 3(2):1338–1348, 2020.
- [82] Kyu-Nam Jung, Jong-Hyuk Jung, Won Bin Im, Sukeun Yoon, Kyung-Hee Shin, and Jong-Won Lee. Doped lanthanum nickelates with a layered perovskite structure as bifunctional cathode catalysts for rechargeable metal–air batteries. *ACS applied materials & interfaces*, 5(20):9902–9907, 2013.

- [83] Hamidreza Arandiyan, Sajjad S Mofarah, Yuan Wang, Claudio Cazorla, Deshetti Jampaiah, Magnus Garbrecht, Karen Wilson, Adam F Lee, Chuan Zhao, and Thomas Maschmeyer. Impact of surface defects on lanio3 perovskite electrocatalysts for the oxygen evolution reaction. *Chemistry–A European Journal*, 27(58):14418–14426, 2021.
- [84] Nan Li, Jingjia Guo, Yiwen Ding, Yaqi Hu, Chunhua Zhao, and Chongjun Zhao. Direct regulation of double cation defects at the a1a2 site for a high-performance oxygen evolution reaction perovskite catalyst. *ACS Applied Materials & Interfaces*, 13(1):332–340, 2020.
- [85] Zhaohui Xiao, Yu-Cheng Huang, Chung-Li Dong, Chao Xie, Zhijuan Liu, Shiqian Du, Wei Chen, Dafeng Yan, Li Tao, Zhiwen Shu, et al. Operando identification of the dynamic behavior of oxygen vacancy-rich co3o4 for oxygen evolution reaction. *Journal of the American Chemical Society*, 142(28):12087–12095, 2020.
- [86] Haotian Wang, Hyun-Wook Lee, Yong Deng, Zhiyi Lu, Po-Chun Hsu, Yayuan Liu, Dingchang Lin, and Yi Cui. Bifunctional non-noble metal oxide nanoparticle electrocatalysts through lithium-induced conversion for overall water splitting. *Nature communications*, 6(1):1–8, 2015.
- [87] Bo Zhang, Xueli Zheng, Oleksandr Voznyy, Riccardo Comin, Michal Bajdich, Max García-Melchor, Lili Han, Jixian Xu, Min Liu, Lirong Zheng, et al. Homogeneously dispersed multimetal oxygen-evolving catalysts. *Science*, 352(6283):333–337, 2016.
- [88] Xu Zou, Yipu Liu, Guo-Dong Li, Yuanyuan Wu, Da-Peng Liu, Wang Li, Hai-Wen Li, Dejun Wang, Yu Zhang, and Xiaoxin Zou. Ultrafast formation of amorphous bimetallic hydroxide films on 3d conductive sulfide nanoarrays for large-current-density oxygen evolution electrocatalysis. *Advanced Materials*, 29(22):1700404, 2017.
- [89] Lili Zhu, Haiping Lin, Youyong Li, Fan Liao, Yeshayahu Lifshitz, Minqi Sheng, Shuit-Tong Lee, and Mingwang Shao. A rhodium/silicon co-electrocatalyst design concept to surpass platinum hydrogen evolution activity at high overpotentials. *Nature communications*, 7(1):1–7, 2016.
- [90] Yipu Liu, Xiao Liang, Lin Gu, Yu Zhang, Guo-Dong Li, Xiaoxin Zou, and Jie-Sheng Chen. Corrosion engineering towards efficient oxygen evolution electrodes with stable catalytic activity for over 6000 hours. *Nature communications*, 9(1):1–10, 2018.

- [91] A Ramus Moreira, Z Panossian, PL Camargo, M Ferreira Moreira, IC Da Silva, and JE Ribeiro De Carvalho. Zn/55al coating microstructure and corrosion mechanism. *Corrosion science*, 48(3):564–576, 2006.
- [92] Xupo Liu, Mingxing Gong, Shaofeng Deng, Tonghui Zhao, Tao Shen, Jian Zhang, and Deli Wang. Transforming damage into benefit: Corrosion engineering enabled electrocatalysts for water splitting. *Advanced Functional Materials*, 31(11):2009032, 2021.
- [93] Helmut Schäfer, Shamaila Sadaf, Lorenz Walder, Karsten Kuepper, Stephan Dinklage, Joachim Wollschläger, Lilli Schneider, Martin Steinhart, Jörg Hardege, and Diemo Daum. Stainless steel made to rust: a robust water-splitting catalyst with benchmark characteristics. *Energy & Environmental Science*, 8(9):2685–2697, 2015.
- [94] Sofyane Abbou, Raphaël Chattot, Vincent Martin, Fabien Claudel, Lluís Solà-Hernández, Christian Beauger, Laetitia Dubau, and Frédéric Maillard. Manipulating the corrosion resistance of SnO_2 aerogels through doping for efficient and durable oxygen evolution reaction electrocatalysis in acidic media. *ACS Catalysis*, 10(13):7283–7294, 2020.
- [95] Hongxing Liang, Min Xu, and Edouard Asselin. Corrosion of monometallic iron-and nickel-based electrocatalysts for the alkaline oxygen evolution reaction: A review. *Journal of Power Sources*, volume=510, pages=230387, year=2021, publisher=Elsevier,.
- [96] Yufei Zhang, Laiquan Li, Haiquan Su, Wei Huang, and Xiaochen Dong. Binary metal oxide: advanced energy storage materials in supercapacitors. *Journal of Materials Chemistry A*, 3(1):43–59, 2015.
- [97] CP De Pauli and S Trasatti. Composite materials for electrocatalysis of O_2 evolution: $\text{Fe}_2\text{O}_3/\text{SnO}_2$ in acid solution. *Journal of Electroanalytical Chemistry*, 538:145–151, 2002.
- [98] Thomas Audichon, Sophie Morisset, Teko W Napporn, K Boniface Kokoh, Clément Comminges, and Cláudia Morais. Effect of adding CeO_2 to $\text{RuO}_2/\text{Fe}_2\text{O}_3$ mixed nanocatalysts: activity towards the oxygen evolution reaction and stability in acidic media. *ChemElectroChem*, 2(8):1128–1137, 2015.
- [99] OR Camara and S Trasatti. Surface electrochemical properties of $\text{Ti}/(\text{RuO}_2/\text{ZrO}_2)$ electrodes. *Electrochimica acta*, 41(3):419–427, 1996.

- [100] TAF Lassali, JFC Boodts, and LOS Bulhoes. Charging processes and electrocatalytic properties of $\text{irO}_2/\text{tio}_2/\text{sno}_2$ oxide films investigated by in situ ac impedance measurements. *Electrochimica acta*, 44(24):4203–4216, 1999.
- [101] J Gaudet, AC Tavares, a S Trasatti, and D Guay. Physicochemical characterization of mixed ruo_2 - sno_2 solid solutions. *Chemistry of Materials*, 17(6):1570–1579, 2005.
- [102] Jia-Jia Zhang, Ji-Ming Hu, Jian-Qing Zhang, and Chu-Nan Cao. Iro_2 - sio_2 binary oxide films: Geometric or kinetic interpretation of the improved electrocatalytic activity for the oxygen evolution reaction. *international journal of hydrogen energy*, 36(9):5218–5226, 2011.
- [103] JC Cruz, A Ramos Hernández, M Guerra-Balcazar, AU Chávez-Ramirez, J Ledesma-García, and LG Arriaga. Electrochemical evaluation of a ir - ru binary oxide for oxygen evolution reaction. *Int J Electrochem Sci*, 7:7866–7876, 2012.
- [104] Yang Yang, Huilong Fei, Gedeng Ruan, Changsheng Xiang, and James M Tour. Efficient electrocatalytic oxygen evolution on amorphous nickel-cobalt binary oxide nanoporous layers. *ACS nano*, 8(9):9518–9523, 2014.
- [105] Xiuli Song, Tailai Yang, Haiyan Du, Wenyan Dong, and Zhenhai Liang. New binary mn and cr mixed oxide electrocatalysts for the oxygen evolution reaction. *Journal of Electroanalytical Chemistry*, 760:59–63, 2016.
- [106] Li Liu, Huijuan Zhang, Yanping Mu, Yuanjuan Bai, and Yu Wang. Binary cobalt ferrite nanomesh arrays as the advanced binder-free electrode for applications in oxygen evolution reaction and supercapacitors. *Journal of Power Sources*, 327:599–609, 2016.
- [107] Nimai Bhandary, Pravin P Ingole, and Suddhasatwa Basu. Electrosynthesis of mn - fe oxide nanopetals on carbon paper as bi-functional electrocatalyst for oxygen reduction and oxygen evolution reaction. *International Journal of Hydrogen Energy*, 43(6):3165–3171, 2018.
- [108] Lili Pan, Qingqing Wang, Yongdan Li, and Cuijuan Zhang. Amorphous cobalt-cerium binary metal oxides as high performance electrocatalyst for oxygen evolution reaction. *Journal of Catalysis*, 384:14–21, 2020.
- [109] Zhen-Feng Huang, Jiajia Song, Shuo Dou, Xiaogang Li, Jiong Wang, and Xin Wang. Strategies to break the scaling relation toward enhanced oxygen electrocatalysis. *Matter*, 1(6):1494–1518, 2019.

- [110] Joseph H Montoya, Linsey C Seitz, Pongkarn Chakthranont, Aleksandra Vojvodic, Thomas F Jaramillo, and Jens K Nørskov. Materials for solar fuels and chemicals. *Nature materials*, 16(1):70–81, 2017.
- [111] Jiajia Song, Chao Wei, Zhen-Feng Huang, Chuntai Liu, Lin Zeng, Xin Wang, and Zhichuan J Xu. A review on fundamentals for designing oxygen evolution electrocatalysts. *Chemical Society Reviews*, 49(7):2196–2214, 2020.
- [112] Emanuel Ronge, Jonas Lindner, Ulrich Ross, Jens Melder, Jonas Ohms, Vladimir Roddatis, Philipp Kurz, and Christian Jooss. Atom surface dynamics of manganese oxide under oxygen evolution reaction-like conditions studied by in situ environmental transmission electron microscopy. *The Journal of Physical Chemistry C*, 125(9):5037–5047, 2021.
- [113] Wan-Jian Yin, Baicheng Weng, Jie Ge, Qingde Sun, Zhenzhu Li, and Yanfa Yan. Oxide perovskites, double perovskites and derivatives for electrocatalysis, photocatalysis, and photovoltaics. *Energy & Environmental Science*, 12(2):442–462, 2019.
- [114] Denis Antipin and Marcel Risch. Trends of epitaxial perovskite oxide films catalyzing the oxygen evolution reaction in alkaline media. *Journal of Physics: Energy*, 2(3):032003, 2020.
- [115] Jia-Wei Zhao, Zi-Xiao Shi, Cheng-Fei Li, Qian Ren, and Gao-Ren Li. Regulation of perovskite surface stability on the electrocatalysis of oxygen evolution reaction. *ACS Materials Letters*, 3(6):721–737, 2021.
- [116] Wei Wang, Meigui Xu, Xiaomin Xu, Wei Zhou, and Zongping Shao. Perovskite oxide based electrodes for high-performance photoelectrochemical water splitting. *Angewandte Chemie International Edition*, 59(1):136–152, 2020.
- [117] Feifei Dong, Lu Li, Ziqi Kong, Xiaomin Xu, Yaping Zhang, Zhenghui Gao, Biaokui Dongyang, Meng Ni, Quanbing Liu, and Zhan Lin. Materials engineering in perovskite for optimized oxygen evolution electrocatalysis in alkaline condition. *Small*, 17(2):2006638, 2021.
- [118] Thi Xuyen Nguyen, Yi-Cheng Liao, Chia-Chun Lin, Yen-Hsun Su, and Jyh-Ming Ting. Advanced high entropy perovskite oxide electrocatalyst for oxygen evolution reaction. *Advanced Functional Materials*, page 2101632, 2021.
- [119] Meilan Peng, Jijie Huang, Yinlong Zhu, Hua Zhou, Zhiwei Hu, Yi-Kai Liao, Yu-Hong Lai, Chien-Te Chen, Ying-Hao Chu, Kelvin HL Zhang, et al. Structural anisotropy determining the oxygen evolution mechanism of strongly

- correlated perovskite nickelate electrocatalyst. *ACS Sustainable Chemistry & Engineering*, 9(11):4262–4270, 2021.
- [120] Marc De Graef and Michael E McHenry. *Structure of materials: an introduction to crystallography, diffraction and symmetry*. Cambridge University Press, 2007.
- [121] Hee Jo Song, Hyunseok Yoon, Bobae Ju, and Dong-Wan Kim. Highly efficient perovskite-based electrocatalysts for water oxidation in acidic environments: A mini review. *Advanced Energy Materials*, 11(27):2002428, 2021.
- [122] Jin Suntivich, Kevin J May, Hubert A Gasteiger, John B Goodenough, and Yang Shao-Horn. A perovskite oxide optimized for oxygen evolution catalysis from molecular orbital principles. *Science*, 334(6061):1383–1385, 2011.
- [123] Yun Tong, Junchi Wu, Pengzuo Chen, Haifeng Liu, Wangsheng Chu, Changzheng Wu, and Yi Xie. Vibronic superexchange in double perovskite electrocatalyst for efficient electrocatalytic oxygen evolution. *Journal of the American Chemical Society*, 140(36):11165–11169, 2018.
- [124] Dong Liu, Pengfei Zhou, Haoyun Bai, Haoqiang Ai, Xinyu Du, Mingpeng Chen, Di Liu, Weng Fai Ip, Kin Ho Lo, Chi Tat Kwok, et al. Development of perovskite oxide-based electrocatalysts for oxygen evolution reaction. *Small*, 17(43):2101605, 2021.
- [125] Jan Rossmeisl, Ashildur Logadottir, and Jens Kehlet Nørskov. Electrolysis of water on (oxidized) metal surfaces. *Chemical physics*, 319(1-3):178–184, 2005.
- [126] J Tyler Mefford, Xi Rong, Artem M Abakumov, William G Hardin, Sheng Dai, Alexie M Kolpak, Keith P Johnston, and Keith J Stevenson. Water electrolysis on $\text{La}_{1-x}\text{Sr}_x\text{CoO}_{3-\delta}$ perovskite electrocatalysts. *Nature communications*, 7(1):1–11, 2016.
- [127] Xi Rong, Jules Parolin, and Alexie M Kolpak. A fundamental relationship between reaction mechanism and stability in metal oxide catalysts for oxygen evolution. *Acs Catalysis*, 6(2):1153–1158, 2016.
- [128] Jonathan R Petrie, Valentino R Cooper, John W Freeland, Tricia L Meyer, Zhiyong Zhang, Daniel A Lutterman, and Ho Nyung Lee. Enhanced bifunctional oxygen catalysis in strained LaNiO_3 perovskites. *Journal of the American Chemical Society*, volume=138, (8):2488–2491, 2016.

- [129] Jieyu Liu, Meng Yu, Xuwei Wang, Jie Wu, Changhong Wang, Lijun Zheng, Dachi Yang, Hui Liu, Yan Yao, Feng Lu, et al. Investigation of high oxygen reduction reaction catalytic performance on mn-based mullite smmn 2 o 5. *Journal of Materials Chemistry A*, 5(39):20922–20931, 2017.
- [130] Jong Suk Yoo, Yusu Liu, Xi Rong, and Alexie M Kolpak. Electronic origin and kinetic feasibility of the lattice oxygen participation during the oxygen evolution reaction on perovskites. *The journal of physical chemistry letters*, 9(7):1473–1479, 2018.
- [131] Linsey C Seitz, Colin F Dickens, Kazunori Nishio, Yasuyuki Hikita, Joseph Montoya, Andrew Doyle, Charlotte Kirk, Aleksandra Vojvodic, Harold Y Hwang, Jens K Nørskov, et al. A highly active and stable irox/srro3 catalyst for the oxygen evolution reaction. *Science*, 353(6303):1011–1014, 2016.
- [132] Kevin J May, Christopher E Carlton, Kelsey A Stoerzinger, Marcel Risch, Jin Suntivich, Yueh-Lin Lee, Alexis Grimaud, and Yang Shao-Horn. Influence of oxygen evolution during water oxidation on the surface of perovskite oxide catalysts. *The journal of physical chemistry letters*, 3(22):3264–3270, 2012.
- [133] Gaurav Lole, Vladimir Roddatis, Ulrich Ross, Marcel Risch, Tobias Meyer, Lukas Rump, Janis Geppert, Garlef Wartner, Peter Blöchl, and Christian Jooss. Dynamic observation of manganese adatom mobility at perovskite oxide catalyst interfaces with water. *Communications Materials*, 1(1):1–10, 2020.
- [134] Louis De Broglie. The wave nature of the electron. *Nobel lecture*, 12:244–256, 1929.
- [135] Max Knoll and Ernst Ruska. Das elektronenmikroskop. *Zeitschrift für physik*, volume=78, (5):318–339, 1932.
- [136] C Barry Carter David B Williams. Transmission electron microscopy: A textbook for materials science. *Springer, Boston, MA*, 2009.
- [137] Brent Fultz and James M Howe. Transmission electron microscopy and diffractometry of materials. [SpringerLink](#), 2012.
- [138] Peter Moeck and Sergei Rouvimov. Precession electron diffraction and its advantages for structural fingerprinting in the transmission electron microscope. *Zeitschrift für Kristallographie*, 225(2-3):110–124, 2010.
- [139] Eric Stach. Mse 582 lecture 10: Diffraction contrast imaging. [nanoHUB.org](#), 2008.

- [140] ZL Wang. Transmission electron microscopy of shape-controlled nanocrystals and their assemblies, 2000.
- [141] RD Twesten and JM Gibson. Kinematic analysis of transmission electron diffraction data from si (111)-7× 7. *Ultramicroscopy*, 53(3):223–235, 1994.
- [142] Eric Stach. Mse 640 lecture 7: Dynamical effects in diffraction patterns. nanoHUB.org, 2008.
- [143] Nestor J Zaluzec. The influence of cs/cc correction in analytical imaging and spectroscopy in scanning and transmission electron microscopy. *Ultramicroscopy*, 151:240–249, 2015.
- [144] Bernd Kabius, Peter Hartel, Maximilian Haider, Heiko Müller, Stephan Uhlemann, Ulrich Loebau, Joachim Zach, and Harald Rose. First application of cc-corrected imaging for high-resolution and energy-filtered tem. *Journal of electron microscopy*, 58(3):147–155, 2009.
- [145] Stephan Uhlemann and Maximilian Haider. Residual wave aberrations in the first spherical aberration corrected transmission electron microscope. *Ultramicroscopy*, 72(3-4):109–119, 1998.
- [146] Dmitry Tyutyunnikov. *High resolution transmission electron microscopy investigations of FePt and Au nanoparticles*. PhD thesis, Dissertation, University Duisburg-Essen. Germany, 2010.
- [147] Christoph Tobias Koch. *Determination of core structure periodicity and point defect density along dislocations*. Arizona State University, 2002.
- [148] Lukas Rump. *Determination of Electron Optical Aberrations by Image Matching: Implementation of a Simulated Annealing Approach*. Bachelor's Thesis, *Georg-August-Universität, Göttingen*. 2018.
- [149] Ray F Egerton. Electron energy-loss spectroscopy in the tem. *Reports on Progress in Physics*, 72(1):016502, 2008.
- [150] RF Egerton. Electron energy-loss spectroscopy in the electron microscope. *Springer Science and Business Media*, 2011.
- [151] RF Egerton. Application of electron energy-loss spectroscopy to the study of solid catalysts. *Topics in catalysis*, 21(4):185–190, 2002.
- [152] David C Bell and Natasha Erdman. Low voltage electron microscopy: Principles and applications. In *John Wiley and Sons*. 2012.

- [153] Spectrum imaging. [Gatan](#).
- [154] Huairuo Zhang, R Egerton, and Marek Malac. Eels investigation of the formulas for inelastic mean free path. *Microscopy and Microanalysis*, 17(S2):1466–1467, 2011.
- [155] RWH Webster, AJ Craven, B Schaffer, Sam McFadzean, Ian MacLaren, and DA MacLaren. Correction of eels dispersion non-uniformities for improved chemical shift analysis. *Ultramicroscopy*, 217:113069, 2020.
- [156] Eels information. [Gatan](#).
- [157] Knut W Urban. Studying atomic structures by aberration-corrected transmission electron microscopy. *Science*, 321(5888):506–510, 2008.
- [158] JR Jinschek and S Helveg. Image resolution and sensitivity in an environmental transmission electron microscope. *Micron*, 43(11):1156–1168, 2012.
- [159] Lionel Cervera Gontard, Lan-Yun Chang, Crispin JD Hetherington, Angus I Kirkland, Dogan Ozkaya, and Rafal E Dunin-Borkowski. Aberration-corrected imaging of active sites on industrial catalyst nanoparticles. *Angewandte Chemie*, 119(20):3757–3759, 2007.
- [160] Çağlar Ö Girit, Jannik C Meyer, Rolf Erni, Marta D Rossell, C Kisielowski, Li Yang, Cheol-Hwan Park, MF Crommie, Marvin L Cohen, Steven G Louie, et al. Graphene at the edge: stability and dynamics. *science*, 323(5922):1705–1708, 2009.
- [161] Christian Kisielowski, Quentin M Ramasse, Lars P Hansen, Michael Brorson, Anna Carlsson, Alfons M Molenbroek, Henrik Topsøe, and Stig Helveg. Imaging mos2 nanocatalysts with single-atom sensitivity. *Angewandte Chemie International Edition*, 49(15):2708–2710, 2010.
- [162] Bastian Barton, Bin Jiang, ChengYu Song, Petra Specht, Hector Calderon, and Christian Kisielowski. Atomic resolution phase contrast imaging and in-line holography using variable voltage and dose rate. *Microscopy AND Microanalysis*, 18(5):982–994, 2012.
- [163] Renu Sharma and Peter A Crozier. Environmental transmission electron microscopy in nanotechnology. *Springer*, pages 531–565, 2005.
- [164] Takeo Kamino, Toshie Yaguchi, Mitsuru Konno, Akira Watabe, Tomotaka Marukawa, Takayuki Mima, Kotaro Kuroda, Hiroyasu Saka, Shigeo Arai, Hiroshi Makino, et al. Development of a gas injection/specimen heating

- holder for use with transmission electron microscope. *Microscopy*, 54(6):497–503, 2005.
- [165] ED Boyes and PL Gai. Environmental high resolution electron microscopy and applications to chemical science. *Ultramicroscopy*, 67(1-4):219–232, 1997.
- [166] Titan etem g2 product data. *FEI*.
- [167] Bowen He, Yixiao Zhang, Xi Liu, and Liwei Chen. In-situ transmission electron microscope techniques for heterogeneous catalysis. *ChemCatChem*, 12(7):1853–1872, 2020.
- [168] Andreas M Gänzler, Maria Casapu, Philippe Vernoux, Stéphane Loridant, Francisco J Cadete Santos Aires, Thierry Epicier, Benjamin Betz, Rüdiger Hoyer, and Jan-Dierk Grunwaldt. Tuning the structure of platinum particles on ceria in situ for enhancing the catalytic performance of exhaust gas catalysts. *Angewandte Chemie International Edition*, 56(42):13078–13082, 2017.
- [169] Thomas W Hansen, Jakob B Wagner, Poul L Hansen, Søren Dahl, Hal-dor Topsøe, and Claus JH Jacobsen. Atomic-resolution in situ transmission electron microscopy of a promoter of a heterogeneous catalyst. *science*, 294(5546):1508–1510, 2001.
- [170] Xi Liu, Chenghua Zhang, Yongwang Li, JW Niemantsverdriet, Jakob B Wagner, and Thomas W Hansen. Environmental transmission electron microscopy (etem) studies of single iron nanoparticle carburization in synthesis gas. *ACS Catalysis*, 7(7):4867–4875, 2017.
- [171] Stephan Hofmann, Renu Sharma, Caterina Ducati, Gaohui Du, Cecilia Mattevi, Cinzia Cepek, Mirco Cantoro, Simone Pisana, Atlus Parvez, Felipe Cervantes-Sodi, et al. In situ observations of catalyst dynamics during surface-bound carbon nanotube nucleation. *Nano letters*, 7(3):602–608, 2007.
- [172] Tetsuya Uchiyama, Hideto Yoshida, Yasufumi Kuwauchi, Satoshi Ichikawa, Satoshi Shimada, Masatake Haruta, and Seiji Takeda. Systematic morphology changes of gold nanoparticles supported on ceo2 during co oxidation. *Angewandte Chemie*, 123(43):10339–10342, 2011.
- [173] Hideto Yoshida, Yasufumi Kuwauchi, Joerg R Jinschek, Keju Sun, Shingo Tanaka, Masanori Kohyama, Satoshi Shimada, Masatake Haruta, and Seiji Takeda. Visualizing gas molecules interacting with supported nanoparticulate catalysts at reaction conditions. *Science*, 335(6066):317–319, 2012.

- [174] SB al Vendelbo, Christian Fink Elkjær, H Falsig, I Puspitasari, P Dona, L Mele, B Morana, BJ Nelissen, R Van Rijn, JF Creemer, et al. Visualization of oscillatory behaviour of pt nanoparticles catalysing co oxidation. *Nature materials*, 13(9):884–890, 2014.
- [175] Liuxian Zhang, Benjamin K Miller, and Peter A Crozier. Atomic level in situ observation of surface amorphization in anatase nanocrystals during light irradiation in water vapor. *Nano letters*, 13(2):679–684, 2013.
- [176] Santhosh Chenna, Ritubarna Banerjee, and Peter A Crozier. Atomic-scale observation of the ni activation process for partial oxidation of methane using in situ environmental tem. *ChemCatChem*, 3(6):1051–1059, 2011.
- [177] Peter A. Crozier and Thomas W. Hansen. In situ and operando transmission electron microscopy of catalytic materials. *MRS Bulletin*, 40(1):38–45, 2015.
- [178] Stephanie Mildner, Marco Beleggia, Daniel Mierwaldt, Thomas W Hansen, Jakob B Wagner, Sadegh Yazdi, Takeshi Kasama, Jim Ciston, Yimei Zhu, and Christian Jooss. Environmental tem study of electron beam induced electrochemistry of pr0. 64ca0. 36mno3 catalysts for oxygen evolution. *The Journal of Physical Chemistry C*, volume=119, number=10, pages=5301–5310, year=2015, publisher=ACS Publications.
- [179] Collaborative laboratory and user facility for electron microscopy. *FEI Titan ETEM G2 80–300*.
- [180] John Melngailis. Focused ion beam technology and applications. *Journal of Vacuum Science & Technology B: Microelectronics Processing and Phenomena*, 5(2):469–495, 1987.
- [181] Jacques Gierak. Focused ion beam technology and ultimate applications. *Semiconductor science and technology*, 24(4):043001, 2009.
- [182] Meltem Sezen and M Janecek. Focused ion beams (fib)—novel methodologies and recent applications for multidisciplinary sciences. *Modern Electron Microscopy in Physical and Life Sciences*, 2016.
- [183] Lucille A Giannuzzi et al. Introduction to focused ion beams: instrumentation, theory, techniques and practice. In *SpringerLink*. 2004.
- [184] Alkali-stable positive resist sx ar-p 5900/4. https://www.allresist.com/wp-content/uploads/sites/2/2020/03/SXAR-P5900-4_english_Allresist_product_information.pdf Allresist GmbH, Germany.

- [185] Nicholas TH Farr, Gareth M Hughes, and Cornelia Rodenburg. Monitoring carbon in electron and ion beam deposition within fib-sem. *Materials*, 14(11):3034, 2021.
- [186] Michael Herbig and Ankit Kumar. Removal of hydrocarbon contamination and oxide films from atom probe specimens. *Microscopy Research and Technique*, 84(2):291–297, 2021.
- [187] Vladimir Roddatis, Gaurav Lole, and Christian Jooss. In situ preparation of pr1-xcaxmno3 and la1-xsrxmno3 catalysts surface for high-resolution environmental transmission electron microscopy. *Catalysts*, 9(9), 2019.
- [188] T.C. Isabell and P.E. Fischione. Applications of plasma cleaning for electron microscopy of semiconducting materials. *Materials Research Society*, 1998.

List of Figures

1.1	NOAA Climat change	2
1.2	Electrolytic water splitting	2
1.3	Hydrogen production and safe transport	3
1.4	Electrochemical water splitting	4
2.1	Gibbs free energies	13
2.2	Perovskite structure	15
2.3	OER mechanism	16
3.1	Schematics of Optic ray diagram	20
3.2	Schematics of optic ray diagram	20
3.3	Thickness gradient	21
3.4	Conventional TEM	22
3.5	C_s corrector	25
3.6	Random contrast of A-site	27
3.7	Single A-site unit cell	28
3.8	Adatom contrast calibration	29
3.9	$\text{Pr}_{0.9}\text{Ca}_{0.1}\text{MnO}_3$ A-site and B-site contrast	31
3.10	Elastic and Inelastic scattering	32
3.11	EELS spectrometer	33
3.12	Relative thickness	35
3.13	t/λ of $\text{Pr}_{0.9}\text{Ca}_{0.1}\text{MnO}_3$	36
3.14	Spectrum	37
3.15	Dual EELS	38
3.16	EELS background	39
3.17	Mn valence	40
3.18	Monochromated EELS	41
3.19	ETEM	43
3.20	FIB	45
3.21	Ga Ion-Solid interation	46
3.22	Procedure of surface cleaning and recrystallization	48

List of Tables

3.1	Aberration values for uncorrected state	26
3.2	Aberration values for corrected state	26
3.3	Contrast fitting parameters	30

Author contributions and publications

This cumulative thesis includes the following reprinted publication, manuscripts ready for submission.

The sample preparation and in-situ ETEM experimental work carried out in Chapters 4, 5, 6, and 7 are conducted at Collaborative Laboratory and User Facility for Electron Microscopy in Institut für Materialphysik - Georg-August-Universität Göttingen. Janis Geppert prepared thin films and performed electrochemical measurements for the materials mentioned in Chapters 4, 5, 6. Thin films preparation and electrochemical measurements in Chapter 7 are performed in the group of Dr. Felix Gunkel in Peter Gruenberg Institute, Juelich, Germany. Gaurav Lole performed ETEM observations with the support of Dr. Vladimir Roddatis, Dr. Ulrich Ross, and Dr. Tobias Meyer.

Chapter 4

Vladimir Roddatis (VR), **Gaurav Lole** (GL), and Christian Jooss (CJ). In Situ Preparation of $\text{Pr}_{1-x}\text{Ca}_x\text{MnO}_3$ and $\text{La}_{1-x}\text{Sr}_x\text{MnO}_3$ Catalysts Surface for High-Resolution Environmental Transmission Electron Microscopy. *Catalysts*, 9(9), 2019;

doi.org/10.3390/catal9090751 (see ref [187]).

CJ and VR - conceptualization, GL and VR did ETEM experiments and analysis, VR wrote draft manuscript. VR, GL and CJ did writing, review and editing. VR and GL did visualization. CJ and VR did supervision. CJ and VR did project administration and funding acquisition.

Chapter 5

Gaurav Lole (GL), Vladimir Roddatis (VR), Ulrich Ross (UR), Marcel Risch (MR), Tobias Meyer (TM), Lukas Rump (LR), Janis Geppert (JG), Garlef Wartner (GW), Peter Blöchl (PB), and Christian Jooss (CJ). Dynamic observation of manganese adatom mobility at perovskite oxide catalyst interfaces with wa-

ter. *Communications Materials*, 1(1):1–10, 2020;
doi.org/10.1038/s43246-020-00070-6 (see ref [133]).

GL did most of TEM Lamella preparation. GL did analyse all ETEM experiments, did the pre- and post mortem characterisation of the lamella, carried out image drift correction, and the movies. GL did the EELS analysis, including space dependent valence determination. The ETEM experiments were carried out by GL and VR. GL, UR and TM carried the image simulation analysis. JG and GW performed manganite epitaxy, structural, and electrochemical analysis. MR analyzed and commented on electrochemical data. LR has provided Image simulation software. PB contributed to the theory of the experimental results. CJ calculated the beam effects and water adsorption. GL and CJ wrote the manuscript. All authors discussed, commented, and edited the manuscript.

Publications reprinted in Chapters 4 and 5 present original work by the author. The articles are reprinted under the Creative Commons CC BY 4.0.

Chapter 6

Gaurav Lole (GL), Fatemeh Ebrahimi (FI), Tobias Meyer (TM), Daniel Mierwaldt (DM), Vladimir Roddatis (VR), Janis Geppert (JG), Marcel Risch (MR) & Christian Jooss (CJ). Contrasting PCMO OER catalyst with different valence and covalence: $x = 0.1$ and $x = 0.33$

GL did most of TEM Lamella preparation. GL performed the ETEM experiments with some support of VR and TM. GL did the data analysis as well as did the pre- and post mortem characterisation of the lamella, carried out image drift correction, and the movies. GL did the EELS experiments and data analysis. TM also supported for image simulations. FI and MR analyzed electrochemical data. GL wrote the manuscript under the supervision of CJ. All authors discussed, commented, and edited the manuscript.

Chapter 7

Moritz L. Weber (MW), **Gaurav Lole** (GL), Attila Kormanyos, Alexander Schwiers, Lisa Heymann, Florian D. Speck, Tobias Meyer (TM), Regina Dittmann, Rainer Waser, Serhiy Cherevko, Christian Jooss (CJ), Christoph Baeumer, and Felix Gunkel (FG). Surface dynamics of $\text{La}_{0.6}\text{Sr}_{0.4}\text{CoO}_3$ electrocatalysts during oxygen evolution in alkaline media

Electrochemical, x-ray spectroscopic, and X-ray diffraction experiments and data analysis is carried out in the group of FG. GL performed ETEM experiments. TM supported for ETEM experiments, EELS analysis and image simulations. GL wrote the TEM section of the manuscript and CJ did text polishing.

Chapters 6 and 7 present the submitted manuscripts. The thesis will publish with a one-year restriction to complete the publication procedure in international scientific journals.

List of Abbreviations

ECPT	Electron coupled proton transfer
EELS	Electron energy loss spectroscopy
EFTEM	Energy filter transmission electron microscope
ETEM	Environmental transmission electron microscope
EWS	Electrochemical water splitting
FIB	Focused ion beam
HER	Hydrogen evolution reaction
HRTEM	High resolution transmission electron microscope
LMIS	Liquid metal ion source
NM	Nobel metal
OER	Oxygen evolution reaction
STEM	Scanning transmission electron microscope
TEM	Transmission electron microscope
TM	Transition metal
ZLP	Zero loss peak

Acknowledgments

I am thankful to thesis supervisor Prof Dr. Christian Jooss for his enduring guidance, motivation, and confidence in my doctoral work. I also appreciate Prof Dr. Michael Seibt and Prof Dr. Simone Techert for their support and fruitful discussion throughout this research work.

In-situ ETEM work would not have been possible without Matthias Hahn, Volker Radisch, Tobias Schulz, Dr. Vladimir Roddatis, Dr. Ulrich Ross, and Dr. Tobias Meyer. I want to thank several people for their help and support during the entirety of this thesis.

I am grateful for excellent collaborative work with Dr. Felix Gunkel, Dr. Christoph Baumer and Moritz Weber from the Peter Gruenberg Institute, Juelich. I want to thank Dr. Sreeju Sreekantan Nair Lalithambika for helpful scientific discussions. I thank Prof. Dr. Peter Blöchl and Lukas Rump for their support in theoretical understanding and essential collaboration. I appreciate Dr. Jörg Hoffmann and Dr. Sarah Hoffmann-Urlaub's helpful discussions in the group meetings.

Furthermore, I want to thank all the members of Institut für Materialphysik, Göttingen. Specifically, all my colleagues Saeed, Fatemeh Gottfried, Birte, Max, Frederik, Stephan, Qian, Jonas, Danny, Thomas, Florian, Niklas, Tobias, Natalie, and Annika.

Especially I thank Christine Kuba and Carmen Kaspar for all the administrative work. I am also grateful for the support of Elektronische Werkstatt for their help.

I am grateful to the Deutsche Forschungsgemeinschaft (DFG) for the financial support from the SFB 1073 project C02. I am also thankful to the DFG, International Center for Advanced Studies of Energy Conversion (ICASEC), and the University of Goettingen for allowing me to conduct state-of-the-art research.

Finally, I want to thank all my friends from India and family, mother Suvarna, wife Seema, and especially my son Shlok for their Love and consistent moral support for the entire time.